UNIVERSITY OF TURIN

DOCTORAL THESIS

Solar corona studies from ground-based and space-based observatories

Author:
Alessandro LIBERATORE

Advisor:
Prof. Silvano MASSAGLIA
Co-Advisor:
Prof. Silvano FINESCHI

A Thesis submitted in fulfilment of the requirements
for the degree of Doctor of Philosophy

in the

Solar Physics research group
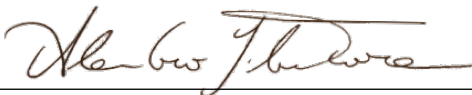INAF - National Institute for Astrophysics

February 28, 2022

Declaration of Authorship

I, Alessandro LIBERATORE, declare that this Thesis titled, "Solar corona studies from ground-based and space-based observatories" and the work presented in it are my own. I confirm that:

- This work was done wholly or mainly while in candidature for a research degree at the University of Turin and as part of the Solar Physics research group at the National Institute for Astrophysics (INAF).

- Where any part of this Thesis has previously been submitted for a degree or any other qualification at this University or any other institution, this has been clearly stated.

- Where I have consulted the published work of others, this is always clearly attributed.

- Where I have quoted from the work of others, the source is always given. With the exception of such quotations, this Thesis is entirely my own work.

- I have acknowledged all main sources of help.

- Where the Thesis is based on work done by myself jointly with others, I have made clear exactly what was done by others and what I have contributed myself.

Signed:

Date: February 28, 2022

Publications

Several original articles, conference papers, and technical reports are part of the results carried out during my PhD research work. In particular, this Thesis contains work that has been adapted from the following list of publications:

1. A. Liberatore et al.; "Sky Brightness Evaluation at Concordia Station, Dome C, Antarctica, for Ground-Based Observations of the Solar Corona", **Solar Physics** 297, 29 (March 2022). DOI: 10.1007/s11207-022-01958-x.

2. A. Liberatore et al.; "In-flight validation of Metis Visible-light Polarimeter Coronagraph on board Solar Orbiter", **Astronomy & Astrophysics**, February 2022 (submitted).

3. A. Liberatore, J. Zender, G. Capobianco, S. Fineschi, L. Zangrilli; "Total Solar Eclipse EKPol data comparison", 2022 (in preparation for **Solar Physics** - results of Chapter 4).

4. A. Liberatore et al.; "PolarCam micropolarizer cameras characterization and usage", **Proc. SPIE** 11852, International Conference on Space Optics — ICSO 2020, 118520W (11 June 2021). DOI: 10.1117/12.2599180.

5. M. Romoli, [...], A. Liberatore, [...]; "First light observations of the solar wind in the outer corona with the Metis coronagraph", **Astronomy & Astrophysics**, 656 (2021) A32. December 14, 2021. DOI: 10.1051/0004-6361/202140980.

6. S. Fineschi, [...], A. Liberatore, [...]; "AntarctiCor: Solar Coronagraph in Antarctica for the ESCAPE Project", **Il Nuovo Cimento (C)**, Article 26 (June 19, 2019). DOI: 10.1393/ncc/i2019-19026-9.

7. V. Andretta, [...], A. Liberatore, [...]; "The first coronal mass ejection observed in both visible-light and UV H I Ly-α channels of the Metis coronagraph on board Solar Orbiter", **Astronomy & Astrophysics**, 656:L14, December 2021. DOI: 10.1051/0004-6361/202142407.

8. C. Grimani, [...], A. Liberatore, [...]; "Cosmic-ray flux predictions and observations for and with Metis on board Solar Orbiter", **Astronomy & Astrophysics**, 656:A15, December 2021. DOI:10.1051/0004-6361/202140930.

9. D. Telloni, [...], A. Liberatore, [...]; "Exploring the Solar Wind from Its Source on the Corona into the Inner Heliosphere during the First Solar Orbiter – Parker Solar Probe Quadrature", **The Astrophysical Journal Letters**, 920(1):L14, October 2021. DOI:10.3847/2041-8213/ac282f.

10. C. Casini, [...], A. Liberatore, [...]; "The Use of the Flat Field Panel for the On-Ground Calibration of Metis Coronagraph on Board of Solar Orbiter.", **International Journal of Aerospace and Mechanical Engineering**, 15(3):128–132, 2021. ISNI:0000000091950263.

Financial supports

Acknowledgements

Abstract

University of Turin
INAF - National Institute for Astrophysics

Doctor of Philosophy

Solar corona studies from ground-based and space-based observatories

by Alessandro LIBERATORE

The present Thesis consists of the experimental study of the solar corona with a focus on data acquisition, data analysis, and instruments calibration. The solar corona is the Sun's outer atmosphere that extends into the solar system. The interaction between plasma and magnetic fields of the solar corona drives the physical phenomena that take place in the heliosphere and that can affect the Earth's magnetosphere. The goal of this work is the diagnostics of some physical parameters of the coronal magnetised plasma as a crucial tool to understand those phenomena. Different instruments designed to diagnose the physical parameters of the coronal plasma through ground-based or space-based are considered for measurements of the polarised continuum or spectral line emissions from the solar corona.

First of all, the results obtained during the total Solar Eclipse in July 2019 in Chile are presented together with the EKPol telescope. The EKPol telescope is equipped with electro-optically modulating Liquid Crystal Variable Retarders (LCVRs) for the polarimetric observation of the solar corona. The use of this technology has been a great ground-based test for the usage of this technology in space-based environments. The results, from the images composition to the electron density profile evaluation, are compared with what was obtained in previous eclipses as well.

After that, the Thesis focuses on the Antarctica solar coronagraph (AntarctiCor) for the "Extreme Solar Coronagraphy Antarctic Program Experiment" (ESCAPE). During three different Antarctic missions (at Concordia Station, Dome-C Antarctic plateau; $\approx$ 3300 m a.s.l.) it was possible to evaluate for the first time the local sky brightness. In optimal atmospheric conditions, the sky brightness has reached very low values of the order of $0.7 - 1 \times 10^{-6} B_{\odot}$. The first observation of the solar corona from Antarctica was possible as well. A quick introduction to the space coronagraph ASPIICS (for the formation flying mission PROBA-3; ready to be launched in 2023) with its peculiarities and analogies with AntarctiCor moves us from the ground-based observations to the space-based ones.

Finally, the last part of this work deals with the Metis space coronagraph onboard Solar Orbiter (launched in February 2020). Metis is a multi-wavelength, externally occulted telescope for the imaging of the solar corona in both visible (polarised) and ultraviolet light. The acquisition of polarised data is possible thanks to the presence of a polarimeter with LCVRs along the Metis visible-light path. It is the first time that this technology is used in a space-based mission. The in-flight validation of the Metis visible light polarimeter, the obtained calibrated polarised brightness, the electron densities map, the first CMEs observation in visible and ultraviolet light, and the first solar wind velocity estimation are presented as part of this Thesis results.

Keywords: Heliophysics; Sun; Solar Corona; Coronagraph; Polarised light.

"I am among those who think that science has great beauty. A scientist in his laboratory is not only a technician, he is also a child place before natural phenomenon, which impress him like a fairy tale."

– Marie Curie

Preface

This Thesis consists of pure experimental and data analysis work on the Solar Corona. On the other hand, having been part of my PhD studies, I introduced also the main theory about the Sun and Solar Physics. My idea is to give a complete overview of the subject to better understand it not only from an experimental point of view but from a theoretical one as well. For this reason, I decided to add some useful complementary theories even if not strictly necessary for a full comprehension of the obtained results. In particular, it could be useful to divide the present work into three main blocks (Figure 1):

- <u>Block 1</u> (Chapter 1, 2): Introduction to the Thesis work and to the main useful physical equations with a focus on the polarised light physics (necessary to present the Thesis results in a proper way).

- <u>Block 2</u> (Chapter 3): General introduction to the solar physics. This Block is focused on the solar corona and its physical laws.

- <u>Block 3</u> (Chapter 4, 5, 6): Description of my PhD project and scientific goals. Each part of the project is introduced with a general overview and deepened with more emphasis and details about personal work and the obtained results.

After that, a final summary on my PhD project results and possible improvements and future works is presented in Chapter 7. A precise colour code[1] is used for the entire work to help the reader.
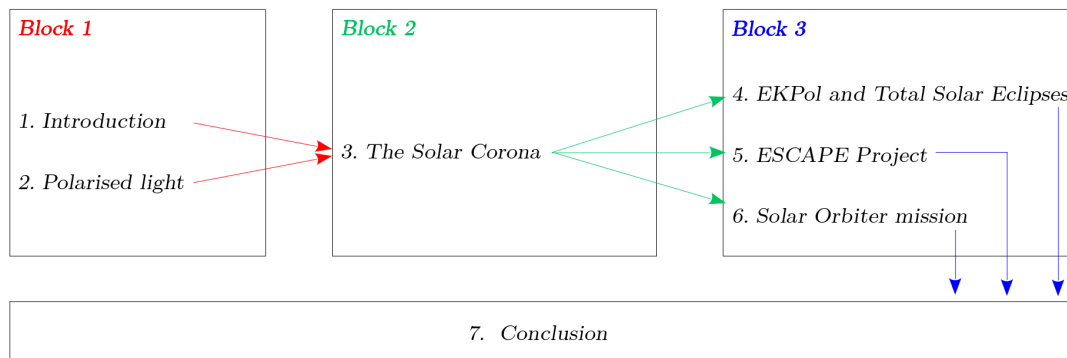
FIGURE 1: Thesis block structure and relative Chapters.

Most of the theory about the Sun and the Solar Corona physics in the present work comes from the course *Heliophysics and Space Weather* (A.Y. 2018-2019) held by Prof. Alessandro Bemporad at the University of Turin and from adaptations of different Chapters of the following books: "Solar Physics" (Degl'Innocenti, 2007) and "Physics of the Solar Corona" (Aschwanden, 2006). Part of the theory comes also from personal notes taken during the NASA Heliophysics School 2020 that I had the opportunity to follow during my PhD studies.

---

[1]Colour code: black (standard text), magenta (citations), light red (references to document elements), dark red (hyperlinks - URLs).

Contents

Chapter 1

Introduction

All we know about life is based on the interpretation of different information coming from the Universe. In particular, the interpretation of photons by our brain is probably the main and most important one. Without sight, humans would not have been able to make an infinite number of fundamental discoveries. Inter alia, we would not have been able to realise that we are living in a sea of planets, stars, and other spectacular objects. However, with our naked eyes, we can extract information from a very small part of the entire variety of photons coming to us. Indeed, just the *visible light range* of the electromagnetic spectrum (Figure 1.1) is not black to our eye. On the other hand, we can cover and study the entire spectrum by using special instruments.
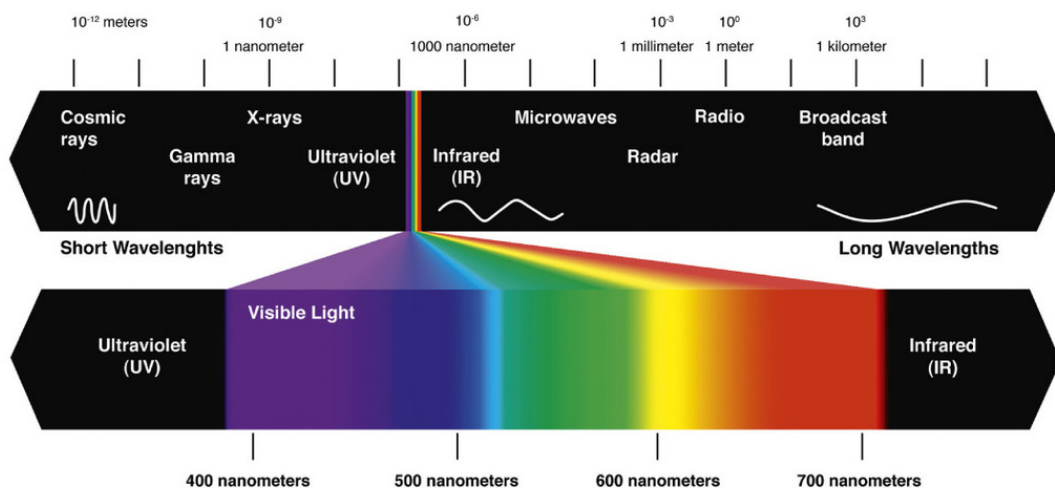
FIGURE 1.1: Electromagnetic spectrum. A human eye can see only in the tiny visible light band ($\approx 380 - 720\,\mathrm{nm}$).

Why can we see just visible light? It is not possible to discuss here a complete response to this question but we can give a first brief outline of the question and underline some crucial facts. Biologically, we evolve by interacting with the environment in which we are immersed. We live on a planet near a star (the Sun) with the peak of emission in the visible wavelength band (Figure 1.2). Moreover, the Earth's atmosphere blocks a large part of the electromagnetic spectrum but it is transparent to the visible light. With an evolutionary adaptation process, our eyes developed the highest sensitivity in this part of the spectrum (where the Sun provides our life-supporting daylight). It is reasonable to think that our knowledge about life and the Universe comes mainly from the interpretation that our brain gives to the photons coming directly, or indirectly, from the Sun.
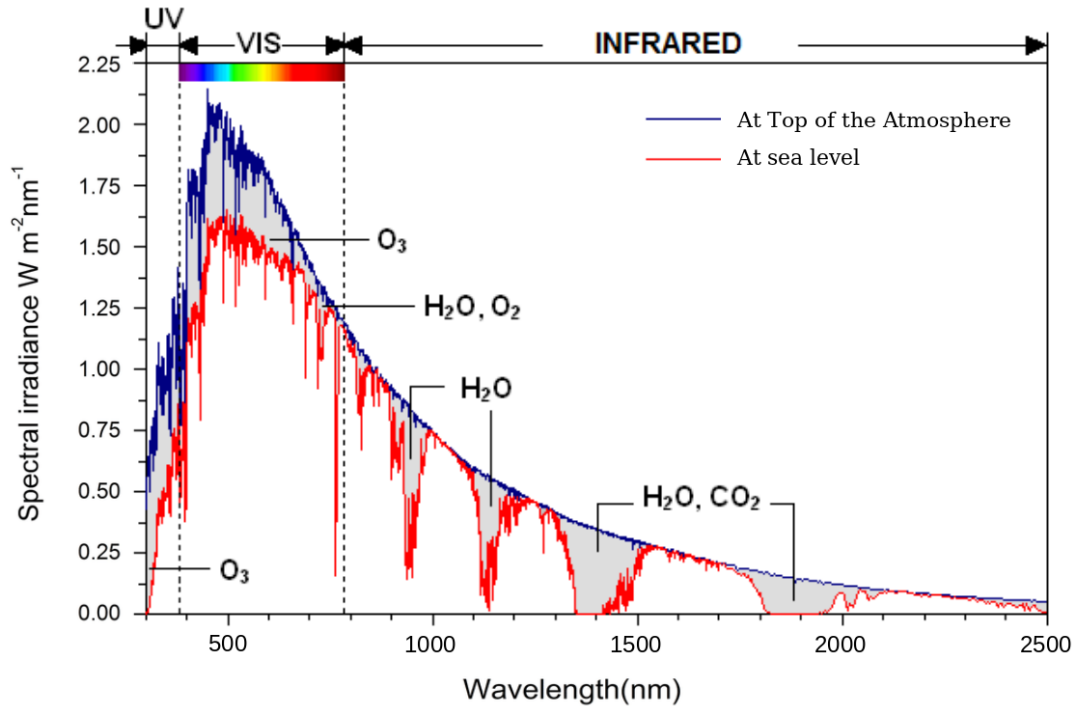
FIGURE 1.2: Standard solar spectrum [adapted from the American Society for Testing and Materials (ASTM)].

1.1 Why do we study the Sun?

It is important to realise that our knowledge and curiosity are born from our senses. We look at the Sun rising every day. It is big, it is bright, it warms us up and gives us light. Its easy visibility and proximity to the Earth, together with the natural curiosity of human beings are enough reasons to push people to study our star over the centuries. But there are many other reasons why we are interested in studying it. The Sun is the fuel of life. Thanks to the Sun, we have solar energy, biomass energy, wind energy, geothermal energy, and hydro-power energy. Moreover, the Earth is immersed in the extended solar atmosphere (the heliosphere) and the life on our planet is strictly connected with the solar behaviour[1]. Furthermore, the Sun is a great laboratory of plasma thanks to which it is possible to study many phenomena otherwise difficult or impossible to reproduce on Earth (e.g., magnetic reconnection processes, emission spectroscopy of highly ionised heavy ions such as FeXIV, etc...).

The research field involved in the study of the Sun and its interaction with the rest solar system is the *Heliophysics*. In this Thesis, we are going to explore one of the many topics covered by the Heliophysics. In particular, we will deal with the outermost layer of the solar atmosphere: the *solar corona*. The solar corona is the Sun's outer atmosphere that extends into the solar system. The interaction between plasma and magnetic fields of the solar corona drives the physical phenomena that take place in the heliosphere and that can affect the Earth's magnetosphere. The goal of this work is the diagnostics of some physical parameters of the coronal magnetised plasma as a crucial tool to understand those phenomena.

---

[1]For example the heliosphere, together with the Earth magnetosphere, gives a magnetic shield to our planet from the cosmic radiations (that we know to be biologically dangerous for human beings).

The study of the Sun-Earth connection can help us to predict/deal with the most violent solar events such as flares or coronal mass ejections (CMEs) and their interaction with our planet. This is essential to prevent damages to satellite communication systems, to on-ground electronics, to astronauts, etc. . . with negative consequences at the economic level as well (Baker et al., 2008). The discipline that deals with all these aspects of the Sun-Earth interaction is known as *Space Weather* and it is of fundamental importance if we want a future outside our planet. Although closely related, we will not delve into many aspects of Space Weather in this Thesis. Anyway, more information about this discipline can be found in: Baker et al., 2019; Moldwin, 2008; Bothmer and Daglis, 2007. For now, it could just be useful to point out its peculiarities and connections with Heliophysics. To do that, we can refer to the "definitions" given by the NASA *Heliophysics research groups* (Baker et al., 2008):

Heliophysics

helio-, **pref.**, on the Sun and environs, from the Greek helios.
physics, **n.**, the science of matter and energy and their interactions.

Heliophysics is the

- *comprehensive new term for the science of the Sun - Solar System Connection.*
- *exploration, discovery, and understanding of our space environment.*
- *system science that unites all of the linked phenomena in the region of the cosmos influenced by a star like our Sun.*

Heliophysics concentrates on the Sun and its effects on Earth, the other planets of the solar system, and the changing conditions in space. Heliophysics studies the magnetosphere, ionosphere, thermosphere, mesosphere, and upper atmosphere of the Earth and other planets. Heliophysics combines the science of the Sun, corona, heliosphere and geospace. *Heliophysics encompasses Space Weather and radiation*, cosmic rays and particle acceleration, dust and magnetic reconnection, solar activity and stellar cycles, aeronomy and space plasmas, magnetic fields and global change, and the interactions of the solar system with our galaxy.

From NASA's "Heliophysics. The New Science of the Sun - Solar System Connection: Recommended Roadmap for Science and Technology 2005 - 2035."

Space weather

Space weather refers to the variable state of the coupled space environment related to changing conditions on the Sun and in the terrestrial atmosphere, specifically those conditions that can influence the performance and reliability of space-borne and ground-based technological systems, and that can directly or indirectly endanger human well-being.

1.2 The study of the Sun over the centuries

All the reasons presented in the previous section still entice scientists all over the world to spend their time and energy studying our stars. Since 5000 years ago the Babylonian priests used the Babel Tower as a solar observatory. They were able to predict the relative positions of the Sun, Earth, and Moon. In 2800 B.C. the pyramids of Giza were built by aligning them with the rising Sun during the spring equinox. Temples were not only dedicated to religious purposes but were astronomical observatories as well. Later in time, in the pre-Columbian era (1300 A.D.), Maya managed to draw up a list of more than a thousand eclipses. They recorded the cycles of the

Sun, Moon, and the planet Venus. At the beginning of 1600 A.D., thanks to the invention of the telescope, the first observations with a large magnification of the Moon, Sun, and planets were performed. In 1610 Galileo Galilei observes, for the first time, the sunspots and the solar rotation. In this period the idea was born that Sun and stars are similar bodies. Moreover, with the discovery of the electromagnetic spectrum (from the beginning of 1800 [IR] to the end of 1800 [X-ray]), the theory of the light (by Maxwell in 1864) and the birth of spectroscopy (1800-1900) the study of the Sun has made progress as well. In 1814, Fraunhofer discovered[2] a set of dark lines in the solar spectrum and began to study and measure the wavelengths where these features were observed (Hearnshaw, 2014). He mapped over 570 lines, designating the principal ones with the letters A, ..., K, and the weaker lines with other letters (Figure 1.3). In Table 1.1, the wavelengths associated with the main Fraunhofer lines are summarised. To date, approximately 25.000 Fraunhofer lines have been identified (Figure 1.4). About 45 years later, Kirchhoff and Bunsen noticed that several of those lines coincide with the characteristic emission lines identified in the spectra of heated elements (Kirchhoff, 1860). It was correctly deduced that those dark lines in the solar spectrum are caused by absorption by chemical elements in the solar atmosphere.[3]
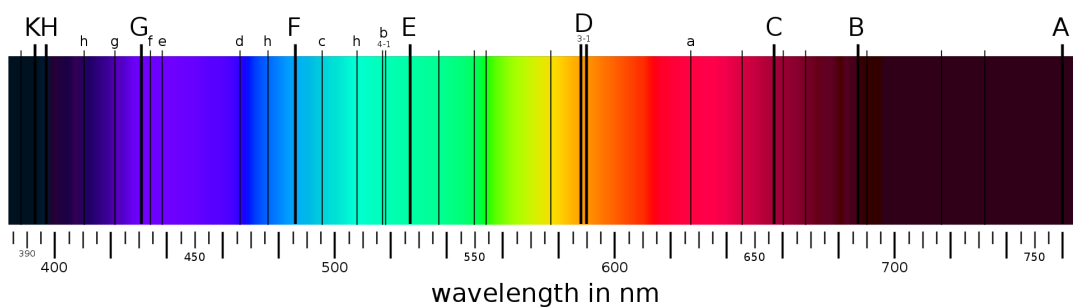
FIGURE 1.3: Solar spectrum with Fraunhofer lines. Fraunhofer used letters from A through H-K for the main lines while other letters for the weaker ones.

Just after the Second World War, the technology of rockets and satellites develops. Thanks to these new technologies, it was possible to observe the sunlight (and the universe) not filtered by the Earth's atmosphere (Figure 1.5). The study of the universe and our Sun in UV, X-ray, and γ-ray began.

Around 1949, thanks to NRL rockets, the HI Lyman α line (121.6 nm) is discovered and in 1963 the first image of the extended corona from space is obtained (Tousey, 1961). From the second half of 1900 many space missions[4] were dedicated to the study of the Sun in different ranges of the electromagnetic spectrum. Among these, we can find the *Solar & Heliospheric Observatory* (SOHO), the *Solar Terrestrial Relations Observatory* (STEREO) and the *Solar Dynamics Observatory* (SDO). SOHO, orbiting in the L1 Lagrange point, is a NASA/ESA mission designed to study the Sun inside

---

[2]In 1802, the English chemist William Hyde Wollaston was the first person to note the appearance of a number of dark features in the solar spectrum (Wollaston, 1802). In 1814, Fraunhofer independently rediscovered those lines and began a systematic study.

[3]Indeed, some of the observed features were identified as *telluric lines*. The *telluric contamination* is the contamination of astronomical spectra by the Earth's atmosphere. In our particular case, the lines originated from absorption by oxygen molecules in the Earth's atmosphere.

[4]There have been many other relevant missions not mentioned in this Thesis for reasons of time and space (Skylab, Hinode, etc...). Only the most recent/still in operation, as well as the most important ones, were explicitly mentioned.

TABLE 1.1: Wavelengths associated with the main Fraunhofer lines. The D_1 and D_2 lines form the so-called *sodium doublet*. Its centre wavelength (589.29 nm) is designated with the letter D (some line name/designation changed a bit during the years). Today we know that A and B are telluric lines due to the presence of O_2 molecules in the Earth's atmosphere (grey in table).

Designation	Element	Wavelength λ [nm]
A	O_2	759.370
B	O_2	686.719
C	H_α	656.281
D_1	Na	589.592
D_2	Na	588.995
E_2	Fe	527.039
F	H_β	486.134
G'	H_γ	434.047
H	Ca^+	396.847
K	Ca^+	393.366
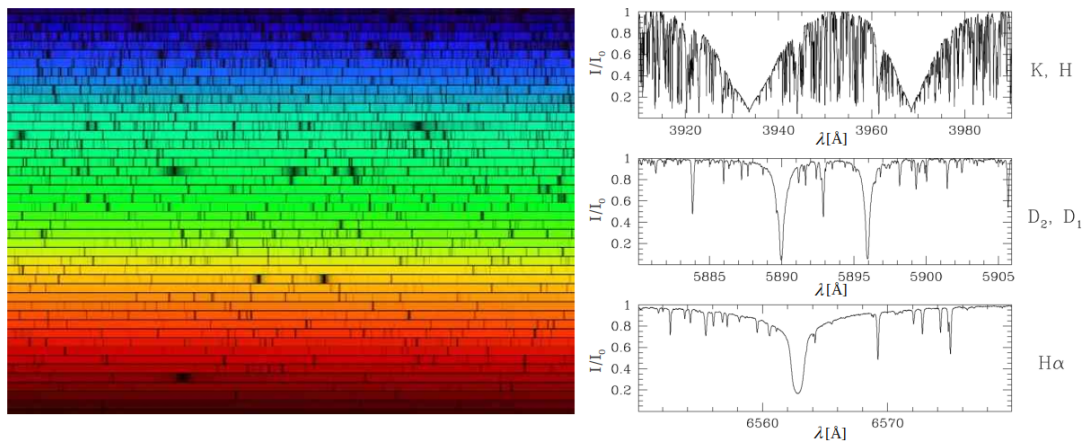
FIGURE 1.4: Visible solar spectrum. The left image contains many spectra of about 100 Å. It is possible to see that, for the lower wavelengths, the density and the width of the lines increases. On the right, a focus on five different Fraunhofer lines (CaII doublet on the top, NaI doublet in the middle, and HI on the bottom).

out, from its internal structure to the extensive outer atmosphere, to the solar wind that blows across the solar system. SOHO was launched on a Lockheed Martin Atlas II AS launch vehicle in December 2nd, 1995 from Cape Canaveral. The STEREO NASA mission was instead composed of two nearly identical spacecraft (STEREO-A and STEREO-B; one ahead of Earth in its orbit, the other trailing behind) that enable stereoscopic imaging of the Sun and solar phenomena (such as Coronal Mass Ejections - CMEs) tracing the flow of energy and matter from the Sun to Earth. The two STEREO spacecraft were launched on October 26, 2006, from Cape Canaveral on a Delta II 7925-10L launcher into highly elliptical geocentric orbits. Finally, SDO is a NASA mission designed to help us to understand the Sun's influence on Earth and near-Earth space by studying the solar atmosphere in many wavelengths simultaneously. SDO was launched on February 11th, 2010 on an Atlas V from SLC 41 still
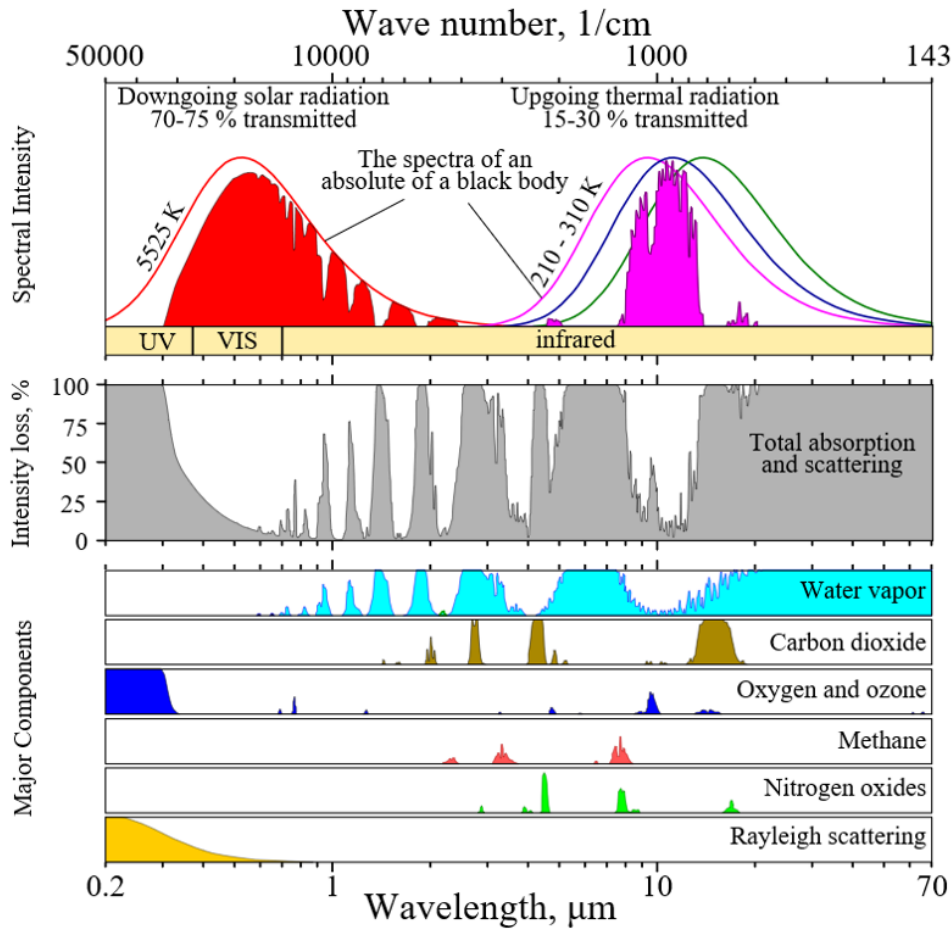
FIGURE 1.5: Earth atmospheric transmission for different wavelength
and major absorption components.

from Cape Canaveral and was placed into a circular geosynchronous orbit around the Earth. To date, both SOHO and SDO are still working together with many other space missions. STEREO-A is also still operational but contact with STEREO-B was lost in 2014 after entering an uncontrolled spin preventing its solar panels from generating enough power.

Among the most recent space missions we can find the *Parker Solar Probe* (PSP), *Solar Orbiter* (SolO) and the *Project for On-Board Autonomy-3* (PROBA-3). The PSP NASA space mission is the first spacecraft to fly into the low solar corona. It will assess the structure and dynamics of the solar coronal plasma and magnetic field, the energy flow that heats the solar corona and propel the solar wind, and the mechanisms that accelerate solar energetic particles (SEPs). PSP was launched on August 12th, 2018 from Cape Canaveral on a Delta IV-Heavy with Upper Stage. On October 29th, 2018 (at about 18:04 UTC) the spacecraft became the closest-ever artificial object to the Sun.[5] Solar Orbiter is an ESA mission with a strong NASA contribution that wants to perform detailed measurements of the inner heliosphere and nascent solar wind and close observations of the polar regions of the Sun. Launched on February 10th, 2020 from Cape Canaveral, it is the first solar mission to go outside the ecliptic plane. The S/C will reach a minimum distance of 0.28 AU from

---

[5]Considering the extreme proximity to the Sun ($\approx 6.9 \times 10^6$ km from the Sun surface), the spacecraft's systems are protected from the extreme heat and radiation by a carbon-foam-filled solar shield atop the spacecraft body.

the Sun with remote sensing instruments on-board! Finally, the PROBA-3 ESA mission consists of two independent spacecraft: a Coronagraph Spacecraft (CSC) and an Occulter Spacecraft (OSC). Both spacecraft will fly close to each other on a highly elliptical orbit around the Earth and they will line up to cast a precise shadow across space to block out the solar disc and recreate an artificial solar eclipse to study the solar corona. To date, the launch is planned for half of 2023. Being part of the Thesis work, more details about the last two missions can be found in the next Chapters.

Many other space missions study the Sun's influence on space, Earth and other planets. The main ones are summarised in Figure 1.6.
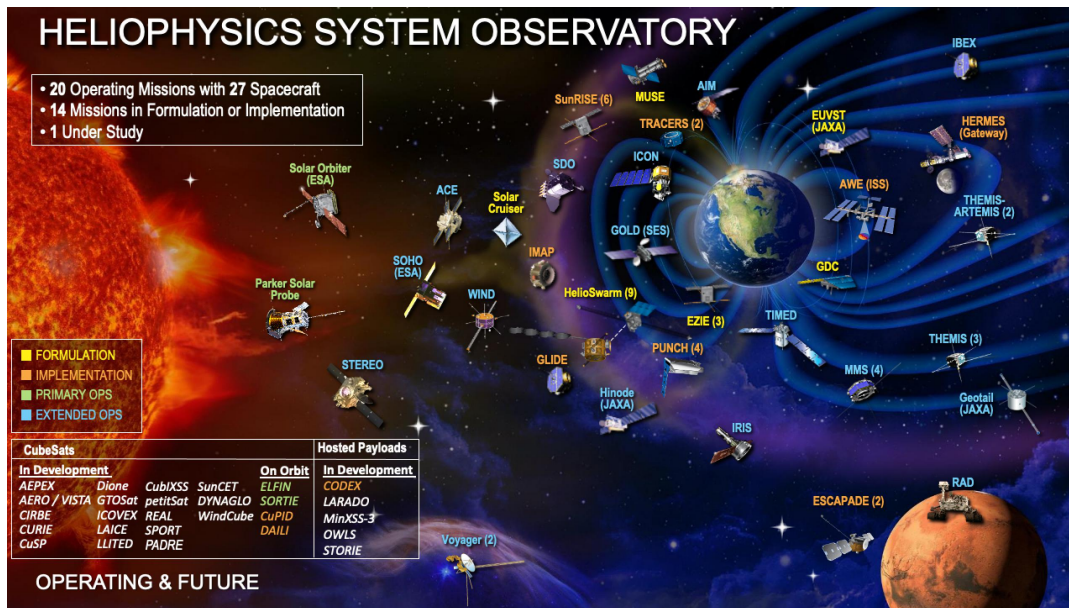
FIGURE 1.6: Heliophysics fleet diagram (updated April 7, 2022). A fleet of spacecraft strategically placed by space agencies throughout our heliosphere for a holistic study of the Sun's influence on space, Earth and other planets (© NASA).

With this Thesis, I would like to continue the journey on the discovery of our star. In the next Chapters, after an introduction to some useful fundamental physics (Chapter 2 - for a full comprehension of the results presented in this work), I summarised the main Sun characteristic by moving from the Sun centre to the solar atmosphere (Chapter 3) with a focus on the solar outer atmosphere: the solar corona. After these Chapters, I show in detail the projects I worked on during my PhD studies. This part of the Thesis is fully based on personal experimental researches and contains new scientific results. In particular, in these Chapters, I will deal with the calibration, the data acquisition, and the data-analysis aspects of different ground-based and space-based missions with the respective instrumentation. Starting from ground-based observations, I introduce the EKPol telescope and the results obtained during the *total solar eclipse* in July 2019 (Chapter 4). Later, I describe the ESCAPE project for the ground-based observation of the solar corona from Antarctica and its connection with the PROBA-3 space mission (Chapter 5). After that, I show the main calibrations and the first mission results of Metis; the coronagraph on-board the Solar Orbiter ESA mission (Chapter 6). Finally, a summary of all the obtained results is presented as the conclusion of the Thesis work (Chapter 7).

Chapter 2

Polarised light

In this Chapter we go more into detail about the physics of polarised light obtaining the main equations and physics laws necessary for a full comprehension of the results presented in Chapters 4, 5, 6. This Chapter is mainly based on Collett, 1992 and Degl'Innocenti, 2007.

Let's start underlying that the light consists of a *transverse electromagnetic wave*. This means that the electric and magnetic field vectors oscillate perpendicular to the direction of propagation. The *polarisation* describes the vector properties of the oscillating electric field.[1]

A monochromatic wave of constant intensity propagating along the z-axis [thus, $E(z = 0, t)$] will have the electric field lying on the xy-plane (Figure 2.1) and we can write its components as:

$$\begin{cases} E_x(z,t) = E_{0x} \cos\left(\tau + \delta_x(t)\right) \\ E_y(z,t) = E_{0y} \cos\left(\tau + \delta_y(t)\right) \end{cases} \quad (2.1)$$

FIGURE 2.1: Electric field components for a monochromatic wave moving along the z-axis.

where E_{0i} are the *amplitudes*, $\tau = \omega t - kz$ is the propagator, ω the *wave frequency* and the $\delta_i(t)$ are the *instantaneous phases*. The difference between the instantaneous phases gives the *relative phase* $\delta(t)$ defined as: $\delta(t) = \delta_y(t) - \delta_x(t)$.

By propagating, $E_x(z,t)$ and $E_y(z,t)$ generate a vector $\vec{E}$ which describes a locus of points in space that give life to an *ellipse*. Indeed, from the previous equations we obtain the following equations:

$$\begin{cases} E_x/E_{0x} = \cos\tau\cos\delta_x - \sin\tau\sin\delta_x \\ E_y/E_{0y} = \cos\tau\cos\delta_y - \sin\tau\sin\delta_y \end{cases} \quad (2.2)$$

Then, we have:

$$\frac{E_x^2}{E_{0x}^2} + \frac{E_y^2}{E_{0y}^2} - 2\frac{E_x E_y}{E_{0x}E_{0y}}\cos\delta = \sin^2\delta \quad (2.3)$$

---

[1]The choice to consider the oscillation of the electric field rather than that of the magnetic field is just a convention. In particular, as we will see, the phase difference between the E_x and E_y components of the electric field highlights the polarisation state of the light beam.

All quantities are intended as function of time (e.g., $E_x \equiv E_x(t)$). The *Lissajous curve*[2] obtained from Eq. 2.3 is the so-called *polarisation ellipse*[3] (Figure 2.2). The presence of the third term in Eq. 2.3 shows that, generally, the ellipse is rotated by an angle ψ (Eq. 2.4).
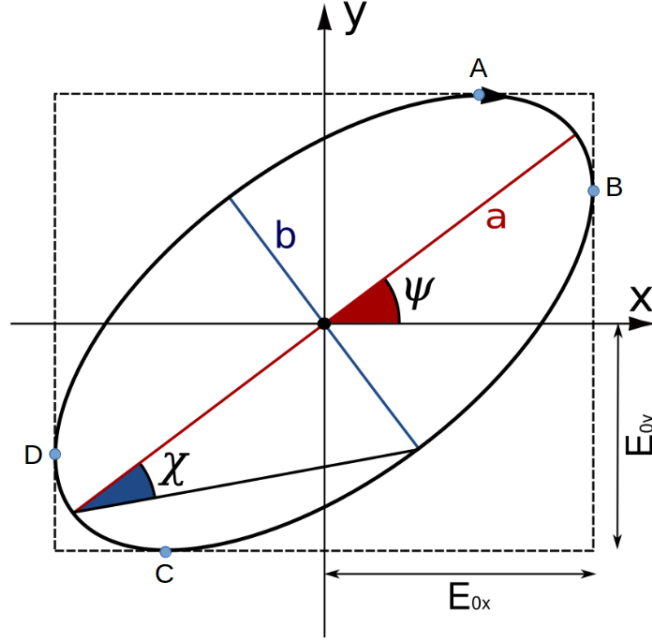
FIGURE 2.2: Polarisation ellipse.

Based on the values of δ, the ellipse can degenerate into a straight line or a circle as shown in Figure 2.3.

The *orientation* of the polarisation ellipse (i.e., the direction of the major semi-axis) is given by the angle ψ. It is the so-called *rotation angle* or *orientation angle* and it is defined as (Shurcliff, 1962):

$$\tan 2\psi = \frac{2E_{0x}E_{0y}}{E_{0x}^2 - E_{0y}^2} \cos \delta \qquad (0 \le \psi < \pi) \tag{2.4}$$

Instead, the *shape* of the ellipse is described by the χ angle called *ellipticity angle* and defined, in terms of phase and electric field components, as (Shurcliff, 1962):

$$\sin 2\chi = \frac{2E_{0x}E_{0y}}{E_{0x}^2 + E_{0y}^2} \sin \delta \qquad \left(-\frac{\pi}{4} < \chi \le \frac{\pi}{4}\right) \tag{2.5}$$

When the relative phase is not constant over time but varies randomly (i.e., the time average is $\langle \delta(t) \rangle = 0$), the light is *completely non-polarised*: in this case, it is an inconsistent superposition of linearly polarised light.[4]

---

[2] A Lissajous curve is an oval with eccentricity and direction of rotation determined by a phase shift.

[3] The maximum ellipse area is obtained as: $A_{max} = \pi E_{0x}E_{0y} \sin \delta = \pi E_{0x}E_{0y}$.

[4] Between the two extremes (totally polarised and *non*-polarised light), the case of partially polarised light is the superposition of a fully polarised part with a completely non-polarised one. Its degree of polarisation is given by the ratio of the amplitudes of the two components.
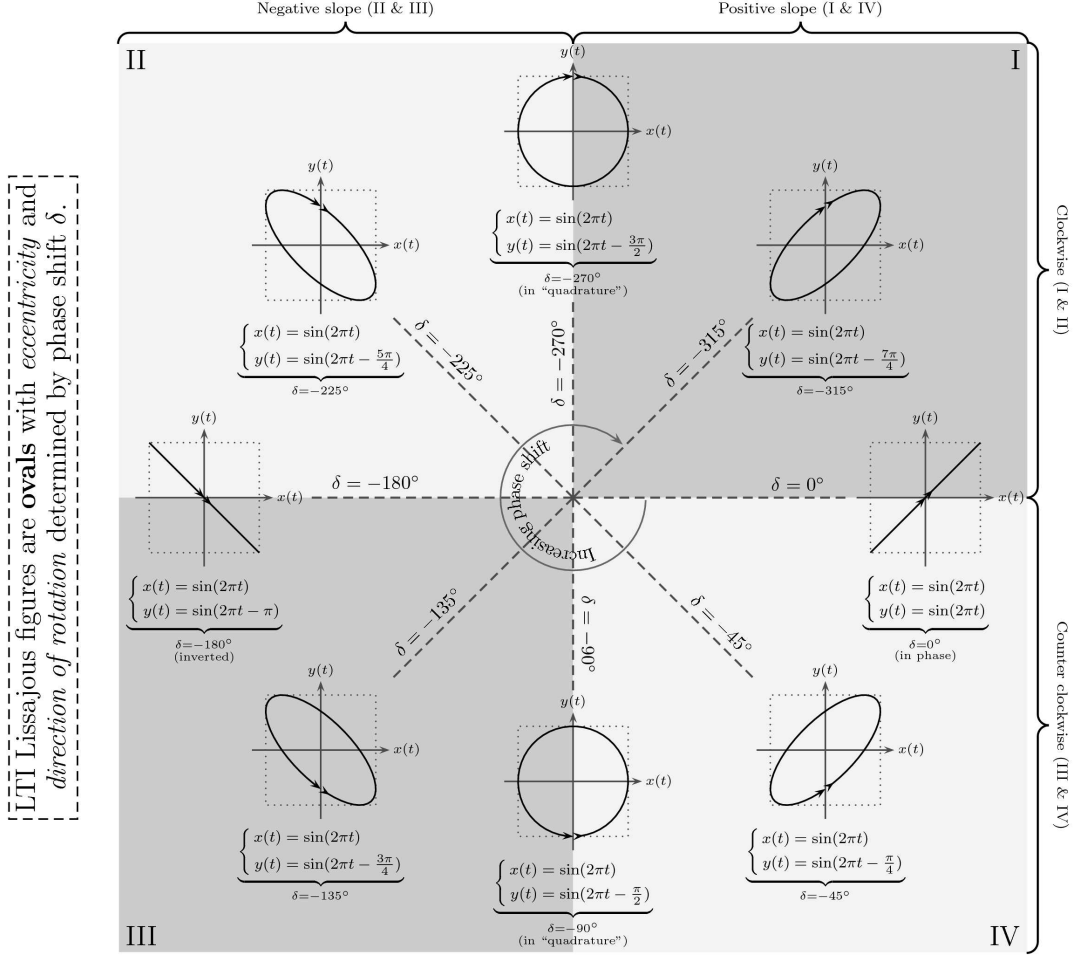
FIGURE 2.3: Polarisation ellipses for unitary values of E_{0x}, E_{0y} and ω for different relative phase $\delta(t)$ values.

2.1 Stokes formalism

The polarisation ellipse provides a valid mathematical model for the description of the polarimetric properties of light. However, this model is inadequate if measurements are to be made. Experimentally it is not possible to observe the polarisation ellipse. In 1852 Stokes introduced four parameters known as *Stokes parameters* (defined starting from the temporal averages of the radiation intensity values) through which it is now possible to describe the polarisation of light.

Considering monochromatic waves, the amplitude and phase remain constant over time and Eq. 2.3 becomes:

$$\frac{E_x^2(t)}{E_{0x}^2} + \frac{E_y^2(t)}{E_{0y}^2} - 2\frac{E_x(t)E_y(t)}{E_{0x}E_{0y}}\cos\delta = \sin^2\delta \qquad (2.6)$$
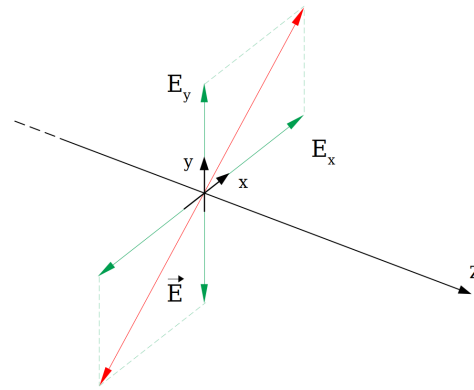
In order to represent this equation in terms of observables of the optical field, we have to take a temporal average over the observation time:[5]

$$\frac{\langle E_x^2(t)\rangle}{E_{0x}^2} + \frac{\langle E_y^2(t)\rangle}{E_{0y}^2} - 2\frac{\langle E_x(t)E_y(t)\rangle}{E_{0x}E_{0y}}\cos\delta = \sin^2\delta \qquad (2.7)$$

---

[5]We can consider time $\to \infty$ since it is much greater than a single oscillation.

where:

$$\langle E_i(t)E_j(t)\rangle = \lim_{T\to\infty} \frac{1}{T}\int_0^T E_i(t)E_j(t)dt \qquad (2.8)$$

Multiplying Eq. 2.7 by $4E_{0x}^2 E_{0y}^2$:

$$4E_{0y}^2\langle E_x^2(t)\rangle + 4E_{0x}^2\langle E_y^2(t)\rangle - 8E_{0x}E_{0y}\langle E_x(t)E_y(t)\rangle\cos\delta = (2E_{0x}E_{0y}\sin\delta)^2 \qquad (2.9)$$

From Eqs. 2.1 and considering that:

$$\begin{cases} \langle E_x^2(t)\rangle = \frac{1}{2}E_{0x}^2 \\ \langle E_y^2(t)\rangle = \frac{1}{2}E_{0y}^2 \\ \langle E_x(t)E_y(t)\rangle = \frac{1}{2}E_{0x}E_{0y}\cos\delta \end{cases} \qquad (2.10)$$

we obtain:

$$2E_{0x}^2 E_{0y}^2 + 2E_{0x}^2 E_{0y}^2 - (2E_{0x}E_{0y}\cos\delta)^2 = (2E_{0x}E_{0y}\sin\delta)^2 \qquad (2.11)$$

If we subtract $E_{0x}^4 + E_{0y}^4$ from both sides of Eq. 2.11 it is possible to rearrange it obtaining:

$$(E_{0x}^2 + E_{0y}^2)^2 - (E_{0x}^2 - E_{0y}^2)^2 - (2E_{0x}E_{0y}\cos\delta)^2 = (2E_{0x}E_{0y}\sin\delta)^2 \qquad (2.12)$$

The quantities in the brackets can be renamed as:

$$\begin{aligned} S_0 &= E_{0x}^2 + E_{0y}^2 \\ S_1 &= E_{0x}^2 - E_{0y}^2 \\ S_2 &= 2E_{0x}E_{0y}\cos\delta \\ S_3 &= 2E_{0x}E_{0y}\sin\delta \end{aligned} \qquad (2.13)$$

$$\Rightarrow S_0^2 = S_1^2 + S_2^2 + S_3^2 \qquad (2.14)$$

that are the so called *Stokes parameters*. These parameters are real quantities (all four parameters are in terms of intensity!) and they are just the *observables* of the polarisation ellipse. In particular, we have:

- S_0 = total intensity;

- S_1 = parameter for the horizontal/vertical polarisation;

- S_2 = parameter for the polarisation at $\pm 45°$;

- S_3 = parameter that describes the circular polarisation [Left Hand Circular (LHC) and Right Hand Circular (RHC)].

Eq. 2.14 is valid only for *fully* polarised waves. In general (therefore also for *partially* polarised light) we have that:[6]

$$S_0^2 \geq S_1^2 + S_2^2 + S_3^2 \qquad (2.15)$$

---

[6]It can be proved through the Schwartz inequality.

The set of Stokes parameters forms the so-called *Stokes vector*. It is possible to represent the Stokes vector as a column vector:

$$\mathbf{S} = \begin{pmatrix} S_0 \\ S_1 \\ S_2 \\ S_3 \end{pmatrix} = \begin{pmatrix} E_{0x}^2 + E_{0y}^2 \\ E_{0x}^2 - E_{0y}^2 \\ 2E_{0x}E_{0y}\cos\delta \\ 2E_{0x}E_{0y}\sin\delta \end{pmatrix} \tag{2.16}$$

Stokes' parameters allow us to derive the *polarised light intensity*: [7]

$$P = \sqrt{S_1^2 + S_2^2 + S_3^2} \tag{2.17}$$

If we are interested in the only linear polarisation, the S_3 term is null and we can write the *linearly* polarised light intensity as:

$$P = \sqrt{S_1^2 + S_2^2} \tag{2.18}$$

From P we are able to evaluate the *degree of polarisation DoP* for each state of polarisation. To derive its explicit form with the use of Stokes' parameters, we can consider two beams of light; a polarised and a not-polarised one. We have that:

$$\mathbf{S}^{(p)} = \begin{pmatrix} \sqrt{S_1^2 + S_2^2 + S_3^2} \\ S_1 \\ S_2 \\ S_3 \end{pmatrix} \rightarrow \mathbf{S}^{(u)} = \begin{pmatrix} S_0 - S_0^{(p)} \\ 0 \\ 0 \\ 0 \end{pmatrix} \tag{2.19}$$

Where $p \equiv$ polarised and $u \equiv$ unpolarised. From which we can rewrite P as:

$$DoP = \frac{I_{pol}}{I_{tot}} = \frac{S_0^{(p)}}{S_0^{(p)} + S_0^{(u)}} = \frac{\sqrt{S_1^2 + S_2^2 + S_3^2}}{S_0} \qquad (0 \leq DoP \leq 1) \tag{2.20}$$

If the light is fully polarised $\rightarrow DoP = 1$, if the light is not polarised $\rightarrow DoP = 0$ and if the light is partially polarised $\rightarrow 0 < DoP < 1$. It is also possible to distinguish between a degree of *linear* polarisation $DoLP$ and a degree of *circular* polarisation $DoCP$:

$$DoLP = \frac{\sqrt{S_1^2 + S_2^2}}{S_0} \qquad\qquad DoCP = \frac{S_3}{S_0} \tag{2.21}$$

It is also possible to evaluate the *Angle of Linear Polarisation* (AoLP) by using:

$$AoLP = \frac{1}{2}\arctan\left(\frac{S_2}{S_1}\right) \tag{2.22}$$

---

[7]Solar physicists usually refer to this quantity as *pB*. In the following Chapters, we will generally accept this convention.

Considering the Stokes vector we can also write the column vectors associated with a particular states of polarisation. In particular:

- No-Polarisation (NP)

$$\mathbf{S} = I_0 \begin{pmatrix} 1 \\ 0 \\ 0 \\ 0 \end{pmatrix} \qquad (2.23)$$

where $I_0 \equiv$ total intensity.

- Linear Horizontal Polarisation (LHP)

$$\mathbf{S} = I_0 \begin{pmatrix} 1 \\ 1 \\ 0 \\ 0 \end{pmatrix} \qquad (2.24)$$

where $I_0 = E_{0x}^2 \equiv$ total intensity (considering that $E_{0y}^2 = 0$).

- Linear Vertical Polarisation (LVP)

$$\mathbf{S} = I_0 \begin{pmatrix} 1 \\ -1 \\ 0 \\ 0 \end{pmatrix} \qquad (2.25)$$

where $I_0 = E_{0y}^2 \equiv$ total intensity (considering that $E_{0x}^2 = 0$).

- Linear Horizontal at 45° (L+45)

$$\mathbf{S} = I_0 \begin{pmatrix} 1 \\ 0 \\ 1 \\ 0 \end{pmatrix} \qquad (2.26)$$

where $I_0 = 2E_0^2 \equiv$ total intensity (considering $E_{0x} = E_{0y} = E_0$ and $\delta = 0°$).

- Linear Horizontal at -45° (L-45)

$$\mathbf{S} = I_0 \begin{pmatrix} 1 \\ 0 \\ -1 \\ 0 \end{pmatrix} \qquad (2.27)$$

where $I_0 = 2E_0^2 \equiv$ total intensity (considering $E_{0x} = E_{0y} = E_0$ and $\delta = 180°$).

- Right-Hand Circular Polarisation (RHC)

$$\mathbf{S} = I_0 \begin{pmatrix} 1 \\ 0 \\ 0 \\ 1 \end{pmatrix} \tag{2.28}$$

where $I_0 = 2E_0^2 \equiv$ total intensity (considering $E_{0x} = E_{0y} = E_0$ and $\delta = 90°$).

- Left-Hand Circular Polarisation (LHC)

$$\mathbf{S} = I_0 \begin{pmatrix} 1 \\ 0 \\ 0 \\ -1 \end{pmatrix} \tag{2.29}$$

where $I_0 = 2E_0^2 \equiv$ total intensity (considering $E_{0x} = E_{0y} = E_0$ and $\delta = 270°$).

Commonly, considering Eq. 2.15, the vectors are normalised for I_0 in order to remove this factor in front of the column vectors and obtain values of S_1, S_2 and S_3 belonging at the range $[-1, 1]$.

It is also useful to represent the amplitudes E_{0x} and E_{0y} in terms of an *auxiliary angle* α. In the case of a linear polarisation:

$$\begin{cases} E_{0x} = E_0 \cos \alpha \\ E_{0y} = E_0 \sin \alpha \end{cases} \tag{2.30}$$

where $E_0 = \sqrt{E_{0x}^2 + E_{0y}^2}$ and $0 \leq \alpha \leq \pi/2$. Thus, in the linear case ($\delta = 0 \mod \pi$):

$$\mathbf{S} = I_0 \begin{pmatrix} 1 \\ \cos 2\alpha \\ \sin 2\alpha \\ 0 \end{pmatrix} \tag{2.31}$$

where $I_0 = E_0^2$. On the other hand, for an elliptical polarisation:

$$\mathbf{S} = I_0 \begin{pmatrix} 1 \\ \cos 2\alpha \\ \sin 2\alpha \cos \delta \\ \sin 2\alpha \sin \delta \end{pmatrix} \tag{2.32}$$

2.2 Stokes parameters measurement

The Stokes parameters are directly measurable. The measurement of the polarisation properties of light is carried out through the use of a polarimeter. A simple example of an ideal polarimeter that allows the measurement of all four Stokes parameters is represented in Figure 2.4. The retarder is a phase-shifting element that increases the phase of the wave along the x-axis of $\phi/2$ and decrease the one along the y-axis of $\phi/2$. The θ angle is the inclination of the acceptance axis of the polariser.
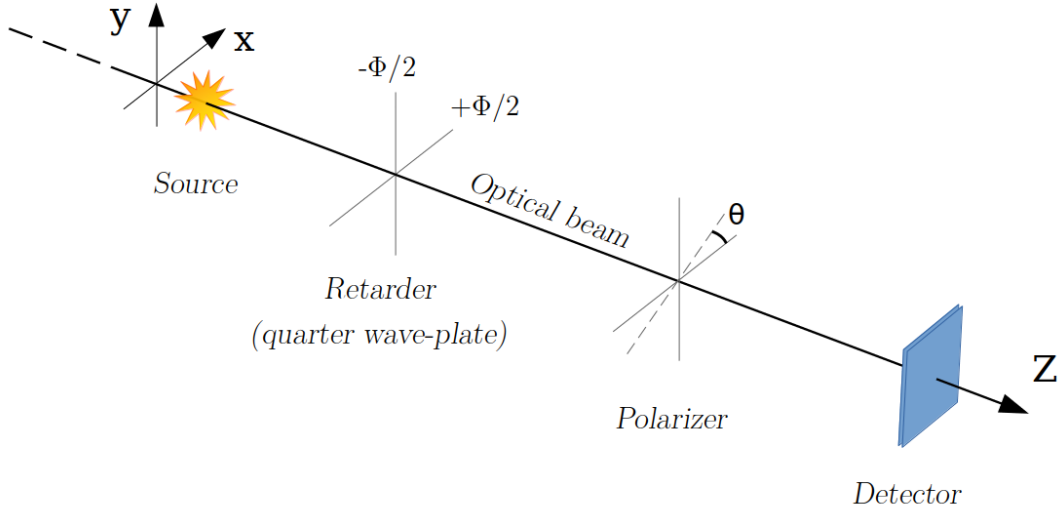
FIGURE 2.4: Diagram of an ideal polarimeter composed of a quarter
wave sheet and a linear polariser.

The components of the incident ray can be written in the complex form as:

$$\begin{cases} E_x(t) = E_{0x}e^{i\delta_x}e^{i\omega t} \\ E_y(t) = E_{0y}e^{i\delta_y}e^{i\omega t} \end{cases} \tag{2.33}$$

The Stokes parameter results to be as shown in Eqs. 2.34.

$$\begin{aligned} S_0 &= E_x E_x^* + E_y E_y^* \\ S_1 &= E_x E_x^* - E_y E_y^* \\ S_2 &= E_x E_y^* + E_y E_x^* \\ S_3 &= i(E_x E_y^* - E_y E_x^*) \end{aligned} \tag{2.34}$$

where i is the imaginary unit and the apex "$\star$" denotes the complex conjugate. The
E'_x and E'_y components emerging from the retarder are:

$$\begin{cases} E'_x = E_x e^{i\phi/2} \\ E'_y = E_y e^{-i\phi/2} \end{cases} \tag{2.35}$$

The outgoing beam from the polariser (after passing its acceptance axis) is:

$$E = E'_x \cos\theta + E'_y \sin\theta = E_x e^{i\phi/2}\cos\theta + E_y e^{-i\phi/2}\sin\theta \tag{2.36}$$

Considering that the intensity of the beam is defined as $I = EE^*$, we have:

$$\begin{aligned} I(\theta,\phi) &= E_x E_x^* \cos^2\theta + E_y E_y^* \sin^2\theta + E_x^* E_y e^{-i\phi}\sin\theta\cos\theta + E_x E_y^* e^{-i\phi}\sin\theta\cos\theta \\ &= \frac{1}{2}[(E_x E_x^* + E_y E_y^*) + (E_x E_x^* - E_y E_y^*)\cos 2\theta \\ &\quad + (E_x E_y^* + E_y E_x^*)\cos\phi\sin 2\theta + i(E_x E_y^* - E_y E_x^*)\sin\theta\sin 2\theta] \end{aligned} \tag{2.37}$$

The terms in the round brackets are the Stokes parameters! Then we get the so-called *Stokes intensity formula* from which it is possible to measure the four parameters:

$$I(\theta, \phi) = \frac{1}{2}[S_0 + S_1 \cos 2\theta + S_2 \cos \phi \sin 2\theta + S_3 \sin \phi \sin 2\theta] \qquad (2.38)$$

In particular, the first three Stokes parameters (S_0, S_1, S_2) are measurable by removing the retarder (i.e., $\phi = 0$) and rotating the polariser obtaining the acceptance axis set to $\theta = 0°$, $45°$, $90°$. S_3, on the other hand, can be measured by introducing the retarder again with $\phi = 90°$ (*quarter wave-plate*) and setting the polariser to $+45°$. At the end we get (the values of θ and ϕ are meant in degrees):

$$\begin{cases} I(0,0) = \frac{1}{2}[S_0 + S_1] \\ I(+45,0) = \frac{1}{2}[S_0 + S_2] \\ I(+90,0) = \frac{1}{2}[S_0 - S_1] \\ I(+45,90) = \frac{1}{2}[S_0 + S_3] \end{cases} \qquad (2.39)$$

Inverting the equations:

$$\begin{cases} S_0 = I(0,0) + I(90,0) \\ S_1 = I(0,0) - I(90,0) \\ S_2 = 2I(45,0) - I(0,0) - I(90,0) \\ S_3 = 2I(45,90) - I(0,0) - I(90,0) \end{cases} \qquad (2.40)$$

S_2 can also be calculated as: $S_2 = I(45,0) - I(-45,0)$. Indeed, from Eq. 2.37:

$$S_2 = 2I(45,0) - I(0,0) - I(90,0) = E_x E_y^* + E_y E_x^* \qquad (2.41)$$

On the other hand, by considering the parity proprieties of the *sine* and *cosine* functions [i.e., $\sin(-\theta) = -\sin(\theta)$; $\cos(-\theta) = \cos(\theta)$] we have also:

$$\begin{aligned} S_2 = I(45,0) - I(-45,0) &= \frac{1}{2}E_x E_x^* + \frac{1}{2}E_y E_y^* + \frac{1}{2}E_x^* E_y + \frac{1}{2}E_x E_y^* \\ &\quad - \frac{1}{2}E_x E_x^* - \frac{1}{2}E_y E_y^* + \frac{1}{2}E_x^* E_y + \frac{1}{2}E_x E_y^* \qquad (2.42) \\ &= E_x E_y^* + E_y E_x^* \end{aligned}$$

Comparing the results from Eq. 2.41 and Eq. 2.42 we can conclude that S_2 can be obtained by $I(45,0) - I(-45,0)$ as well. Similarly, it can be deduced that the fourth Stokes parameter can be obtained as $S_3 = I_{LHC} - I_{RHC}$.

An analogous representation for the description of the polarised light is the use of the *Wolf matrices* (generally indicated with the letter "J"). The Wolf matrices are 2×2 matrices whose elements are directly related to Stokes parameters. More details can be found in (Collett, 1992).

2.3 Müller matrices

We now want to see what happens after the interaction of polarised light with one or more elements that can change its polarisation state (i.e., elements that change

the Stokes parameters of the incident beam). We assume[8] that an outgoing beam (characterised by the Stokes elements S_i') from a polarising element can be expressed as a linear combination of the incoming S_i. Then, we have:

$$\begin{cases} S_0' = m_{00}S_0 + m_{01}S_1 + m_{02}S_2 + m_{03}S_3 \\ S_1' = m_{10}S_0 + m_{11}S_1 + m_{12}S_2 + m_{13}S_3 \\ S_2' = m_{20}S_0 + m_{21}S_1 + m_{22}S_2 + m_{23}S_3 \\ S_3' = m_{30}S_0 + m_{31}S_1 + m_{32}S_2 + m_{33}S_3 \end{cases} \tag{2.43}$$

It is therefore possible to express any polarimetric element through a 4×4 matrix, called *Muller matrix* (M). We can write:

$$\begin{pmatrix} S_0' \\ S_1' \\ S_2' \\ S_3' \end{pmatrix} = \begin{pmatrix} m_{00} & m_{01} & m_{02} & m_{03} \\ m_{10} & m_{11} & m_{12} & m_{13} \\ m_{20} & m_{21} & m_{22} & m_{23} \\ m_{30} & m_{31} & m_{32} & m_{33} \end{pmatrix} \begin{pmatrix} S_0 \\ S_1 \\ S_2 \\ S_3 \end{pmatrix} \tag{2.44}$$

which can be rewritten in a more compact form as:

$$S' = MS \tag{2.45}$$

An element that alters the polarisation state of an incident beam (i.e., a *polarising element*) can be, for example, a *polariser* (unequally alteration[9] of the amplitudes $E_{0,i}$) or a *retarder* (phase change δ_i) or a *rotator* (direction change E_i).

2.3.1   Müller matrix of a polariser

If we call p_x and p_y the *attenuation coefficients* of the amplitudes along x and y induced by a polariser (Figure 2.5) we have:

$$\begin{cases} E_x' = p_x E_x & 0 \leq p_x \leq 1 \\ E_y' = p_y E_y & 0 \leq p_y \leq 1 \end{cases} \tag{2.46}$$

If $p_{x,y} = 1$ we have perfect transmission. If $p_{x,y} = 0$ there is complete attenuation. An intermediate situation if $0 < p_{x,y} < 1$.
By substituting Eq. 2.46 in Eq. 2.34 considering the quantities after the polariser (thus $S \rightarrow S'$) we obtain:

$$\begin{pmatrix} S_0' \\ S_1' \\ S_2' \\ S_3' \end{pmatrix} = \frac{1}{2} \begin{pmatrix} p_x^2 + p_y^2 & p_x^2 - p_y^2 & 0 & 0 \\ p_x^2 - p_y^2 & p_x^2 + p_y^2 & 0 & 0 \\ 0 & 0 & 2p_x p_y & 0 \\ 0 & 0 & 0 & 2p_x p_y \end{pmatrix} \begin{pmatrix} S_0 \\ S_1 \\ S_2 \\ S_3 \end{pmatrix} \tag{2.47}$$

---

[8]In retrospect, it is observed to be a correct assumption.
[9]An element which equally alters all amplitudes is a *Neutral Density filter* (ND) and does not change the polarisation state.
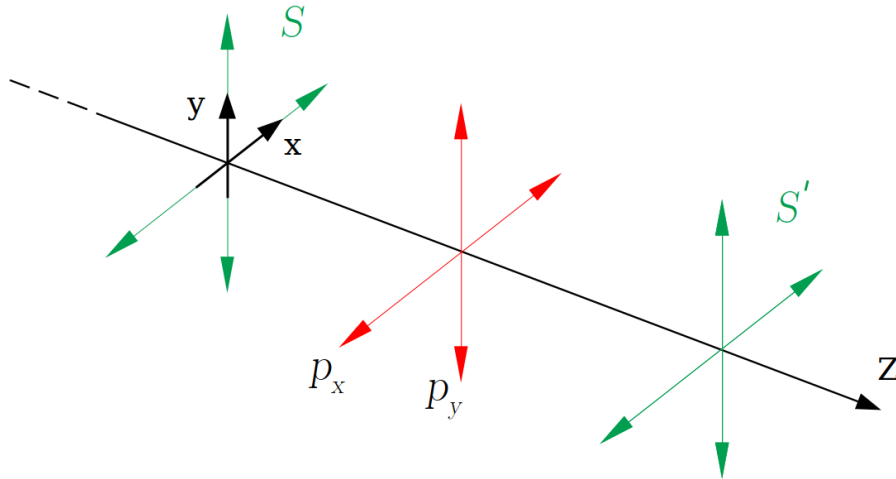
FIGURE 2.5: Configuration with a polariser.

If m_{33} is not null, the out-coming polarisation will be elliptical. Instead, if $p_x = p_y = p$ we have a *neutral density filter* with a Müller matrix equal to:

$$M = p^2 \begin{pmatrix} 1 & 0 & 0 & 0 \\ 0 & 1 & 0 & 0 \\ 0 & 0 & 1 & 0 \\ 0 & 0 & 0 & 1 \end{pmatrix} \quad (2.48)$$

Therefore, a neutral density filter does not compromise the polarisation state but the incident beam will have the intensity reduced by a factor of p^2 (i.e., $I' = p^2 I$ where I is the intensity of the incident beam). With an ideal linear polariser ($p_y = 0$ and $p_x = 1$ or vice versa) we have:

$$M = \frac{1}{2} \begin{pmatrix} 1 & -1 & 0 & 0 \\ -1 & 1 & 0 & 0 \\ 0 & 0 & 0 & 0 \\ 0 & 0 & 0 & 0 \end{pmatrix} \quad (2.49)$$

An ideal polariser[10] with $p_x = 1$ will decrease the intensity of the unpolarised incident beam by 50%! This is the price to pay to have a polarisation. Analogously, with an ideal linear polariser with $p_y = 1$ and $p_x = 0$ we have:

$$M = \frac{1}{2} \begin{pmatrix} 1 & 1 & 0 & 0 \\ 1 & 1 & 0 & 0 \\ 0 & 0 & 0 & 0 \\ 0 & 0 & 0 & 0 \end{pmatrix} \quad (2.50)$$

To have a general form of M for a polariser, it is convenient to rewrite all in a trigonometric form:

$$p^2 = p_x^2 + p_y^2 \quad (2.51)$$

---

[10]There is only one "ideal-like" polariser material in nature; the *calcite*. Instead, the *polaroid* is used as a synthetic material (polarisers made of this material are less good than those made in calcite but are cheaper!).

where:

$$\begin{cases} p_x = p \cos \alpha \\ p_y = p \sin \alpha \end{cases} \tag{2.52}$$

where $0 \leq \alpha \leq 90$ (for an ideal horizontal polariser $\alpha = 0°$; for an ideal vertical polariser $\alpha = 90°$). Thus, we obtain:

$$M = \frac{p_x^2}{2} \begin{pmatrix} 1 & \cos 2\alpha & 0 & 0 \\ \cos 2\alpha & 1 & 0 & 0 \\ 0 & 0 & \sin 2\alpha & 0 \\ 0 & 0 & 0 & \sin 2\alpha \end{pmatrix} \tag{2.53}$$

Let us consider the case of several polarisers in a row. We can suppose to be in the case schematised in Figure 2.6 (a horizontal polariser followed by a vertical one). In this case, we have:

$$S'' = M_V S' = M_V M_H S = MS \tag{2.54}$$

where $M = M_V M_H$. As is possible to see, M can also be the combination of several objects. It is obtained by multiplying, from the last to the first, the elements encountered by the beam.

$$M_{tot} = M_N M_{N-1} \ldots M_3 M_2 M_1 \quad \Rightarrow \quad S' = \prod_{i=0}^{N} M_{N-i} S = M_{tot} S \tag{2.55}$$
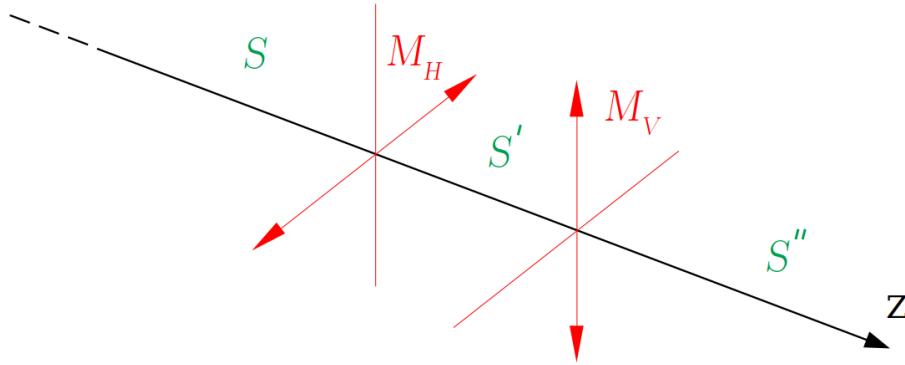
FIGURE 2.6: Example of a configuration with more polarisers.

In our particular case, we obtain:

$$M = M_V M_H = \frac{1}{4} \begin{pmatrix} 1 & -1 & 0 & 0 \\ -1 & 1 & 0 & 0 \\ 0 & 0 & 0 & 0 \\ 0 & 0 & 0 & 0 \end{pmatrix} \begin{pmatrix} 1 & 1 & 0 & 0 \\ 1 & 1 & 0 & 0 \\ 0 & 0 & 0 & 0 \\ 0 & 0 & 0 & 0 \end{pmatrix} = \begin{pmatrix} 0 & 0 & 0 & 0 \\ 0 & 0 & 0 & 0 \\ 0 & 0 & 0 & 0 \\ 0 & 0 & 0 & 0 \end{pmatrix} \tag{2.56}$$

as expected, if we put two linear polarisers at 90°to each other, we don't have an outgoing beam.

2.3.2 Müller matrix of a retarder

As previously said, a retarder (Figure 2.7) is an optical device that changes the phase of the incoming optical beam. A retarder that shifts the phase by an angle ϕ therefore causes a shift of $+\phi/2$ on one axis (called *fast axis*) and $-\phi/2$ on the other axis (called *slow axis*). In particular, considering Eq. 2.35 and Eq. 2.34, we have:

$$\begin{pmatrix} S_0' \\ S_1' \\ S_2' \\ S_3' \end{pmatrix} = \frac{1}{2} \begin{pmatrix} 1 & 0 & 0 & 0 \\ 0 & 1 & 0 & 0 \\ 0 & 0 & \cos\phi & -\sin\phi \\ 0 & 0 & \sin\phi & \cos\phi \end{pmatrix} \begin{pmatrix} S_0 \\ S_1 \\ S_2 \\ S_3 \end{pmatrix} \tag{2.57}$$

Note that for an ideal retarder there is no loss of intensity ($S_0' = S_0$). Looking at Eq. 2.57, we understand that there may be noteworthy cases for particular values of ϕ; specifically for $\phi = 90°, 180°$. Indeed, we have:

- $\phi = 90° \rightarrow$ *quarter-wave retarder* ($\lambda/4$)

$$M = \begin{pmatrix} 1 & 0 & 0 & 0 \\ 0 & 1 & 0 & 0 \\ 0 & 0 & 0 & -1 \\ 0 & 0 & 1 & 0 \end{pmatrix} \tag{2.58}$$

It transforms a $\pm 45°$ linear polarisation into a right (if $+45°$) or left (if $-45°$) circular polarisation. Indeed, if I consider a linear polarised beam at $\pm 45°$ we have: $S = I_0(1 \ 0 \ \pm1 \ 0)^T$, thus: $S' = MS = I_0(1 \ 0 \ 0 \ \pm1)^T$ which is a circular one. It can be verified that the opposite is also true (from circular to linear). Intuitively, it is possible to reach the same results by looking at the polarisation ellipse (Figure 2.3).
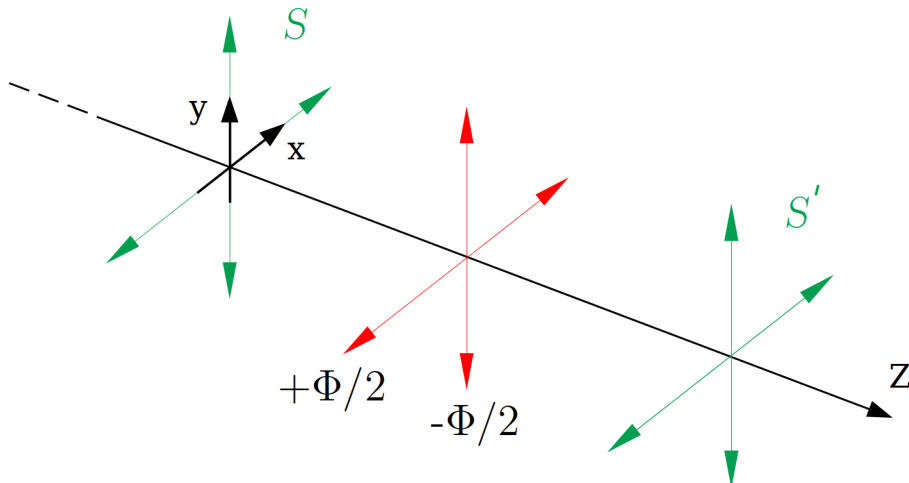
FIGURE 2.7: Configuration with a quarter-wave retarder.

- $\phi = 180° \rightarrow$ *half-wave retarder* $(\lambda/2)$

$$M = \begin{pmatrix} 1 & 0 & 0 & 0 \\ 0 & 1 & 0 & 0 \\ 0 & 0 & -1 & 0 \\ 0 & 0 & 0 & -1 \end{pmatrix} \tag{2.59}$$

Note that this is a diagonal matrix. The terms $m_{22} = m_{33} = -1$ reverse the ellipticity and orientation of the polarisation state of the incident ray.

Finally, it could be useful to show the Müller matrix for a general linear retarder:[11]

$$M = \begin{pmatrix} 1 & 0 & 0 & 0 \\ 0 & \cos^2(2\theta) + \sin^2(2\theta)\cos(\delta) & \cos(2\theta)\sin(2\theta)[1 - \cos(\delta)] & \sin(2\theta)\sin(\delta) \\ 0 & \cos(2\theta)\sin(2\theta)[1 - \cos(\delta)] & \cos^2(2\theta)\cos(\delta) + \sin^2(2\delta) & -\cos(2\theta)\sin(\delta) \\ 0 & -\sin(2\theta)\sin(\delta) & \cos(2\theta)\sin(\delta) & \cos(\delta) \end{pmatrix} \tag{2.60}$$

where δ is the phase difference between the fast and slow axis and θ is the angle of the fast axis.

2.3.3 Müller matrix of a rotator

The rotators rotate the perpendicular components $E_x(z, t)$ and $E_y(z, t)$ of the electric field by an angle θ (Figure 2.8).
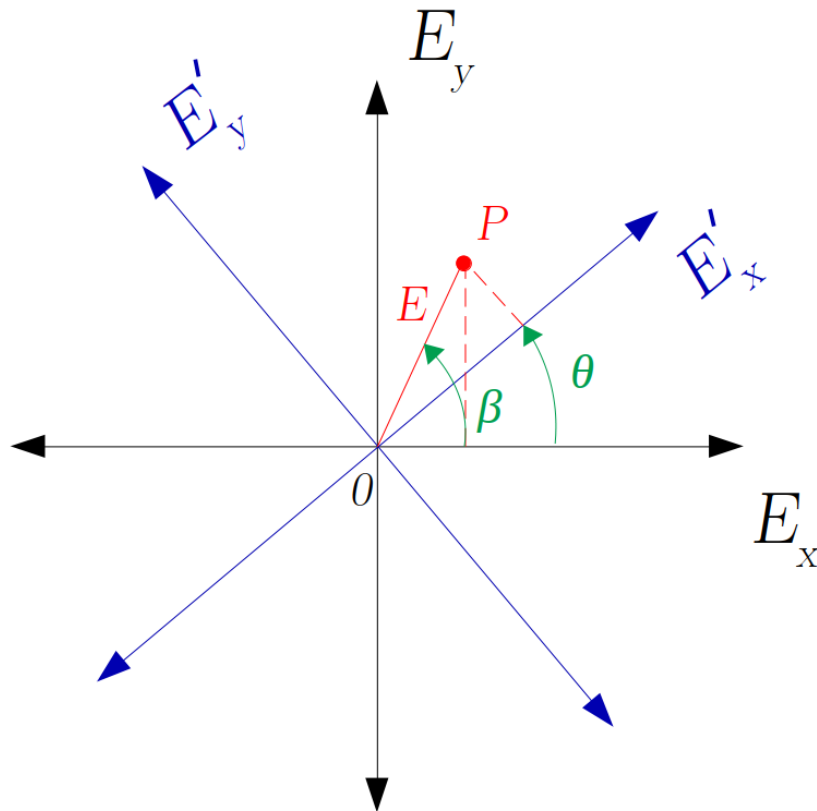
FIGURE 2.8: Rotation of the optical field components by a rotator.

---

[11] Wave plate calculations are made from this matrix.

In the (x, y) reference system we have:

$$\begin{cases} E_x = E\cos\beta \\ E_y = E\sin\beta \end{cases} \tag{2.61}$$

while, in the (x', y') reference system:

$$\begin{cases} E'_x = E\cos(\beta - \theta) \\ E'_y = E\sin(\beta - \theta) \end{cases} \tag{2.62}$$

Expanding trigonometrically E'_x and E'_y we obtain:

$$\begin{cases} E'_x = E(\cos\beta\cos\theta + \sin\beta\sin\theta) \\ E'_y = E(\sin\beta\cos\theta - \sin\theta\cos\beta) \end{cases} \tag{2.63}$$

grouping the terms and considering Eq. 2.61 and Eq. 2.62 we obtain:

$$\begin{cases} E'_x = E_x\cos\theta + E_y\sin\theta \\ E'_y = -E_x\sin\theta + E_y\cos\beta \end{cases} \tag{2.64}$$

As for the previous cases, by considering the Stokes parameters and Eq. 2.64, we can obtain the Müller matrix associated with this element:

$$M = \begin{pmatrix} 1 & 0 & 0 & 0 \\ 0 & \cos 2\theta & \sin 2\theta & 0 \\ 0 & -\sin 2\theta & \cos 2\theta & 0 \\ 0 & 0 & 0 & 1 \end{pmatrix} \tag{2.65}$$

Note that in the intensity domain a physical rotation of θ leads to an effective rotation of 2θ. In the amplitude domain, I would have always obtained θ.

In general, we can say that when a polarimetric element is rotated by an angle θ with respect to the reference system considered, the corresponding Muller matrix is:

$$M(\theta) = R(-2\theta)MR(2\theta) \tag{2.66}$$

where M indicates the Müller matrix of the non-rotated element and $R(2\theta)$ as reported in Eq. 2.65.

Assuming the Müller matrix of the j-th combination of optical devices equal to M_j, the detected intensity in this case is given by:

$$m_j^{out} = [M_j]_{00}S_0^{in} + [M_j]_{01}S_1^{in}[M_j]_{02}S_2^{in} + [M_j]_{03}S_3^{in} \tag{2.67}$$

where S_i^{in} are the Stokes vector elements of the input radiation. If we consider the case of linear polarisation, the last term of this equation is null ($[M_j]_{03}S_3^{in} = 0$).

By putting several measurements together, the modulation scheme can be expressed as the following linear system:

$$\mathbf{m} = \mathbf{XS} \quad \rightarrow \quad \mathbf{S} = \mathbf{X}^\dagger\mathbf{m} \tag{2.68}$$

where the vector **m** consists of different intensity measurement and each row of the matrix **X** (the so-called *modulation matrix*) is built with the first rows of the different Müller matrices of the different combinations j of optical elements used in the modulation scheme (e.g., considering a linear polariser with the acceptance axis at different angles). Therefore, the modulation matrix has dimensions $N \times 4$, with N the number of measurements (in the case of linear polarisation, we have an $N \times 3$ matrix). By pseudo-inverting the **X** matrix, we obtain the *demodulation matrix* $X^\dagger$ that connect the measured data **m** with the Stokes vector **S**.

Thus, through the demodulation matrix, it is possible to extrapolate the original **S** as shown in Eq. 2.68. We will see an application of these modulation and demodulation matrices in the next Chapters of this Thesis.

Chapter 3

The Solar Corona

The Sun is the closest star to our planet ($d_{\odot\oplus} = 1\text{AU} \approx 149.6 \times 10^9$ m). It is a hot ball of plasma primarily composed of hydrogen (H $\sim$ 73%) helium (He $\sim$ 25%) and other heavy elements ($\sim$ 2%) such as oxygen, carbon, and so on (Aschwanden, 2006). The solar angular diameter from Earth is $\vartheta_{\odot} = 2R_{\odot}/d_{\odot\oplus} \approx 32$ arcmin even if it changes due to the Earth elliptic orbit (with an eccentricity $e = 0.0167$). In general, we can say that 1 arcsec $\approx$ 725 km on the Sun. The solar irradiance is $I_{\odot}$ [W/m^2] ≈ 1368 W/m^2. This quantity is known as *solar constant*. It is defined as the total amount of radiant solar energy per unit time per unit area reaching the top of the Earth's atmosphere at the Earth's mean distance from the Sun. This value is pretty constant but shows a little variation of about $\pm 0.15\%$ during the so-called *solar cycle*. It consists of a change in solar irradiation due to a change of solar activity[1] every $\sim$ 11.4 years (moving from periods of a maximum solar activity to periods of a minimum solar activity and vice-versa).

3.1   The Sun and its atmosphere

The Sun has a multi-layer structure. The first subdivision can be performed thinking at the different optical depth (defined as $\tau_{\nu} = \int_{s_0}^{s} \alpha_{\nu}(s')ds'$ where α_{ν} is the absorption coefficient of the medium and the integral is measured along the LoS - line of sight). The regions with an optical depth $\tau_{\nu} > 1$ are the interior of the Sun; the regions with an optical depth $\tau_{\nu} < 1$ are the Sun atmosphere. Both can be divided into many other sub-layers in function of some physical parameters such as density and temperature. Figure 3.1 shows the Sun with its layer-subdivision.

The solar atmosphere can be mainly divided into two regions: chromosphere and corona. Most of the solar radiation comes from the photosphere that emits in the continuum. However, there is absorption by atoms in the overlying atmosphere. In these layers, there is a collapse of plasma densities and we pass from an optically thick plasma (photosphere) to an optically thin plasma (chromosphere and corona).

The chromosphere[2] is the first solar optical thin layer. Its thickness is about 4000 km ($\approx$ 5 arcsec) just over the photosphere. It is responsible for the absorption lines of the solar spectrum. The temperature reaches the 10^4 K starting from the approx 5800 K of the photosphere.

The outermost layer of the Sun's atmosphere is the solar corona. It has an optical thickness $\tau \ll 1$ and it extends millions of kilometres into outer space. The solar corona brightness does not exceed that of the full moon. Among the interesting features of the Sun, it is probably the one that most directly affects the Earth and

---

[1]An indication of the solar activity is given by the number of sunspots on the photosphere.

[2]The name comes from the Greek "chromos" = colour and it is due to the chromosphere colour features (mainly red; due to the emission in the *Hα* line of the Balmer series).
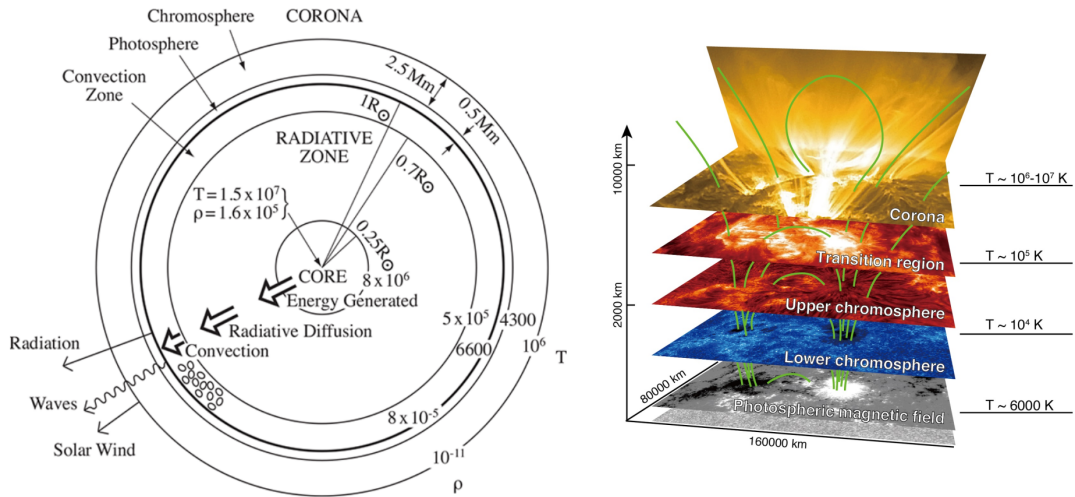
FIGURE 3.1: **Left:** The structure of the Sun (Priest, 2014). It is possible to distinguish the main inner-layers (core, radiative zone, convection zone), the photosphere and the main atmosphere layers (chromosphere and corona). All the temperatures and densities are expressed in [K] and [kgm^{-3}] respectively. **Right:** A detail on the Sun's atmosphere layers subdivision (© NAOJ/JAXA, NASA).

human life. Indeed, because it stretches without discontinuity into the Heliosphere, it contains and influences our planet (and all the other planets of the Solar System). The solar corona consists of plasma at very high temperatures. In particular, in this region, the temperature reaches $\sim 10^6$ K and then returns to slowly decrease as the heliocentric height increases. This increase in temperature with respect to the photosphere is known as *coronal heating*. To date, the causes of this phenomenon are still under research. The most accredited theories believe that it is due to the reconnection of the coronal magnetic field lines, with the consequent release of large amounts of energy.

Due to the high temperature, the matter is in form of highly ionised plasma. The solar corona is mostly composed of protons and electrons: hydrogen ($\approx$ 91%), helium ($\approx$ 9%) ions and heavier ions traces (< 1%) as well (Meyer, 1985). In a magnetised fluid with high conductivity, plasma and magnetic field are coupled (*Alfvèn's theorem*). The fundamental parameter to describe the behaviour of plasma in a magnetic field is the *β-plasma*. It is defined as the ratio of the plasma pressure over the magnetic pressure (Aschwanden, 2006):

$$\beta = \frac{p_{gas}}{p_{mag}} = \frac{nkT}{B^2/2\mu_0} \tag{3.1}$$

where $p_{gas} = nkT$ is the gas pressure and $p_{mag} = B^2/2\mu_0$ is the magnetic pressure. It is possible to distinguish two different regimes:

- $\beta \gg 1 \rightarrow$ plasma dominated by thermal phenomena;

- $\beta \ll 1 \rightarrow$ plasma dominated by magnetic phenomena.

Figure 3.2 shows the values of β-plasma for different solar atmosphere regions.[3] As it is possible to see, $\beta \ll 1$ in the solar corona. This means that the coronal plasma is frozen in the $\bar{B}$ field lines which deform the path and create different structures.
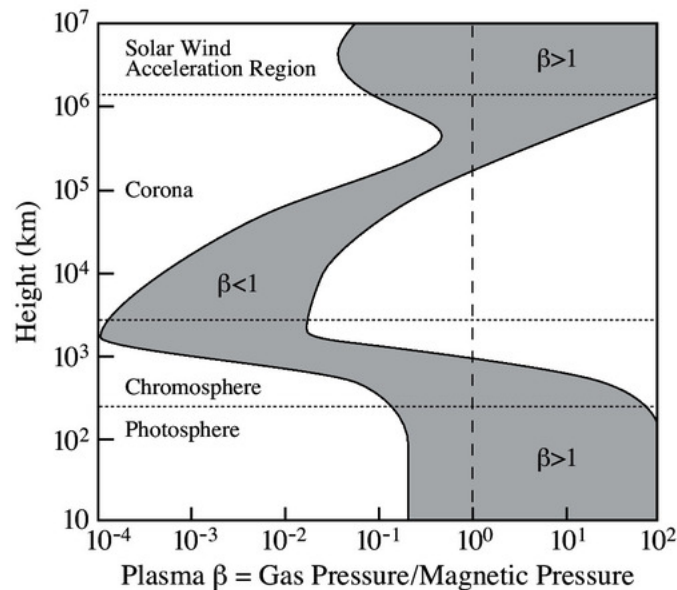
FIGURE 3.2: Values of β-plasma parameter (shaded area) in solar atmosphere as a function of height from the Sun surface.

In Figure 3.3, a summary of the main phenomena in the solar atmosphere is shown. As can be seen from the image, the set of phenomena that occur in this region is extremely various and complex. More information about all these phenomena can be found in Degl'Innocenti, 2007, Aschwanden, 2006 and Kamide and Chian, 2007.
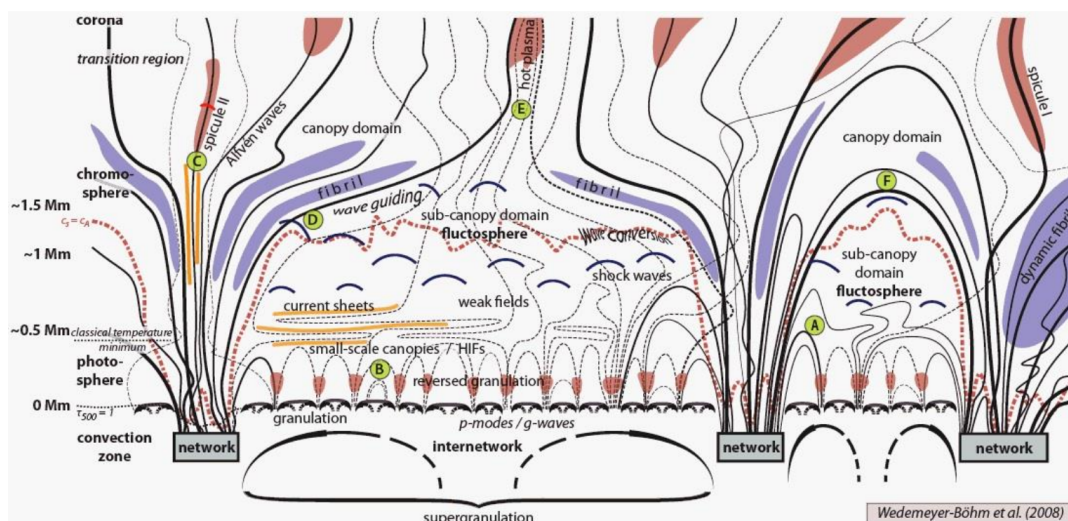
FIGURE 3.3: Summary of the main phenomena in the solar atmosphere with a 2D radial section of the solar magnetic fields immediately above the photosphere.

---

[3]In the convective zone of the Sun ($\beta \gg 1$) the plasma says to the magnetic field how it must move. On the contrary, in the solar corona ($\beta \ll 1$) the magnetic field movements dominate the plasma.

3.2   The solar corona structure

The solar corona (Figure 3.4) is the results of three different main contributions:

- K-Corona (**K**ontinuierlich / "Continuous" in German): it is due to Thomson diffusion by the free coronal electrons of the photospheric radiation. The Fraunhofer lines (typical width: $\sim 1\,\text{Å}$) disappear in the diffuse spectrum due to the electrons high thermal velocity.[4] The radiation results to be polarised (Inhester, 2015; Raouafi, 2011) and it is possible to determine the coronal electron density (n_e) from it.

- F-Corona (**F**raunhofer): it is due to diffusion of solar radiation by dust particles ($\sim \mu m$) and it is concentrated on the ecliptic plane. The light is not polarised and it dominates at distances greater than $2 - 3R_\odot$. This is the part of the corona which you try to remove during observations.

- E-Corona (**E**mission): it is due to emission processes by coronal ions with formation temperatures of $\sim 10^6$ K identified as "forbidden" lines. The signal from the emission lines of the E-corona is relatively weak and, although the lines are intense for the continuous background level of the components K and F, it cannot be detected in the case of wide-band observations in the visible. This emission is concentrated on isolated spectral lines and this allows them to be observed using spectroscopic techniques or narrow-band spectral filters. Main lines: FeXIV (530.3 nm, green), CaXV (569.5 nm, yellow), FeX (637.4 nm, red), FeXIII (1074.7 nm, infrared). From E-Corona it is possible to evaluate n_e, T_e, v_{out} and elements abundances.

The observed structures in the solar corona are interpreted in terms of *closed magnetic field* regions (corresponding to areas with opposite polarity on the disc) and *open magnetic field* (when the field lines extend so far in the interplanetary space that can be considered open) and *border and reconnection regions* between open and closed fields. Closed field zones are associated with the brightest regions in EUV (active regions); they are denser and warmer than the surrounding plasma. The open field areas are instead associated with the less bright regions in EUV (coronal holes), less dense than the surrounding plasma.

As an example of a closed field (areas with opposite polarity), we can think about the so-called *helmet streamers*. These streamers are brilliant arches topped with "cusps" that extend radially from the surface of the Sun. The streamers connect opposite polarity regions. Indeed, in the close field regions born the so-called *interplanetary current sheet* that divides the opposite polarity of the interplanetary field. The streamers are not always evenly distributed across the surface of the Sun. During Sun's quiet periods, they are almost confined to the equatorial regions. On the contrary, during the Sun's active periods, the corona is evenly distributed over the equatorial and polar regions, though it is most prominent in areas with sunspot activity (Figure 3.4). A *streamer belt* describes the typically equatorial region in which large groups of streamers are found. Since magnetic polarity inverts over the streamer belt, a *current sheet* must be embedded within it. While streamers are along the equator during the periods of quiet Sun, the polar regions are covered by *coronal holes*. The coronal holes are regions with a very low density if compared with the coronal densities all around. Although during the periods of the minimum they are

---

[4]Considering electrons with $v_{therm} \approx 5 \times 10^3$ km/s, the convolution of the diffuse radiation has a typical spectral profile width of $\Delta\lambda \sim \lambda v_{therm}/c \approx 90\,\text{Å}$ (considering $\lambda \approx 5000\,\text{Å}$).

located towards the poles, during the intermediate phase between minimum and maximum they also appear near the equatorial belt. During a maximum of solar activity, the polar coronal holes disappear and subsequently reform with reversed magnetic polarity.

FIGURE 3.4: Streamers distribution during the maximum (left) and minimum (right) of solar activity. [Source: HAO Archives]

Observations of the disc in soft X-rays show some brighter areas where plasma forms characteristic arches called *coronal loops*[5]. They are formed in closed-field areas extending for about 0.5 $R_\odot$ and, generally, are the streamers' basis.

Similar magnetic structures can be found by looking at the *prominences*. A prominence ("*filament*" if observed looking at the solar disc) is a large plasma and magnetic field structure extending outward from the Sun's surface, often in a loop shape. Prominences are anchored to the Sun's surface in the photosphere, and extend outwards into the solar corona. While the corona consists of extremely hot plasma, prominences contain much cooler plasma, similar in composition to that of the chromosphere (atoms emit in the H_α line and for this reason are visible during eclipses as well). Even if with a similar structure, prominences and coronal loops are quite different. Coronal loops are often seen above sunspot groups as very fine lines; much smoother than for a prominence. Moreover, the coronal loops plasma is far-hotter than in a prominence. This means that coronal loops do not emit light from neutral hydrogen atoms, which are now fully ionized[6], but from the simple thermal emission of the heated plasma at over 100.000 °C.

Several dynamic phenomena take place in the solar corona. The *solar flares* are an example. They are sudden increases in brightness at all λ (from radio to X-rays) that often occur in active regions. Flares are also associated with sudden releases of energy in regions of the corona with a high magnetic energy density. The energy released is up to 10^{32} erg in a time range of the order of $\sim$ 10 min (equivalent to $\approx 10^{11}$ Hiroshima bombs). This energy is released in the form of radiation, ultra-relativistic particle acceleration (p^+ and e^-), heating of the surrounding plasma, and sometimes expulsion of chromospheric (eruptive prominence) and coronal plasma.

---

[5]The coronal loops are commonly much much bigger than the Earth dimension.

[6]Some other atoms such as iron still have a complement of electrons that can emit light at discrete wavelengths in this plasma, and these lines are often used to determine the exact temperature and density of coronal loop plasma.

Another dynamic phenomena that can occur[7] in the solar corona are the so-called Coronal Mass Ejections (CMEs). A Coronal Mass Ejection[8] is a plasma eruption which, instead of falling on the solar surface, spread in space, involving masses of the order of 10^{10-12} kg (at speeds ranging from 100 km/s up to the order of 10^3 km/s). As shown in Figure 3.5 a CME observed in visible light shows a *three component structure*: a core (i.e., prominence), a front (i.e., "dragged" plasma) and a cavity/void (i.e., expanding streamtube).
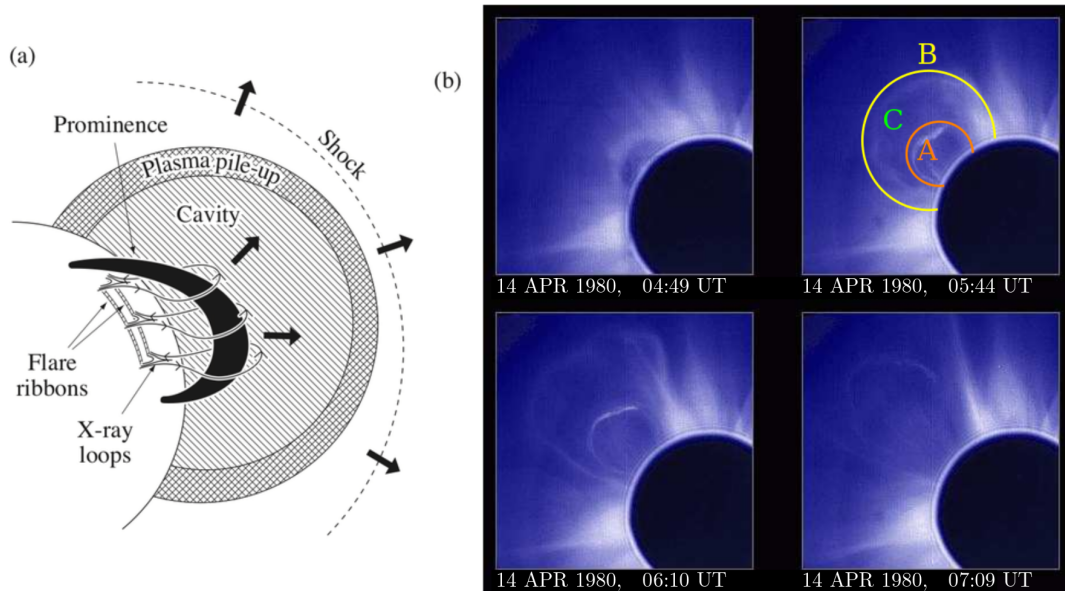

FIGURE 3.5: On the right side, a sequence showing a CME that occurred on April 14, 1980, observed with the coronagraph of the High Altitude Observatory aboard the Solar Maximum Mission. The last three images follow each other at intervals of about an hour. It is possible to distinguish the three main components of a CME; the core (A), the front (B), and the void (C). Courtesy of the High Altitude Observatory. The left side of the figure shows more details on the CME structure (Source: G. Forbes, JGR; 2000).

Like flares, also CMEs are often associated with active regions (therefore with high concentrations of magnetic fields). Still, as with flares, the origin is believed to be magnetic reconnection. In visible light, a brilliant arc structure is typically observed that expands (front of the CME) sometimes containing a brighter core corresponding to any eruptive prominence. The streamers can have a duration of the order of several solar rotations and are the environment in which the phenomenon of *Coronal Mass Ejections* takes place.

3.2.1   Solar wind

The corona observation immediately posed two fundamental problems. One of these two problems is that the solar corona extends about 100 times farther from the Sun than could be predicted based on simple models of balancing the gravitational force and kinetic energy of the gas molecules. The impossibility of a static

---

[7]The frequency depends on the solar cycle: from about 0.2/day during the solar minimum to 3.5/day during the solar maximum (Carroll and Ostlie, 2017).

[8]*Flares* and *CME driven shocks* drive also the Solar Energetic Particles (SEPs); energetic particles coming from the Sun (mainly electrons and protons).

corona and the need for a stationary flow from the Sun (i.e., the existence of a *solar wind*) was demonstrated in 1958 by Parker. This was then verified by in-situ measurements as early as 1963. With this, the problem of the acceleration of the solar wind born as well. This phenomenon is still a subject of study and research today.

The existence of a continuous flow of corpuscular radiation was postulated in 1951 by Biermann thanks to its studies on the angle between the comets *dust* tail and *gas/plasma* tail. He concluded that the solar radiation pressure was not enough.[9] Then, he supposed the existence of a continuous flow of particles that accelerate the ions per momentum transfer. He estimated that the particles must propagate at ≈ 500 km/s. In 1958 Parker demonstrated the need for a continuously expanding solar wind by the thermal pressure gradient opposing gravity. The existence of the solar wind was then definitively demonstrated by the Soviet probes Lunnik-2 and Lunnik-3 (1960) and by the Mariner-2 (1962).

The major constituents of the solar wind are p^+ and e^- (components of ionised hydrogen), as well as α particles (3-4%) and heavy ions. The solar wind density is of the order of $5 - 15$ cm^{-3} at 1 AU (Aschwanden, 2006). The propagation speeds range is from 400 to 700 km/s. The thermal velocity corresponding to the plasma temperatures (of the order of $\sim 1 \times 10^5$ K at Earth) is about a factor 10 smaller than the flow velocity. For this reason, the wind can be considered, as a first approximation, such as a *collimated beam*. Different probes sent at 0.3 AU measured substantially the same speeds (and a wind density ~ 10 times higher). This means that acceleration occurs in the lower layers of the solar corona. During the minimum of solar activity, two types of solar wind are clearly distinguished:

- *fast wind* (≈ 750 km/s), associated with the polar zones $\rightarrow$ open fields $\rightarrow$ coronal holes (Krieger, Timothy, and Roelof, 1973);

- *slow wind* (≈ 400 km/s), associated with equatorial zones $\rightarrow$ closed fields $\rightarrow$ streamers.

During the maximum of solar activity, the two regimes are difficult to distinguish. This is clearly visible in Figure 3.6. The solar wind data obtained by Ulysses S/C outside the ecliptic plane (and above the solar poles) are presented as well.

3.3 Solar corona observation

Observations of the solar corona started with solar eclipses by the Moon, which was the only natural means to suppress the strong contrast caused by the six orders of magnitude brighter solar disc in optical wavelengths. Indeed, the solar corona brightness does not exceed the brightness of a full moon. To date, it can be observed from Earth during total eclipses or with a "special telescope" called *coronagraph* (Lyot, 1932). A coronagraph is a telescope designed to block out the direct light from a star[10] so that nearby objects can be resolved. We will see in the next Subsection how a coronagraph works (Subsection 3.3.3). It is possible to use coronagraphs to observe the solar corona from space as well. They are commonly put on-board a spacecraft pointed to the Sun.[11]

---

[9]Anyway, the effects of the solar wind are also evident by looking at other events/phenomena such as the deformation of planetary magnetospheres (e.g., deformation of the *Van Allen belts*).

[10]Indeed, coronagraphs are used in many fields that aim to observe bodies and/or structures near much brighter sources (e.g., observation of exoplanets around a star).

[11]Recent researches aim to bring a coronagraph on-board the International Space Station (ISS) for almost continuous space-based observations of the solar corona.
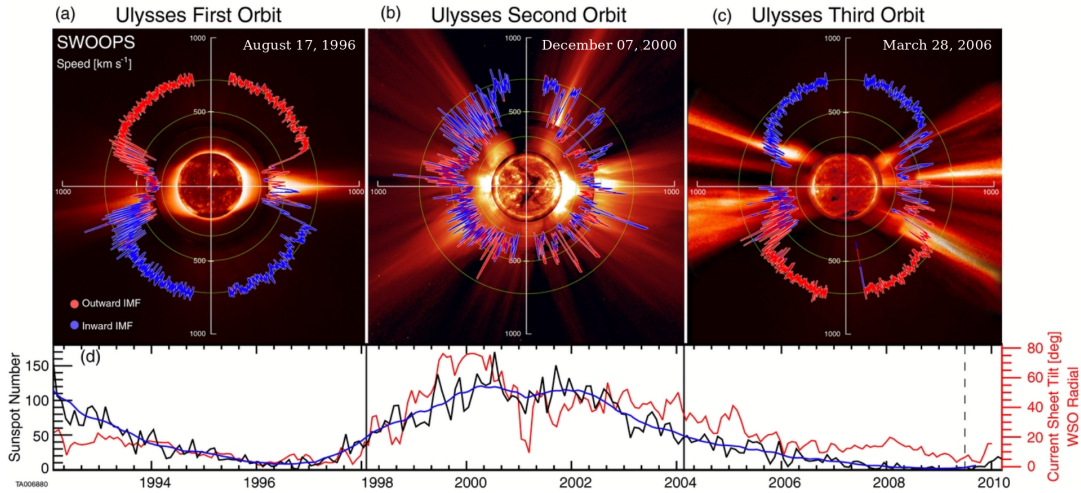
FIGURE 3.6: **Top panel (a, b, c):** Polar plots of the solar wind speed during the minimum and maximum of the solar cycle as measured by the Ulysses mission. The interplanetary magnetic field (IMF) is shown as well. The images are a composition of the SOHO's Extreme ultraviolet Imaging Telescope, the Mauna Loa K coronameter, and the LASCO-C2 coronagraph. **Bottom panel (d):** Sunspot number (black; smoothed in blue) and the Wilcox Solar Observatory heliospheric current sheet tilt angle (red). Figure adapted from Müller et al., 2020.

Let's see in more detail analogies and peculiarities of the solar corona observation from ground-based and space-based observatories.

3.3.1 Ground-based observations

Let's start considering ground-based observations. The brightness of the different solar corona components, in function of the distance from the Sun, can be found in Figure 3.7 (Phillips, 1992; November and Koutchmy, 1996). As is possible to see, the corona can be easily observed during a *total* solar eclipse (i.e., when the sky-brightness is overthrown by the shadow of the Moon projected on Earth). However, the rarity of these events, the short duration (max 7.5 minutes), the possibility of adverse weather conditions, and the frequent need of accessing remote locations for the observing sites, make it difficult to carry out continuous and detailed coronal studies.

It is possible to see how the brightness of the sky itself is high enough to not allow direct observation of the corona. For this reason, if no eclipse occurs, it is necessary to use a coronagraph to observe it. Anyhow, we have to deal with the sky-brightness. A *pure blue sky* ($\sim 10^{-6} B/B_\odot$) is the minimum threshold required to be able to see a part of the solar corona once the Sun can be properly occulted. To date, just the best known coronagraphic site (Haleakala, in Maui, Hawai'i) can perform a continuous study of the solar corona from ground-based instruments. This is possible because this site has a measured sky-brightness value of $\approx 1-5 \times 10^{-6} B/B_\odot$ for different wavelengths (Tomczyk and Elmore, 2015). As we will see in Chapter 5, part of this Thesis wants to find another place on Earth with a sky-brightness value low enough to be able to perform continuous ground-based observation of the solar corona.
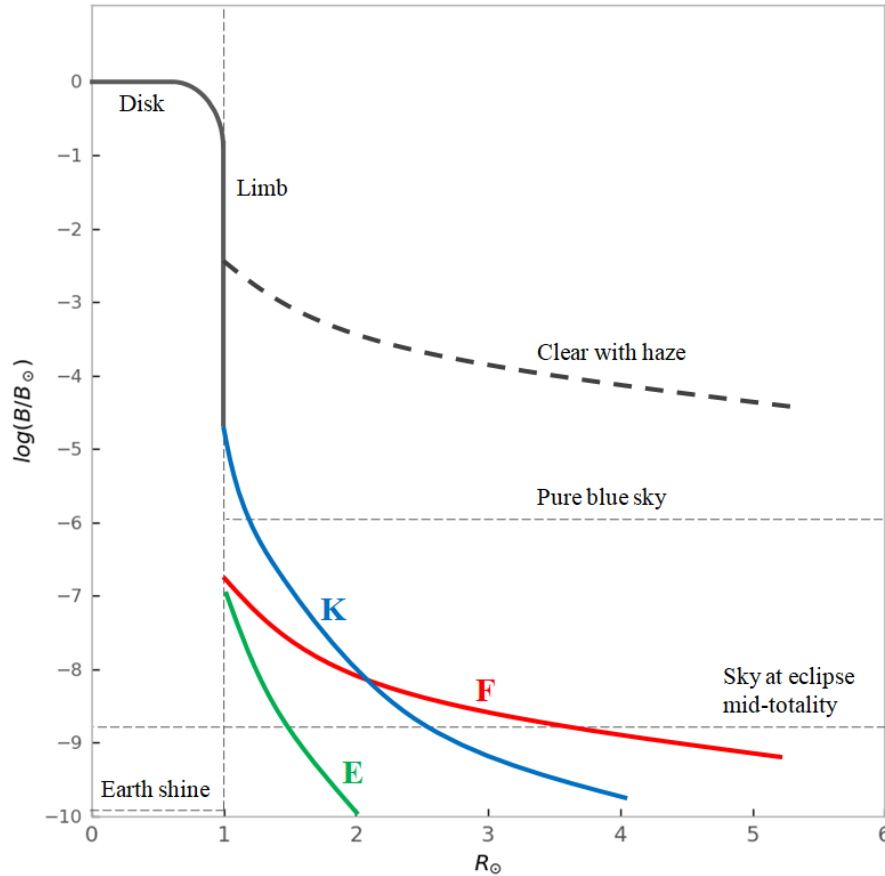
FIGURE 3.7: Solar corona brightness ($B/B_\odot$) in function of the helio-centric distance.

3.3.2 Space-based observations

Observing the solar corona from a space-based observatory removes the problem of the sky-brightness. On the other hand, the costs and the involved technologies are much more than the on-ground option. Moreover, an on-ground observatory can be improved and eventually repaired if necessary. This is not possible for a space-based one. On the other hand, the absence of the sky-brightness and the possibility to go closer to the Sun give the possibility to observe regions and details of the solar corona otherwise extremely difficult to observe. Many examples of space-based observatories were introduced in Section 1.2. Another possibility is to put a coronagraph on-board a stratospheric balloon or on a sounding rocket.[12] In this case, the costs are lower and the sky-brightness is totally irrelevant. However, the observation period is extremely reduced (to minutes -with sounding rockets- or hours/days -with stratospheric balloons-) and you have to deal with different possible technological challenges (e.g., pointing, stabilisation, . . .).

Part of this Thesis consists of the calibration and data analysis aspect of a couple of space-based missions for the observation of the solar corona (Section 5.5 and Chapter 6). Anyhow, both the space-based and ground-based observatories (with respective advantages and disadvantages) are useful for a full characterisation, study, and observation of the solar corona.

---

[12]These options are particularly good as space instrumentation test.

3.3.3 Coronagraphs

Let's see more in detail how a coronagraph works. A coronagraph is an instrument that occults the bright solar disc and thus allows coronal observations, without the need to wait for one of the rare total eclipse events (Aschwanden, 2006). Bernard Lyot built his first coronagraph at the Pic-du-Midi Observatory (France) in 1930. Its solution is highly effective to allow the visibility of the very weak solar corona while masking at the same time the solar disc. We can distinguish two main types of coronagraphs: the internally occulted and the externally occulted coronagraphs. Their structure is shown in Figure 3.8 and Figure 3.9 respectively. The scheme of the internally occulted coronagraphs was originally ideated by Lyot (Lyot, 1932) while J.W. Evans developed the external occultation technique (Evans, 1948) that was refined by Gordon Newkirk and David Bohlin after the Evans' original drawing (Newkirk and Bohlin, 1963; Newkirk and Bohlin, 1964). In both cases the occulter works as an artificial Moon and blocks the direct light from the solar disc.
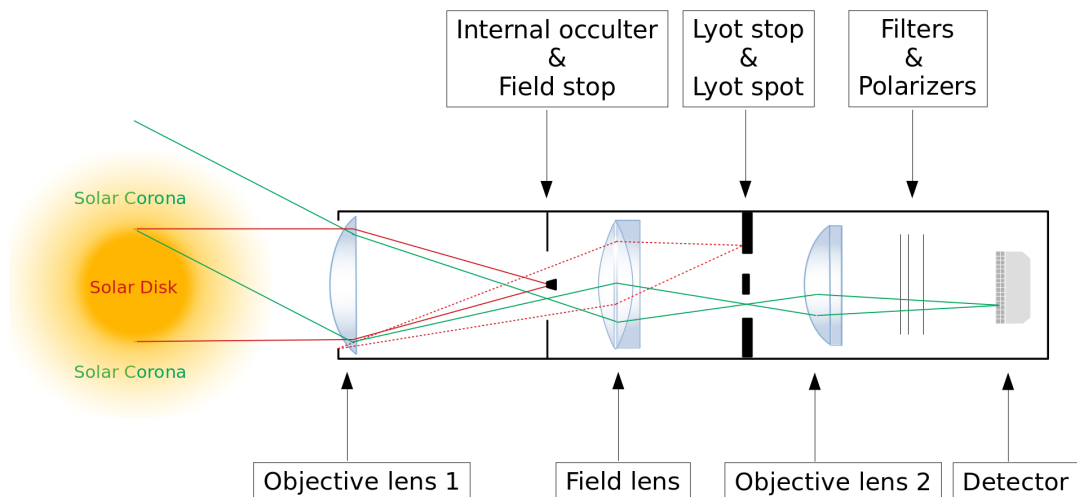

FIGURE 3.8: Schematisation of an internally occulted coronagraph.
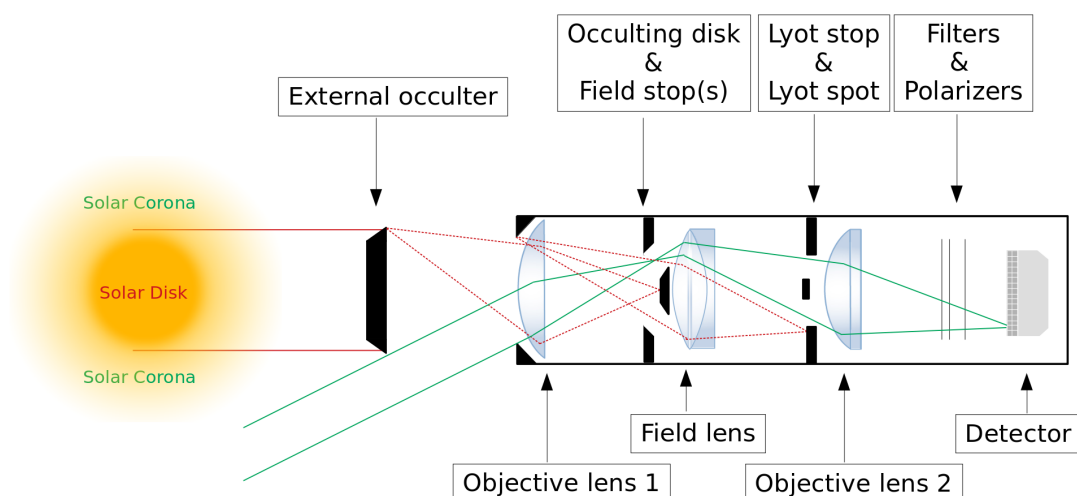The occulter is *inside* the telescope.

FIGURE 3.9: Schematisation of an externally occulted coronagraph.
The occulter is *outside* the telescope.

In the internally occulted configuration, the so-called *Lyot stop* stops the light diffused by the edges of the objective lens while the *Lyot spot* blocks the diffraction coming from the internal occulter (IO). The field stops reduce the field of view but decrease the telescope straylight as well. The coronal signal (green lines in Figure 3.8 and 3.9) pass through the whole telescope and is focused on the detector.

In the externally occulter configuration, an occulting disc blocks the straylight coming from the external occulter and the Lyot stop and spot block the diffusion of the objective lens and the diffraction from the occulting disc respectively. The coronal light passes through the telescope and is finally focused on the detector.

Both internally and externally occulted configurations, present critical issues. For example, in the internally occulted coronagraphs the light from the solar disc (that we want to block) goes physically into the telescope. For this reason it is necessary to pay extreme attention to all reflections to ensure that no residual light remains inside the telescope (for this reason, it is very important to have a high quality/polished primary objective lens). On the other hand, an externally occulted coronagraph needs to have the external occulter far away from the entrance pupil to increase the field of view (which otherwise risks being too far away from the solar limb[13]) and to decrease the diffraction due to the occulter edges. However, the externally occulted coronagraph has a very steep vignetting function that helps to mitigate the large dynamic range of the coronal brightness. Each configuration has pros and cons.

Source of straylight in coronagraphs

There are several possible sources of straylight in a coronagraph. The main sources comes from *diffraction* (despite the presence of the Lyot stops), *optics impurities* and, if from ground-based observation, the *sky*. Of course, any lens imperfection, impurity or dirt inside the telescope is an additional source of scattered light (i.e., straylight). In particular, it was observed that the cleaning of the primary lens is of crucial importance (especially for internally occulted coronagraphs[14]). To avoid these sources of straylight, we look at the polarised brightness (pB). Indeed, all these straylight sources are not polarised. Thus, looking at the polarised light, we can distinguish sky-brightness and other sources of straylight from the image of the corona.

Apodization is a further precaution to decrease straylight/increase contrast in coronagraphs reducing the effect of diffracted light (Aime, 2013). However, this approach is more common when coronagraphs are used to occult point-like sources (like stars for the search of exoplanets; e.g., Soummer et al., 2011).

3.4 Polarisation in solar corona

As anticipated, the solar corona is the result of three different main contributions (K, F, and E corona). The main origin of polarisation in the solar corona comes from K-corona and is due to *Thomson scattering*. The polarised intensity coming from the solar corona is called *polarised brightness* (pB). By considering the definitions given in Chapter 2, it is possible to express the scattered radiation for *Thomson scattering* through the Stokes parameters to easily derive the polarisation properties.

Let us consider a single electron placed in the origin of a reference system with an incident planar electromagnetic wave propagating along the z-axis (Figure 3.10).

---

[13]For this reason ground-based observations need an internally occulted coronagraph. Indeed, as shown in Figure 3.7, the sky-brightness dominates the coronal signal after a few solar radii.

[14]During the calibrations of the AntarctiCor coronagraph of the ESCAPE project (Chapter 5), we observed an improvement of a factor of 10 between the pre-/post- objective lens cleaning.
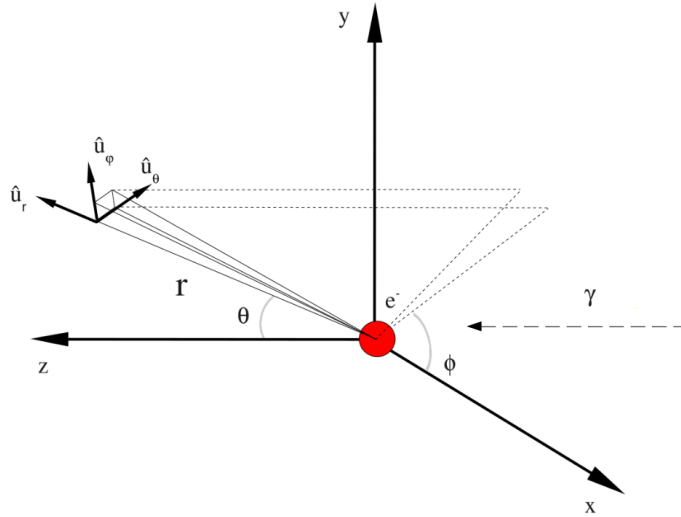
FIGURE 3.10: Thomson scattering scheme in which an electromagnetic wave coming along the *z*-axis hit an electron at rest at the origin of the reference system.

For an observer placed in (r, ϕ, θ) the Stokes vector relative to the diffuse radiation is equal to (Shurcliff, 1962):

$$S' = \frac{3\sigma_T}{16\pi R^2} \begin{pmatrix} S_0(1+\cos^2\theta) + S_1 \sin^2\theta \\ S_0 \sin^2\theta + S_1(1+\cos^2\theta) \\ 2S_2 \cos\theta \\ 2S_3 \cos\theta \end{pmatrix} \tag{3.2}$$

If we consider the Sun (the incident radiation comes from the photosphere and is generally not polarised $\rightarrow Q = U = V = 0$), the expression is equal to:

$$S' = \frac{3\sigma_T}{16\pi R^2} \begin{pmatrix} 1+\cos^2\theta \\ \sin^2\theta \\ 0 \\ 0 \end{pmatrix} \tag{3.3}$$

Starting with a non-polarised plane wave, the Thomson scattering will produce partially linearly polarised light with a degree of polarisation given by Eq. 2.21:

$$DoLP = \frac{\sqrt{S_1^2 + S_2^2}}{S_0} = \frac{\sqrt{(\sin^2\theta)^2}}{1+\cos^2\theta} = \frac{1-\cos^2\theta}{1+\cos^2\theta} \tag{3.4}$$

therefore it is equal to zero for an observer placed along the *z*-axis but unitary (i.e., the maximum degree of polarisation) for an observer placed in the *xy*-plane.

The light of the K-corona, coming from the Thomson scattering, is therefore polarised. On the other hand, it is only partially polarised. This is due to different geometric factors, the diffusion process, and the physical characteristics of the solar corona. For example, the Sun is not a point source but has an angular dimension 2Ω, so the wave incident on the single electron is not flat. Consequently, it is not possible to identify a real and unique plane perpendicular to the direction of propagation of the incident beam in which the scattered radiation is completely polarised. Furthermore, since the solar corona is optically thin, the radiation that reaches an observer

from a given direction is the sum of the contributions along the line of sight. Each contribution has a different value of angle θ and therefore a different degree of polarisation. If we take these factors (and the limb-darkening phenomenon) into account, the resulting Stokes vector along the line of sight is given by (Cranmer, 1997):

$$
\begin{pmatrix} S'_0 \\ S'_1 \\ S'_2 \\ S'_3 \end{pmatrix} = \frac{B_\odot}{1 - u/3} \frac{3\sigma_T}{16\pi}
$$

$$
\int_{-\infty}^{+\infty} dl N_e \begin{pmatrix} 2[(1-u)C(r) + D(r)] - \sin^2\theta[(1-u)A(r) + uB(r)] \\ \sin^2\theta[(1-u)A(r) + uB(r)] \\ 0 \\ 0 \end{pmatrix} \tag{3.5}
$$

where u is the linear *limb-darkening coefficient*, N_e is the *electron density* and A, B, C, D are *geometrical factors* (see next Chapter for more details on all these quantities). As we will see in the next Sections of this Chapter, if we derive the intensity of linearly polarised radiation, we obtain the pB equation shown in Eq. 3.16.

3.5 Electron density

Thanks to the polarised brightness, it is possible to obtain the electron density. The procedure and the equations reported below are based on the works of Van De Hulst, 1950; Minnaert, 1930; Billings, 1966. An analogous treatment of this study can be found in Cranmer, 1997.

First of all, it is possible to divide the intensity of the polarised light of the K-corona into two components (Figure 3.11), one with radial polarisation and one with tangential polarisation which can be written as:

$$
K_t = KN_e[(1-u)C(r) + uD(r)] \tag{3.6}
$$

$$
K_r = KN_e[(1-u)C(r) + uD(r)] - sin^2\theta[(1-u)A(r) + uB(r)] \tag{3.7}
$$

where u is the linear limb-darkening coefficient and K is a constant equal to:

$$
K = \frac{3I_0\sigma_T}{16\pi} \tag{3.8}
$$

having expressed with I_0 the solar intensity at the centre of the disc and σ_T the Thomson cross-section. Often, rather than I_0, it is more convenient to use the solar intensity averaged over the entire solar disc. In this case, we have:

$$
B_\odot = I_0 \left(1 - \frac{u}{3}\right) \tag{3.9}
$$

$$
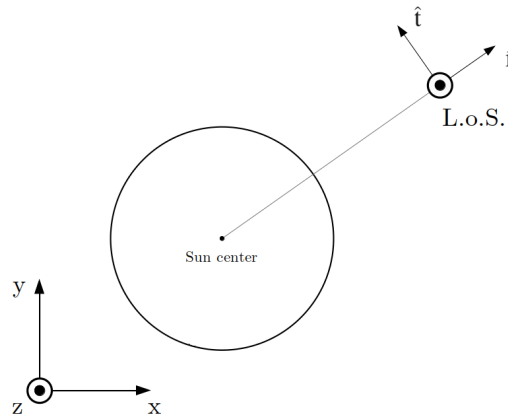K = \frac{B_\odot}{1 - \frac{u}{3}} \frac{3\sigma_T}{16\pi} \tag{3.10}
$$

FIGURE 3.11: Orientation of the considered K_r and K_t components of the coronal polarised intensity.

The quantities $A(r)$, $B(r)$, $C(r)$, $D(r)$ are geometric factors; explicitly:

$$A(r) = \cos\Omega\sin^2\Omega \tag{3.11}$$

$$B(r) = -\frac{1}{8}\left[1 - 3\sin^2\Omega - \cos^2\Omega\left(\frac{1+3\sin^2\Omega}{\sin\Omega}\right)\ln\left(\frac{1+\sin\Omega}{\cos\Omega}\right)\right] \tag{3.12}$$

$$C(r) = \frac{4}{3} - \cos\Omega - \frac{\cos^3\Omega}{3} \tag{3.13}$$

$$D(r) = \frac{1}{8}\left[5 + \sin^2\Omega - \cos^2\Omega\left(\frac{5-\sin^2\Omega}{\sin\Omega}\right)\ln\left(\frac{1+\sin\Omega}{\cos\Omega}\right)\right] \tag{3.14}$$

having defined the angle Ω as $\sin\Omega = R_\odot/r$ and $\cos\Omega = \sqrt{1-\sin^2\Omega}$. For an observer the intensity recorded is given by the sum of the contributions along the line of sight, therefore:

$$I_{K_t} = \int_{-\infty}^{+\infty} K_t dl \qquad \text{and} \qquad I_{K_r} = \int_{-\infty}^{+\infty} K_r dl \tag{3.15}$$

and the total intensity of polarised light due to Thomson scattering result to be:

$$pB \equiv I_{K_t} - I_{K_r} = K\int_{-\infty}^{+\infty} N_e \sin^2\theta[(1-u)A(r) + uB(r)]dl \tag{3.16}$$

It is possible to express the differential dl in terms of the distance from the centre of the Sun (r) like:

$$dl = \frac{rdr}{\sqrt{r^2 - \rho^2}} \tag{3.17}$$

so, by rewriting Eq. 3.16, we obtain:

$$pB = K\int_{\rho}^{+\infty} N_e\frac{\rho^2}{r^2}[(1-u)A(r) + uB(r)]\frac{rdr}{\sqrt{r^2 - \rho^2}} \tag{3.18}$$

Since the pB values can be obtained from polarimetric measurements of the K-corona, the electron density in the solar corona can be obtained by inverting the expression 3.18. In general, however, $N_e = N_e(\vec{x})$ for which it is not possible to analytically analyse the relationship. To do this it is necessary to add geometric hypotheses (e.g., spherical symmetry).

In the approximation to spherical symmetry, it is assumed that the electron density in the corona is a function of the only heliocentric distance, for which $N_e = N_e(r)$. From Eq. 3.18 we have:

$$pB(\rho) = 2K\int_{\rho}^{+\infty} F(r)\frac{\rho^2}{r^2}\frac{rdr}{\sqrt{r^2 - \rho^2}} \tag{3.19}$$

where we defined:

$$F(r) = N_e(r)[(1-u)A(r) + uB(r)] \tag{3.20}$$

Expressing the pB values as a series of negative powers:

$$pB(\rho) = \sum_i c_i \left(\frac{\rho}{R_\odot} \right)^{-d_i} \tag{3.21}$$

we obtain:

$$F(r) = \sum_i a_i \left(\frac{r}{R_\odot} \right)^{-b_i} \tag{3.22}$$

Indeed, by substituting Eq. 3.21 and 3.22 in Eq. 3.19, and rewriting $r = \rho x$:

$$\sum_i c_i \left(\frac{\rho}{R_\odot} \right)^{-d_i} = 2KR_\odot \sum_i a_i \left(\frac{\rho}{R_\odot} \right)^{-b_i - 1} \int_1^{+\infty} x^{-b_i - 1} \frac{dx}{\sqrt{x^2 - 1}} \tag{3.23}$$

To be valid, this expression required that the exponents of the powers of ρ of the two members of this equation must coincide. For this reason:

$$b_i = d_i + 1 \tag{3.24}$$

Substituting in Eq. 3.23 we obtain:

$$\sum_i c_i = 2KR_\odot \sum_i a_i \int_1^{+\infty} x^{-d_i - 2} \frac{dx}{\sqrt{x^2 - 1}} \tag{3.25}$$

From the table of integrals of (Gradshteyn, Ryzhik, and Jeffrey, 1994) we have that:

$$\int_1^{+\infty} x^{\mu - 1} (x^p - 1)^{\nu - 1} dx = \frac{1}{p} \beta \left(1 - \nu - \frac{\mu}{p}, \frac{1}{2} \right) \tag{3.26}$$

for $p > 0$, $\Re \nu > 0$, $\Re \mu < p(1 - \Re \nu)$, having indicated with β the Euler beta function. In our case: $p = 2$, $\nu = 1/2$, $\mu = -d_i - 1$. Euler beta function can be expressed via the gamma function as (Abramowitz and Stegun, 1964):

$$\beta(y, z) = \beta(z, y) = \frac{\Gamma(y)\Gamma(z)}{\Gamma(y + z)} \tag{3.27}$$

Then, Eq. 3.25 is equal to:

$$\sum_i c_i = \sqrt{\pi} KR_\odot \sum_i a_i \frac{\Gamma\left(\frac{d_i + 2}{2} \right)}{\Gamma\left(\frac{d_i + 3}{2} \right)} \tag{3.28}$$

so we have:

$$a_i = \frac{1}{\sqrt{\pi} KR_\odot} \frac{\Gamma\left(\frac{d_i + 3}{2} \right)}{\Gamma\left(\frac{d_i + 2}{2} \right)} c_i \tag{3.29}$$

Finally, the electron density can be derived as:

$$N_e(r) = \frac{\sum_i a_i \left(\frac{r}{R_\odot}\right)^{-b_i}}{[(1-u)A(r) + uB(r)]} \tag{3.30}$$

using Eq. 3.24 and Eq. 3.29 to derive the coefficients and the exponents of the series development.

The electron density allows to immediately derive some physical parameters of the solar corona such as the effective temperature, and, under particular conditions, to give an estimate of the upper abundance limit of the α particles in the corona.

Then, to calculate the electron density it is necessary to start from a pB profile (i.e., from the values in a given direction in heliocentric coordinates). This means that the hypothesis of spherical symmetry is local: in fact, it is required that it is valid only in the semi-plane originating from the conjunction of the centre of the Sun (SC) and the observer and passing through the line of sight (Fig. 3.12). For each direction the pB data were interpolated using Eq. 3.21 stopped at the second term:

$$pB\left(\frac{\rho}{R_\odot}\right) = c_0 \left(\frac{\rho}{R_\odot}\right)^{-d_0} + c_1 \left(\frac{\rho}{R_\odot}\right)^{-d_1} \tag{3.31}$$

By using the relations in Eq. 3.24 and 3.29, we can immediately obtain the electron density profiles for each pB profile by considering Eq. 3.30. If performed for an entire turn, we obtain an electron density map. From the electron density, it is possible to estimate different physical quantities (such as the limit of helium abundance in solar corona; Habbal and Esser, 1994) and an estimations of the solar wind velocity as well (Kohl et al., 1998; Romoli et al., 2021).
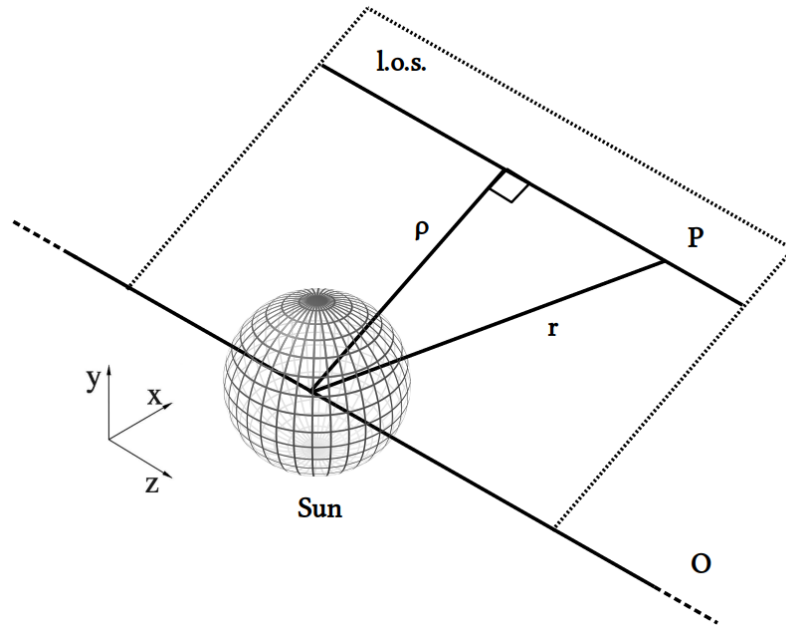

FIGURE 3.12: Scheme for the calculation of the electron density in spherical symmetry. The hypothesis of symmetry must be satisfied locally, i.e., in the semi-plane that originates from the joining centre of the Sun / observer and passing through the line of sight (l.o.s.).

Chapter 4

EKPol and Total Solar Eclipses

In this Chapter we deal with the data analysis of the total solar eclipse that occurred in Chile on July 2, 2019. As explained in Section 3.3.1, a total solar eclipse happens when the Moon passes exactly in front of the Sun. Because of its angular dimension, equal to the angular dimension of the Sun, the Moon totally occults the Sun and the corona becomes visible (up to different solar radii).[1] This is possible because during this phenomenon the brightness of the sky is drastically reduced (Figure 3.7). On average, there is one total solar eclipse per 1.5 years. However, the totality is visible only along a very small area of the Earth called the *zone of totality* (or *path of totality*). On the other hand, the partiality (even if it is in a restricted area as well) is broader.

The main geometrical aspects of a solar eclipse (total, partial, annular) are shown in Figure 4.1. A useful tool are the maps of Fred Espenak.[2] The maps show the full path of the solar eclipse across Earth's surface underling where is possible to observe the totality.

During the total solar eclipse observational campaign, we used the "Eclipse K-corona Polarimeter" (EKPol instrument) from the Astrophysical Observatory of Turin (OATo-INAF). In the next section, we will see more in detail how this instrument works and the analysis of the data acquired during the total solar eclipse.
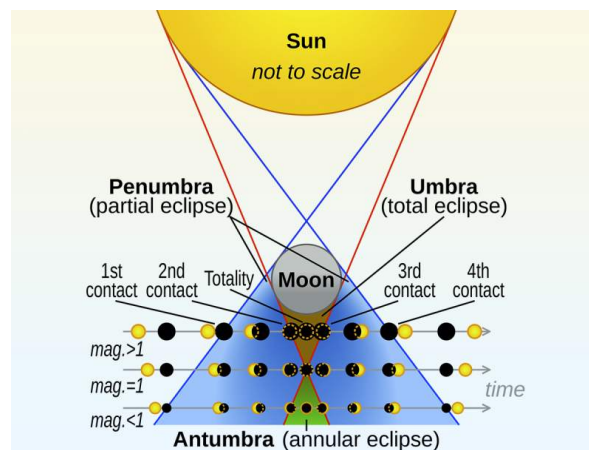

FIGURE 4.1: Geometry of solar eclipses The black spots represent the Moon (© 2022 Newport Corporation).

4.1 EKPol instrument

EKPol instrument is based on an optical telescope supplemented by an electronic controllable liquid-crystal variable retarder together with a specific CCD camera (Zangrilli, Fineschi, and Capobianco, 2009). It was designed and assembled in the

---

[1] When the Moon does not pass exactly in front of the Sun or the Moon angular dimension are not enough to perfectly cover the Sun, the Sun results to be only partially covered. In these cases we have a *partial* eclipse. The percentage of partiality changes in function of "how much Sun" is occulted by the Moon. In this case, independently of the percentage of occultation, the corona will be not visible.

[2] Better known as "Mr. Eclipse", he is an emeritus American astrophysicist that worked at the NASA Goddard Space Flight Center. He provided NASA's eclipse bulletins since 1978.

laboratories of the Turin Astronomical Observatory in collaboration with the Astronomical Observatory of the Valle d'Aosta (Zangrilli et al., 2006). The main EKPol characteristics are summarised in Table 4.1. More information can be found in Balboni, 2009 and Zangrilli, Fineschi, and Capobianco, 2009.

TABLE 4.1: Main EKPol characteristics.

Specification	Value
Aperture	50 mm
Effective focal length	600 mm
Plate scale	8.5 arcsec/pixel
Bandpass	$610 - 630$ nm (centre: 620 nm)
Objective lens	N-BK7/N-SF5
Camera type	CCD (funded by the ESA)
Frame dimension	1024×1024 pixels
Pixel size	24×24 μm
Bit depth	16 bit

The general optical scheme of EKPol in shown in Figure 4.2. The instrument calibration (not explicitly treated in this Thesis) was performed in ESTEC facilities obtaining results consistent with previous ones[3] (Zender J. and Capobianco G., 2019; Balboni, 2009).
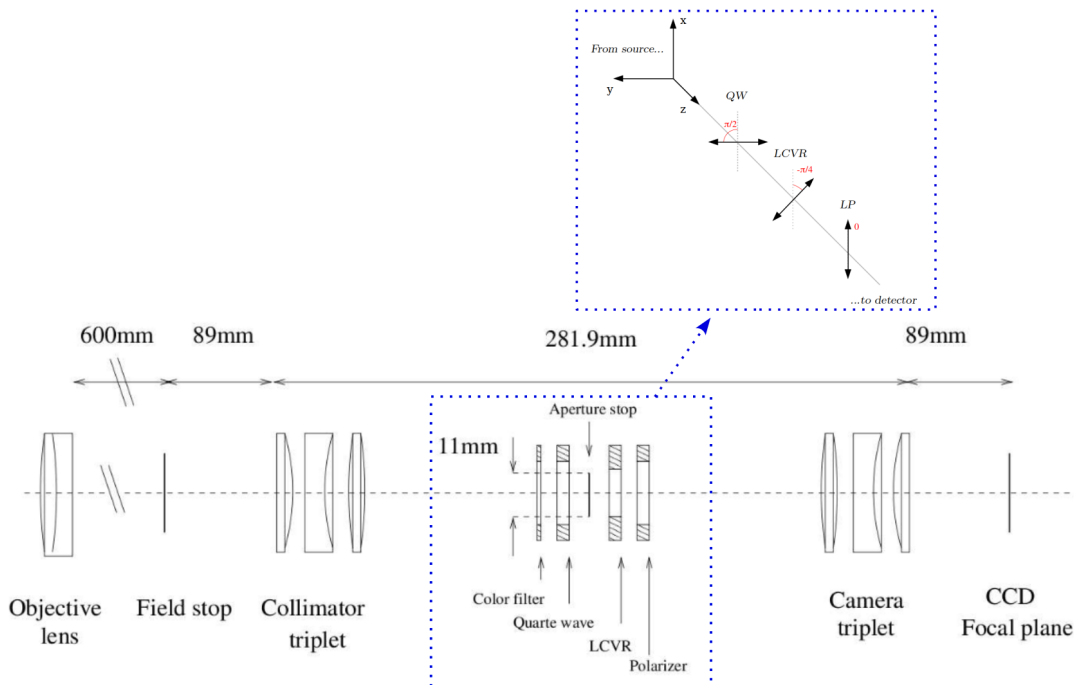

FIGURE 4.2: EKPol optical scheme (Zangrilli et al., 2006) with a zoom on the EKPol polarimeter (with the essential optical components).

---

[3]EKPol was used in the study of the K-corona during other total solar eclipses as well (e.g., the total solar eclipse on March 29, 2006, and July 11, 2010).

4.1.1 Liquid Crystals Variable Retarder

As the instrument name suggests, EKPol wants to measure the brightness of the K-corona. As seen in Chapter 3, the K-corona is linearly polarised (due to the Thomson scattering of the solar disc radiation by the free electrons in the coronal medium). Thus, a polarimeter can be used to distinguish it from the other components. For this reason, the EKPol instrument is provided with a polarimetric group. The innovation of the EKPol instruments is exactly here. Indeed, the EKPol polarimetric group consists of using a nematic[4] Liquid Crystal Variable Retarder plate (LCVR), in a rotator configuration, allowing to replace mechanically rotating retarders with electro-optical devices without moving parts. Indeed, EKPol was developed as a technology demonstrator for the Metis coronagraph on-board Solar Orbiter. Metis is the instrument that, for the first time ever[5], use this technology in space! More information about this topic is in Chapter 6. The EKPol polarimeter consists of a quarter-wave, a LCVR, and a linear polariser whose transmission axis identifies the x-axis of the reference system.

The LCVR consists of optically anisotropic liquid crystal molecules embedded between two glasses with a conductive film. These molecules are accommodated in cells with an ordered orientation. They have an effective birefringence value that can be changed by applying an electric field to the cells that rotates the molecules (Figure 4.3). A change in orientation of the molecules modifies the optical retardance in the orthogonal polarisation components of the incoming light. There are several advantages introduced by this technology. For example, liquid crystal-based retarders have a very quick response. More information about LCVRs can be found in Subsection 6.2.1.
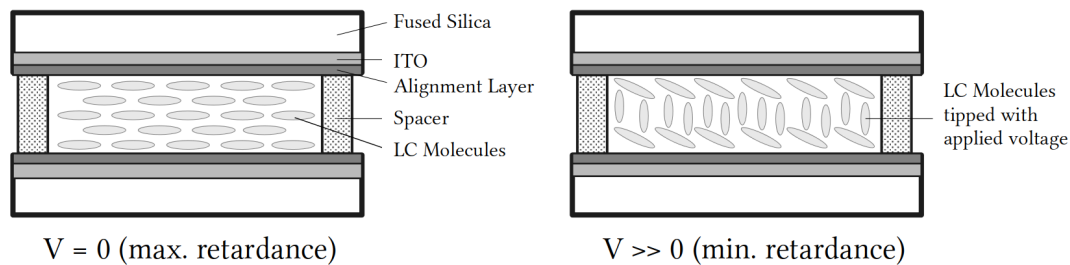

FIGURE 4.3: Schematic representation of a Liquid Crystal Variable Retarder (LCVR) operation.

In our particular case, polarisation measurements were measured using observations at four different polarisation angles (0, 45, 90, and 135 degrees). These angles are set by changing the applied voltages respectively to: 10000 mV, 8020 mV, 6610 mV and 5450 mV (from calibration). Finally, it is fundamental to underline that LCVR devices are sensitive to temperature; the retardance depends on temperature cells. For this reason, it is necessary to thermally control the device and to perform, during the instrument calibration, a characterisation for the different temperatures of usage (e.g., Zangrilli, Fineschi, and Capobianco, 2009).

---

[4]State of matter that has properties between those of conventional liquids and those of solid crystals.
[5]A LCVR is also used in the Polarimetric and Helioseismic Imager (PHI) instrument on-board Solar Orbiter (Solanki et al., 2020).

4.1.2   Müller matrix of EKPol polarimeter

By exploiting the formalism presented in Chapter 2, it is possible to derive the Muller matrix of the ideal EKPol polarimeter. In particular, for the quarter-wave plate and the linear polariser we have the Müller matrices reported in Eq. 2.58 and Eq. 2.50 respectively. Instead, for LCVR we have (Eq. 2.60, Balboni, 2009):

$$LCVR(-\pi/4, \delta) = \begin{pmatrix} 1 & 0 & 0 & 0 \\ 0 & \cos\delta & 0 & -\sin\delta \\ 0 & 0 & 1 & 0 \\ 0 & \sin\delta & 0 & \cos\delta \end{pmatrix} \tag{4.1}$$

where δ is the LCVR retardance value. The Muller matrix of the entire polarimeter is therefore given by (Figure 4.2):

$$\text{EKPol}(\delta) = LP(0) \cdot LCVR(-\pi/4, \delta) \cdot QW(\pi/2)$$

$$= \frac{1}{2} \begin{pmatrix} 1 & \cos\delta & \sin\delta & 0 \\ 1 & \cos\delta & \sin\delta & 0 \\ 0 & 0 & 0 & 0 \\ 0 & 0 & 0 & 0 \end{pmatrix} \tag{4.2}$$

The last column of Eq. 4.2 is composed of null terms since the instrument cannot measure circular polarization (and we are not interested in it since the K-corona is linearly polarised). It is also possible to see that the form obtained for Eq. 4.2 is equivalent to $\mathbf{M} = \mathbf{M}_{LP}\mathbf{M}_{rot}(2\theta = \delta)$ where $\mathbf{M}_{rot}$ is the Müller matrix of a rotating element. This means that the EKPol polarimeter (with the LCVR assembly) is equivalent to having a rotating linear polariser.

Knowing the EKPol Muller matrix, it is possible to derive the Stokes vector of the incident radiation. The signal recorded by an ideal sensor at the output of the polarimeter will be:

$$m_k = \frac{1}{2}(I + Q\cos\delta_k + U\sin\delta_k) \tag{4.3}$$

with $k = 0, 1, 2, 3$ indicating the LCVR retardances. So we have:

$$M = XS \quad\equiv\quad \begin{pmatrix} m_0 \\ m_1 \\ m_2 \\ m_3 \end{pmatrix} = \frac{1}{2} \begin{pmatrix} 1 & \cos\delta_0 & \sin\delta_0 \\ 1 & \cos\delta_1 & \sin\delta_1 \\ 1 & \cos\delta_2 & \sin\delta_2 \\ 1 & \cos\delta_3 & \sin\delta_3 \end{pmatrix} \begin{pmatrix} I \\ Q \\ U \end{pmatrix} \tag{4.4}$$

In the following analysis, we considered the theoretical modulation matrix $\mathbf{X}$. Further analysis will be performed by retrieving a calibrated demodulation tensor similarly to what is described in Subsections 5.3.8 and 6.2.2. We applied to the LCVR voltages such as $\delta_0 = \frac{3\pi}{2}$, $\delta_1 = \pi$, $\delta_2 = \frac{\pi}{2}$, $\delta_3 = 0$. Thus, we can rewrite Eq. 4.4 as:

$$\begin{pmatrix} m_0 \\ m_1 \\ m_2 \\ m_3 \end{pmatrix} = \frac{1}{2} \begin{pmatrix} 1 & 0 & -1 \\ 1 & -1 & 0 \\ 1 & 0 & 1 \\ 1 & 1 & 0 \end{pmatrix} \begin{pmatrix} I \\ Q \\ U \end{pmatrix} \tag{4.5}$$

The solution of Eq. 4.5 is obtained by inverting the modulation matrix:

$$S = X^\dagger M = \frac{1}{2} \begin{pmatrix} 1 & 1 & 1 & 1 \\ 0 & -2 & 0 & 2 \\ -2 & 0 & 2 & 0 \end{pmatrix} M \tag{4.6}$$

4.2 Total solar eclipse 2019

A total solar eclipse happened on July 2, 2019. This eclipse lasted roughly two and a half hours, with almost two minutes of totality at 20:39 UT. It was visible across a narrow band of Chile and Argentina. The Espenak map of this event is shown in Figure 4.4. The data acquisition during the total eclipse was performed by Joe Zender (ESA/ESTEC) from ESO - La Silla Observatory in Chile (Figure 4.5).
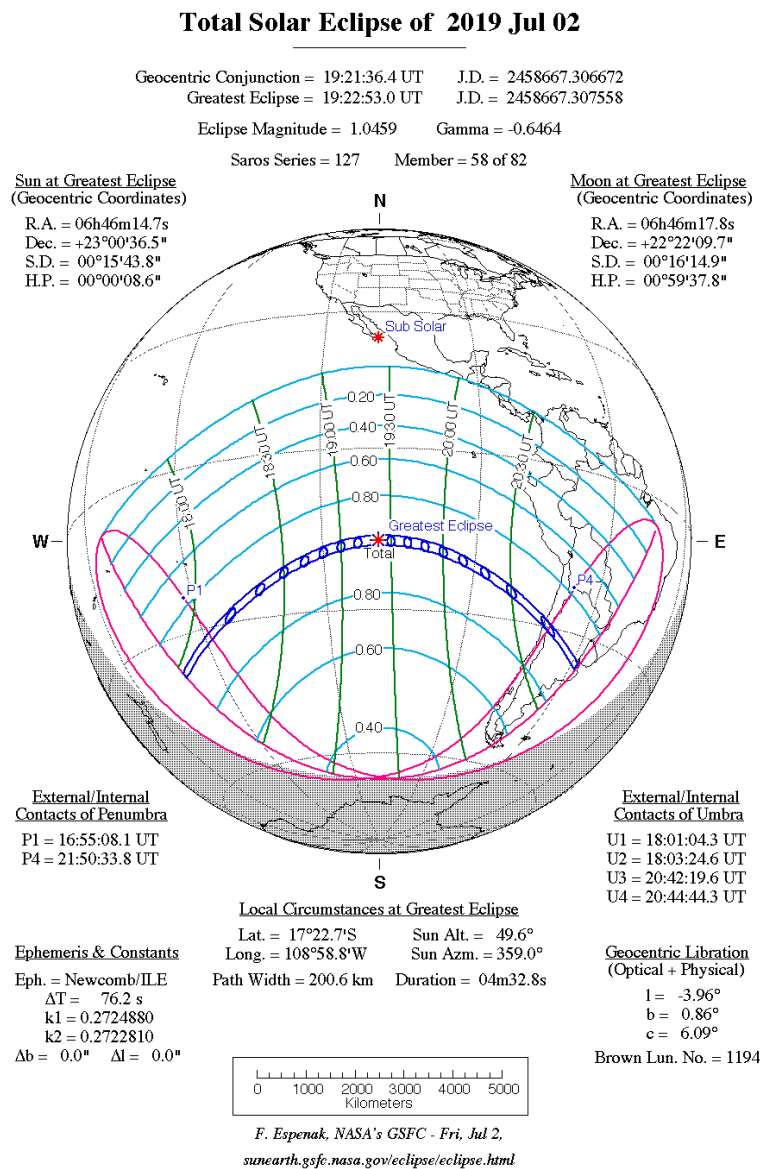

Total Solar Eclipse of 2019 Jul 02

Geocentric Conjunction = 19:21:36.4 UT   J.D. = 2458667.306672
Greatest Eclipse = 19:22:53.0 UT   J.D. = 2458667.307558

Eclipse Magnitude = 1.0459   Gamma = -0.6464

Saros Series = 127   Member = 58 of 82

Sun at Greatest Eclipse (Geocentric Coordinates)
R.A. = 06h46m14.7s
Dec. = +23°00'36.5"
S.D. = 00°15'43.8"
H.P. = 00°00'08.6"

Moon at Greatest Eclipse (Geocentric Coordinates)
R.A. = 06h46m17.8s
Dec. = +22°22'09.7"
S.D. = 00°16'14.9"
H.P. = 00°59'37.8"

External/Internal Contacts of Penumbra
P1 = 16:55:08.1 UT
P4 = 21:50:33.8 UT

External/Internal Contacts of Umbra
U1 = 18:01:04.3 UT
U2 = 18:03:24.6 UT
U3 = 20:42:19.6 UT
U4 = 20:44:44.3 UT

Local Circumstances at Greatest Eclipse
Lat. = 17°22.7'S   Sun Alt. = 49.6°
Long. = 108°58.8'W   Sun Azm. = 359.0°
Path Width = 200.6 km   Duration = 04m32.8s

Ephemeris & Constants
Eph. = Newcomb/ILE
ΔT = 76.2 s
k1 = 0.2724880
k2 = 0.2722810
Δb = 0.0"   Δl = 0.0"

Geocentric Libration (Optical + Physical)
l = -3.96°
b = 0.86°
c = 6.09°
Brown Lun. No. = 1194

0 1000 2000 3000 4000 5000
Kilometers

F. Espenak, NASA's GSFC - Fri, Jul 2,
sunearth.gsfc.nasa.gov/eclipse/eclipse.html

FIGURE 4.4: Solar eclipse on July 2nd, 2019 (© F. Espenak).

FIGURE 4.5: Total solar eclipse on July 2nd, 2019 as seen from ESO's La Silla Observatory in Chile (© 2019 CESAR/ESA).

4.2.1 Image composition

During the two minutes of totality, we acquired images at different exposure times for each voltage applied to the LCVR. In particular, we set: $T_{exp} = 400$ ms, 1000 ms, 4000 ms for each of the four applied voltage (for a total of 12 images). Dark images were also acquired (for each exposure time) immediately before and immediately after the solar eclipse. The dark used to correct the images was obtained as the average of these two runs (for each exposure time, Figure 4.6).
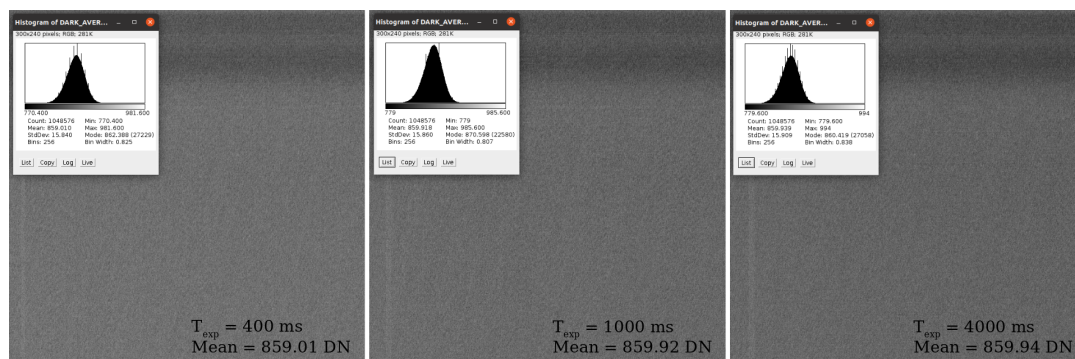
FIGURE 4.6: EKPol dark images at different exposure time. The average value over the frame seems not to change too much in these time ranges.

An example of eclipse images for a fixed exposure time is shown in Figure 4.7. To obtain the final coronal image, we composed them into a unique one. The complete log of the data collected during the solar eclipse is available under request.
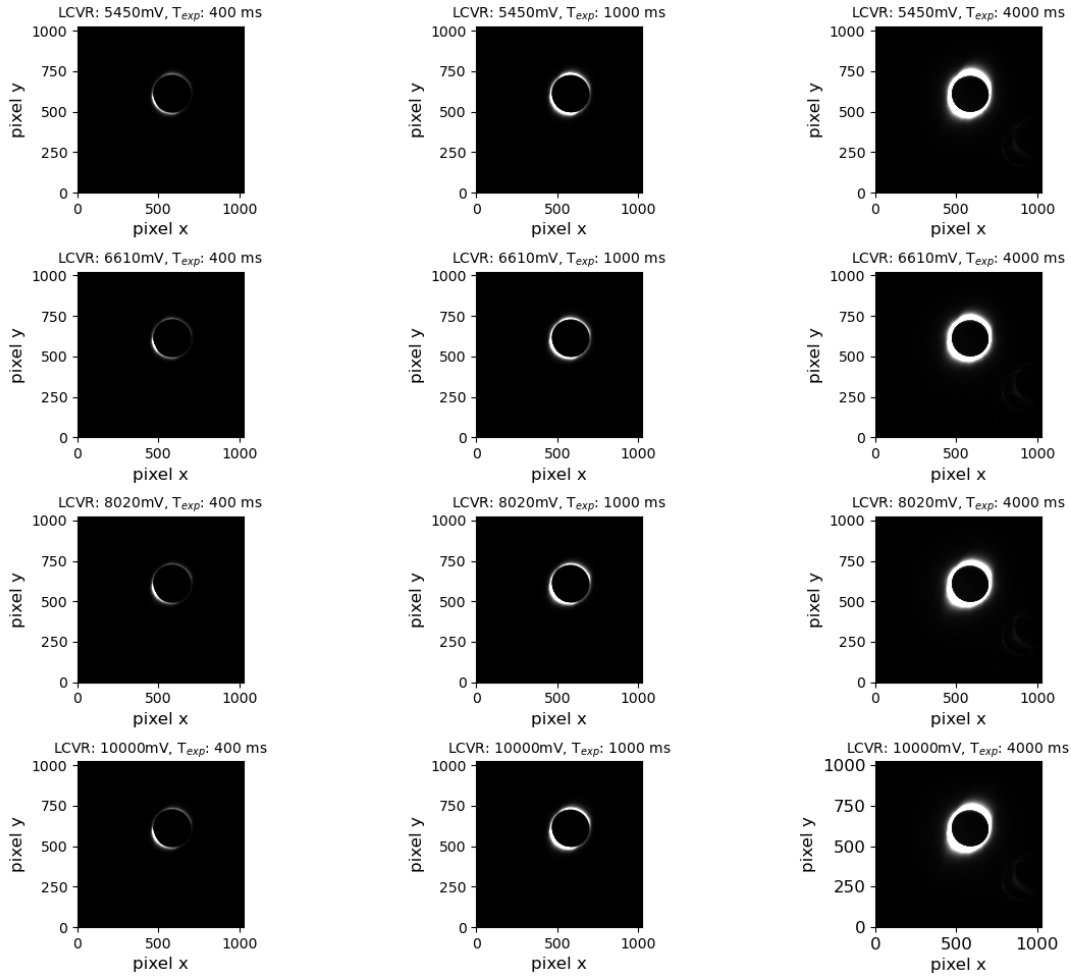
FIGURE 4.7: EKPol total solar eclipse images at different exposure time. Some images present saturated areas (especially for higher exposure times).

Starting with the raw images, we removed the dark. Then, by combining the three different exposure times we obtain a single image with a high dynamic range. As is possible to see in Figure 4.7, in some images there are saturated areas (sometimes affected by *blooming* -i.e., spread of charge to adjacent pixels-). These regions have no physical information even if with the greatest signal-to-noise ratio (SNR). Thus, it is necessary to remove these regions before proceeding with the combination of the images. We considered the linearity of the detector up to the 90% of the detector saturation value:

$$\xi = 0.9 \left(2^{16} - 1\right) = 58981.5 \tag{4.7}$$

Then, we looked at the three different exposure times and we considered the pixels with the highest SNR but inferior to the threshold ξ as defined in Eq. 4.7. We performed the same procedure for all the four different applied voltages on the LCVR (i.e., we obtain four high dynamic range images). The result of the image composition (for a fixed applied voltage) is shown in Figure 4.8.
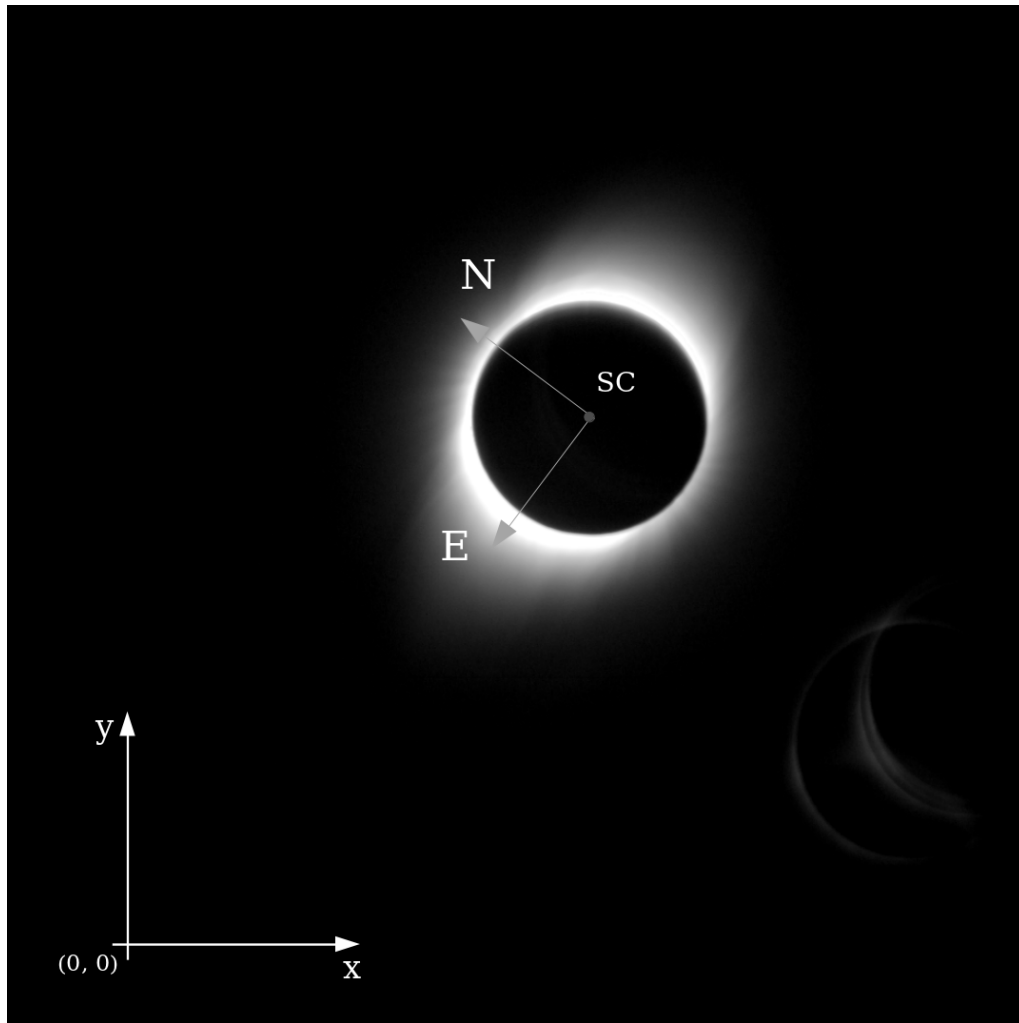
FIGURE 4.8: Composition of three images at different exposure time
for a fixed applied voltage to the LCVR (logarithmic scale). The frame
reference system and the sun center (SC) reference system are pre-
sented as well.

The same procedure was performed for the four different voltages applied to the
LCVR obtaining four images at different linear polarisation.

The artifacts visible in the bottom-right side of Figure 4.8 are ghosts due to in-
ternal reflections generated by the filter present in EKPol (Figure 4.2). Indeed, by
moving this filter, it was possible to shift the ghosts to the side of the image so that
they do not interfere with the measurements.

4.3   Polarimetric study

As described in Chapter 3, the K-corona is linearly polarised through Thomson scat-
tering. Thanks to different applied voltages to the LCVR we are able to obtain images
at four different linear polarisations (Subsection 4.1.1). Thus, we are able to perform
a polarimetric study of the solar corona.

4.3.1 Polarised Brightness

By considering the four different linear polarisations (0, 45, 90, 180 degree) we are able to extract the first polarimetric results. The Stokes parameters (I, Q, U) are obtained as previously presented in Subsection 4.1.2. What has been obtained is shown in Figure 4.9. It is possible to notice the "four-quadrants" subdivision in the Q and U parameters and the shift of $\approx 45°$ between them. This is due to how these Stokes parameters are defined and considering the geometric properties of the linear polarisation around the solar disc (Section 3.4).
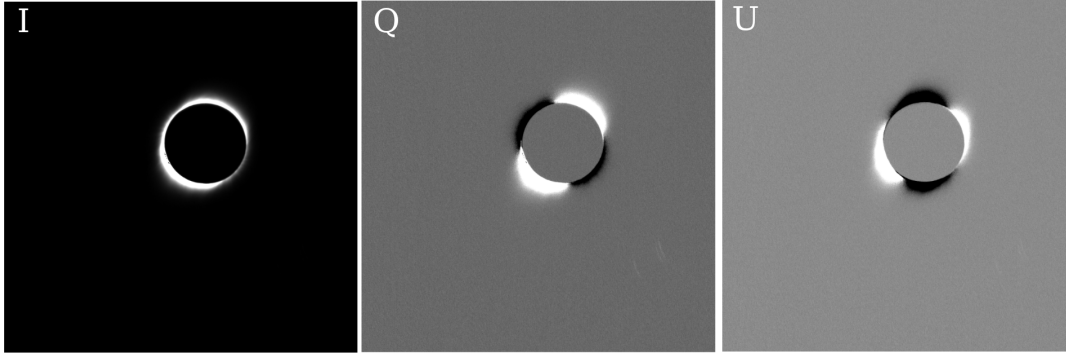
FIGURE 4.9: Stokes parameters (I, Q, U).

From the Stokes parameters, we can obtain the polarised brightness pB using Eq. 2.18. The result is shown in Figure 4.10 (in logarithmic scale). We can compare what was obtained with EKPol during the total solar eclipse with what was observed, on the same day, from KCor instrument at the Mauna-Loa Observatory (Hou, de Wijn, and Tomczyk, 2013) and LASCO-C2 on-board SOHO (Brueckner et al., 1995). In Figure 4.11 we compare the $pB[B_\odot]$ values along the East streamer. A comparison for different polar angles between EKPol and KCor polarised brightness is shown in Figure 4.12.
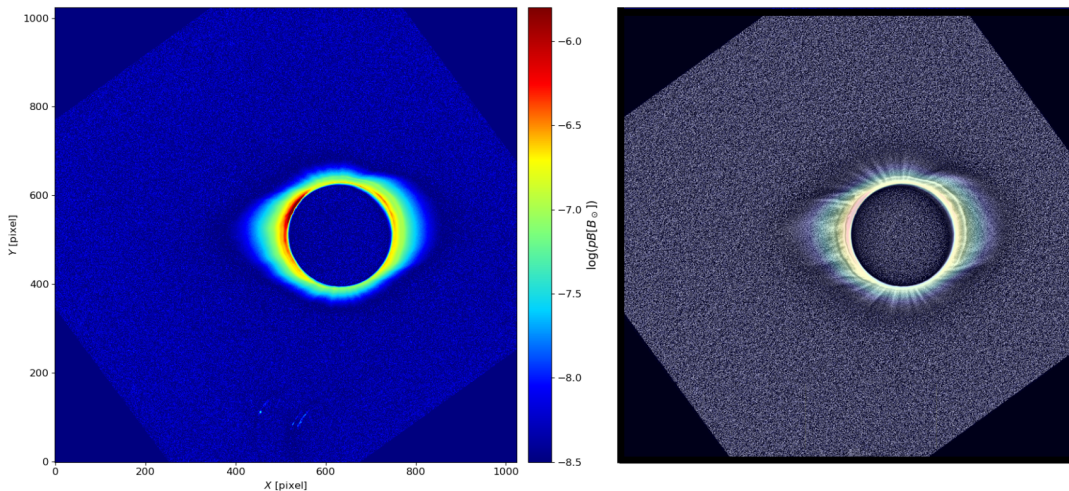

FIGURE 4.10: **Left:** Polarised brightness obtained with EKPol instrument during the total solar eclipse (logarithmic scale). Being a solar minimum, it is possible to notice just two equatorial streamers and some plumes at the poles. **Right:** Logarithmic polarised brightness processed through a Multi-scale Gaussian Normalization (MGN) filter (Morgan and Druckmüller, 2014) to highlight coronal structures.
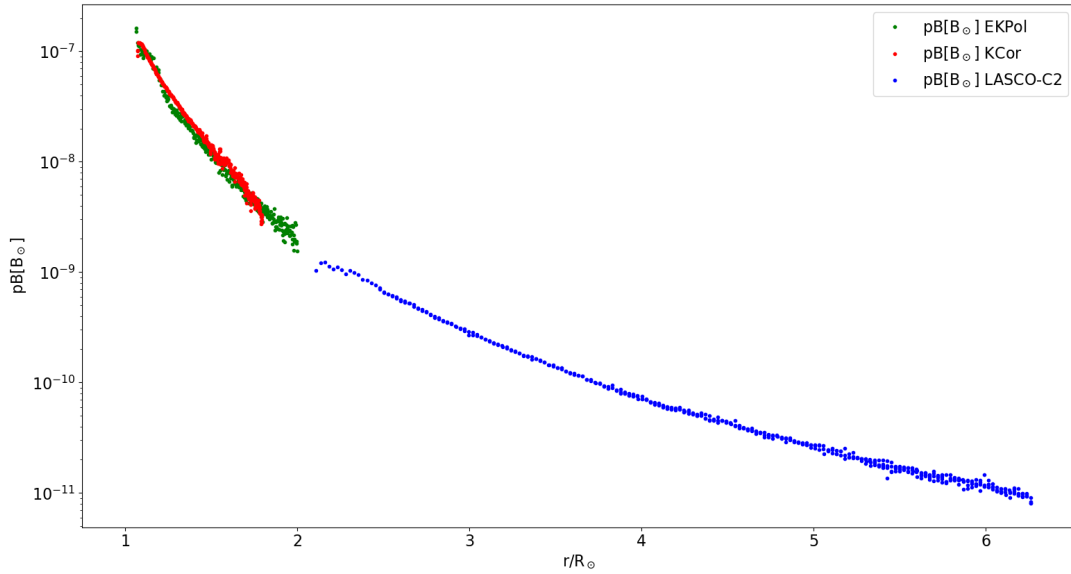
FIGURE 4.11: Comparison between the polarised brightness $pB[B_\odot]$ as measured by EKPol, LASCO-C2 and KCor on July 2, 2019. In this example, we compared the values along the East streamer.
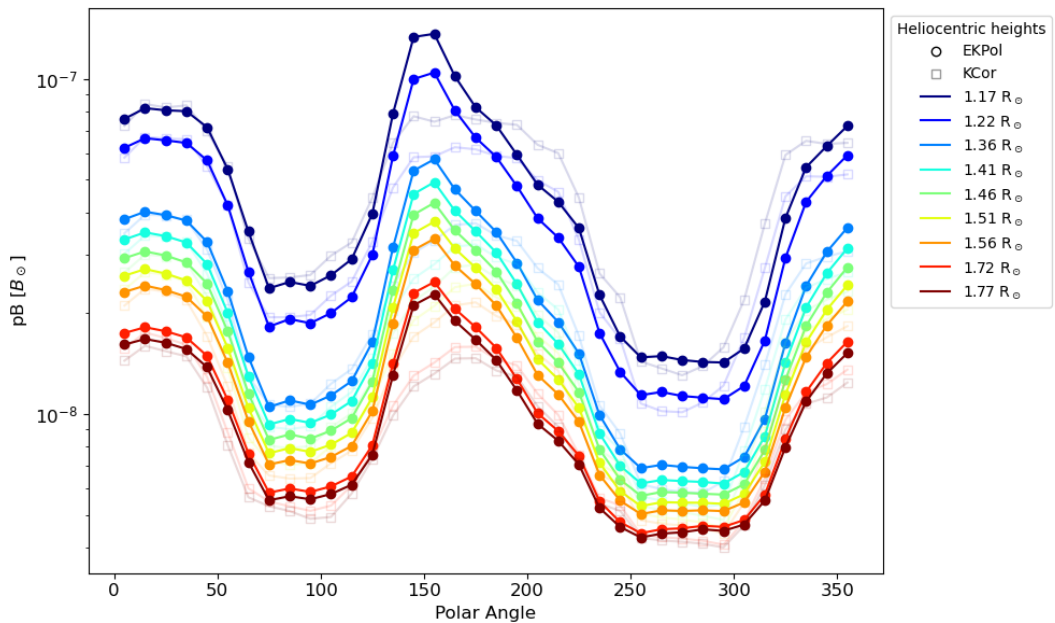

FIGURE 4.12: Comparison between the pB as measured at different polar angle by EKPol and KCor on July 2, 2019. The polar angle is zero along the West streamer and moving counterclockwise.

4.3.2 Degree and angle of linear polarisation

Considering Eq. 2.21, we can evaluate the degree of linear polarisation (pB/I). The result is shown in Figure 4.13. The maximum degree of polarisation at about 1.4 R$_\odot$ is equal to $\approx 36\%$. It is consistent with what reported on Allen, 2002. As expected, the degree of linear polarisation has a slight increase before starting to decrease moving away from the solar limb. This is because, at short distances from the solar surface, the source cannot be considered a point-like source.

From Eq. 2.22, we can evaluate the angle of linear polarisation (Figure 4.14). The vector map in Figure 4.15 underline the geometry of the linear polarisation in the solar corona that is tangent to the solar limb (Elmore et al., 2000).
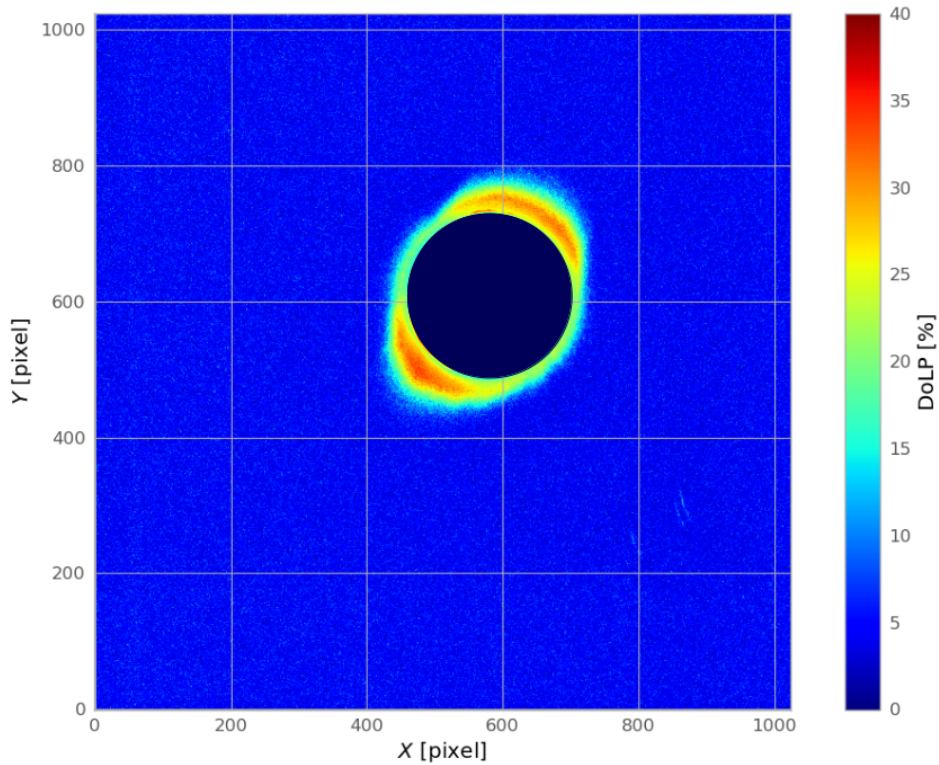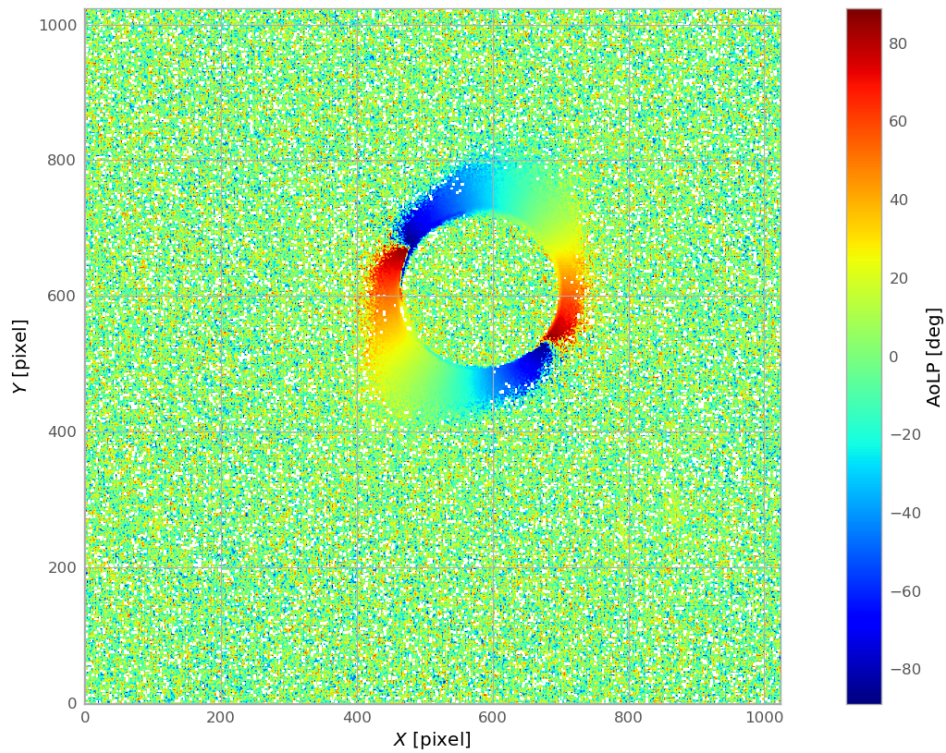

FIGURE 4.13: Degree of linear polarisation.
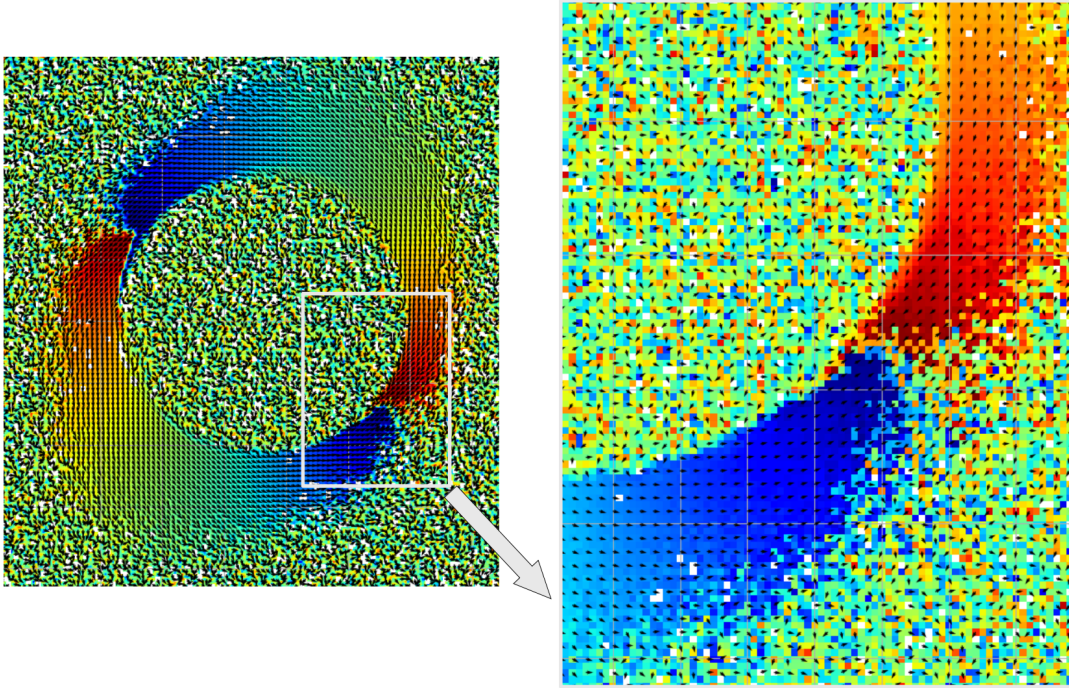

FIGURE 4.14: Angle of linear polarisation.

FIGURE 4.15: Detail on the angle of linear polarisation. The polarisation in the solar corona is tangent to the solar limb (binning 2×2).

4.4   Electron density evaluation

Thanks to the polarised brightness, it is possible to obtain the electron density (N_e) as described in Section 3.5. Thus, we can interpolate the pB radial profiles with Eq. 3.31:

$$pB\left(\frac{\rho}{R_\odot}\right) = c_0 \left(\frac{\rho}{R_\odot}\right)^{-d_0} + c_1 \left(\frac{\rho}{R_\odot}\right)^{-d_1} \tag{4.8}$$

It is possible to perform these interpolations on the entire round angle, with a step of one degree. From the fit function we can obtain the c_0, c_1, d_0 and d_1 free parameters. Knowing these parameters it is possible to evaluate the a_i and b_i ones by considering Eq. 3.29 and Eq. 3.24 respectively. It is now possible to perform the N_e calculation through Eq. 3.30:

$$N_e(r) = \frac{\sum_i a_i \left(\frac{r}{R_\odot}\right)^{-b_i}}{[(1-u)A(r) + uB(r)]} \tag{4.9}$$

In particular, we considered a limb-darkening coefficient $u = 0.63$ in the considered VL range (empirically determined, Minnaert, 1930). The results are shown in Figure 4.16 (a radial profile) and in Figure 4.17 (map). As expected, the electron density is higher in the equatorial regions (with the presence of streamers) than in the solar poles.

EKPol was used in the study of the K-corona during different total eclipses. We can compare the electron density with what obtained during other eclipses (Figure 4.18).
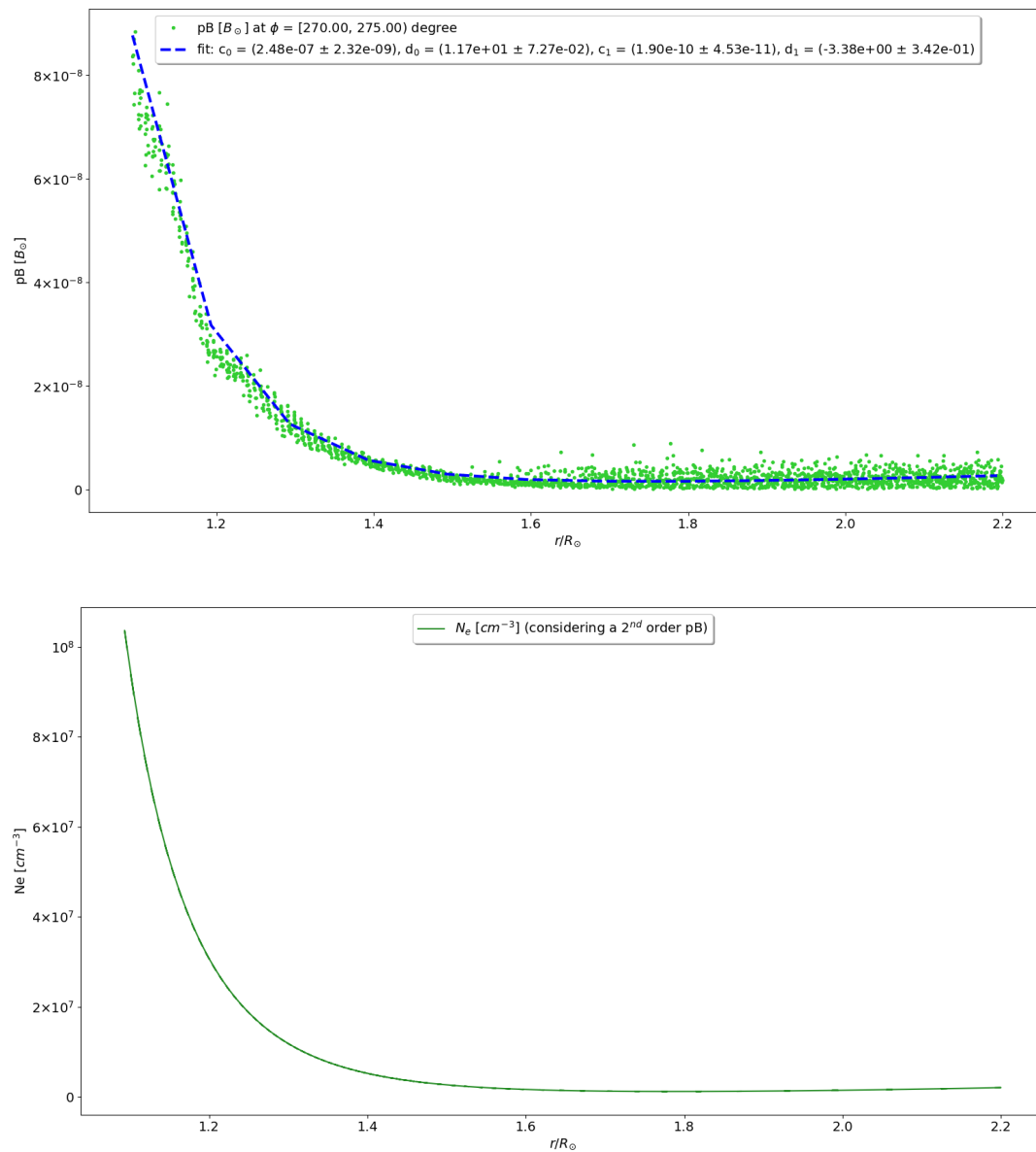
FIGURE 4.16: **(a) Top:** Example of the fit of a radial profile of the polarised brightness and c_0, c_1, d_0, and d_1 parameters evaluation through Eq. 4.8. In this particular case, we considered a profile near the East equatorial streamer. **(b) Bottom:** Electron density extrapolated from the interpolation of the polarised brightness radial profile.
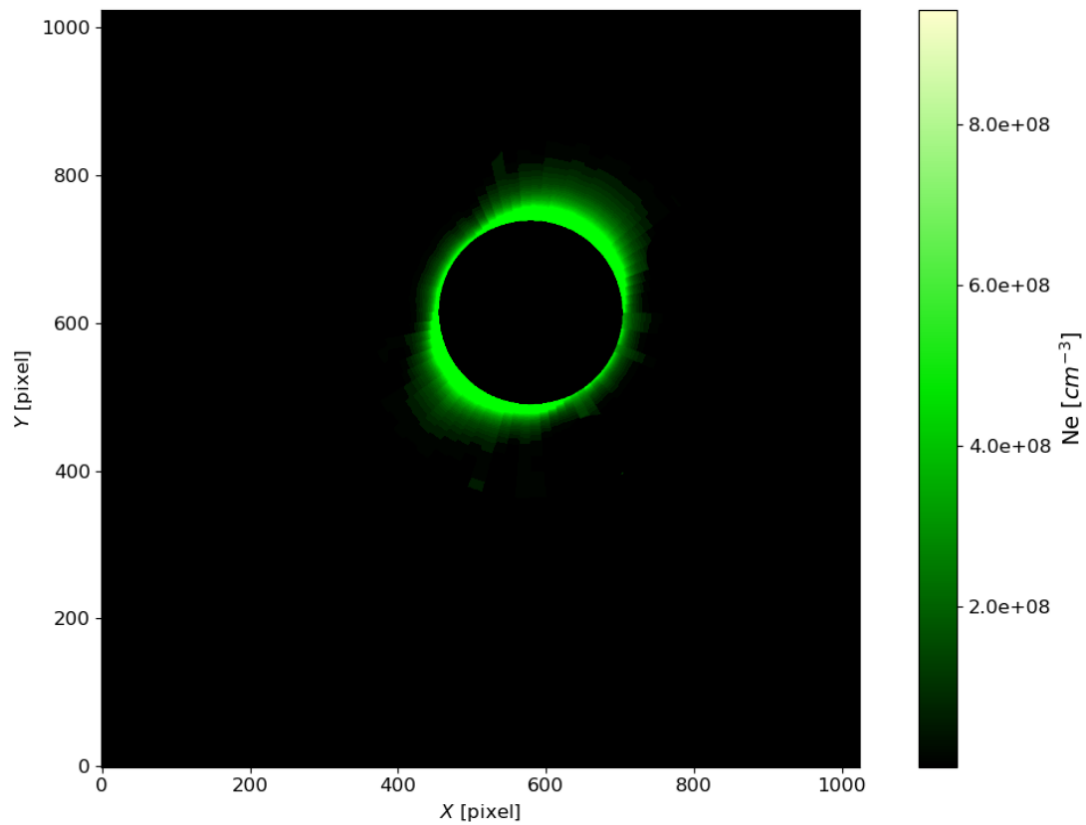
FIGURE 4.17: Electron density map obtained from the total solar eclipse on July 02, 2019 with EKPol telescope. It is evaluated with a polar angle step of five degrees.
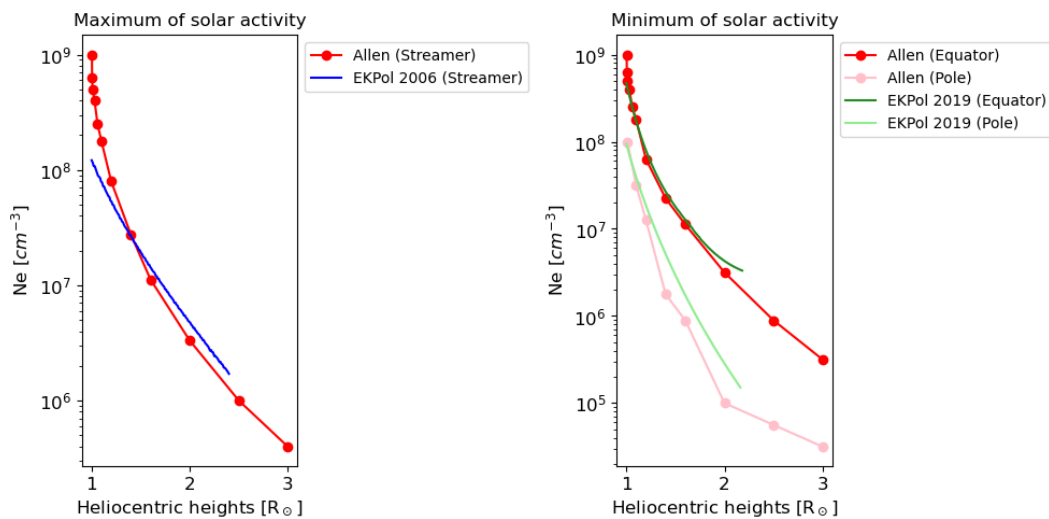

FIGURE 4.18: Comparison between the electron density obtained during the total solar eclipse on July 02, 2019 (during a *minimum* of solar activity) and the total solar eclipse on March 29, 2006 (during a *maximum* of solar activity) with EKPol telescope. The values are consistent with what reported in Allen, 2002.

4.5   Composite image with space-based instruments

It was possible to perform a composite image of the total solar eclipse with the EKPol image and other images from ground-based and space-based instruments. In particular, Figure 4.19 shows the composite image of the solar corona obtained by merging the total solar eclipse observations performed by EKPol and CESAR team (Figure 4.5) and the space-based solar corona images from SDO/AIA 171, SOHO/LASCO-C2 and SOHO/LASCO-C3.

The images were processed via the Normalizing Radial Graded Filter (NRGF) described in Morgan, Habbal, and Woo, 2006 while the EKPol logarithmic image was processed through a Multi-scale Gaussian Normalization (MGN) filter to highlight the coronal structures (Morgan and Druckmüller, 2014).
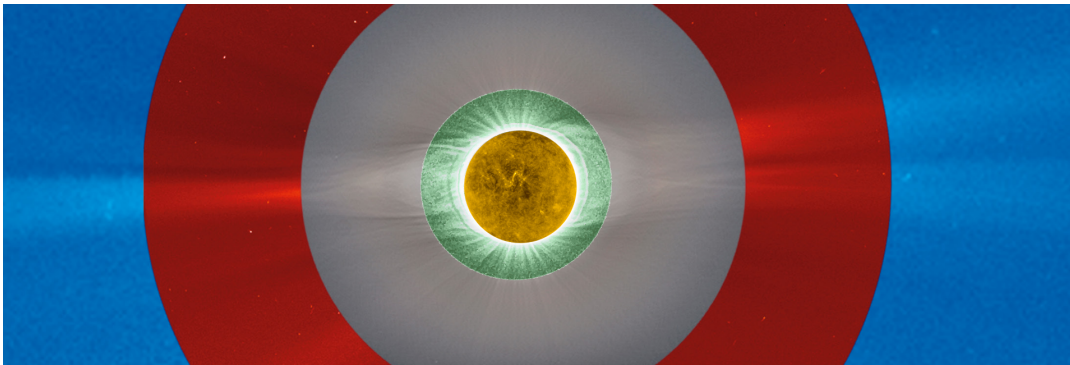

FIGURE 4.19: A composite image of the solar eclipse made from ground and space observations: SDO/AIA 171 solar disc, EKPol in green, CESAR corona in grey, SOHO/LASCO-C2 outer corona in red, SOHO/LASCO-C3 extended corona in blue.

The EKPol image seems to be in good accordance with what observed by the other instruments. Thanks to ESA/CESAR team, SOHO (ESA & NASA), and the Royal Observatory of Belgium (ROB) for providing their images composition (Christensen et al., 2019).

Chapter 5

ESCAPE Project

As described in Section 3.3 the solar corona is the result of three different main contributions. The brightness of each component decreases with a power-law moving away from the Sun as shown in Figure 3.7 (Phillips, 1992; Rycroft, 1993; November and Koutchmy, 1996). This figure underlines why the ground-based observations of the solar corona are so difficult in absence of a total solar eclipse; the sky brightness is a huge source of straylight. That's the reason why it is necessary to find a place with a very low sky brightness. Just a few places on Earth match such requirements for ground-based, out-of-eclipse coronagraphic measurements. One of these places is, for instance, the Mauna Loa Observatory ($\approx$ 3400m a.s.l.). To date, that is the only place on Earth where continuous coronagraphic observations are possible. On the other hand, another candidate coronagraphic site is the Dome C plateau in Antarctica. In this Chapter, we show the first results of the Extreme Solar Coronagraphy Antarctic Program Experiment (ESCAPE). We were able to perform sky brightness measurements and solar corona observations at the Italian-French Concordia Station, on Dome C, Antarctica ($\approx$ 3300m a.s.l.) during the summer 34th, 35th, and 37th Expeditions of the Italian Piano Nazionale Ricerche Antartiche (PNRA).

Antarctica offers a great opportunity for ground-based observations of the solar corona thanks to the high altitude of the Antarctic plateau of Dome C ($\approx$ 3233m a.s.l.), the high latitude (75° 06′ S; 123° 20′ E), the large number of daily hours of observations during the Antarctic summer (Figure 5.1) and the almost total absence of anthropic pollution, are necessary conditions for a low sky brightness. First attempts to characterise the sky brightness at Dome C were performed in 2008 by the pioneering observations of J. Arnaud (Faurobert, M., Arnaud, J., and Vernisse, Y., 2012). One of the goals of the ESCAPE Project is to quantitatively evaluate the sky brightness at the Dome C plateau. In particular, the data during the whole missions were acquired with the internally-occulted Antarctic coronagraph, AntarctiCor (Figure 5.2). As we will see in the next Section, AntarctiCor is designed to work in visible light and at low temperatures. Thanks to its particular detector (PolarCam), it is also able of capturing, at the same time, images with four different linear polarisations (Section 5.2). In particular, thanks to this instrument, we carried out sky brightness measurements and the observations of the K-corona polarised brightness (generated by Thomson scattering of photospheric light of coronal free electrons - see Chapter 3). From the polarised brightness, it will be possible to determine the coronal electron density as well (Van De Hulst, 1950). The evaluation of the sky brightness was performed during the 34th and 35th Italian Expeditions. More details about ESCAPE and its science objectives can be found in Fineschi et al., 2019a.

FIGURE 5.1: Composition of hourly images showing the Sun's position during the Antarctic summer (Concordia Base; December 26, 2021). In the bottom, 360° images from Baseline Surface Radiation Network (BSRN) project - PI, Dr. A. Lupi (Lupi, 2021). It is possible to observe a very good sky condition in the left image. In the middle, the presence of a solar halo is a sign of ice crystals in the atmosphere that can potentially compromise observations by producing straylight. Worst sky conditions are shown on the right with a slight cloud cover as well. By using the full sky camera it is possible to have a general view of sky conditions to avoid the worst days.

FIGURE 5.2: AntarctiCor hosted by the Antarctic Search for Transiting ExoPlanet (ASTEP) project equatorial mount during the 34th and 37th Expedition (red box) and in the Baeder dome during the 35th Expedition (green box) at Concordia station for the ESCAPE project. (Credits: A. Liberatore and G. Capobianco @PNRA/IPEV)
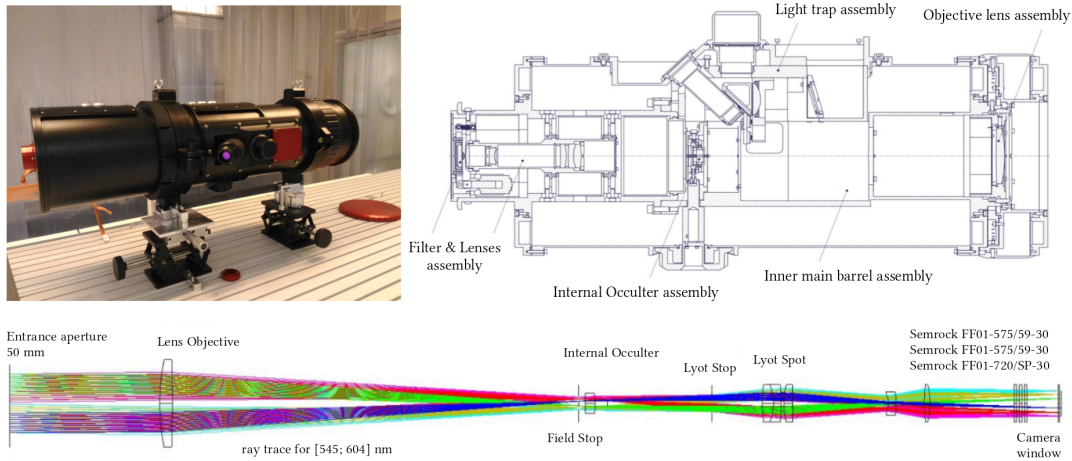
FIGURE 5.3: **Top left:** AntarctiCor in the INAF Optical Payload Systems facility (OPSys) - clean room ISO 5 in Turin (Italy) for tests and calibrations (Fineschi et al., 2019b). The main sub-assembly diagram (top right panel) comprises: objective lens assembly, inner main barrel assembly, internal occulter assembly, lenses assembly, filter assembly, light trap assembly, microscope assembly. **Bottom:** AntarctiCor ray tracing in the wide-band (591 ± 5) nm.

5.1 Antarctic solar coronagraph

The instrument deployed during all campaigns was the Antarctica solar Coronagraph, AntarctiCor (Figure 5.3). The main features of the instrument are summarised in Table 5.1. It is a classical Lyot internally-occulted coronagraph (Lyot, 1932) based on the externally-occulted ASPIICS (Association of Spacecraft for Polarimetric and Imaging Investigation of the Corona of the Sun) coronagraph for the European Space Agency (ESA) formation-flying PROBA-3 (Project for On-Board Autonomy-3) mission (Galy et al., 2015).

TABLE 5.1: AntarctiCor characteristics (Fineschi et al., 2019b).

Telescope design	Classical internally-occulted Lyot coronagraph
Aperture	50 mm
Eff. Focal Length	700 mm
f/ratio	14
Spectral Ranges	(591 ± 5) nm – see Figure 5.4
Camera type	Interline transfer CCD PolarCam;
	Model: U4 (Zecchino, 2017)
Camera format	1950×1950 pixels
Pixel size	7.4 μm × 7.4 μm
Plate scale	2.15 arcsec/pixel $\equiv$ 4.30 arcsec/superpixel
Field of View (FoV)	$\pm 0.58° \equiv \pm 2.24\,R_\odot$ (along x and y axis)
	$\pm 0.82° \equiv \pm 3.14\,R_\odot$ (along diagonal)
Polarisation analysis	Spatial modulation (linear micropolarisers on the sensor)

The main characteristics of the AntarctiCor band-pass filter used during the missions are shown in Figure 5.4 and in Table 5.2. More information can be found in Semrock, 2019.
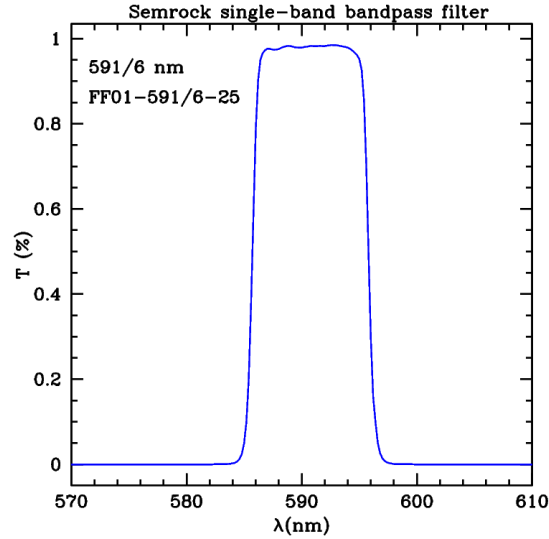
FIGURE 5.4: Semrock band-pass filter transmissivity (591 ± 5) nm.

TABLE 5.2: Main filter specifications (Semrock, 2019).

Specification	Value
Transmission band	$T_{avg} > 93\%$ at $588 - 594.5$ nm
Centre wavelength	591.25 nm
FWHM bandwidth (nominal)	10 nm
Transverse dimensions (diameter)	25 mm
Filter thickness	5.0 mm

Indeed, the telescope design is derived from the design of the ASPIICS space coronagraph (Galy et al., 2015). Some modifications from the original design have been adopted due to the main difference between ASPIICS and AntarctiCor: the former is externally-occulted, and the latter is internally occulted. For example, since the objective doublet lens of ASPIICS operates in the shadow of the external occulter while the AntarctiCor objective is directly illuminated by the Sun-disc light, to minimise the internal reflection in the objective lens, this has been changed into a highly polished singlet, i.e., 0.5 nm rms (Fineschi et al., 2019b).

The telescope temperature is acquired at three different points by three PT100 and it is controlled by using three heaters with a power of 90 W, 100 W, 40 W in the front, central, and rear sub-assembly, respectively. The closed-loop heater system keeps the instrument at the set temperature (Figure 5.5, right plot). The entire structure is kept at a constant temperature of $\approx 28°$. An infrared camera is used to verify the temperature of the telescope, mount, and the whole instrumentation (Figure 5.5, left panel).

5.2 PolarCam Micropolariser Camera

The telescope detector is the PolarCam$^{©}$ micropolariser camera, U4 model.[1] This camera captures simultaneously 4 images at multiple polarised angles ($0°$, $45°$, $90°$, and $135°$) thanks to an array of linear micropolarisers directly applied on the camera

---

[1] The PolarCam$^{©}$ is manufactured by 4-D Technology Corporation, Arizona, United States (4D Technology, 2021)
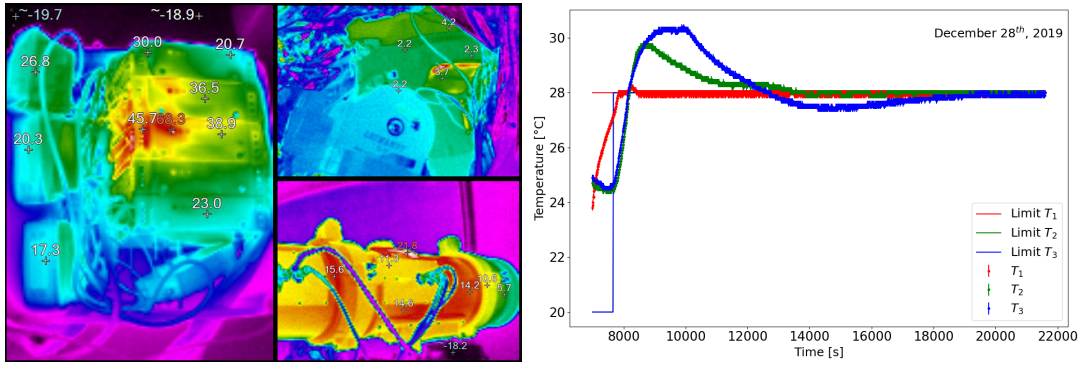
FIGURE 5.5: **Left:** Infrared camera thermal image of the instrumentation. **Right:** Example of temperature control with a limit set of 28°.
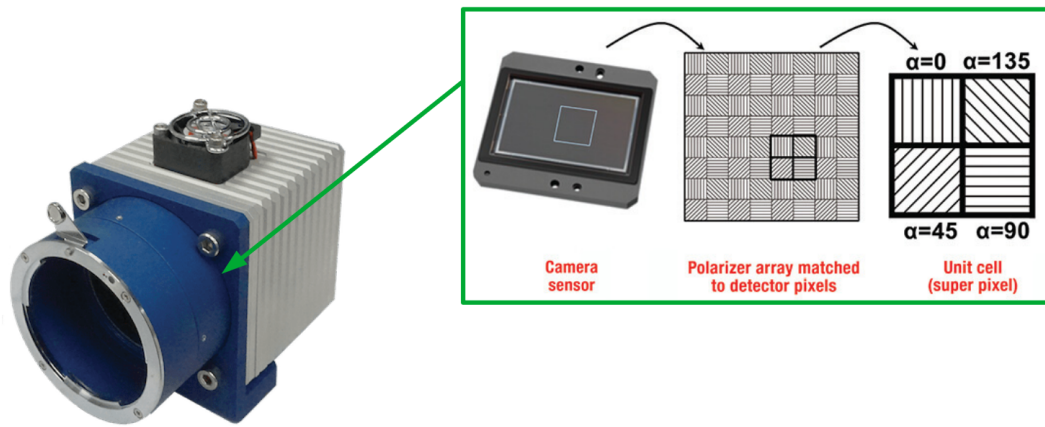

FIGURE 5.6: PolarCam detector. An array of linear micropolarisers with different orientation are matching the pixels of the sensor (Zecchino, 2017).

sensor. This array consists of repeated "super-pixels" composed of a fixed pattern of four pixels (Figure 5.6). The upper left pixel of the camera is a 0-phase (vertical polarisation) state. A single acquisition can return the linear polarisation of the image as derived from the Stokes vector parameters: **S** = (I, Q, U) = $(I_0 + I_{90}, I_0 - I_{90}, I_{45} - I_{135})$ where I_0, I_{90}, I_{45}, I_{135}, are the intensities of the linear polarisation components at 0°, 90°, 45°, 135°. Indeed, the linearly polarised light requires the measurement of the I, Q, U quantities to be fully characterised (Collett, 1992).

5.2.1 Polarimetric measurements

In this Subsection we recall just the fundamentals of polarimetry described in detail in Chapter 2 considering the PolarCam characteristic. As shown, a complete polarimetric study of the light incident to the detector sensor requires the evaluation of the Stokes vector **S**. The Stokes vector elements are given by Eq. 2.40:

$$\mathbf{S} = \begin{bmatrix} S_0 \\ S_1 \\ S_2 \\ S_3 \end{bmatrix} = \begin{bmatrix} I_0 + I_{90} \\ I_0 - I_{90} \\ I_{45} - I_{135} \\ I_{LHC} - I_{RHC} \end{bmatrix} \tag{5.1}$$

where I_0, I_{90}, I_{45}, I_{135}, are the intensities of the linear polarisation components at 0, 90, 45, 135 degrees, and I_{LHC}, I_{RHC} are the left hand and right-hand circular polarisation intensities respectively. In particular, the linearly polarised light requires the measurement of the I, Q, and U quantities to be fully characterised. Being the S_3 ($\equiv V$) parameter associated with circular polarisation (and considering that the camera is sensitive just to the linear one) we are only interested in the first three Stokes parameters ($\equiv [I, Q, U]$). There are several equations that relate to all these quantities. In particular, we can consider:

$$Q = I p \cos 2\theta \tag{5.2}$$

$$U = I p \sin 2\theta \tag{5.3}$$

where p is the Degree of Linear Polarisation (DoLP, Eq. 2.21) and θ is the Angle of Linear Polarisation (AoLP, Eq. 2.22):

$$DoLP[\%] = \frac{\sqrt{Q^2 + U^2}}{I} \cdot 100 \tag{5.4}$$

$$AoLP[rad] = \frac{1}{2} \arctan\left(\frac{U}{Q}\right) \tag{5.5}$$

Anyhow, all these intrinsic properties of the radiation should not be confused with the properties of the polarising elements (see Subsection 5.3.8).

Finally, part of the PolarCam characterisation aims at achieving the camera demodulation tensor $\mathbf{X}^\dagger$. This tensor (obtained from a modulation matrix $\mathbf{X}$ associated *with each pixel* of the acquired polarimetric images) allows us to measure the incoming light associated with Stokes vector S as shown in Eq. 2.68 (where m is the vector of the acquired images at different polarisation).

According to the equations showed before, it is necessary to acquire images at four different polarizations. With the PolarCam we obtain images at $\theta = (0°, 45°, 90°, 135°)$ with a single shot. Thus we have $m = (m_0, m_{45}, m_{90}, m_{135})$.

From the Müller matrix (Collett, 1992) it is possible to obtain a theoretical modulation matrix $\mathbf{X}$. In particular, considering the angles $\theta_i = (0°, 45°, 90°, 135°)$, it results to be equal to:

$$\mathbf{X} = \frac{1}{2} \begin{pmatrix} 1 & \cos 2\theta_1 & \sin 2\theta_1 \\ 1 & \cos 2\theta_2 & \sin 2\theta_2 \\ 1 & \cos 2\theta_3 & \sin 2\theta_3 \\ 1 & \cos 2\theta_4 & \sin 2\theta_4 \end{pmatrix} = \frac{1}{2} \begin{pmatrix} 1 & 1 & 0 \\ 1 & 0 & 1 \\ 1 & -1 & 0 \\ 1 & 0 & -1 \end{pmatrix} \tag{5.6}$$

Now we can retrieve the theoretical demodulation matrix $\mathbf{X}^\dagger$ as Moore-Penrose inverse (pseudo-inverse) of the theoretical modulation matrix $\mathbf{X}$. Remember that to obtain a pseudo-inverse A^* of a matrix A (with dimension $n \times m$ and $n \geq m$):

$$A^* = (A^T A)^{-1} A^T \tag{5.7}$$

We obtain:

$$\mathbf{X}^\dagger = \frac{1}{2} \begin{pmatrix} 1 & 1 & 1 & 1 \\ 2 & 0 & -2 & 0 \\ 0 & 2 & 0 & -2 \end{pmatrix} = \begin{pmatrix} 0.5 & 0.5 & 0.5 & 0.5 \\ 1 & 0 & -1 & 0 \\ 0 & 1 & 0 & -1 \end{pmatrix} \tag{5.8}$$

Then, the theoretical Stokes parameters can be easily obtained by solving Eq. 2.68:

$$\begin{pmatrix} I \\ Q \\ U \end{pmatrix} = \begin{pmatrix} 0.5 & 0.5 & 0.5 & 0.5 \\ 1 & 0 & -1 & 0 \\ 0 & 1 & 0 & -1 \end{pmatrix} \begin{pmatrix} m_1 \\ m_2 \\ m_3 \\ m_4 \end{pmatrix} = \mathbf{X}^{\dagger} \begin{pmatrix} m_1 \\ m_2 \\ m_3 \\ m_4 \end{pmatrix} \tag{5.9}$$

Performing this study pixel by pixel we obtain the full theoretical demodulation tensor $X^{\dagger}$ instead of a single matrix. The results in the next Section were obtained by using both the theoretical demodulation tensor and the one we got during the PolarCam calibration campaign (Subsection 5.3.8).

5.3 PolarCam Characterisation

All the following PolarCam characterisations were performed in the Astrophysical Observatory of Turin (OATo) clean room - ISO7 or in the OATo Space Optics Calibration Chamber (SPOCC) in the Optical Payload Systems facility (OPSys) placed at the Aerospace Logistics Technology Engineering Company (ALTEC) in Turin, Italy (Fineschi et al., 2011; Capobianco et al., 2019).

5.3.1 Camera description

Before describing the PolarCam, it is good to remember that the general camera features change in function of the camera model: G1, G2, U2, U4. The peculiarities of each model -detector type (CCD/CMOS), bit depth, pixel dimension, etc. . .- are summarised in Zecchino, 2017. In particular, we considered the U4 model and, from now on, all information and results obtained are based on this model.

This camera has a monochrome charge-coupled device (CCD) of size 1950×1950 pixels. Each pixel has dimensions $7.4 \, \mu m \times 7.4 \, \mu m$ with a 12 bit depth. The maximum camera frame-rate is equal to 14 fps. The PolarCam dimension and its nominal main features are summarised in Table 5.3 and Figure 5.7. Furthermore, the camera has a control software and a Software Development Kit (SDK) that assists the user to access information from PolarCam for analysis and further manipulation. From the software is possible, for example, change the exposure time (minimum $T_{exp} = 0.02 \, \mu s$). Moreover, being the PolarCam detector managed by two different ADCs, it is possible, through the software, set a particular gain value for each one. For this reason, when we will talk about analog gain (AG), we will always report two values. More information about this camera and its usage can be found in Liberatore et al., 2021a and Zecchino, 2017.

5.3.2 Raw image demosaicing

To obtain the images at different polarisation (0°, 45°, 90°, 135°) from the original raw, a demosaic process is required. Let's suppose we want to obtain a single I_i (where $i = 0°, 45°, 90°, 135°$); for example I_0. The values of the three remaining pixels in the considered super-pixel[2] are obtained as the average between the pixels with the considered polarisation (I_0) in each adjacent super-pixel as shown in Figure 5.8, Output 2. The same procedure can be applied to get the images with the other orientations.

---

[2]A super-pixel is the "pixel" obtained by considering the four adjacent pixels with different micropolariser orientations (0°, 45°, 90°, and 135°).

TABLE 5.3: PolarCam U4 model main features (Zecchino, 2017).

Sensor Type	Interline transfer CCD ON Semiconductor KAI04070
Micropolarisers orientation	0°, 45°, 90°, 135°
Pixel Size	7.4 μm × 7.4 μm
Usable Pixels	1950 × 1950, 3.8 MP
Bit depth	12 bit
Frame Rate	14 fps
Saturation Capacity	44 ke$^-$
Dark Noise	3 e$^-$/s
Quantum Efficiency	76% @ 470 nm
Physical Envelope	60 × 60 × 95 mm
Weight	210 g
Power Requirement	8 W, 12 VDC
Interface	USB 3.0
Lens Mounting Type	F-Mount
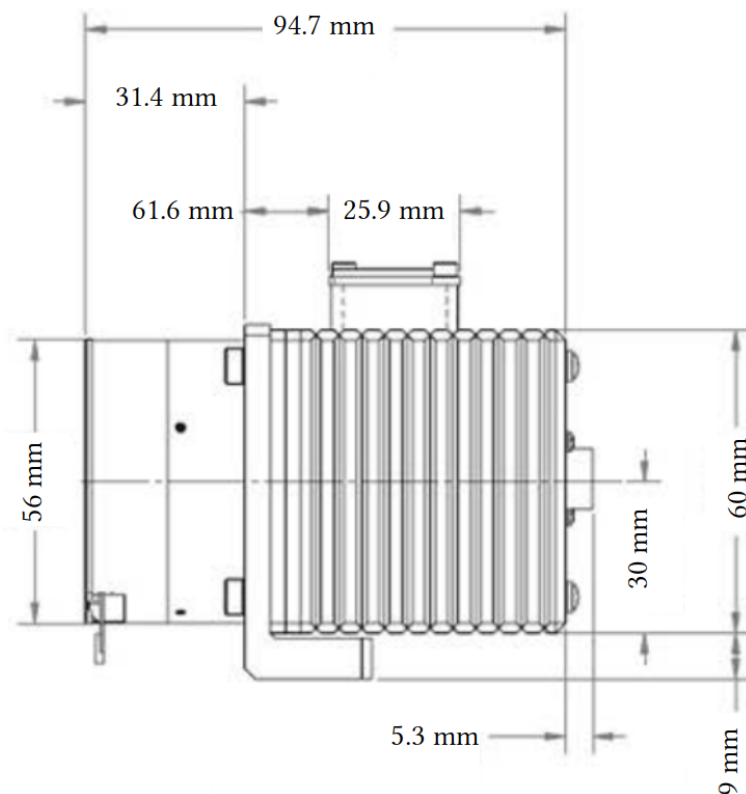
FIGURE 5.7: PolarCam size (Zecchino, 2017).
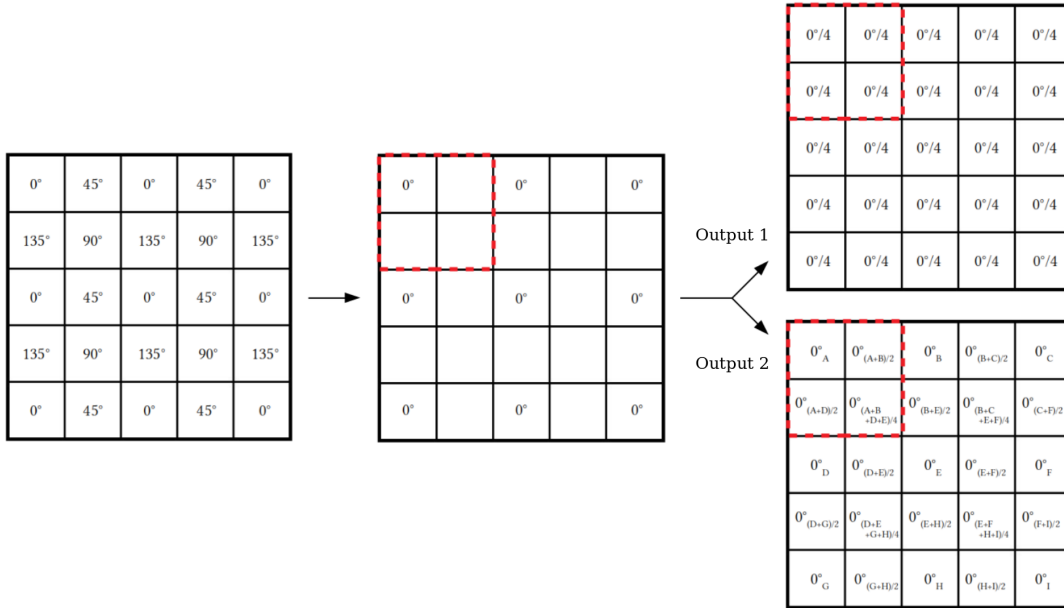
FIGURE 5.8: Demosaic example to obtain a polarised image from the original raw image. In this example, the image with a polarisation angle of 0° (I_0) is obtained considering each super-pixel equal to the pixel value with the micropolariser at 0° (Output 1) or considering each super-pixel obtained considering the pixel values with the micropolariser at 0°-pixels (Output 2).

5.3.3 Detector resolution

To evaluate the detector resolution we used a resolution target USAF-1951 (MKS-Newport, 2019) illuminated by a white led source with a light diffuser, powered at 3.2 V (Figure 5.9). A collimator was placed between the detector and the resolution target. The collimator aperture is ≈ 50mm with a focal length of ≈ 300mm.

Thanks to a Modulation Transfer Function, it is possible to evaluate the resolution through the Rayleigh criterion (Figure 5.10). In particular, when the modulation is equal to 0.20 we obtain that the frequency is almost 22[linepairs/mm] (i.e., ≈ 22µm) that corresponds to the *group 4 element 4* of the resolution target (Table 5.4).

TABLE 5.4: Line pairs per millimetre for each group element of the resolution target (MKS-Newport, 2019).

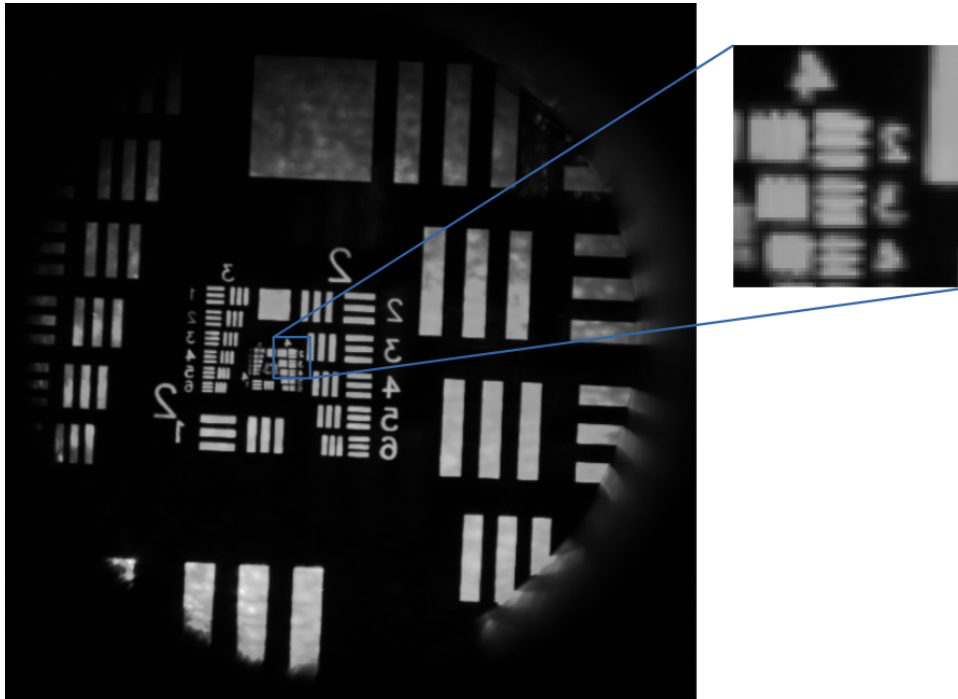| Element Number	Group Number							
	0	**1**	**2**	**3**	**4**	**5**	**6**	**7**
1	1.00	2.00	4.00	8.00	16.00	32.00	64.00	128.00
2	1.12	2.24	4.49	8.89	17.96	35.92	71.84	143.70
3	1.26	2.52	5.04	10.08	20.16	40.32	80.63	161.30
4	1.41	2.83	5.66	11.31	22.63	45.25	90.51	181.00
5	1.59	3.17	6.35	12.70	25.40	50.80	101.60	203.20
6	1.78	3.56	7.13	14.25	28.51	57.02	114.00	228.10

FIGURE 5.9: An image of a resolution target as seen by the PolarCam with gain = 1 and T_{exp} = 71.86 ms. To avoid values conditioned by the polarisation, this image is obtained as the sum of the intensities of the linear polarisation components at 0° and 90° (i.e., the first element of the Stokes vector).
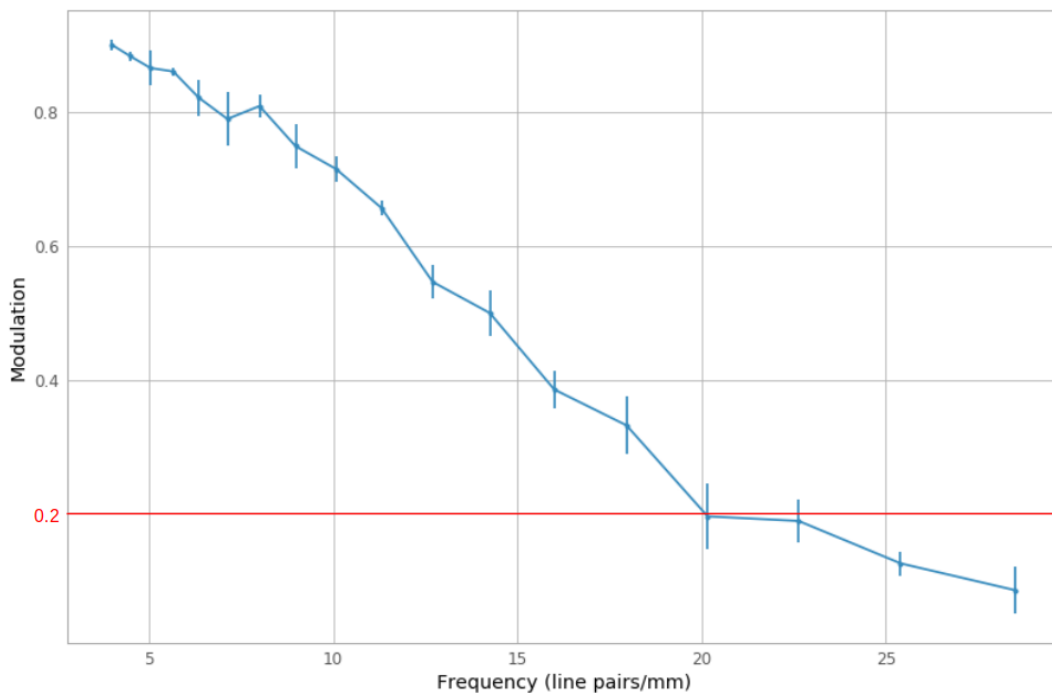

FIGURE 5.10: PolarCam Modulation Transfer Function (MTF).

5.3.4 Gain evaluation

The gain of the camera is settable through special commands in the camera user interface. In particular, there is the possibility to modify both the analog and the digital gain. The digital gain results in an amplification of the incoming signal proportional to the set value[3] (e.g., DG = 2 digitally doubles the signal). The analog gain, instead, is variable from AG = 0 to AG = 123. These are engineering values. To obtain a gain in physical units it is required to evaluate the *Photon Transfer Curve* (PTC). The PTC is a plot of noise versus signal for a digital sensor (Figure 5.12). More information about PTC can be found in Janesick, 2007. To evaluate the PTC we set an AG = 30 for the left ADC and AG = 5 for the right one.[4] These are the same settings set during the data acquisitions in Antarctica. The PTC was obtained by placing the PolarCam and a photodiode in front of a flat field (FF) panel. A picoammeter reads the photodiode signal to monitor the intensity fluctuations of the FF panel (Figure 5.11). The considered PTC was obtained by performing a *temporal* averaging and σ^2 evaluation.
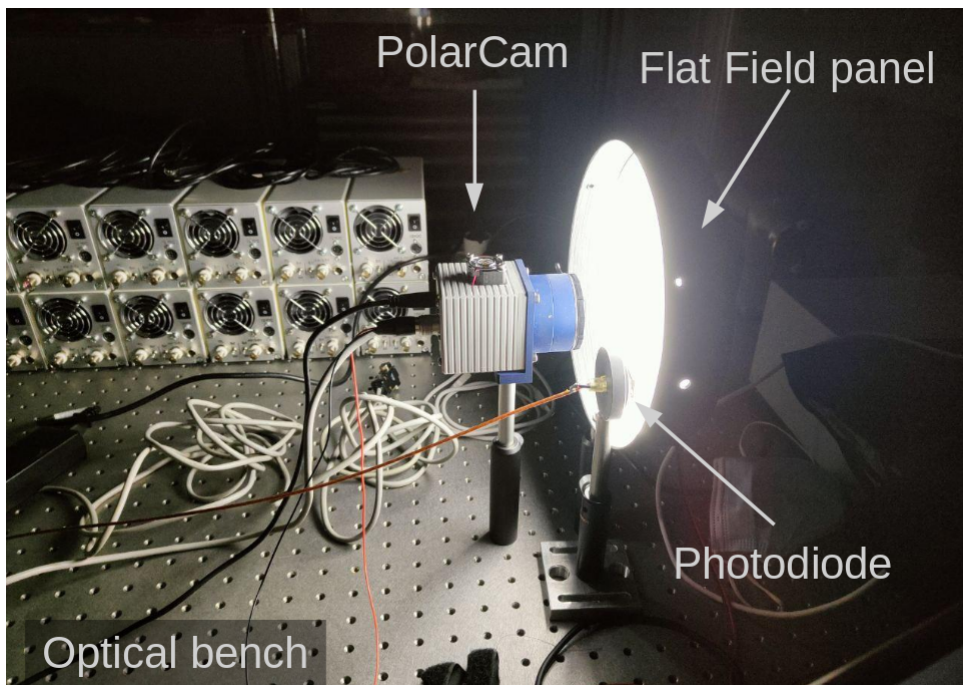

FIGURE 5.11: Set up during Photon Transfer Curve evaluation.

By evaluating the angular coefficient of the linear part of the plot in Figure 5.12 we obtain a gain of $\approx 10\,\mathrm{e}^-/\mathrm{DN}$ for both ADCs (left-red and right-blue).

5.3.5 Detector linearity

With the same set-up shown is Figure 5.11, by changing the camera exposure time, it is possible to check the PolarCam linear response (Figure 5.13). In particular, the camera linear response was evaluated by averaging over the entire frame and by separating the contributions given by the pixels with different orientations of the micropolarisers. It is possible to check also the average dark for different exposure

---

[3]The digital gain is a value $DG \in \mathbb{N}$ in the range $[1, 16]$.

[4]The values of AG were previously chosen to have a qualitatively uniform response from the detector avoiding to highlight the gap between the two ADCs.
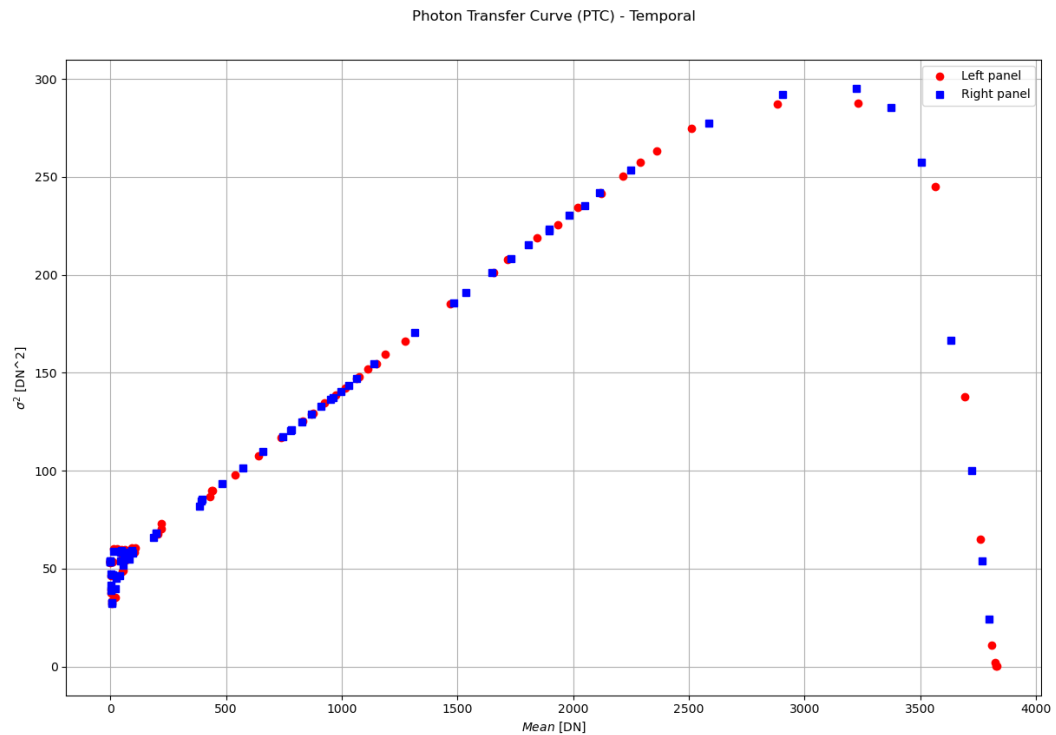
FIGURE 5.12: PolarCam Photon Transfer Curve.

times and different digital gains. What we obtain is shown in Figure 5.14. As expected, the average dark values increase for higher DG. Moreover, it is almost constant in the considered exposure time range. The same study was performed for different analog gains as well. The results are consistent with what was just obtained.
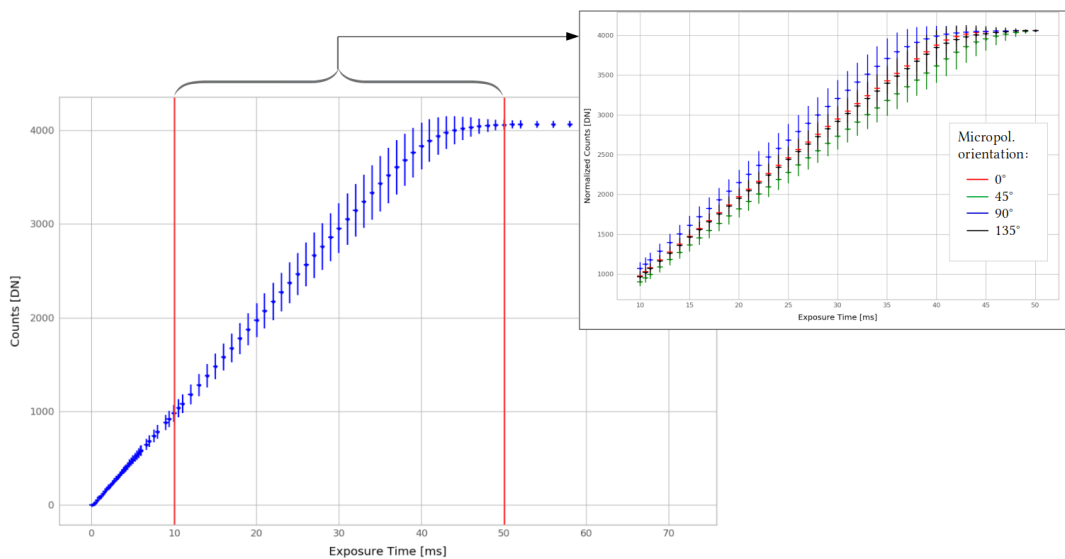

FIGURE 5.13: PolarCam linear response averaging over the whole
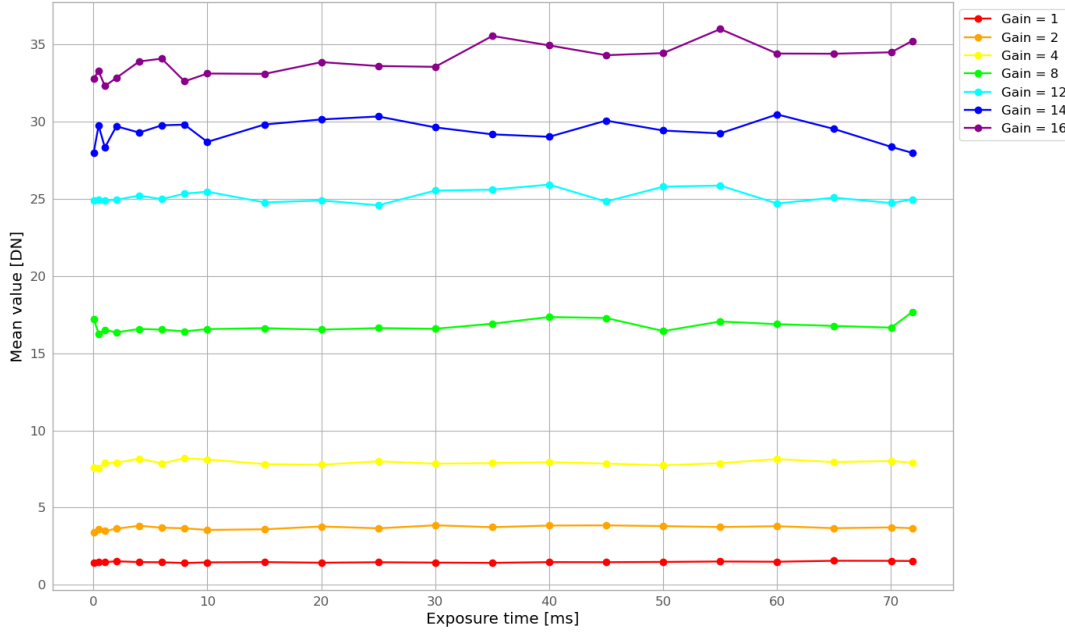frame and considering the four different micropolariser array orientation (grey box).

FIGURE 5.14: PolarCam dark measurement for different digital gain.

5.3.6 Point Spread Function

We can compare the result just obtained with the telescope Point Spread Function
(PSF). To do that, we used a pinhole (50 μm) on the Illumination System Visible Light
(ISVL, Tordi et al., 2015) in the Optical Payload System (OPSys) Facility (Fineschi et
al., 2011; Capobianco et al., 2019) in ALTEC, Turin, Italy. In particular, 10 images
are summed to increase the SNR. The image region with the pinhole (Figure 5.15) is
selected as the Region Of Interest (ROI) to evaluate the PSF. For these measurements,
the following settings of the PolarCam were used: exposure time equal to 71.82 ms
and digital gain equal to 16. Then, for the two dimensions, rows (red) and columns
(blue), the, pixel values are plotted and a best-fit ("horizontal" and "vertical" fit
respectively) has been performed with a Gaussian function. The results are shown
in Figure 5.16.

From the variance it is possible to obtain the HWHM (Half Width at Half Max-
imum) for both the horizontal and vertical fit: $HWHM_h = \sqrt{2 \cdot \log 2} \cdot \sigma_h = 1.38 \pm
0.05$ and $HWHM_v = \sqrt{2 \cdot \log 2} \cdot \sigma_v = 1.36 \pm 0.06$ respectively. Averaging between
them, we obtain: $\overline{HWHM} = 1.37 \pm 0.04$ pixels. Then, a point-like signal is spread
over $\overline{FWHM} = 2.74 \pm 0.08$ pixels ($\equiv 20.28$ μm). As shown in Table 5.1, we know that
$\lambda = 591$ nm and the f-ratio F/# = 14. We can also evaluate the telescope diffraction
limit as:

$$\text{Spot size } [\mu m] = 1.22 * \lambda \, [\mu m] * F/\# \approx 10.1 \, \mu m \tag{5.10}$$

5.3.7 Angle and Degree of Linear Polarisation

As introduced at the beginning of this Section, with a single shot, we can evaluate
the Stokes I, Q, and U parameters using the theoretical demodulation tensor (Sub-
section 5.3.2) and then calculate the DoLP and AoLP (Eqs. 5.4 and 5.5).

Considering a flat-field panel as the light source (i.e., unpolarised light source),
what we expect to obtain is an almost zero degree of polarisation (DoLP). The mea-
sured DoLP could be interpreted as instrumental polarisation, or the polarisation
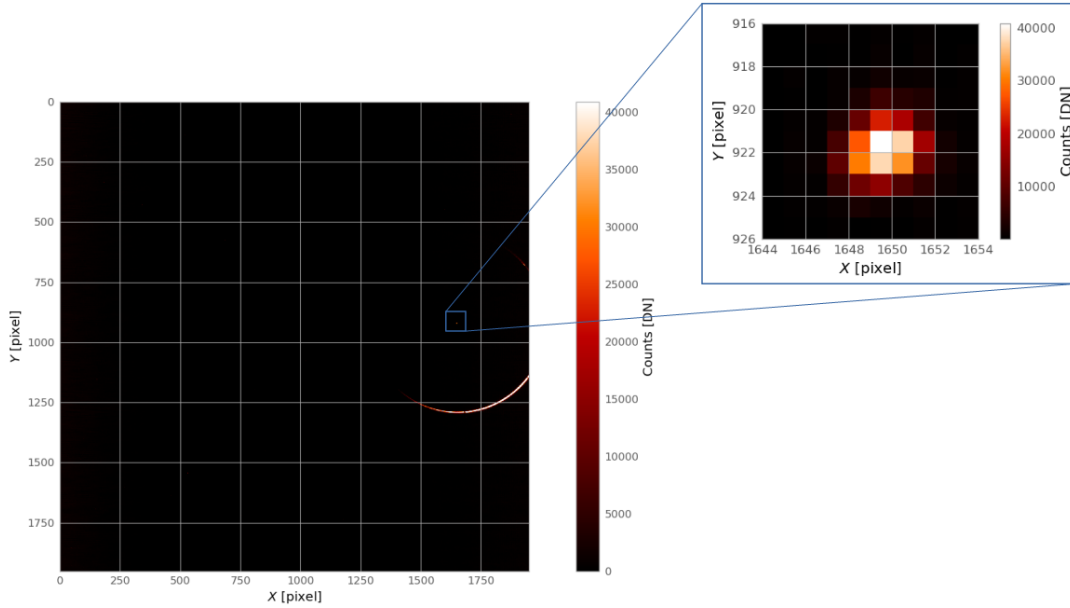
FIGURE 5.15: Sum of 10 pinhole images with region of interest (ROI). A leak of light from the edge of the pinhole mask is also visible around the region [1750, 1250] as a thin line. It is possible to look at that to easily find the pinhole point-like signal over the frame.
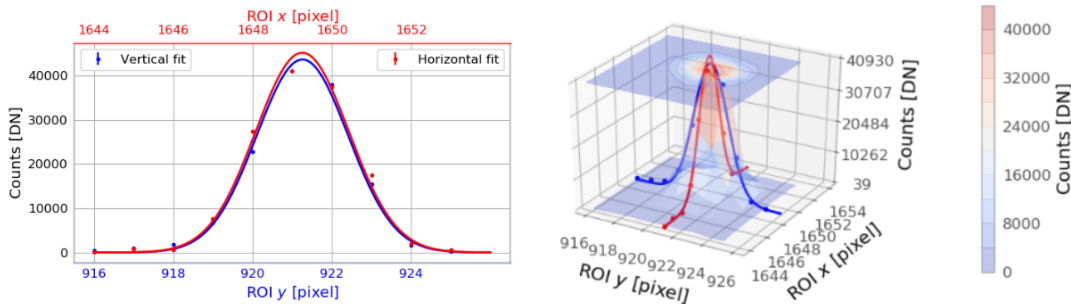

FIGURE 5.16: Gaussian best-fit of the Region of Interest (ROI) for rows and columns. On the right side, a 3D representation of the considered fit-geometry. The error bars are negligible and not visible in the plots (Liberatore et al., 2021a).

introduced by the PolarCam itself and as a consequence it will not be possible to measure a polarisation lower than this one. The results are shown on the right side of Figure 5.17. It is possible to see that the polarisation introduced by the camera on the left side of the frame is at the order of $\approx 4\%$ on the Stokes Q and U parameters and as shown in the right panel, the DoLP increases up to the $\approx 10\%$. The average degree of linear polarisation on the whole frame is $(6 \pm 2)\%$. This is a lower limit on the measurement of the degree of linear polarisation.

In addition to these unpolarised flat-field measurements, we performed also the same kind of measurement by introducing a linear polariser (pre-polariser) between the detector and the flat-field panel, obtaining a polarimetric flat-field. By rotating the pre-polariser, at the detector plane, the light is fully linearly polarised in the direction defined by the orientation of the acceptance axis of the pre-polariser. Therefore, what we expect to observe is a DoLP of $\approx 100\%$ and the AoLP having the same angle of the acceptance axis of the pre-polariser. In Figs. 5.18 and 5.19 are shown
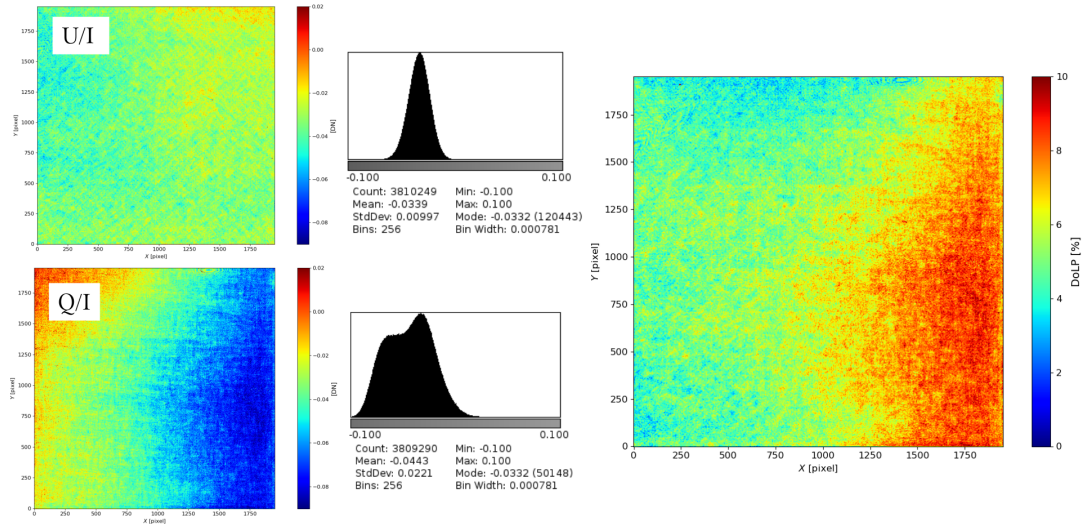
FIGURE 5.17: Stokes parameters (left) and degree of linear polarisation (right) of unpolarised flat-field through the use of the theoretical demodulation tensor.

the DoLP and the AoLP as measured by the PolarCam when the pre-polariser is oriented at the four main angles of 0°, 45°, 90° and 135°. The results are summarised in Table 5.5 (Liberatore et al., 2021a).
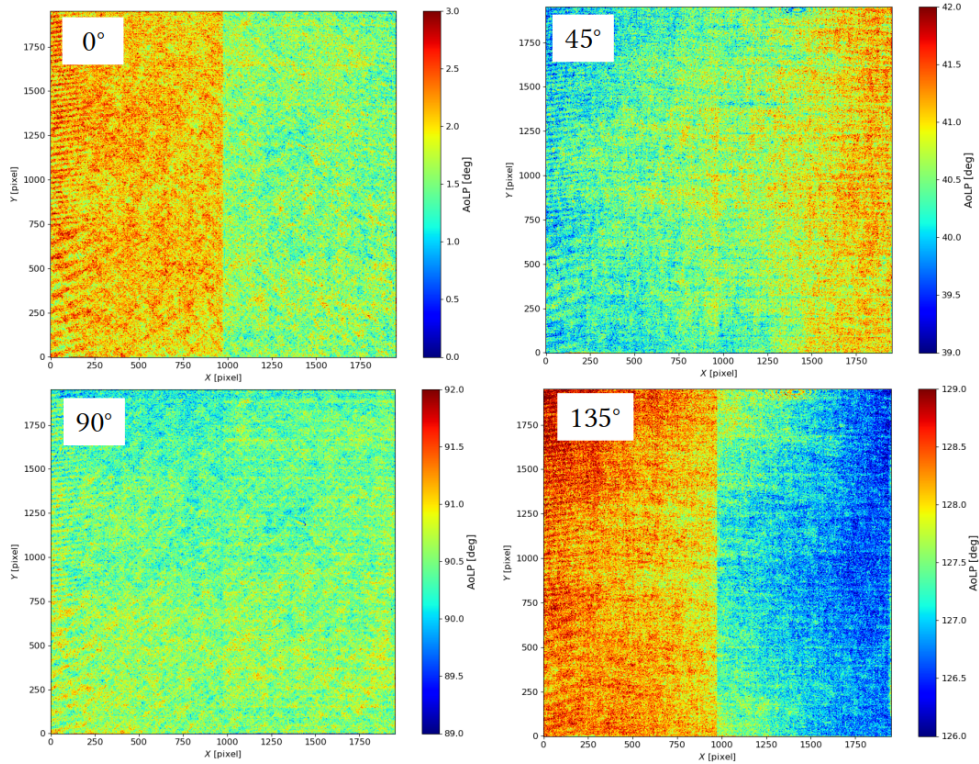

FIGURE 5.18: Measured Angle of Linear Polarisation for different polarised incoming light using the theoretical demodulation tensor. In particular, in this figure we show the 4 angles of 0°, 45°, 90°, 135°.
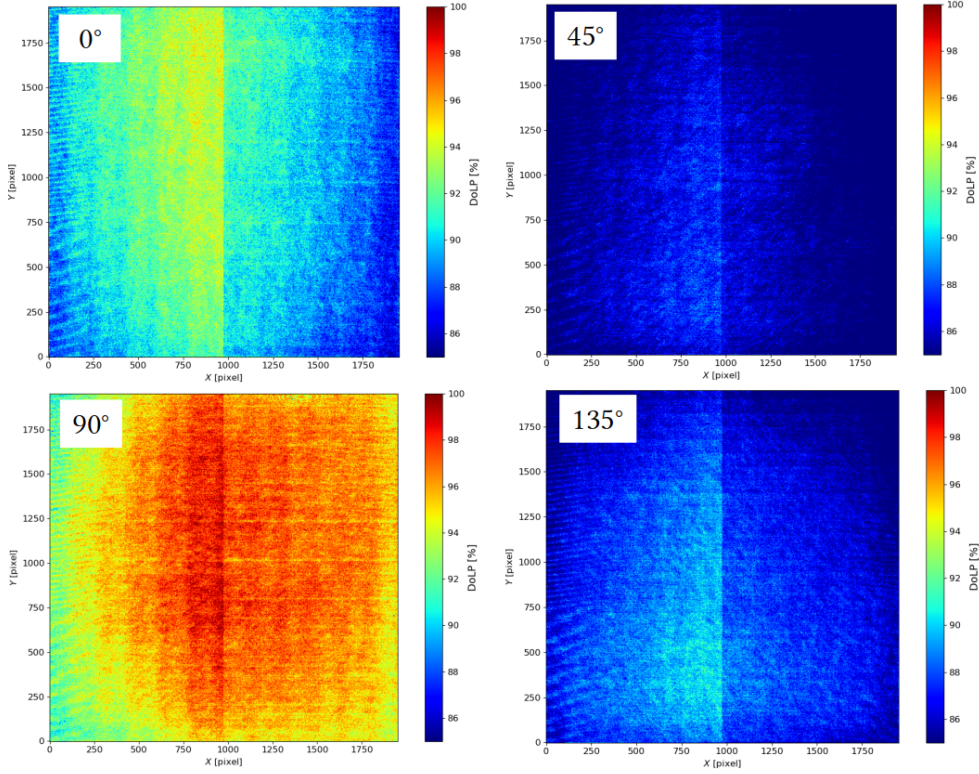
FIGURE 5.19: Measured Degree of Linear Polarisation for different polarised incoming light using the theoretical demodulation tensor.

TABLE 5.5: Unpolarised flat-field (UFF) and polarimetric flat-field (PFF) DoLP and AoLP evaluated by the application of the theoretical demodulation tensor.

Set up	Expected DoLP	Obtained DoLP	Expected AoLP	Obtained AoLP
UFF	0%	$(6 \pm 2)\%$	/	/
PFF (0°)	100%	$(91 \pm 2)\%$	0°	$(2° \pm 1°)$
PFF (45°)	100%	$(85 \pm 2)\%$	45°	$(41° \pm 1°)$
PFF (90°)	100%	$(96 \pm 2)\%$	90°	$(91° \pm 1°)$
PFF (135°)	100%	$(87 \pm 2)\%$	135°	$(128° \pm 1°)$

5.3.8 Micro-polarisers orientation and demodulation tensor

As shown in the previous Section, the degrees and angles of linear polarisation results to be not much consistent with the expected theoretical ones. To improve these results we need to consider a calibrated demodulation tensor. This new demodulation tensor must take into account different aspects not considered in the theoretical one (e.g., the effective orientation of each micro-polariser and other characteristics of the polarising elements upon each pixel). As first step, it is useful to point out that, exactly like for the study of polarised light, to characterise the behaviour of a linearly polarising element, it is necessary to have three quantities as well. These

quantities are: *efficiency* (i.e., its ability to reject the unwanted polarisation states), *throughput*, and *position angle*.

There are different conventions commonly used to present these three quantities. Considering I, Q, and U as the Stokes parameters polarimetrically describing the incident light beam, in this work we adopt the convention that the output beam intensity passing through a polarising element is given by (Sparks and Axon, 1999; Vorobiev, Ninkov, and Brock, 2018):

$$S_k = A_k I + \epsilon_k (B_k Q + C_k U) \tag{5.11}$$

where S_k is the measured signal, A_k, B_k, C_k are transmissivity terms, and ϵ_k the polarising efficiency that describes each polariser (i.e., each pixel of the PolarCam). The subscript k denotes the polariser orientation. Considering Eqs. 5.2 and 5.3, the above equation can be rewritten as:

$$S_k = A_k I + \epsilon_k (B_k I p \cos 2\psi + C_k I p \sin 2\psi) \tag{5.12}$$

where I is the total intensity, p is the intrinsic fractional polarisation of the source and ψ is the intrinsic polarisation angle. The transmissivity terms can now be written in terms of a generic throughput t_k:

$$S_k = \frac{1}{2} t_k I + \frac{1}{2} t_k \epsilon_k I p \cos 2\phi_k \cos 2\psi + \frac{1}{2} t_k \epsilon_k I p \sin 2\phi_k \sin 2\psi \tag{5.13}$$

where ϕ_k are the position angles of the polarisers. It is possible to simplify the equation by setting $p = 1$. In this way, the equation results be:

$$S_k = \frac{1}{2} t_k I [1 + \epsilon_k (\cos 2\phi_k \cos 2\psi + \sin 2\phi_k \sin 2\psi)] \tag{5.14}$$

By fitting to the response curves it is possible to determine the efficiency ϵ_k and orientation ϕ_k of every (micro)polariser. This fit was performed for each PolarCam pixel since each pixel corresponds to a different micropolariser. The transmissivity t_k was evaluated before the data fitting. These values have been obtained searching the pixel with the highest transmissivity with the same input, considered as $1/2(S_k^{\psi_0} + S_k^{\psi_{45}} + S_k^{\psi_{90}} + S_k^{\psi_{135}})$, and normalising the others t_k as a function of it. An example of what we obtain from a fit is shown in Figure 5.20. This study was performed setting the camera analog gain AG = (44, 44), the digital gain DG = 1 and and exposure time of $t_{exp} = 71.36$ms. In particular, instead of S_k, we considered a normalised irradiance S defined as:

$$S = \frac{S_k}{\frac{1}{2}(S_k^{\psi_0} + S_k^{\psi_{45}} + S_k^{\psi_{90}} + S_k^{\psi_{135}})} \tag{5.15}$$

where $k = [0°, 45°, 90°, 135°]$ are the micropolarisers orientations.

At this point it is possible to estimate the Stokes parameters of the incident light. To do that, as illustrated in Subsection 5.2.1, we have to solve the following equation:

$$\mathbf{m} = \mathbf{X} \mathbf{S}_{input} \tag{5.16}$$

where $\mathbf{m}$ is the vector of the images with the four different linear polarisation, $\mathbf{X}$ is the modulation matrix and $\mathbf{S}_{input}$ is the Stokes vector associated with the incoming
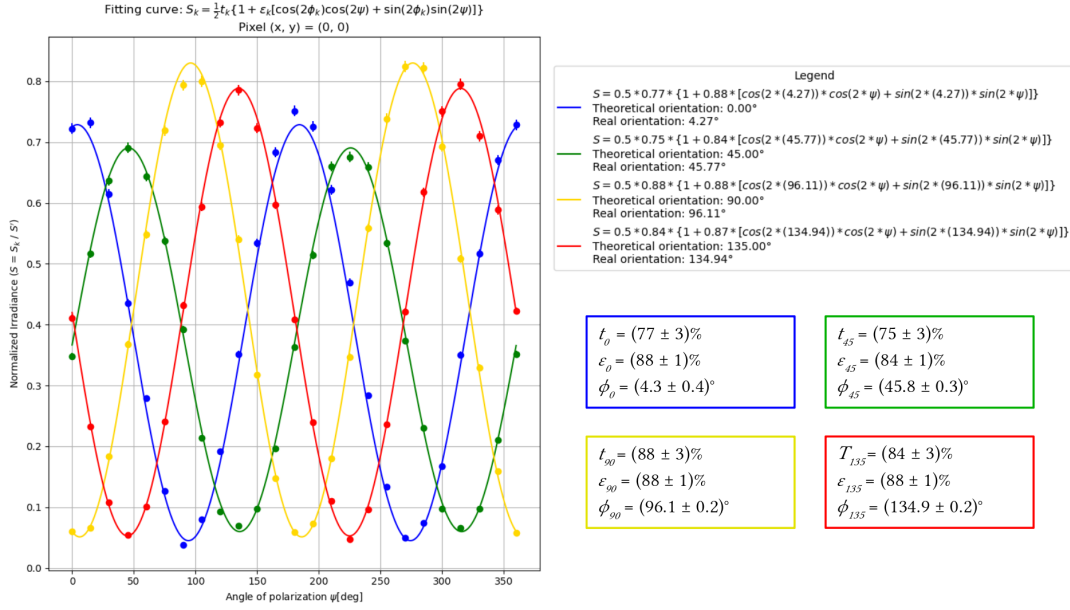
FIGURE 5.20: Example of curve fit for a particular super-pixel [in this case, the super-pixel associated to the pixel (0, 0)]. It is possible to see that the obtained values for the ϕ_k parameters are pretty consistent with the expected ones.

light. In particular, considering the ϵ_i and ϕ_i obtained from the data fit, we get the matrix in Eq. 5.17.

$$\mathbf{X} = \frac{1}{2} t_k \begin{pmatrix} 1 & \epsilon_1 \cos 2\phi_1 & \epsilon_1 \sin 2\phi_1 \\ 1 & \epsilon_2 \cos 2\phi_2 & \epsilon_2 \sin 2\phi_2 \\ 1 & \epsilon_3 \cos 2\phi_3 & \epsilon_3 \sin 2\phi_3 \\ 1 & \epsilon_4 \cos 2\phi_4 & \epsilon_4 \sin 2\phi_4 \end{pmatrix} = \frac{1}{2} t_k \begin{pmatrix} 1 & 0.898 & 0.148 \\ 1 & -0.032 & 0.870 \\ 1 & -0.890 & -0.188 \\ 1 & 0.006 & -0.910 \end{pmatrix} \tag{5.17}$$

By (pseudo)inverting the $\mathbf{X}$ matrix it is possible to obtain the demodulation matrix:

$$\mathbf{X}^\dagger = (\mathbf{X}^T \mathbf{X})^{-1} \mathbf{X}^T = \begin{pmatrix} 0.619 & 0.572 & 0.542 & 0.485 \\ 1.189 & -0.185 & -1.172 & 0.301 \\ 0.070 & 1.301 & -0.017 & -1.303 \end{pmatrix} \tag{5.18}$$

Then, from Eq. 5.16 and Eq. 5.18 we can obtain $\mathbf{S}_{input} = \mathbf{X}^\dagger \mathbf{m}$:

$$\begin{pmatrix} 0.619 & 0.572 & 0.542 & 0.485 \\ 1.189 & -0.185 & -1.172 & 0.301 \\ 0.070 & 1.301 & -0.017 & -1.303 \end{pmatrix} \begin{pmatrix} IMG_0 \\ IMG_{45} \\ IMG_{90} \\ IMG_{135} \end{pmatrix} = \begin{pmatrix} I_{input} \\ Q_{input} \\ U_{input} \end{pmatrix} \tag{5.19}$$

Performing this process for the entire frame (pixel by pixel) we obtain a demodulation tensor $\mathbf{X}^\dagger$ where each of the 12 elements is a matrix (Figure 5.21). A summary of this process is shown in Figure 5.22.

Using this specific demodulation tensor (specific for our camera), we obtain, using the same procedure already applied for the theoretical demodulation tensor (Subsection 5.3.7), the Stokes parameters, the DoLP, and the AoLP. The results for the unpolarised light case (flat-field source) are shown in Figure 5.23.
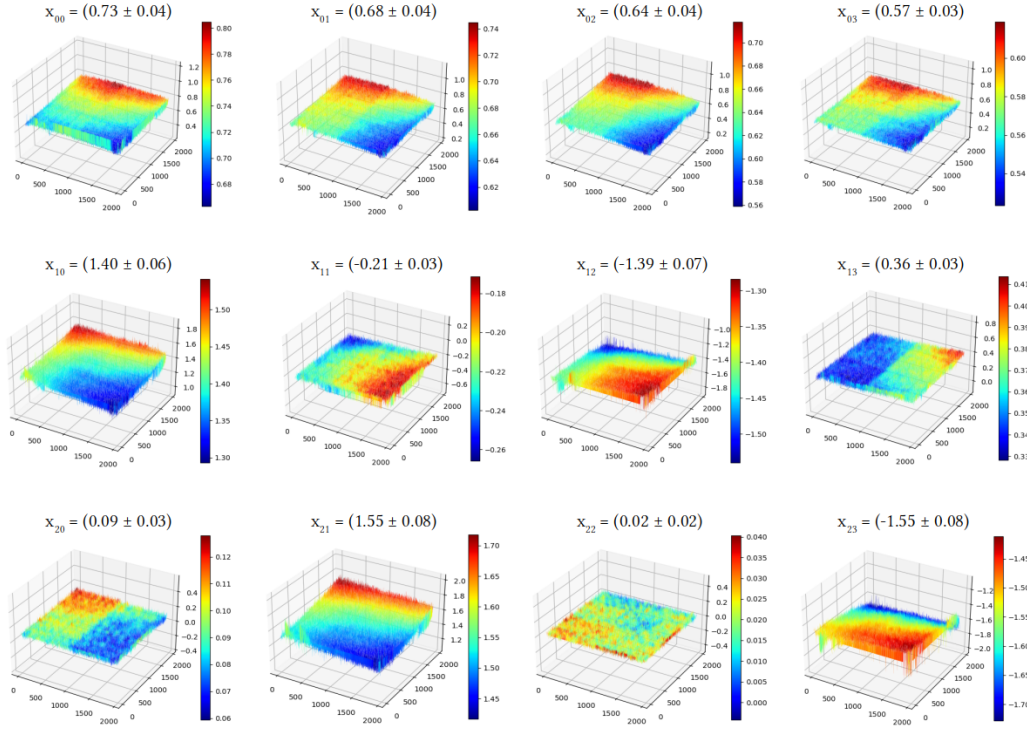
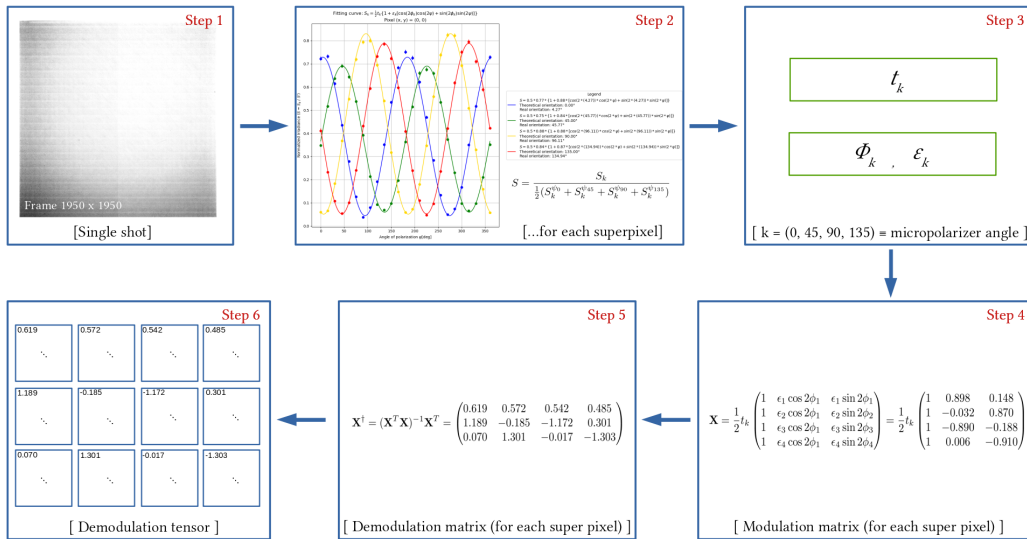FIGURE 5.21: Elements x_{ij} of the demodulation tensor.

FIGURE 5.22: Procedure for the demodulation tensor evaluation.

In Figure 5.24, 5.25, and 5.26 are depicted the results for the polarised light. As expected, the use of a calibrated demodulation tensor improves significantly the accuracy in the measurements of the polarisation state of the light detected by the PolarCam. In particular, it is possible to see how the new demodulation tensor removes (almost totally) the residual instrumental polarisation. Moreover, the frames acquired with the polarimetric flat-field show an almost perfect agreement between the flat-field polariser orientation and the measured one (the differences between the expected angles of linear polarisation and the obtained ones are shown in Figure 5.25). A summary and comparison of these results is reported in Table 5.6 (Liberatore et al., 2021a).
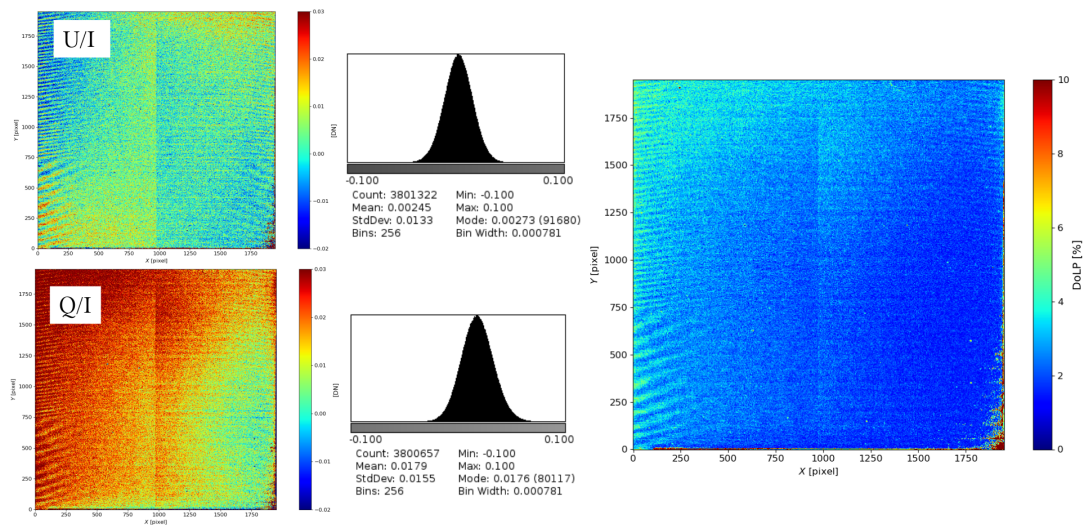
FIGURE 5.23: Stokes parameters (left) and degree of linear polarisation (right) of unpolarised flat-field through the use of the calibrated demodulation tensor. The reason for those kinds of "fringes" on the frame boundaries is still under study. However, being interested in the values that we will obtain more in the middle of the frame, this effect will not affect our measurements.
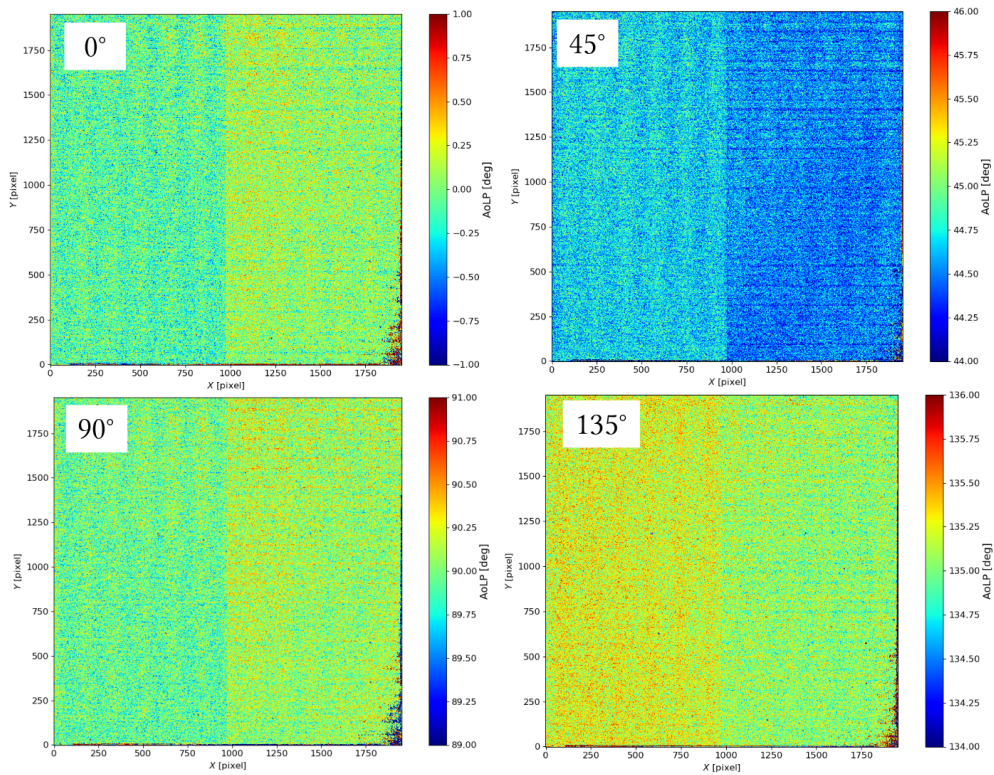

FIGURE 5.24: Measured Angle of Linear Polarisation (AoLP) for different polarised incoming light using the calibrated demodulation tensor. In particular, in this picture, the results for the angles of 0°, 45°, 90°, 135° are shown.
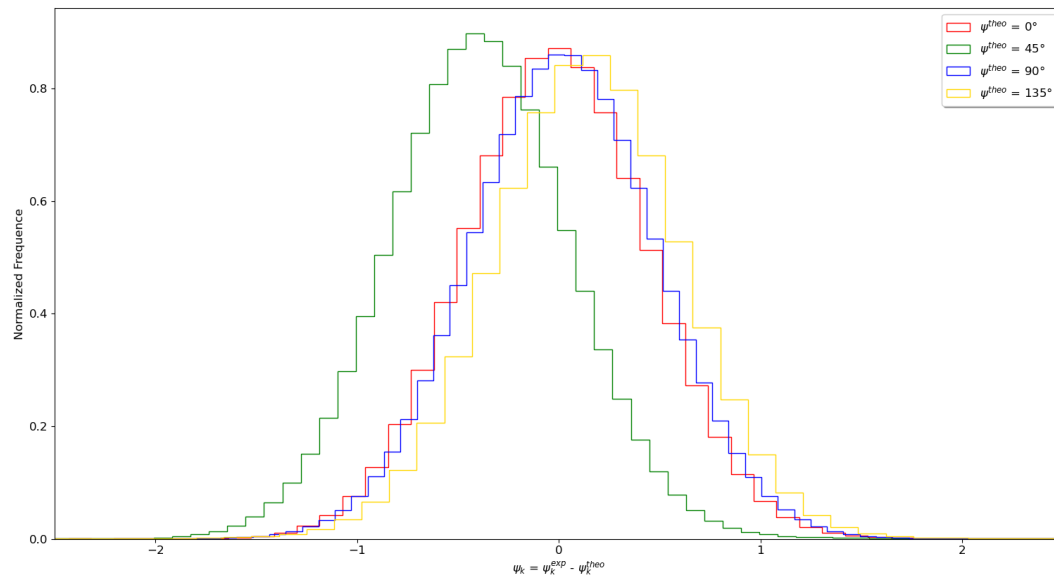
FIGURE 5.25: Histograms of the differences between the measured Angle of Linear Polarisation (ψ^{exp}) and the orientation of the acceptance axis of the pre-polariser (ψ^{theo}).
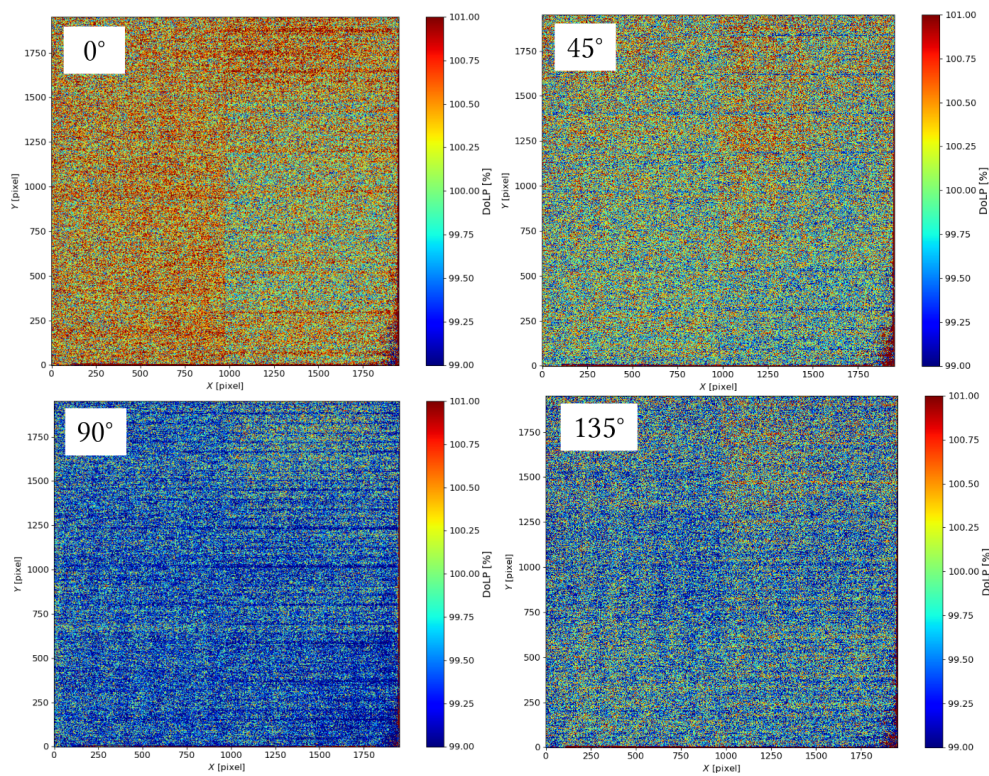

FIGURE 5.26: Measured Degree of Linear Polarisation (DoLP) for different polarised light using the calibrated demodulation tensor.

TABLE 5.6: DoLP and AoLP of unpolarised (UFF) and polarimetric
flat-field (PFF) by using calibrated demodulation tensor.

Set up	Expected DoLP	Obtained DoLP	Expected AoLP	Obtained AoLP
UFF	0%	$(2 \pm 2)\%$	/	/
PFF (0°)	100%	$(100 \pm 2)\%$	0°	$(0.0° \pm 0.5°)$
PFF (45°)	100%	$(100 \pm 2)\%$	45°	$(44.6° \pm 0.5°)$
PFF (90°)	100%	$(99 \pm 2)\%$	90°	$(90.0° \pm 0.5°)$
PFF (135°)	100%	$(100 \pm 2)\%$	135°	$(135.2° \pm 0.5°)$

Finally, Figure 5.27 and Figure 5.28 show the maps for the different micropo-
larisers efficiency ϵ_k and throughput t_k respectively (with $k = 0, 45, 90, 135$ degree).
Moreover, looking at Figure 5.29, it is possible to see that the throughput seems to be
systematically different for pixels with different orientations. In Figure 5.30, a map
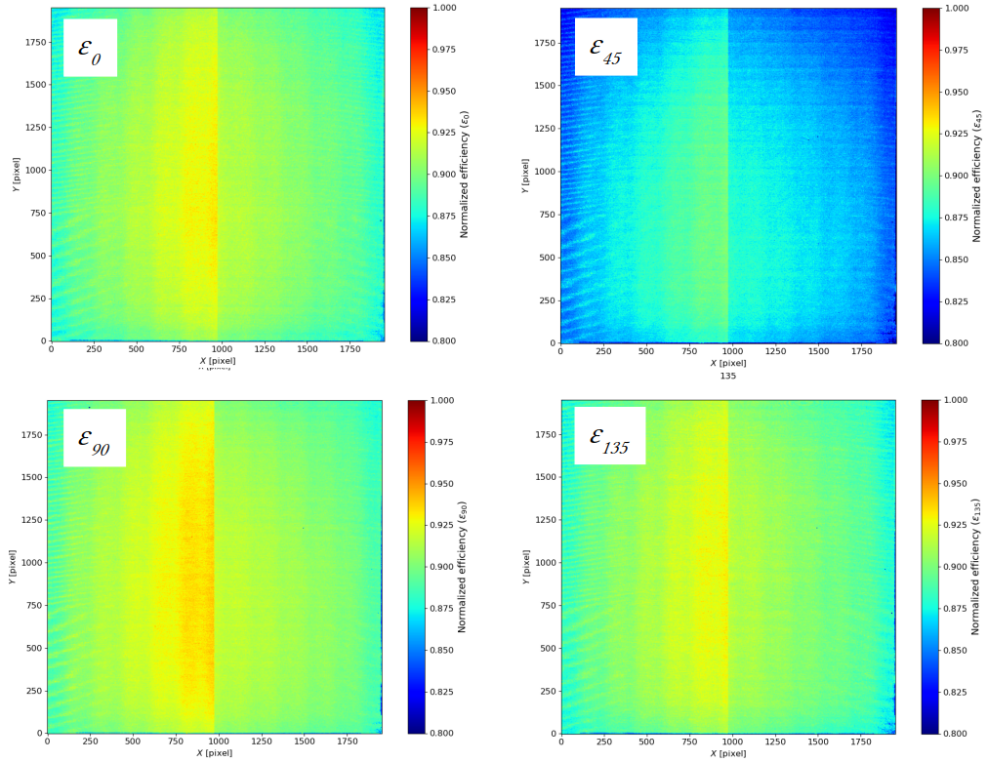of the effective micro-polariser orientation is shown.

FIGURE 5.27: Efficiency ϵ_k (for each pixel orientation) normalised to
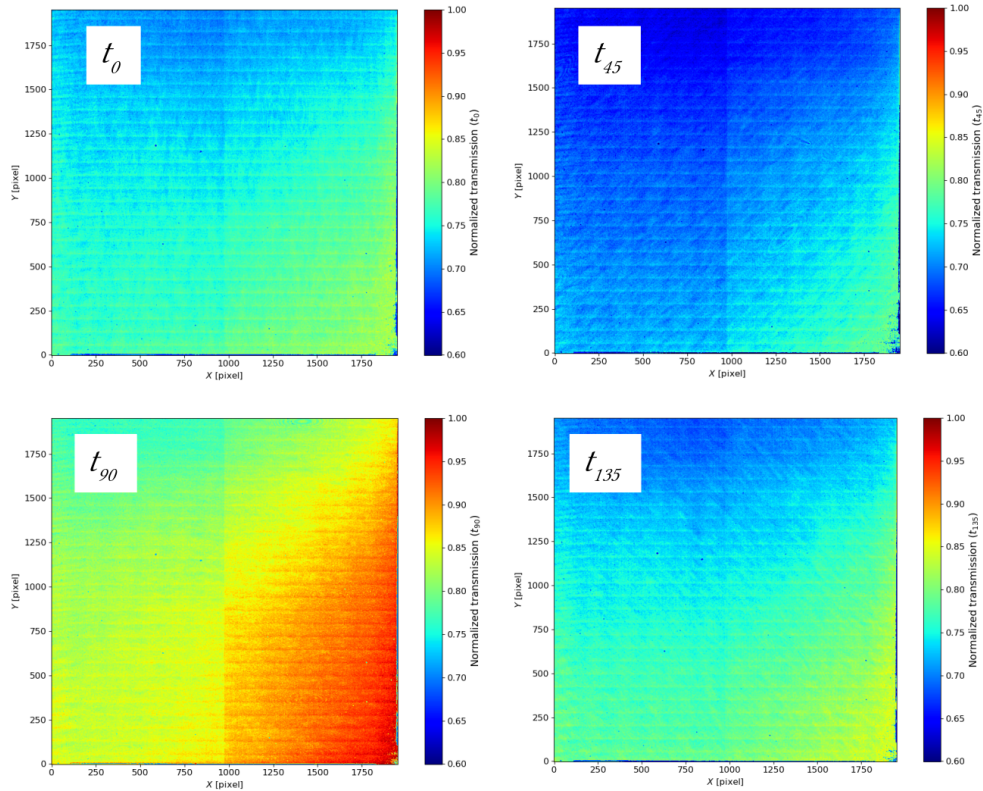the maximum efficiency of all pixels.

FIGURE 5.28: Throughput t_k (for each pixel orientation) normalised to the maximum throughput of all pixels.
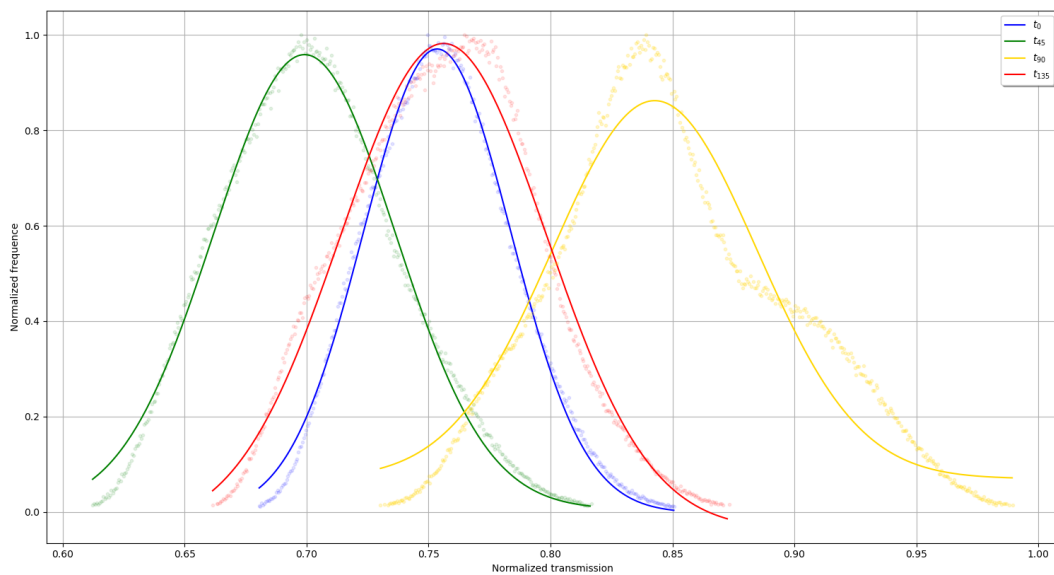

FIGURE 5.29: Histograms of throughput t_k (for each pixel orientation) normalised to the maximum throughput of all pixels.
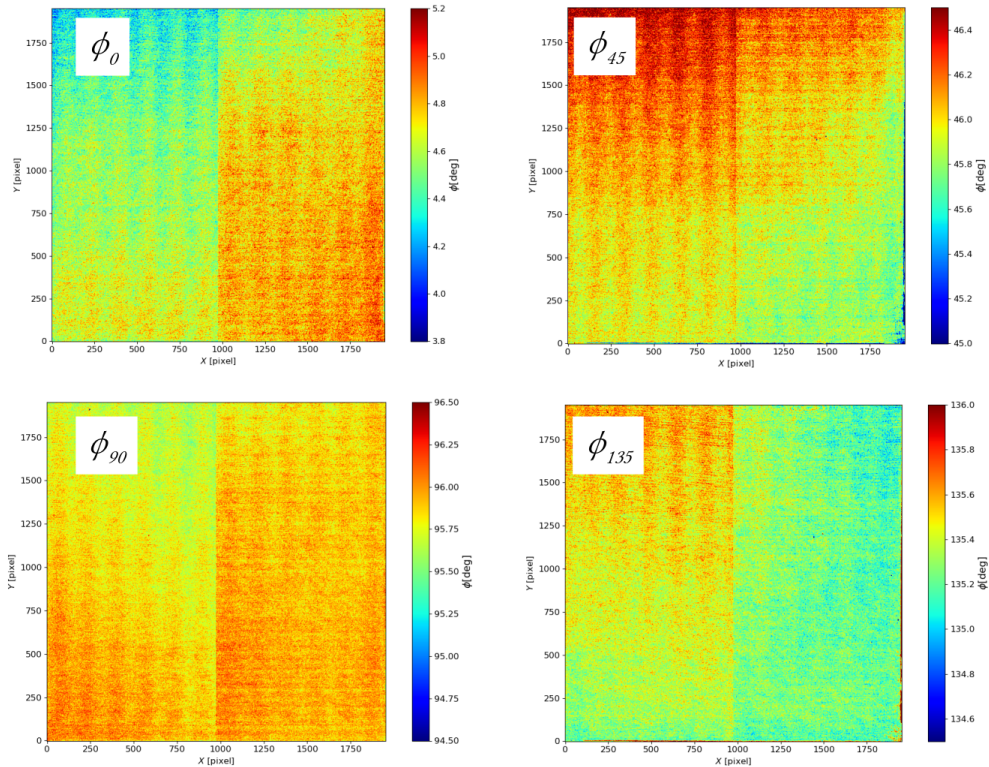
FIGURE 5.30: Maps of the micro-polariser orientations, ϕ_k.

5.4 Campaign results

In the following, we summarise the main results obtained during the 34th, 35th, and 37th Italian Mission in Antarctica.

5.4.1 Sky Brightness evaluation

Figure 3.7 shows that the brightness of the sky ("clear with haze") makes ground-based observations of the solar corona difficult. Total solar eclipses give the opportunity to observe the corona with a reduced sky brightness. A "pure blue sky" for ground-based coronagraphic observations is defined as $\approx 10^{-6}$ of the Sun's disc brightness (B/B$_\odot$). Ground-based observations of the solar corona were made possible with the development of the internally-occulted coronagraph by Lyot (Lyot, 1932) as described in Subsection 3.3.3.

During the Antarctic campaigns, systematic images of the sky were acquired to evaluate its brightness by using the coronagraph. The sky brightness in units of solar disc brightness ($B_{sky}[\text{B}_\odot]$) was measured the first time during the 34th Campaign (austral summer 2018/2019) and during the full data acquisition during the 35th Campaign (austral summer 2019/2020) at almost regular intervals during all days.[5] The $B_{sky}[\text{B}_\odot]$ can be evaluated by considering the first Stokes parameter and performing a ratio between what is obtained pointing to the sky with the Sun outside the field of view (I_{sky}) and what is obtained pointing to the Sun using a diffuser (I_{diff}). Both quantities must be normalised by the respective exposure time t_{exp}^i.

---

[5]The 36th Campaign (austral summer 2020/2021) was limited to logistic operations due to the COVID-19 pandemic.

Then, by considering the diffuser transmissivity $T_{diff} \approx 28\%$ (EdmundOptics, 2019) we obtain:

$$\frac{\overline{I}_{sky}}{\overline{I}_{diff}} = \frac{I_{sky}/t_{exp}^{sky}}{I_{diff}/t_{exp}^{diff}} = \frac{B_{sky}}{(B_\odot \cdot T_{diff})\Omega_\odot/2\pi} \tag{5.20}$$

where we considered the light scattered over the solid angle by the diffuser over the Sun angular radius $\vartheta = 16'$:

$$\frac{\Omega_\odot}{2\pi} = \int_0^{2\pi} \int_0^\vartheta \frac{\sin\vartheta'}{2\pi} d\vartheta' d\varphi = 1 - \cos\vartheta = 1.083 \times 10^{-5} \tag{5.21}$$

The resulting sky brightness B_{sky} $[B_\odot]$ is (Streete J.L., 1989):

$$B_{sky}[B_\odot] = \frac{(I_{sky}/t_{exp}^{sky})}{(I_{diff}/t_{exp}^{diff})} \cdot T_{diff} \cdot \frac{\Omega_\odot}{2\pi} \tag{5.22}$$

In particular, in our case, the acquired B_{sky} $[B_\odot]$ frame was divided into four different regions (Area in Figure 5.31) and the final brightness was obtained by averaging them:

$$B_{sky}[B_\odot] = \frac{\sum_i B_{sky}^i}{4} \qquad [i = 1, 2, 3, 4]. \tag{5.23}$$
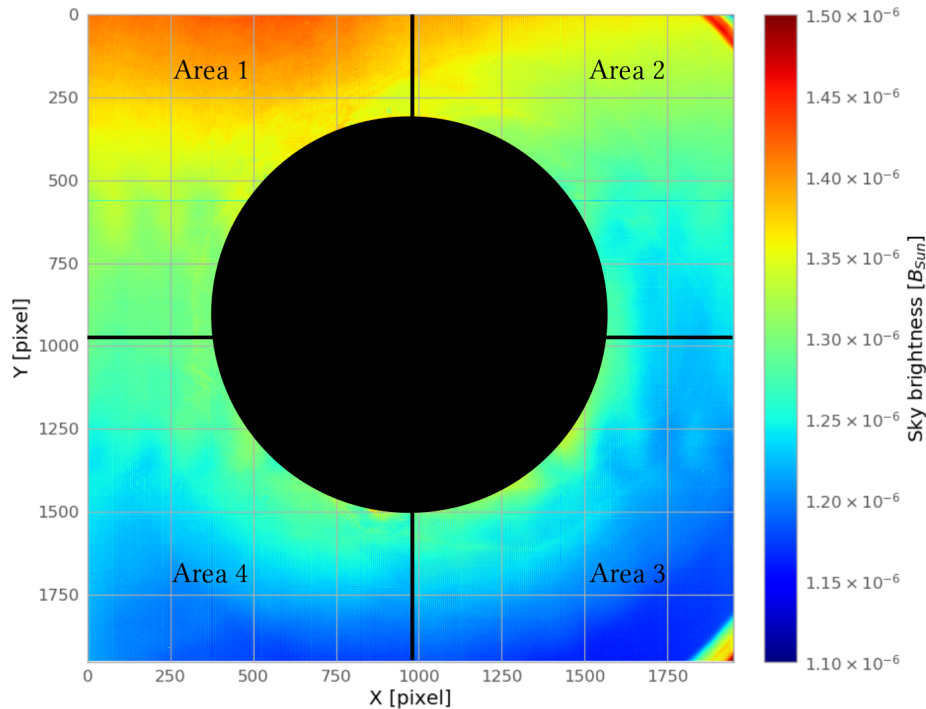

FIGURE 5.31: Example of the measured sky brightness (Dome C, Concordia Station - Antarctica) from the 34th campaign. The entire frame is divided into four different pads. The final sky brightness is obtained by averaging the four areas.

For each B_{sky} we evaluate the dispersion values as the standard deviation over the pixels in a considered area (e.g., σ over Area 1) quadratically added (and then divided by a factor of four) to the standard deviations obtained in the other three regions (Area 2, 3, 4).

A so-called "pure blue sky" (i.e., $B_{sky} \approx 10^6$ B$_\odot$) is necessary to carry out ground-based observations of the corona (Fracastoro, 1948; Fracastoro and Righini, 1949; Elmore, 2007).

Figure 5.32 shows the sky brightness, in B$_\odot$ units, measurements obtained during the 35th Italian Antarctic Expedition (2019-2020), at Concordia Station - Dome C.
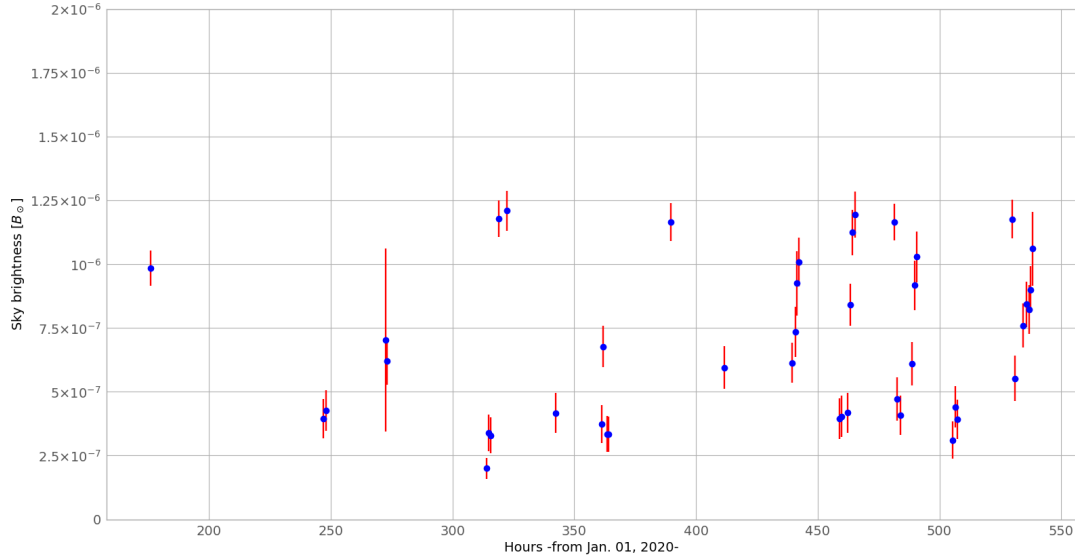

FIGURE 5.32: Sky brightness [B$_\odot$] measurements obtained during the 35th Italian Antarctic Campaign (2019-2020), Concordia Station - Dome C, $\approx$ 3230 m a.s.l., Antarctica. On the *x*-axis, the acquisition time [UTC] from January 1st, 2020 to January 22nd, 2020. On the *y*-axis, the obtained value of sky-brightness pointing at $+9°$ in declination with respect to the Sun position during each acquisition. The bars represent the dispersion values obtained by considering the standard deviations for each of the four different detector frame areas.

From the images acquired during the 34th Campaign on January 08, 2019 (pointing at RA: 22° 42' 32.3", Dec: -22° 11' 22") and January 09, 2019 (pointing at RA: 22° 38' 33.3", Dec: -22° 18' 19"), we obtain that (Liberatore et al., 2022):

$$\bar{B}_{sky} = (1.2 \pm 0.1) \times 10^{-6} \text{ B}_\odot \tag{5.24}$$

During the 35th campaign it was possible to perform more systematic sky brightness measurements. A summary of what obtained is shown in Figure 5.32. Averaging over the different values we obtain (Liberatore et al., 2022):

$$\bar{B}_{sky} = (6.9 \pm 0.2) \times 10^{-7} \text{ B}_\odot \tag{5.25}$$

During these measurements, Dome C showed the characteristics of a "coronagraphic sky". Sometimes, the presence of clouds, high wind or excessive suspended ice in the atmosphere made it impossible to perform good observations. On the other hand, during this campaign, we evaluated a percentage of good-weather days around the 80%!

During the same mission, we evaluated the sky brightness for different right ascensions (RA) and declinations (DEC) for a fixed day (see Figure 5.33). The values of measured B_{sky} are consistent with what obtained in Figure 5.32 and, as expected, it is possible to see a decrease of sky brightness moving away from the Sun. The closest measurements to the solar limb are at about 0.7° [i.e., the declination the closest measurement was at $\approx 1°$ from Sun centre (Figure 5.33, top), so $1 - 0.26 = 0.74°$ from the solar limb (where 0.26° is the solar radii)]. We cannot go much closer than $\approx 1°$ from Sun centre due to the instrument field of view along the x and y axis. The instrument FoV is $\approx \pm 0.6°$ (Table 5.1) and we need that the Sun is completely out of the FoV to take sky brightness measurements.
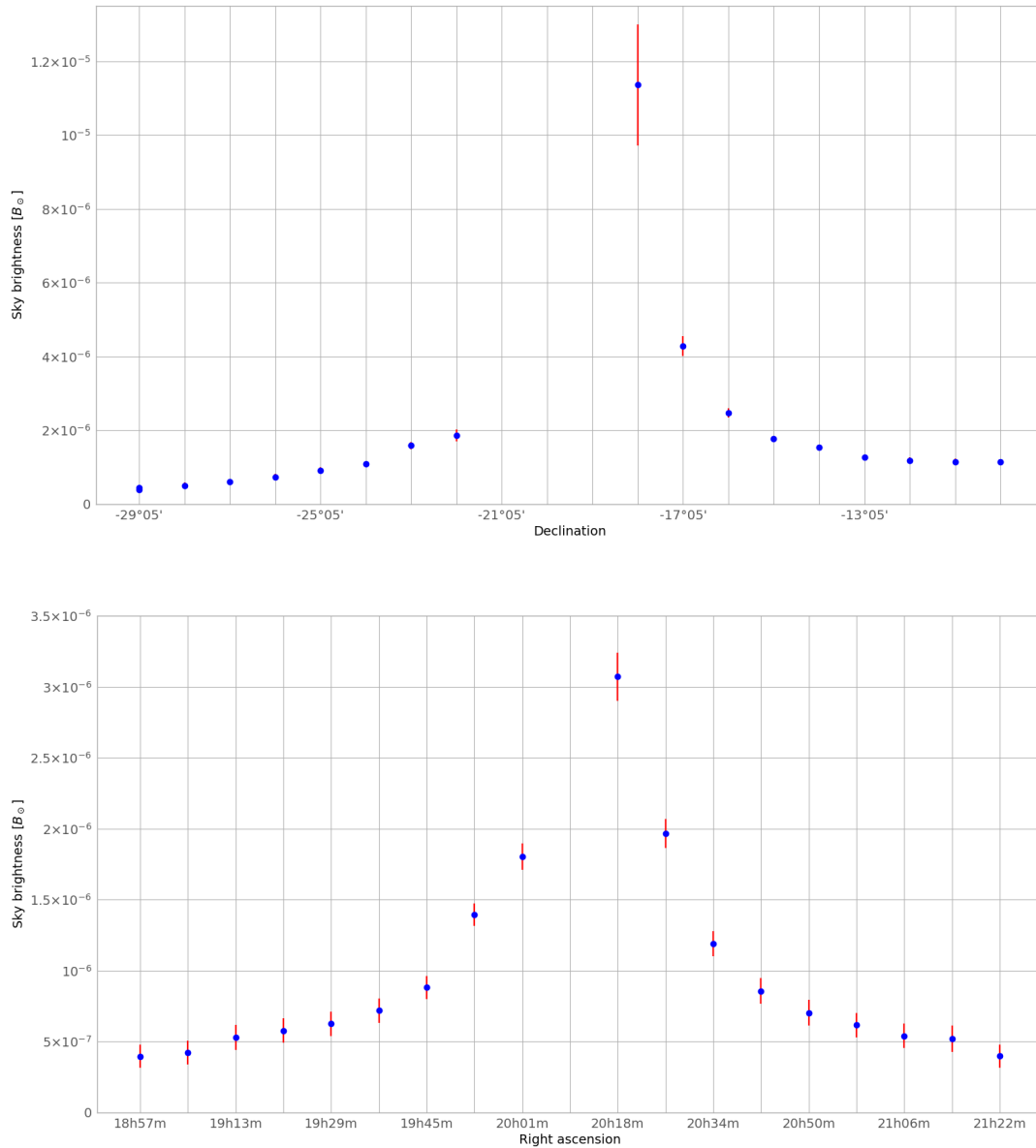

FIGURE 5.33: Sky brightness $[B_\odot]$ measurements during the 35th Italian Antarctic Campaign (2019-2020), Concordia Station, Dome C, ≈ 3230 m a.s.l., for different declinations (top) and different right ascensions (bottom) on January 1, 2020. Sun position (J200 system): RA: 20h 09m 38s, Dec: -20° 05′ 57″ (Liberatore et al., 2022).

From the 37th campaign, we were able to perform new systematic sky brightness measurements (Figure 5.34). From the average of these data we obtain:

$$\bar{B}_{sky} = (1.07 \pm 0.01) \times 10^{-6} \text{ B}_\odot \tag{5.26}$$

This result is consistent with what was obtained in the two previous Antarctic campaigns. As performed during the 35th campaign, we evaluated the sky brightness for different right ascensions (RA) and declinations (DEC) in a specific moment (Figure 5.35). The result is again consistent with what was obtained in the 37th campaign and in the previous ones. The sky brightness values obtained during the different campaigns are summarised in Table 5.7.

Considering all these results, we can conclude that the local sky can be considered a *coronagraphic sky* (Fracastoro, 1948; Elmore, 2007 and Figure 3.7).

TABLE 5.7: Summary of the measured sky brightness Dome C.

Sky Brightness	Antarctic campaign	Observation period
$(1.2 \pm 0.1) \times 10^{-6}$ B$_\odot$	34th (2018-2019)	Jan. 08, 2019 - Jan. 09, 2019
$(0.69 \pm 0.02) \times 10^{-6}$ B$_\odot$	35th (2019-2020)	Jan. 01, 2020 - Jan. 22, 2020
$(1.07 \pm 0.01) \times 10^{-6}$ B$_\odot$	37th (2021-2022)	Dec. 04, 2021 - Jan. 11, 2022

FIGURE 5.34: Sky brightness [B$_\odot$] measurements obtained during the 37th Italian Antarctic Campaign (2021-2022), Concordia Station - Dome C, $\approx$ 3230 m a.s.l., Antarctica. On the *x*-axis, the acquisition UTC time from December 1st, 2021 to January 11th, 2022. On the *y*-axis, the obtained value of sky-brightness pointing at $+9°$ in declination with respect to the Sun position during each acquisition. The bars represent the dispersion values obtained by considering the standard deviations for each of the four different detector frame areas.
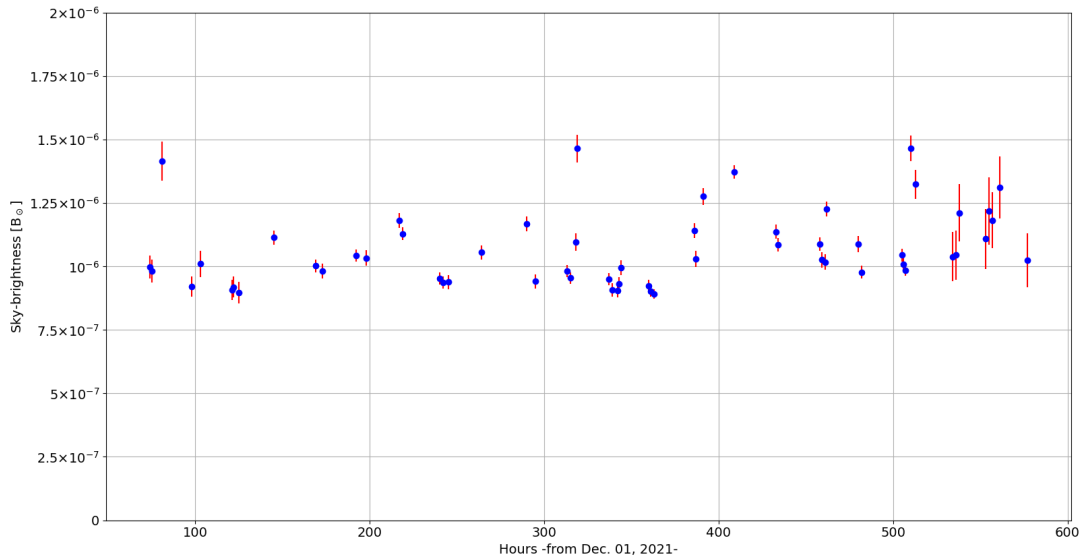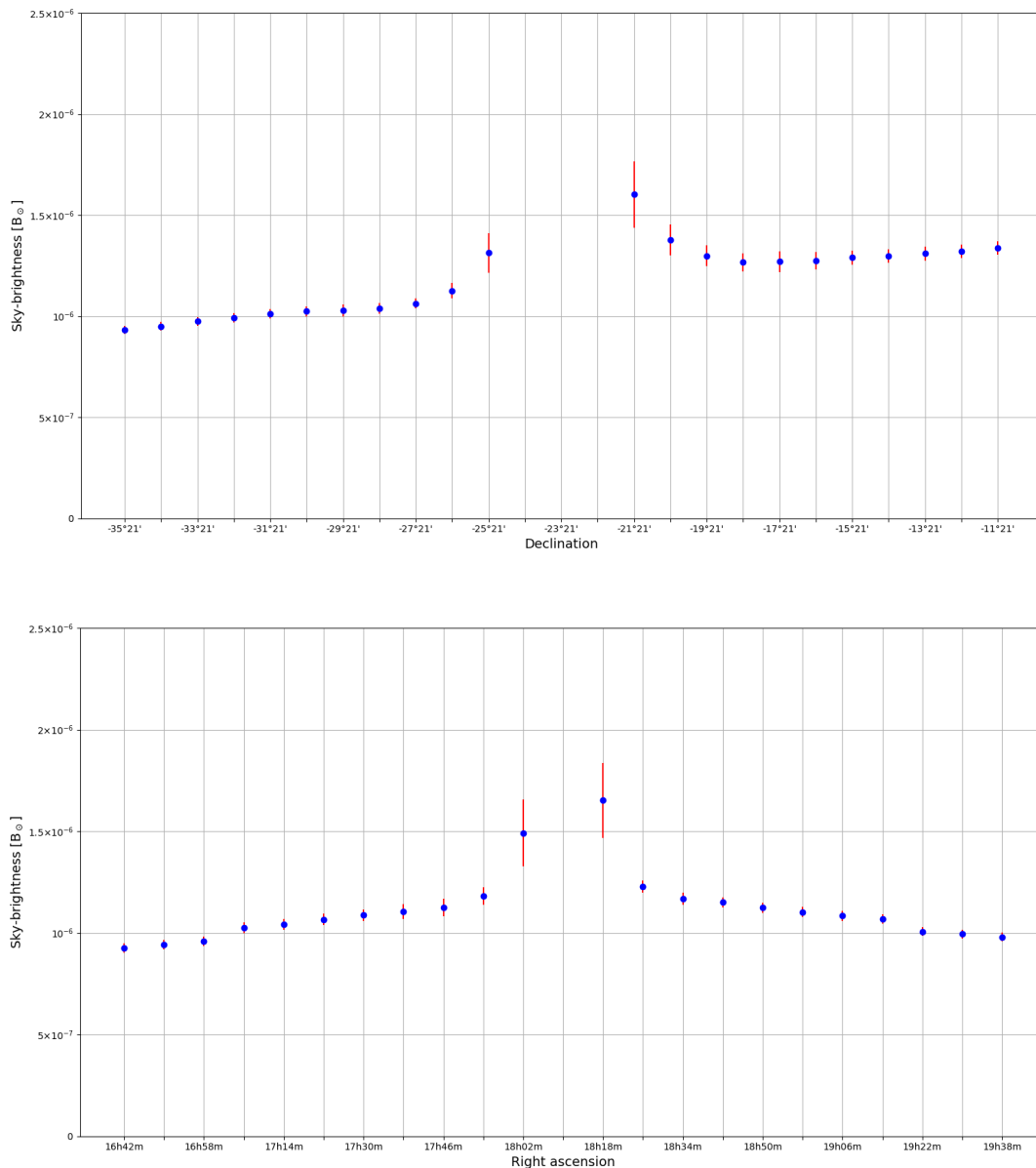
FIGURE 5.35: Sky brightness $[B_\odot]$ measurements during the 37th
Italian Antarctic Campaign (2021-2022), Concordia Station, Dome C,
$\approx$ 3230 m a.s.l., for different declinations (top) and right ascensions
(bottom) on December 24, 2021. Sun position (J200 system):
RA: 18h 10m 24s, Dec: -23° 21′ 48″.

During the 37th mission, a total solar eclipse was visible from the Antarctic peninsula. Unfortunately, as shown in Figure 5.36, it was visible just as partial eclipse[6] ($\approx$ 64%) from Dome C. In Figure 5.37 the sequence of the event as seen from Concordia Base (time moves from right-to-left). Indeed, by comparing the average intensity during the zero-occultation (first image of the sequence) and the average intensity during the maximum occultation (half of the sequence) we obtain a difference of the approx $\approx$ 64%. The images were acquired by using a Mylar filter in front of a commercial camera (Nikon D750; f: 300 mm).

---

[6]The sky-brightness data during this event are not considered for the evaluation of the local standard sky-brightness.

Total Solar Eclipse of 2021 Dec 04

Geocentric Conjunction = 07:56:04.9 UT   J.D. = 2459552.830612
Greatest Eclipse = 07:33:22.5 UT   J.D. = 2459552.814844

Eclipse Magnitude = 1.0367   Gamma = -0.9526

Saros Series = 152   Member = 13 of 70

Sun at Greatest Eclipse
(Geocentric Coordinates)

R.A. = 16h43m32.3s
Dec. = -22°16'29.3"
S.D. = 00°16'13.6"
H.P. = 00°00'08.9"

Moon at Greatest Eclipse
(Geocentric Coordinates)

R.A. = 16h42m34.9s
Dec. = -23°13'22.1"
S.D. = 00°16'44.7"
H.P. = 01°01'27.3"

External/Internal
Contacts of Penumbra

P1 = 05:29:11.3 UT
P4 = 09:37:23.9 UT

External/Internal
Contacts of Umbra

U1 = 07:00:01.0 UT
U2 = 07:05:48.9 UT
U3 = 08:00:40.9 UT
U4 = 08:06:29.2 UT

Local Circumstances at Greatest Eclipse

Lat. = 76°46.7'S   Sun Alt. = 17.2°
Long. = 046°11.9'W   Sun Azm. = 114.8°
Path Width = 418.6 km   Duration = 01m54.4s

Ephemeris & Constants

Eph. = Newcomb/ILE
ΔT =   78.8 s
k1 = 0.2724880
k2 = 0.2722810
Δb = 0.0"   Δl = 0.0"

Geocentric Libration
(Optical + Physical)

l = -0.23°
b =   1.26°
c =   6.09°

Brown Lun. No. = 1224

0   1000   2000   3000   4000   5000
Kilometers

F. Espenak, NASA's GSFC - Fri, Jul 2,
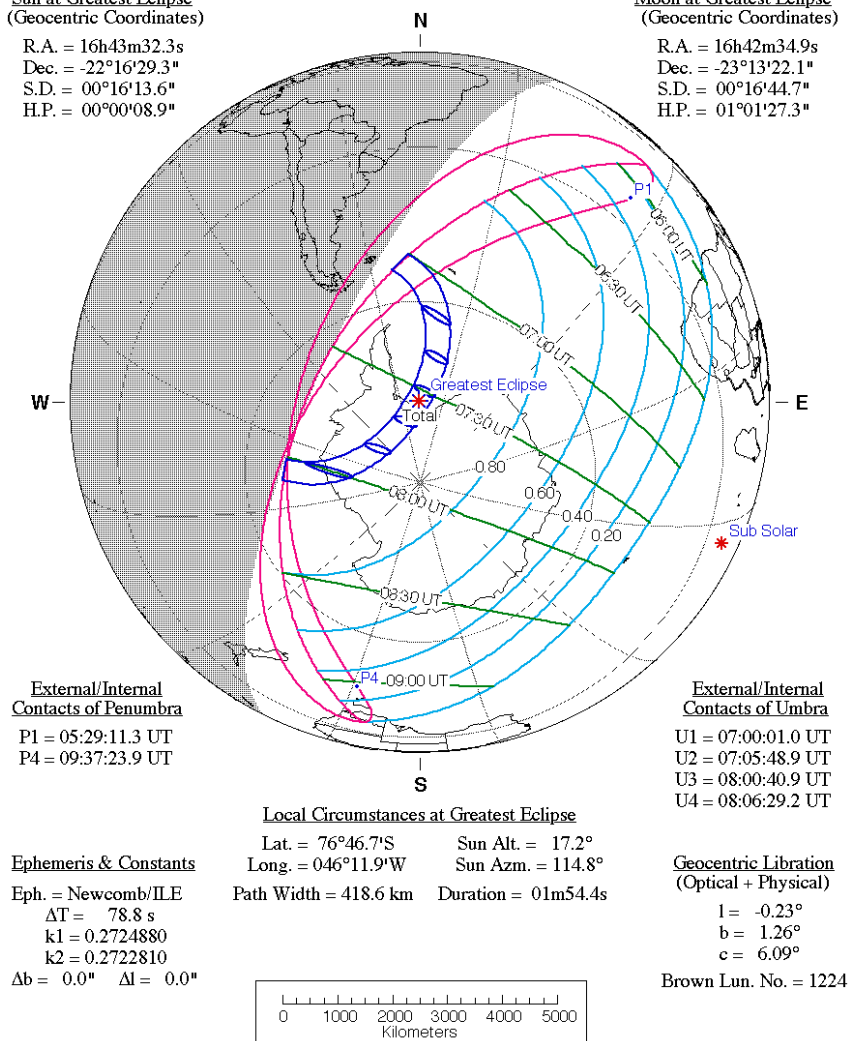*sunearth.gsfc.nasa.gov/eclipse/eclipse.html*

FIGURE 5.36: Espenak map of the December 4, 2021 total solar
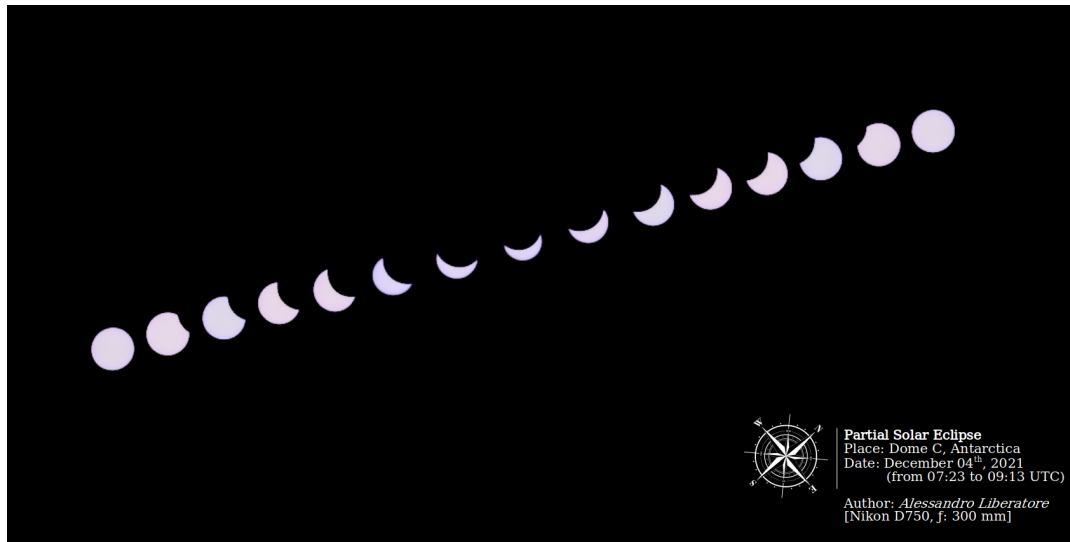eclipse.

FIGURE 5.37: Sequence of the partial solar eclipse from Concordia
Base on December 4, 2021.

5.4.2 Solar Corona observation

During the first campaign (34th) it was not possible to perform coronal observation due to logistic problems. In the second campaign (35th) we tried to observe the solar corona but there were problems with Sun-tracking. The Sun moves out from the occulter every 5-10 seconds. Then, we improved the equatorial mount and developed a control software trying to have the best Sun-tracking possible (ACCS - AntarctiCor Control Software; Figure 5.38).
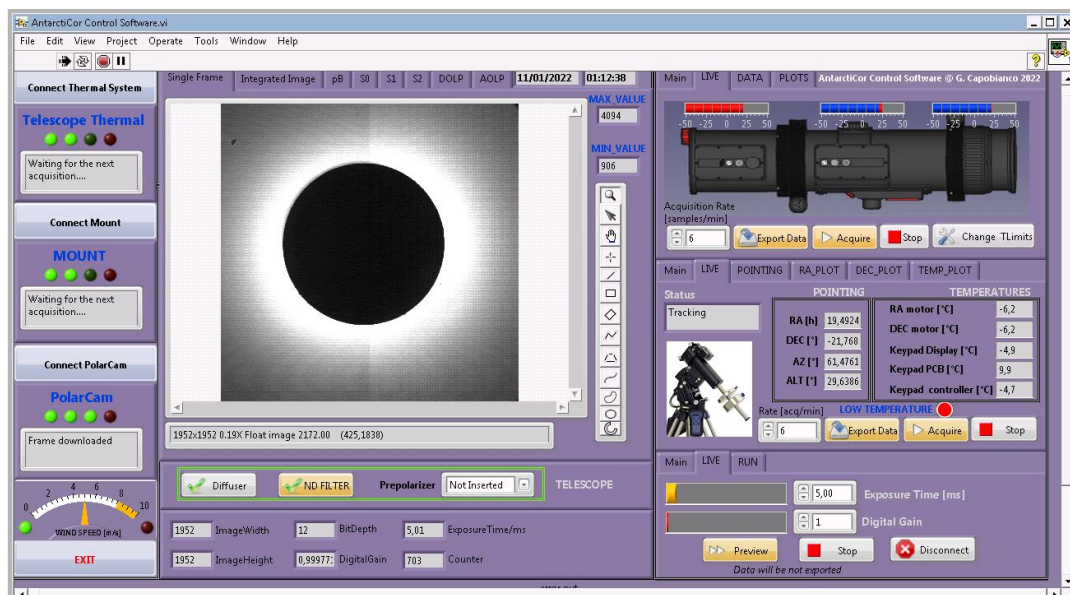

FIGURE 5.38: AntarctiCor Control Software (© G. Capobianco).

Thanks to these improvements, during the last campaign (37th) we observe a shift of ≈ 1 pixel every 10-15 minutes. Indeed, it was possible to acquire the first images with coronal signal (Figure 5.39). More improvements are needed to increase the image quality of these first acquisitions. A preliminary comparison with what

was observed by KCor[7] (Hou, de Wijn, and Tomczyk, 2013) and LASCO-C2 (Brueckner et al., 1995) coronagraphs is shown in Figure 5.40. Further analysis of these data will allow additional improvements and new comparisons with other instruments.
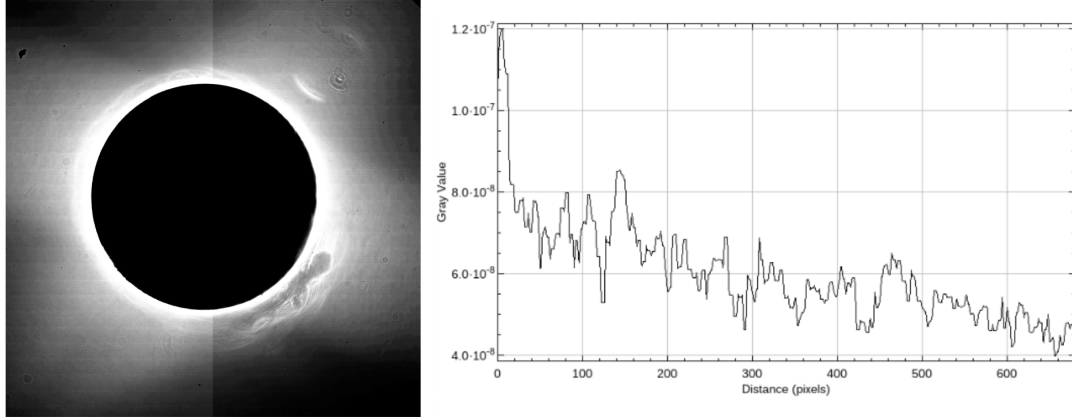

FIGURE 5.39: **(a) Left:** First preliminary image of the total intensity of the solar corona as observed from Dome C, Antarctica (December 11, 2021). The shadow near the bottom-right edge of the internal occulter is an instrumental defect. It is also possible to notice the presence of different ghosts. They disappear in the pB. **(b) Right:** Diagonal cut (along the North-East streamer) of the polarised brightness in unit of $B_\odot$. The x-axis shows the distances in pixels from the IO edge.
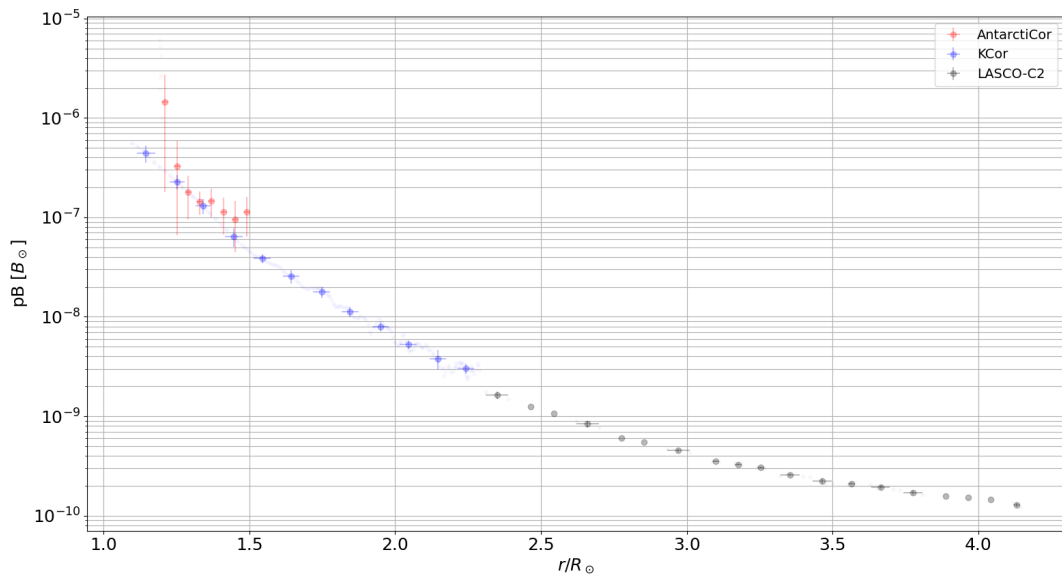
FIGURE 5.40: Preliminary comparison between the polarised brightness of the solar corona observed on December 11, 2021 by AntarctiCor, KCor and LASCO-C2.

---

[7]It is important to notice that AntarctiCor has an aperture of 5 cm while KCor aperture is about 20 cm (Nelson P. G., 2010). This means that has a signal to noise ration four times higher! Even for this reason KCor telescope can see more easily coronal signal at higher heliocentric heights.

5.5 PROBA-3

The AntarctiCor internally-occulted coronagraph (Figure 5.3) is based on the optical design[8] of the "Association of Spacecraft for Polarimetric and Imaging Investigation of the Corona of the Sun" (ASPIICS) externally-occulted coronagraph for the ESA formation-flying PROBA-3 mission (Galy et al., 2015; Fineschi et al., 2019a).

PROBA-3 is an in-orbit[9] demonstration mission (the launch is planned for half 2023) that consists of two independent minisatellites at $\approx$ 150 m apart in a precise formation flying (Figure 5.41). The relative position control accuracy is about 1 mm! Eight different Shadow Position Sensor (SPS) verifies the safe centering of the entrance pupil of the coronagraph into the shadow cone of the occulting disc. The two satellites are referred to as Coronograph SpaceCraft (CSC) with a mass of $\approx$ 320 kg and Occulter SpaceCraft (OSC) with a mass of $\approx$ 180 kg (Galy et al., 2019). The CSC carries the camera and the OSC carries the 1.4 m diameter occulting disc. When the two satellites are co-aligned with the Sun, the occulting disk will produce an artificial eclipse (i.e., an externally-occulted coronagraph; see Subsection 3.3.3).
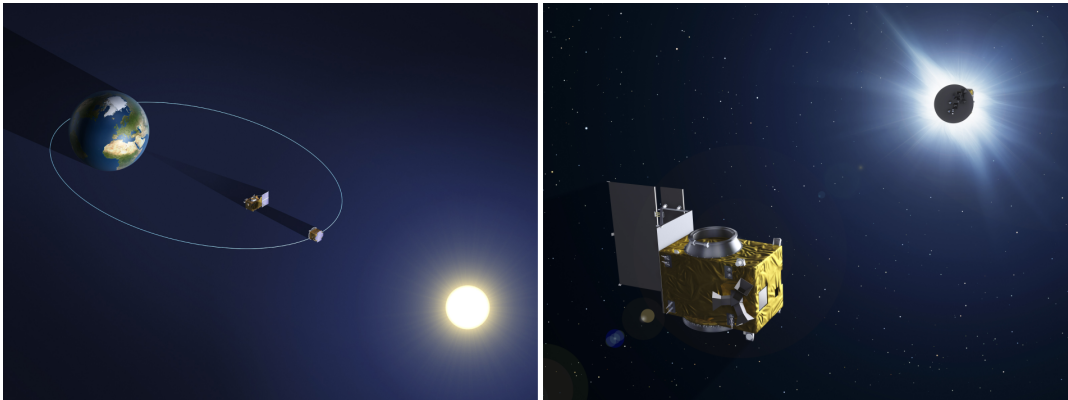

FIGURE 5.41: Artistic representation of the PROBA-3 formation flight mission (© ESA - P. Carril, 2013).

PROBA-3 will fly ASPIICS[10] as the primary payload. The AntarctiCor telescope design is derived from the design of the ASPIICS coronagraph, whose Demonstration Model lenses are available and are used to minimize the development of additional, new lenses. Some modifications from the design of ASPIICS have been adopted due to the main difference between ASPIICS and AntarctiCor (Fineschi et al., 2019a):

- ASPIICS has an external occulter (located 150 m ahead of the first imaging lens), while AntarctiCor is internally occulted;

- the ASPIICS's objective doublet lens operates in the shadow of the external occulter, while the AntarctiCor objective lens is directly illuminated by the Sun-disc light;

- in order to minimize the internal reflection in the objective lens (directly illuminated by the Sun-disc light), this has been changed into an highly polished singlet.

---

[8]The optical design of ASPIICS and its performances are presented in Renotte et al., 2015.
[9]High Earth orbit, 19.7 hours orbital period, 60530 km apogee, 600 km perigee.
[10]Ground calibrations of ASPIICS were performed in mid-2021 in the OPSys facility in ALTEC.

ASPIICS offers a valuable scientific return. Indeed, thanks to the formation fly, the two satellites will together form the equivalent of a huge solar coronagraph that will be able to view close-up the Sun's surface. In particular, we will be able to see the solar corona from three solar radii down to just 1.08 solar radii as a goal. This is not traditionally enabled by smaller-scale coronagraphs. By observing the structure, the dynamics, and the heating process that occurs very close to the Sun's surface, we will be able to acquire new data to answer the problem of the coronal heating (Chapter 3). Moreover, achieving precise formation flying could open up a new era not only for solar physics but for space science in general.

Chapter 6

Solar Orbiter mission

Solar Orbiter (SolO) is the first mission of ESA Cosmic Vision 2015–2025 program. It was launched in February 2020 and it is an ESA-led mission with a strong NASA participation. On-board Solar Orbiter there are six remote-sensing instruments and four sets of in-situ instruments for a total of 10 different experiments (Figure 6.1). The complete list of the Solar Orbiter instruments can be found in Table 6.1. It is possible to have a general idea of the effective dimension of the S/C by looking at Figure 6.2. Among the Solar Orbiter remote-sensing instruments, there is the Metis[1] coronagraph (see Section 6.2). In the next Sections, we will go more into detail about its structure and scientific goals.
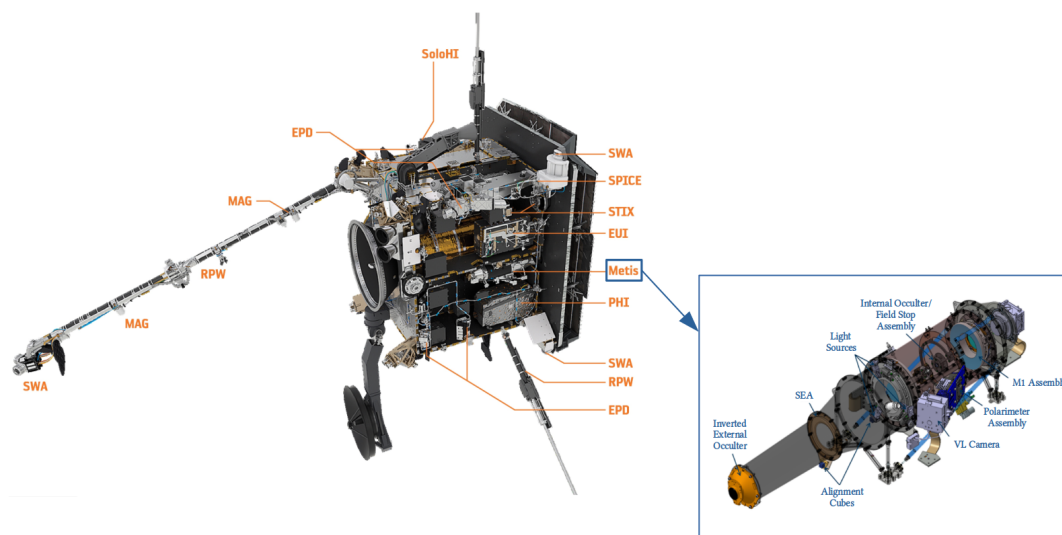

FIGURE 6.1: Solar Orbiter payload (adapted from Müller et al., 2020). Among the instruments on-board the spacecraft, there is the Metis coronagraph. A 3D CAD of Metis is show in the blue rectangle.

The goal of the mission is to perform coordinated remote-sensing and in-situ observations to obtain detailed measurements of the inner heliosphere and solar wind. What drives the solar wind? Where does the coronal magnetic field originate? How does the solar dynamo work and drive Sun-Heliosphere connections? These are just a few of the top-level science questions that seek answers through this mission. This will be possible thanks to the peculiar spacecraft orbit. Indeed, thanks to different gravity assist manoeuvres (GAM), Solar Orbiter will arrive close to the Sun and will be progressively inclined to the ecliptic plane as described in Section 6.1.

---

[1]In ancient Greek religion, Metis was a mythical goddess symbol of wisdom and deep thought and first wife of Zeus.

TABLE 6.1: List of the instruments on-board Solar Orbiter.

| In-situ	PI	Description
EPD 🇪🇸 [*Energetic Particle Detector*]	J. Rodríguez-Pacheco	Distribution functions, timing and composition of energetic particles.
MAG 🇬🇧 [*Magnetometer*]	T. Horbury	High-precision measurements of the heliospheric magnetic field.
RPW 🇫🇷 [*Radio and Plasma Waves*]	M. Maksimovic	Electromagnetic and electrostatic waves, magnetic and electric fields at high time resolution.
SWA 🇬🇧 [*Solar Wind Analyser*]	C. Owen	Sampling protons, electrons and heavy ions in the solar wind.
Remote-sensing	**PI**	**Description**
EUI 🇧🇪 [*Extreme Ultraviolet Imager*]	P. Rochus	High-resolution and full-disc (E)UV imaging of the on-disc corona.
Metis 🇮🇹 [*Coronagraph*]	M. Romoli	Visible and UV Imaging of the off-disc corona.
PHI 🇩🇪 [*Polarimetric Helioseismic Imager*]	S. Solanki	High-resolution vector magnetic field, line-of-sight velocity in photosphere, visible imaging.
SoloHI 🇺🇸 [*Heliospheric Imager*]	R. Howard	Wide-field visible imaging of the solar off-disc corona.
SPICE 🇪🇺 [*Spectral Imaging of the Coronal Environment*]	ESA facility instrument	EUV imaging spectroscopy of the solar disc and near-Sun corona.
STIX 🇨🇭 [*Spectrometer/Telescope for Imaging X-rays*]	S. Krucker	Imaging spectroscopy of solar X-ray emission.
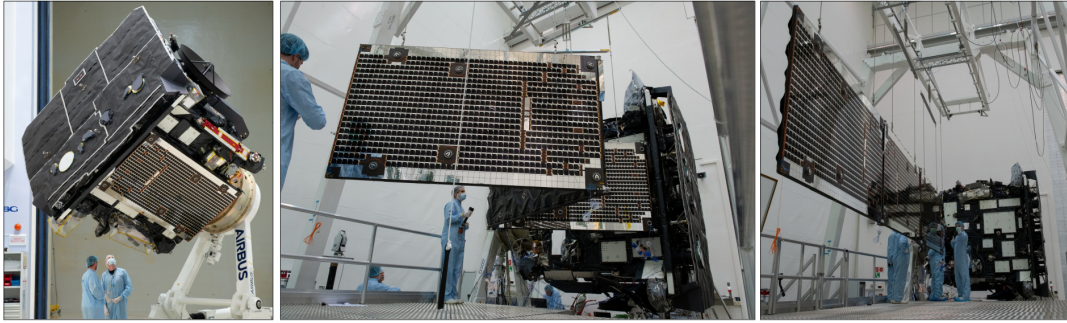
FIGURE 6.2: Solar Orbiter during the *Array Deployment Test* (March 2019 at IABG facilities in Ottobrunn, Germany). The spacecraft dimensions are 2.5m $\times$ 3.1 m $\times$ 2.7 m in the launch configuration (i.e., with folded solar arrays) and reach a total length of 18 m with solar arrays deployed. Images from ESA website (© S. Corvaja).

6.1 Mission profile

The spacecraft was launched[2] aboard a NASA-provided Atlas V 411 launch vehicle (Figure 6.3) from Cape Canaveral on February 10th, 2020 at 04:03 UTC. The nominal mission duration is 7 years. The nominal mission includes the cruise phase and the nominal phase (start: Earth GAM on 26 November 2021; end: fifth Venus GAM on 24 December 2026). The extended mission consists of the addition of 3 more years. This mission will allow for the first time, the remote-sensing observation of the Sun from as close as 0.28AU $\approx$ 42 million kilometres from the Sun (furthest aphelion: 1.02 AU). In the dark of space, Solar Orbiter faces temperatures of about -180°C. In opposition, at closest approach, the spacecraft will test 13 times the intensity of terrestrial sunlight and temperatures of up to 520°C (García Marirrodriga et al., 2021).[3] To protect the spacecraft bus from this flux a Sun shield is used.

As shown in Figure 6.4, thanks to several gravitational assist with Venus and Earth, the S/C orbit will be progressive more inclined to the ecliptic plane (until ecliptic latitudes as high as 33°) observing, for the first time, the polar regions of the Sun (Müller et al., 2020). In particular, the S/C will reach 7° during the cruise phase, 18° during the nominal mission (reached first on 22 March 2025), 24° when the extended mission start (reached first on 28 January 2027), 33° during the extended mission (reached first on 24 July 2029). The orbital period is of about $150 - 180$ days.

In the next sections, we will focus on the Metis coronagraph; one of the remote-sensing instruments on-board the S/C. However, more information about the mission profile and the other instruments on-board can be found in Müller et al., 2020.

6.2 Metis

Metis is one of the six remote-sensing instruments on-board Solar Orbiter (blue rectangle in Figure 6.1). It is a multi-wavelength, externally occulted telescope for simultaneous UV and VL imaging of the solar corona. In particular, the instrument acquires images in the $580 - 640$ nm visible range and in the ultraviolet HI Lyman-α

---

[2]Launch mass: $\approx$ 1720 kg with a science payload mass of 209 kg (Müller et al., 2020).

[3]At closest approach, the S/C will experience a solar flux of approximately 17.500 W/m^2 (García Marirrodriga et al., 2021; Jacobs, Morgan, and Damasio, 2020; Lyngvi et al., 2005).
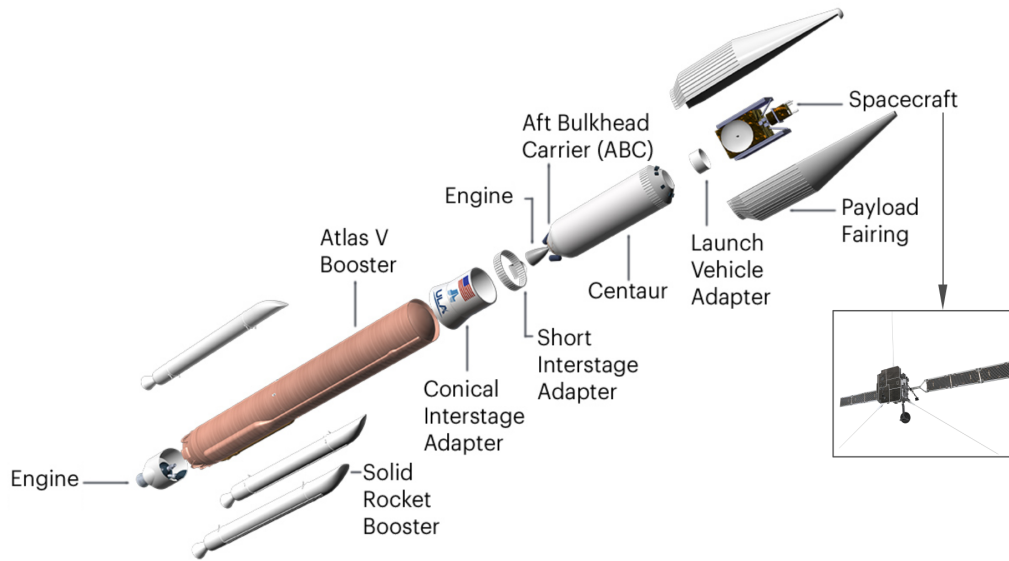
FIGURE 6.3: Atlas V 411 Launch Vehicle (adapted from García Marir-rodriga et al., 2021).

line (centred at 121.6 nm with a FWHM of 15 nm). Metis will allow to diagnose, with unprecedented temporal coverage and spatial resolution, the structures and dynamics of the solar corona in the $1.6 - 2.9$ degree of field of view (FoV), which corresponds to $1.7 - 3.1$ R$_\odot$ at the minimum perihelion distance (0.28 AU). These measurements will allow for the first time the simultaneous characterisation of the main physical parameters of the solar corona such as electron and hydrogen densities, their temperatures, and the study of the solar wind in the region where the acceleration process takes place (Fineschi et al., 2020).

The most commonly used optical design for visible light solar coronagraphs is based on the traditional design proposed by Bernard Lyot (Lyot, 1932) with a stop along the optical path to block the light diffraction off the entrance pupil as shown in Section 3.3. However, this solution gives the possibility to observe only at small distances from the disc limb. To include the fainter outer corona, a modified design has then been introduced adopting external occultation as well. In this way, there is a decrease in the Sun disc stray light (to levels as low as 10^{-9} inside the instrument). Moreover, it is possible to obtain a very high dynamic range thanks to the pupil vignetting at the brighter coronal regions (i.e., closer to the solar disc). Metis has been designed starting from these concepts (Fineschi et al., 2020). In addition, the design had to implement the two following requirements: the maintenance of the instrument stability in very variable thermal conditions and the possibility to observe the solar corona in both visible (polarised) light and UV spectral band. The request to be able to observe polarimetrically in visible light derives from the possibility of studying in detail the K-corona. Indeed, as explained in Chapter 3 and Section 3.4, the K-corona results to be linearly polarised by Thomson scattering.

The stability in very variable thermal conditions is necessary because Solar Orbiter cover a wide range of distances from the Sun. For this reason, the on-board instruments need a particular design to be able to be operational both in classical space conditions and to sustain the high thermal flux when the S/C is at the perihelion. That is the reason why the Metis occultation scheme is based on an "inverted" external-occulter (IEO) to reduce the high thermal load on the instrument (temperatures higher than 400 °C) when is near to the Sun. In a classical externally-occulted
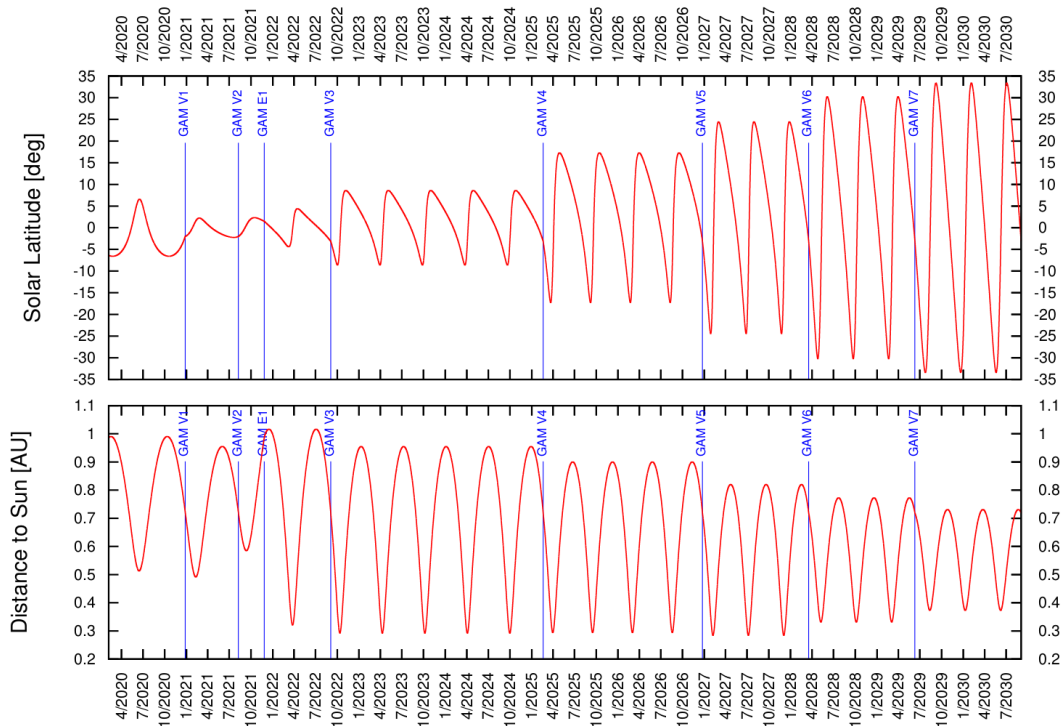
FIGURE 6.4: Solar Orbiter distance to Sun and latitude during the mission (García Marirrodriga et al., 2021). The S/C will reach about 0.28 AU and 33° of latitude outside the ecliptic plane.

coronagraph, the disc-light rejecting mirror is much larger than the circular one used in the inverted-occultation scheme (M0 in Figure 6.5). This reduces by almost two orders of magnitude the thermal load on the rejection mirror (Fineschi et al., 2020). In particular, the IEO consists of a circular aperture ($\varnothing 40.0$ mm) at the narrow end of a truncated cone. The disc-light is rejected back by a spherical heat-rejection mirror M0 ($\varnothing 71.0$ mm) distant 800 mm from the IEO. The coronal light, is instead collected by an on-axis aplanatic Gregorian telescope. The suppression of the diffracted light off the edges of the IEO and M0 is achieved, respectively, with an internal occulter (IO) and a Lyot trap (LS) (Antonucci et al., 2020). In particular, the primary and secondary telescope mirrors (M1 and M2 respectively) have an Al/MgF$_2$ coating to enhance the reflectivity at Ly-α (HI 121.6 nm) and has a high reflectivity also for the visible wavelength range $580 - 640$ nm. After these reflections, the coronal light is then split by a UV interferential filter (12° of inclination with respect to the optical axis) that works by selecting the 121.6 nm UV band in transmission and reflecting the VL to the polarimeter. Inside the polarimeter, a broadband filter selects the VL band-pass $580 - 640$ nm. The coronal light, entering the polarimeter, sequentially encounters the following elements: a collimating doublet (CD), the VL band-pass filter (BP), a quarter-wave (QW) plate retarder, a polarisation modulation package (PMP) composed of two liquid crystals variable retarders (LCVRs) -more information in the next subsection-, a linear polariser (LP) and a focus lens system (FLS). A detail of the Metis polarimeter is shown in the blue insert in Figure 6.5. Finally, on the focal planes of the two optical paths, there are the UV and VL detectors. The plate scale of the UV and VL detectors are 20 arcsec/pixel and 10 arcsec/pixel respectively. In this way, it is possible to perform simultaneous acquisitions of VL and UV images. All these, and other, optical performances are summarised in Table 6.2 and more detailed opto-mechanical information can be found in the cited articles.

TABLE 6.2: Main optical performances of Metis instrument.

Spectral range	
Multi-wavelength	VL: $580 - 640$ nm
	UV: HI Ly-α, 121.6 ± 7.5 nm (FWHM)
Telescope	
Type	(Inverted) Externally occulted
	on-axis aplanatic Gregorian
Overall length	1309 mm
Effective focal length	VL: 200 mm
	UV: 300 mm
Inverted External Occulter (IEO)	Circular aperture: $\varnothing 40.0$ mm
Distance IEO-M0 (boom)	800.0 mm
Sun-light rejection mirror (M0)	Spherical: $\varnothing 71.0$ mm
	Curvature radius: 1600.0 mm
Primary mirror (M1)	On axis ellipsoidal:
	outer $\varnothing 160.0$ mm, inner $\varnothing 88.0$ mm
	Curvature radius: 272.0 mm
Secondary mirror (M2)	On axis ellipsoidal:
	outer $\varnothing 216.0$ mm, inner $\varnothing 125.0$ mm
	Curvature radius: 312.4 mm
Internal occulter (IO)	Distance M1-IO: 154.8 mm
	Circular: $\varnothing 5.0$ mm
Detectors	
Plate scale	VL: 10 arcsec/pixel
	UV: 20 arcsec/pixel
Image size	VL: 2048×2048, 10 µm pixel size
	UV: 1024×1024, 30 µm pixel size equivalent
Field of view (FoV)	1.6°- 2.9° annular, off-limb corona
	$1.7 - 3.1 R_\odot$ @ 0.28 AU
	$3.0 - 5.5 R_\odot$ @ 0.50 AU

6.2.1 Liquid Crystals Variable Retarders

Along the Metis VL optical path, just before the detector, is set a polarimeter assembly with a couple of electro-optically modulating Liquid Crystals Variable Retarders (Fineschi et al., 2005; Zangrilli, Fineschi, and Capobianco, 2009). As previously said (see Section 4.1) the LCVRs consist of optically anisotropic liquid crystal molecules embedded between two glasses with a conductive film. These molecules are accommodated in cells with an ordered orientation. They have an effective birefringence
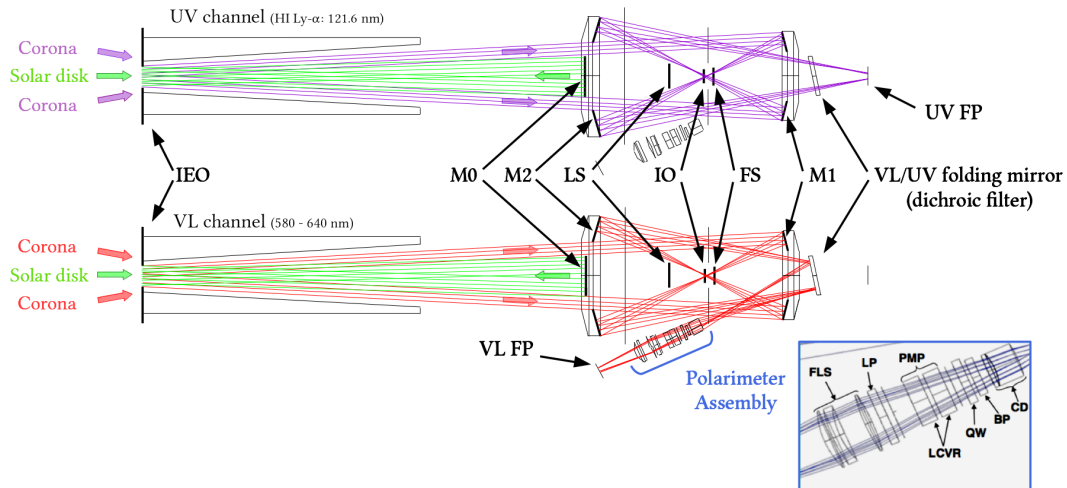
FIGURE 6.5: Metis ray trace for he UV and VL channels.

value that can be changed by applying an electric field to the cells that rotate the molecules (Figure 4.3). A change in orientation of the molecules introduces an optical retardance in the orthogonal polarisation components of the incoming light. There are several advantages introduced by this technology. Retarders based on liquid crystals permit to avoid the use of mechanical parts, reducing noise, failure probability, and mass. Moreover, the power consumption of the liquid crystal-based retarders is reduced and have a very quick response (providing a fast modulation of the polarisation state of light). On the other hand, LCVR devices are sensitive to temperature: retardance depends on temperature cells. For this reason, Metis PMP has been provided with a temperature controller (to guarantee the temperature uniformity on liquid crystal cells). A characterisation for different temperature was performed during on-ground calibration. Finally, the LCVR cells in the PMP have been assembled with the fast axes aligned and the molecules pre-tilt angle in opposite direction (Figure 6.6) obtaining a wider acceptance angle (equal to $\pm 4°$; Alvarez-Herrero et al., 2011 and Casti et al., 2018).

Obviously, to evaluate the effective polarisation angle corresponding to a fixed applied tension, we have to consider the entire polarimeter assembly (which includes, in addition to the PMP, also a LP and a QW). To analyse the data acquired for the polarimetric VL channel calibration, a dedicated reference frame has been introduced; the Polarimeter Instrument Level System (PILS) reference frame (Casti et al., 2018). Therefore, the on-ground data analysis is based on the PILS reference frame (Figure 6.7) which is defined as follows:
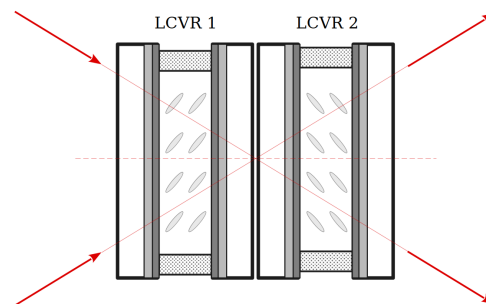

FIGURE 6.6: Pre-tilt angle of the LCVRs molecules.

- X_{PILS} = parallel to the incoming light direction, pointing the VL detector;

- Z_{PILS} = parallel to the Metis linear polarise acceptance axis;

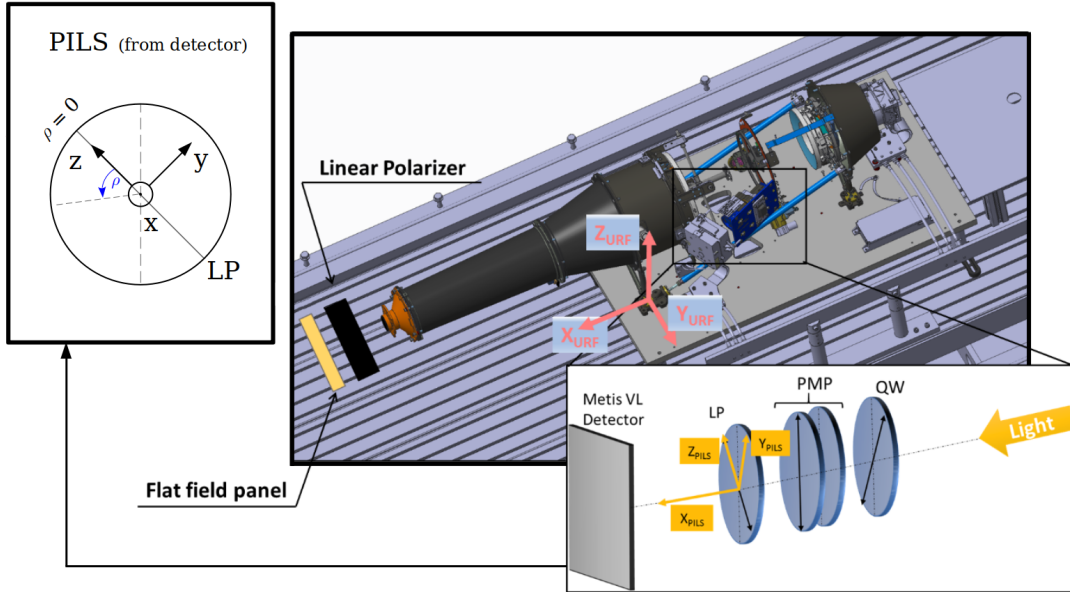- Y_{PILS} = to complete the right-handed reference system.

FIGURE 6.7: Schematic view of the set up used for data acquisition and Metis polarimeter optical elements relative orientations in PILS reference frame. The URF (Unit Reference Frame) is another existing reference frame that results to be rotate of 45° with respect to the PILS. The black arrows in the optical elements represent, respectively: the fast axes for both the QW and the LP, and the PMP polarisation axis.

Looking at the PILS reference frame (Figure 6.7 and Table 6.3, 6.4), we can define the Stokes parameters as:

$I \equiv$ Intensity of the linearly polarized radiation beam along $\hat{n}_{Z_{PILS}}$ plus

intensity of linearly polarized radiation along $\hat{n}_{Y_{PILS}}$:

$$I_{\hat{n}_{Z_{PILS}}} + I_{\hat{n}_{Y_{PILS}}}$$

$Q \equiv$ Intensity of linearly polarized radiation along $\hat{n}_{Z_{PILS}}$ minus intensity

of linearly polarized radiation along $\hat{n}_{Y_{PILS}}$:

$$I_{\hat{n}_{Z_{PILS}}} - I_{\hat{n}_{Y_{PILS}}}$$

$U \equiv$ Intensity of linearly polarized radiation along $(\hat{n}_{Z_{PILS}} + \hat{n}_{-Y_{PILS}})/\sqrt{2}$

minus intensity of linearly polarized radiation along $(\hat{n}_{Y_{PILS}} + \hat{n}_{Z_{PILS}})/\sqrt{2}$:

$$I_{(\hat{n}_{Z_{PILS}}+\hat{n}_{-Y_{PILS}})/\sqrt{2}} - I_{(\hat{n}_{Y_{PILS}}+\hat{n}_{Z_{PILS}})/\sqrt{2}}$$

where $\hat{n}_{X_{PILS}}$, $\hat{n}_{Y_{PILS}}$, and $\hat{n}_{Z_{PILS}}$ are the unit vectors parallel to the x, y, and z-axis in the PILS reference frame. From the Stokes parameters it is possible to define the polarized brightness as shown in Eq. 2.18: $pB = \sqrt{Q^2 + U^2}$.

TABLE 6.3: Pre-polariser position during data acquisition and the cor-
respondent angles in the PILS and URF reference frames (Figure 6.7).
In the last column, the associated theoretical Stokes vector. In this
respect, it is necessary to analyse the pre-polariser fast axis position
with respect to the polarimeter analyser, the PILS z-axis.

Pre-Pol rotation angle [$\theta_{LP} = 0$ when LP axis $//~z_{URF}$] (wrt URF)	xdeg [Pre-Pol angle] (wrt PILS)	Theoretical Stokes Vector (wrt PILS)
0°	-45°	$\begin{pmatrix} 1 & 0 & -1 \end{pmatrix}$
45°	0°	$\begin{pmatrix} 1 & 1 & 0 \end{pmatrix}$
90°	45°	$\begin{pmatrix} 1 & 0 & 1 \end{pmatrix}$
135°	90°	$\begin{pmatrix} 1 & -1 & 0 \end{pmatrix}$

TABLE 6.4: Stokes parameters in the PILS reference frame (Figure 6.7).

	45°	90°	-45°	0°
$\rho_i = \delta_i/2$				
$S = \begin{pmatrix} 1 & \cos\delta_i & \sin\delta_i \end{pmatrix}$	$\begin{pmatrix} 1 & 0 & 1 \end{pmatrix}$	$\begin{pmatrix} 1 & -1 & 0 \end{pmatrix}$	$\begin{pmatrix} 1 & 0 & -1 \end{pmatrix}$	$\begin{pmatrix} 1 & 1 & 0 \end{pmatrix}$
$I \equiv I_{\hat{n}_z} + I_{\hat{n}_y}$	1/2 + 1/2 = **1**	0 + 1 = **1**	1/2 + 1/2 = **1**	1 + 0 = **1**
$Q \equiv I_{\hat{n}_z} - I_{\hat{n}_y}$	1/2 - 1/2 = **0**	0 - 1 = **-1**	1/2 - 1/2 = **0**	1 - 0 = **1**
$U \equiv I_{(\hat{n}_z+\hat{n}_{-y})/\sqrt{2}}$ $+I_{(\hat{n}_y+\hat{n}_z)/\sqrt{2}}$	1 - 0 = **1**	1/2 - 1/2 = **0**	0 - 1 = **-1**	1/2 - 1/2 = **0**

6.2.2 On-ground calibration

Being the Thesis work not specifically dedicated to the on-ground calibration, it can be useful an introduction for a fully understand the in-flight validation. If necessary, more information about on-ground calibration can be found in Fineschi et al., 2020 and Casti et al., 2019.

Demodulation tensor

Part of the Metis on-ground calibration aims at characterising the polarimetric response in visible light. This goal is achieved by retrieving the Metis polarimeter demodulation tensor $\mathbf{X}^\dagger$ (obtained by computing and inverting the modulation matrix $\mathbf{X}$ associated with each pixel of the acquired polarimetric images). This tensor will allow us to polarimetrically characterise the incoming light from the intensity. In particular, as described in detail in Chapter 2, a full polarimetric characterisation requires to find the Stokes vector $\mathbf{S} = (S_0, S_1, S_2, S_3) = (I, Q, U, V)$. Being the V Stokes parameter associated with circular polarisation, we are interested just in the first three Stokes parameters (for the study of the *linear* polarisation present in the solar corona due to the Thomson scattering - see Sec. 3.4). If we modulate the incoming light by varying the voltage applied to the LCVRs obtaining four images $\mathbf{m} = (m_1, m_2, m_3, m_4)$ at different retardance values, we can obtain the Stokes vector $\mathbf{S}$ of the incoming radiation by solving the linear system:

$$\mathbf{m} = \mathbf{XS} \quad \rightarrow \quad \mathbf{S} = \mathbf{X}^\dagger \mathbf{m} \tag{6.1}$$

To solve it, we need to know the demodulation matrix $\mathbf{X}^\dagger$. The modulation matrix $\mathbf{X}$ comes from the Müller matrix $\mathbf{M}_{POL}$ associated with Metis polarimeter. In particular, it is obtained as the product of the Müller matrices associated with the polarising elements inside the polarimeter (see Figure 6.7) as follow:

$$\mathbf{M}_{POL} = \mathbf{M}_{LP}(0) \; \mathbf{M}_{PMP}(-\frac{\pi}{4}, \delta) \; \mathbf{M}_{QW}(\frac{\pi}{2})$$

$$= \frac{1}{2} \begin{pmatrix} 1 & 1 & 0 & 0 \\ 1 & 1 & 0 & 0 \\ 0 & 0 & 0 & 0 \\ 0 & 0 & 0 & 0 \end{pmatrix} \begin{pmatrix} 1 & 0 & 0 & 0 \\ 0 & \cos\delta & 0 & -\sin\delta \\ 0 & 0 & 1 & 0 \\ 0 & \sin\delta & 0 & \cos\delta \end{pmatrix} \begin{pmatrix} 1 & 0 & 0 & 0 \\ 0 & 1 & 0 & 0 \\ 0 & 0 & 0 & 1 \\ 0 & 0 & -1 & 0 \end{pmatrix} \tag{6.2}$$

$$= \frac{1}{2} \begin{pmatrix} 1 & \cos\delta & \sin\delta & 0 \\ 1 & \cos\delta & \sin\delta & 0 \\ 0 & 0 & 0 & 0 \\ 0 & 0 & 0 & 0 \end{pmatrix}$$

where $\delta = 2\rho$ is the retardance. It is possible to see that the form obtained for Eq. 6.2 is equivalent to $\mathbf{M}_{POL} = \mathbf{M}_{LP}\mathbf{M}_{rot}(2\rho = \delta)$ where $\mathbf{M}_{rot}$ is the Müller matrix of a rotating element. More details and a step by step description of $\mathbf{M}_{POL}$ can be found in Casti et al., 2018.

The last column of the retrieved Müller matrix is composed of elements equal to zero; this proves that this configuration does not suffer from the possible presence of circularly polarised radiation. It is now possible to retrieve the Metis polarimeter modulation matrix. Each row of the Metis polarimeter modulation matrix corresponds to the first row of the Müller matrix, assuming a different retardance angle

and, consequently, a different applied voltage. Then, the theoretical modulation matrix is equal to:

$$\mathbf{X} = \frac{1}{2} \begin{pmatrix} 1 & \cos\delta_1 & \sin\delta_1 \\ 1 & \cos\delta_2 & \sin\delta_2 \\ 1 & \cos\delta_3 & \sin\delta_3 \\ 1 & \cos\delta_4 & \sin\delta_4 \end{pmatrix} = \frac{1}{2} \begin{pmatrix} 1 & 0 & 1 \\ 1 & -1 & 0 \\ 1 & 0 & -1 \\ 1 & 1 & 0 \end{pmatrix} \tag{6.3}$$

where the values of the quadruplet retardances, δ_i, $i = 1, 2, 3, 4$, of the LCVR in the polarimeter are $\delta_1 = 90°$, $\delta_2 = 180°$, $\delta_3 = 270°$, and $\delta_4 = 0°$. The theoretical demodulation matrix $\mathbf{X}^\dagger$ is obtained as the Moore-Penrose inverse (Eq. 5.7) of the theoretical modulation matrix $\mathbf{X}$. We obtain:

$$\mathbf{X}^\dagger = \frac{1}{2} \begin{pmatrix} 1 & 1 & 1 & 1 \\ 0 & -2 & 0 & 2 \\ 2 & 0 & -2 & 0 \end{pmatrix} \tag{6.4}$$

As expected, $X^\dagger X = I$ (where I is a 3×3 identity matrix). The theoretical Stokes parameters can be easily obtained just solving Eq. 6.1:

$$\begin{pmatrix} I \\ Q \\ U \end{pmatrix} = \frac{1}{2} \begin{pmatrix} 1 & 1 & 1 & 1 \\ 0 & -2 & 0 & 2 \\ 2 & 0 & -2 & 0 \end{pmatrix} \begin{pmatrix} m_1 \\ m_2 \\ m_3 \\ m_4 \end{pmatrix} = \mathbf{X}^\dagger \begin{pmatrix} m_1 \\ m_2 \\ m_3 \\ m_4 \end{pmatrix} \tag{6.5}$$

To derive the calibrated demodulation tensor associated with the Metis polarimeter, during the on-ground calibration we acquired data related to different well-known polarised light and we modulated them by applying different voltages to the LCVR cells (the considered pre-polariser position are reported in Table 6.3). For each pre-polariser position, the left side of Eq. 6.1 assumes the following expression:

$$\begin{pmatrix} \overline{m}_1^{xdeg} \\ \overline{m}_2^{xdeg} \\ \overline{m}_3^{xdeg} \\ \overline{m}_4^{xdeg} \end{pmatrix} = \mathbf{X} \begin{pmatrix} I^{xdeg} \\ Q^{xdeg} \\ U^{xdeg} \end{pmatrix} = \begin{pmatrix} x_{11} & x_{12} & x_{13} \\ x_{21} & x_{22} & x_{23} \\ x_{31} & x_{32} & x_{33} \\ x_{41} & x_{42} & x_{43} \end{pmatrix} \begin{pmatrix} I^{xdeg} \\ Q^{xdeg} \\ U^{xdeg} \end{pmatrix} \tag{6.6}$$

where xdeg = [-45°, 0°, 45°, 90°] is the angular position of the linear pre-polariser acceptance axis referred to as the PILS reference frame, and:

$$\overline{m}_i^{xdeg} = \frac{m_i^{xdeg}}{\frac{1}{2}\sum_{i=1}^4 m_i^{xdeg}} \tag{6.7}$$

where i is the applied voltage (corresponding to a polarimeter rotation). To solve the linear system in Eq. 6.6 we need at least 12 equations (we have 12 unknown: x_{ij} with $1 \le i, j \le 4$). The analysis is carried out by setting four different voltages (i.e., 16 $\overline{m}_i^{xdeg}$ because we acquire four measurements, $\overline{m}_i^{-45}$, $\overline{m}_i^0$, $\overline{m}_i^{45}$, $\overline{m}_i^{90}$ for $i = 1, 2, 3, 4$), to find the quadruplet related to the most efficient demodulation matrix. Finally, we obtain:

$$M = XS \tag{6.8}$$

whereas we set:

$$M = (\ \overline{m}_1^{-45}\ \ \overline{m}_2^{-45}\ \ \overline{m}_3^{-45}\ \ \overline{m}_4^{-45}\ \ \overline{m}_1^{0}\ \ \overline{m}_2^{0}\ \ \overline{m}_3^{0}\ \ \overline{m}_4^{0}$$

$$\overline{m}_1^{45}\ \ \overline{m}_2^{45}\ \ \overline{m}_3^{45}\ \ \overline{m}_4^{45}\ \ \overline{m}_1^{90}\ \ \overline{m}_2^{90}\ \ \overline{m}_3^{90}\ \ \overline{m}_4^{90}\ )^T$$

$$X = \begin{pmatrix}
I^{-45} & Q^{-45} & U^{-45} & 0 & 0 & 0 & 0 & 0 & 0 & 0 & 0 & 0 \\
0 & 0 & 0 & I^{-45} & Q^{-45} & U^{-45} & 0 & 0 & 0 & 0 & 0 & 0 \\
0 & 0 & 0 & 0 & 0 & 0 & I^{-45} & Q^{-45} & U^{-45} & 0 & 0 & 0 \\
0 & 0 & 0 & 0 & 0 & 0 & 0 & 0 & 0 & I^{-45} & Q^{-45} & U^{-45} \\
I^{0} & Q^{0} & U^{0} & 0 & 0 & 0 & 0 & 0 & 0 & 0 & 0 & 0 \\
0 & 0 & 0 & I^{0} & Q^{0} & U^{0} & 0 & 0 & 0 & 0 & 0 & 0 \\
0 & 0 & 0 & 0 & 0 & 0 & I^{0} & Q^{0} & U^{0} & 0 & 0 & 0 \\
0 & 0 & 0 & 0 & 0 & 0 & 0 & 0 & 0 & I^{0} & Q^{0} & U^{0} \\
I^{45} & Q^{45} & U^{45} & 0 & 0 & 0 & 0 & 0 & 0 & 0 & 0 & 0 \\
0 & 0 & 0 & I^{45} & Q^{45} & U^{45} & 0 & 0 & 0 & 0 & 0 & 0 \\
0 & 0 & 0 & 0 & 0 & 0 & I^{45} & Q^{45} & U^{45} & 0 & 0 & 0 \\
0 & 0 & 0 & 0 & 0 & 0 & 0 & 0 & 0 & I^{45} & Q^{45} & U^{45} \\
I^{90} & Q^{90} & U^{90} & 0 & 0 & 0 & 0 & 0 & 0 & 0 & 0 & 0 \\
0 & 0 & 0 & I^{90} & Q^{90} & U^{90} & 0 & 0 & 0 & 0 & 0 & 0 \\
0 & 0 & 0 & 0 & 0 & 0 & I^{90} & Q^{90} & U^{90} & 0 & 0 & 0 \\
0 & 0 & 0 & 0 & 0 & 0 & 0 & 0 & 0 & I^{90} & Q^{90} & U^{90}
\end{pmatrix}$$

$$S = (\ x_{11}\ \ x_{12}\ \ x_{13}\ \ x_{21}\ \ x_{22}\ \ x_{23}\ \ x_{31}\ \ x_{32}\ \ x_{33}\ \ x_{41}\ \ x_{42}\ \ x_{43}\ )^T$$

Considering the elements of the theoretical Stokes vectors associated with the linear pre-polariser position (Table 6.4 and 6.3) with respect to the PILS reference frame, we have that the X matrix can be written as:

$$X = \begin{pmatrix}
1 & 0 & -1 & 0 & 0 & 0 & 0 & 0 & 0 & 0 & 0 & 0 \\
0 & 0 & 0 & 1 & 0 & -1 & 0 & 0 & 0 & 0 & 0 & 0 \\
0 & 0 & 0 & 0 & 0 & 0 & 1 & 0 & -1 & 0 & 0 & 0 \\
0 & 0 & 0 & 0 & 0 & 0 & 0 & 0 & 0 & 1 & 0 & -1 \\
1 & 1 & 0 & 0 & 0 & 0 & 0 & 0 & 0 & 0 & 0 & 0 \\
0 & 0 & 0 & 1 & 1 & 0 & 0 & 0 & 0 & 0 & 0 & 0 \\
0 & 0 & 0 & 0 & 0 & 0 & 1 & 1 & 0 & 0 & 0 & 0 \\
0 & 0 & 0 & 0 & 0 & 0 & 0 & 0 & 0 & 1 & 1 & 0 \\
1 & 0 & 1 & 0 & 0 & 0 & 0 & 0 & 0 & 0 & 0 & 0 \\
0 & 0 & 0 & 1 & 0 & 1 & 0 & 0 & 0 & 0 & 0 & 0 \\
0 & 0 & 0 & 0 & 0 & 0 & 1 & 0 & 1 & 0 & 0 & 0 \\
0 & 0 & 0 & 0 & 0 & 0 & 0 & 0 & 0 & 1 & 0 & 1 \\
1 & -1 & 0 & 0 & 0 & 0 & 0 & 0 & 0 & 0 & 0 & 0 \\
0 & 0 & 0 & 1 & -1 & 0 & 0 & 0 & 0 & 0 & 0 & 0 \\
0 & 0 & 0 & 0 & 0 & 0 & 1 & -1 & 0 & 0 & 0 & 0 \\
0 & 0 & 0 & 0 & 0 & 0 & 0 & 0 & 0 & 1 & -1 & 0
\end{pmatrix}$$

To compute the modulation matrix, Eq. 6.8 (considering the **X** matrix just obtained) has been solved for each detector pixel. The modulation matrix results be equal to:

$$\mathbf{X} = \frac{1}{2} \begin{pmatrix} 1.00 & -0.14 & 0.99 \\ 1.00 & -0.98 & 0.19 \\ 1.00 & -0.06 & -1.00 \\ 1.00 & 1.00 & 0.06 \end{pmatrix} \pm \begin{pmatrix} 0.00 & 0.04 & 0.01 \\ 0.00 & 0.01 & 0.06 \\ 0.00 & 0.11 & 0.01 \\ 0.00 & 0.01 & 0.17 \end{pmatrix} \tag{6.9}$$

The associated demodulation matrix $\mathbf{X}^\dagger$, can then be obtained by inverting **X**, obtained computing Eq. 6.9 pseudo-inverse. The resulting $\mathbf{X}^\dagger$ is shown in Eq. 6.10:

$$\mathbf{X}^\dagger = \frac{1}{2} \begin{pmatrix} 1.09 & 0.88 & 0.91 & 1.12 \\ -0.01 & -1.88 & -0.25 & 2.14 \\ 1.85 & 0.21 & -2.14 & 0.08 \end{pmatrix} \pm \begin{pmatrix} 0.00 & 0.00 & 0.00 & 0.00 \\ 0.38 & 0.25 & 0.24 & 0.15 \\ 0.34 & 0.20 & 0.31 & 0.03 \end{pmatrix} \tag{6.10}$$

Finally, the error on the demodulation tensor was evaluated as shown in Lefebvre et al., 2000.

Vignetting function

Metis was thought of as an externally occulted coronagraph. The highly vignetted aperture of the externally occulter coronagraph at lower heliocentric height compensates in part the high dynamic range, making possible the observation of the corona at higher heights. To see the real corona profile we considered a vignetting function (VF) for the VL channel obtained from the average of four polarimetric flat field images at different polarisation angles. The on-ground measured VF is shown in Figure 6.9. The dimensionless vignetting function VF is given from on-ground calibration by:

$$VF = \frac{\frac{1}{2} \sum_{i=0}^{3} M_{0i} \varphi_i}{I_0 \cdot \langle G \rangle \cdot \langle \eta \rangle \cdot P_L \cdot A_T \cdot T_{exp}} \tag{6.11}$$

where φ_i are the polarimetric flat field images $[DN/pix]$, M_{ij} the demodulation tensor elements and I_0 $[\text{ph/s/sr/cm}^2]$ is the input radiance (obtained from the diode current measured during the on-ground calibration as shown in Eq. 6.12). The other parameters in Eq. 6.11 are: average gain $\langle G \rangle = 0.119$ $[\text{DN/e}^-]$, average efficiency $\langle \eta \rangle = 0.118 \pm 0.002$ $[\text{e}^-/\text{ph}]$ (inclusive of linear analyser 1/2 transmissivity and the average quantum efficiency), the VL detector plate scale $P_L = 2.5 \times 10^{-9}$ $[\text{sr/pix}]$, the entrance aperture area $A_T = 12.6$ $[\text{cm}^2]$ and the exposure time T_{exp} [s]. In particular, the input radiance I_0 is obtained as:

$$I_0 = \frac{C_d/R}{h\nu} \frac{1}{A_d FoV_d} \frac{1}{T_{filter}} \tag{6.12}$$

where are considered: diode current C_d [A], responsivity (@610 nm)R $[A/(J/s)]$, diode sensitive area A_d $[\text{cm}^2]$, filter transmissivity T_{filter} and the diode field of view FoV_d; obtained as (Ryer, 1998; Held, 2009):

$$FoV_d \text{ [sr]} = 2\pi \left[1 - \cos\left(\frac{\vartheta}{2}\right) \right] = 2\pi \left[1 - \cos\left(\arctan\frac{r_p}{D_p}\right) \right] \tag{6.13}$$
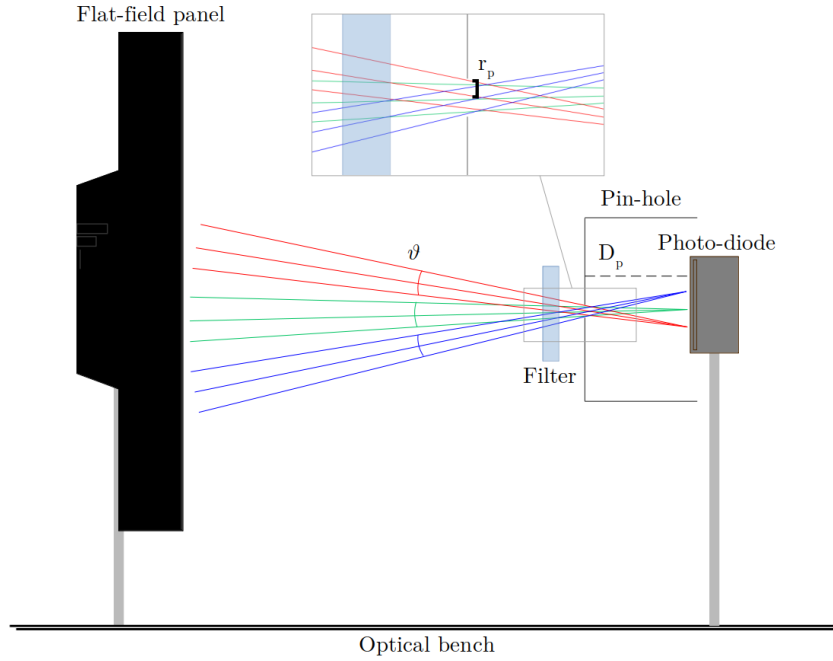
FIGURE 6.8: Schematic view of the set up with the photodiode and
the flat-field.

considering the distance D_p [cm] between the pin-hole and the photo-diode, and the
pin-hole radius r_p [cm] (Figure 6.8).

The final VF was obtained as an average of 4 VFs, each one, with a fixed volt-
age and a different pre-polariser orientation (the same procedure was performed
by keeping fixed the pre-polariser and changing the voltage of the LCVR to obtain
a comparable result). This VF was then obtained with the theoretical demodulation
tensor and the one obtained during on-ground calibration as well. Comparing them,
the difference was at the order of 1‰. In order to keep independent the VF and the
demodulation tensor, we choose to use the VF obtained using the theoretical $\mathbf{X}^\dagger$.

(A) Vignetting function   (B) Diagonal cut
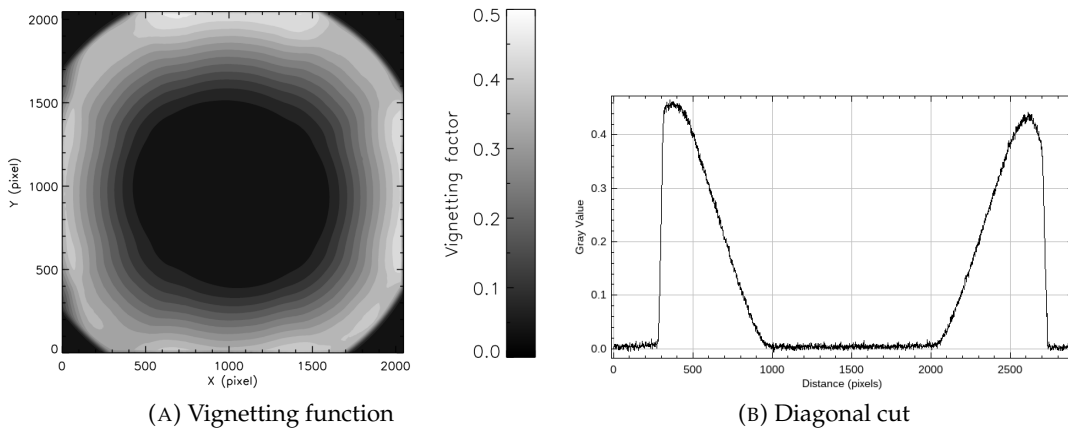
FIGURE 6.9: Metis vignetting function obtained during the on-
ground calibration (A) and its diagonal cut (B).

As we will see in the next Section, the VL vignetting function could be re-adapted
to the UV channel. Indeed, visible and UV light share the same optical path in the
telescope which is the only vignetting optical element.

6.3 Vignetting function recentring

During the Metis first light (March 13, 2020), the images were dominated by stray light. That was due to a misalignment of the IO. This required an adjustment of the position of the IO in order to obtain a correct occultation of the solar disc (Figure 6.11 - left). For this reason, the VF acquired during the on-ground calibration required a "shift" of the same quantity in the same direction in order to be applied to the in-flight images. To evaluate the shift, we considered the isophotes. Indeed, it is possible to fit the points of equal brightness, near the IO, using an ellipse (or a circumference). Repeating this process (*pre* and *post* launch) for different brightness thresholds it is possible to obtain the IO centre (as the average of the output of the fit) and the IO shift. For the in-flight data, we considered the June 08, 2020 data. With the same procedure, it is also possible to check on the field stop (FS) position. An example of this procedure is shown in Figure 6.10 (Liberatore et al., 2021b).
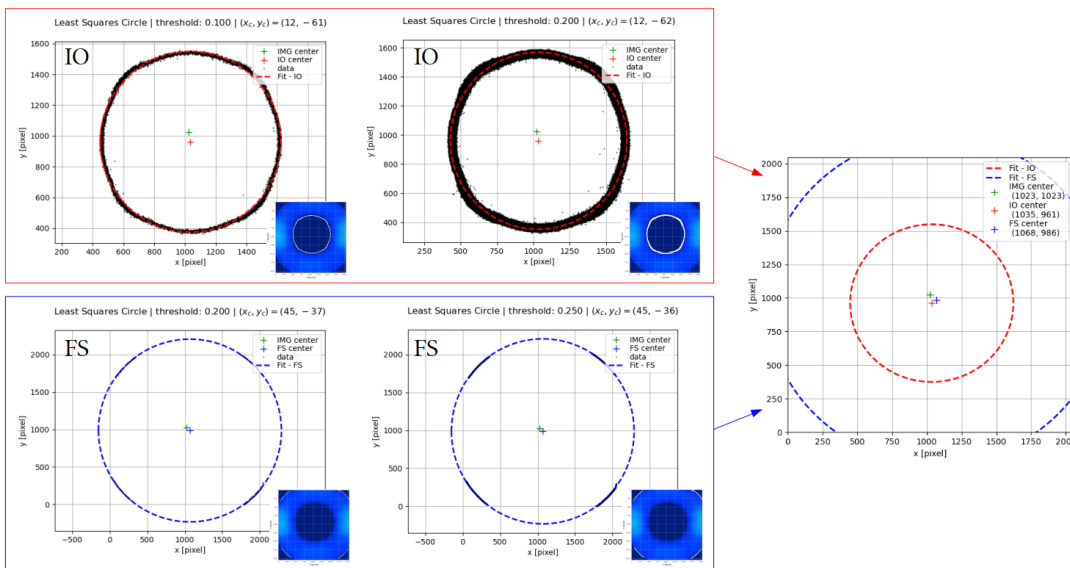
FIGURE 6.10: IO and FS centre evaluation respect to the image centre using isophotes with two different thresholds (actually, the real final centre -on the right- value is obtained by the average of 40 thresholds). In this particular example we considered the on-ground VL vignetting function but the same procedure was performed also for in-flight VL and UV images to evaluate the pre-/post- launch shifts.

The VF can be shifted so that the "on-ground IO" coincides with the flying position. The internal occulter shift did not change the field stop and spiders position. A net shift of the entire vignetting would have an over-/under- correction effect in the proximity to the external FoV. To avoid that, it was decided to stop for the amount of shifted vignetting function near the FS. This partial shift involves the creation of an "empty" area in which the data are missing; a "black belt" all around the frame (Figure 6.11 - right). The values in this "black belt" are extrapolated connecting the internal and external values of this "empty" area. In the first approximation, a linear function was considered for the data fitting (future adjustments can be performed by increasing the order of the fit). For each fit was considered data from angle ranges of 1° (future adjustments can be made by decreasing the angular step). Figure 6.12 shows an example of the linear fit extrapolation and the final VF.
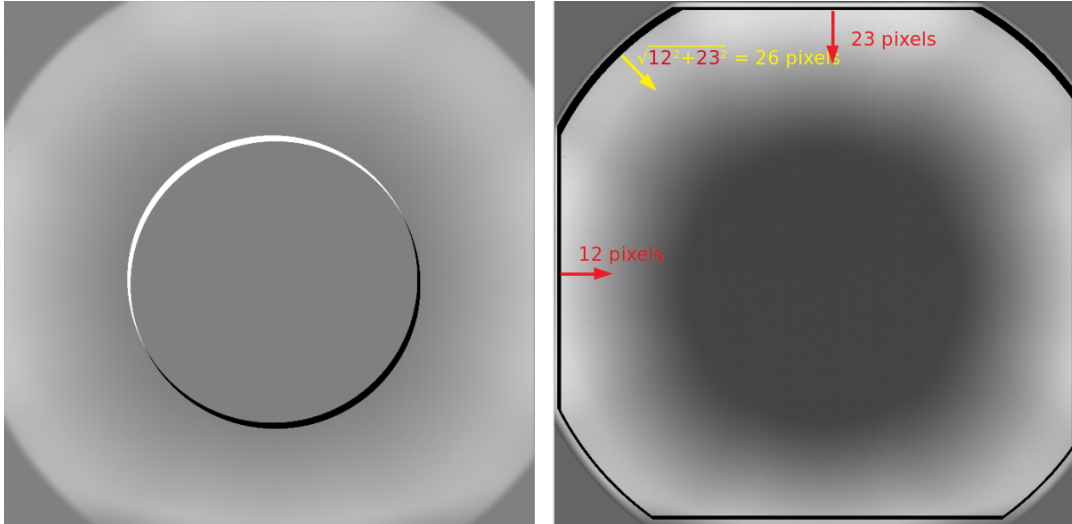
FIGURE 6.11: **Left:** IO centre shift between on-ground VF (white occulter) and a post adjustment in-flight VF (black occulter). This shift seems to be almost diagonal (along a spider). **Right:** VL vignetting function shifted of $d = 26$ pixels to obtain the pre-/post- launch IO centre recentring (obtaining the "black belt").
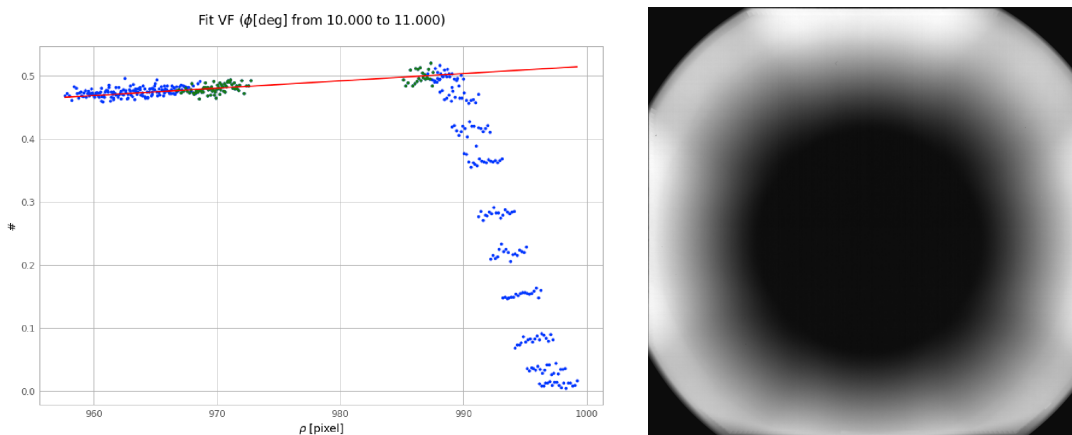

FIGURE 6.12: **Left:** An example of linear fit (for the angle range $11°-12°$; considering the $0°$ at three o'clock and moving clockwise). The blue dots are the vignetting function radial values in the considered angle range and the green ones are the points considered for the fit extrapolation (the red line). **Right:** VF after in-flight IO recentring.

The VL vignetting function can be used, under some considerations, for the ultraviolet images as well. In fact, considering the vignetting function obtained on-ground for the VL channel, the UV one can be obtained by centring the on-ground VL IO with the centre of the in-flight UV IO (both centres can be obtained using the isophotes). As shown before (Figure 6.10), the on-ground VL IO centre coordinates are: $(x, y) = (12 \pm 1, -62 \pm 1)$ with respect to the image centre (1023, 1023). However, in order to use the visible VF as the UV VF, a necessary pre-step is the 2×2 rebinning of the visible VF from a 2048×2048 frame to a 1024×1024 frame. After the rebinning, the centre of the on-ground visible IO is: $(x, y) = (7 \pm 1, -31 \pm 1)$ respect to the image centre (512, 512). With the same method used to evaluate the VL IO centre, it is possible to obtain the in-flight UV IO centre (Figure 6.13).
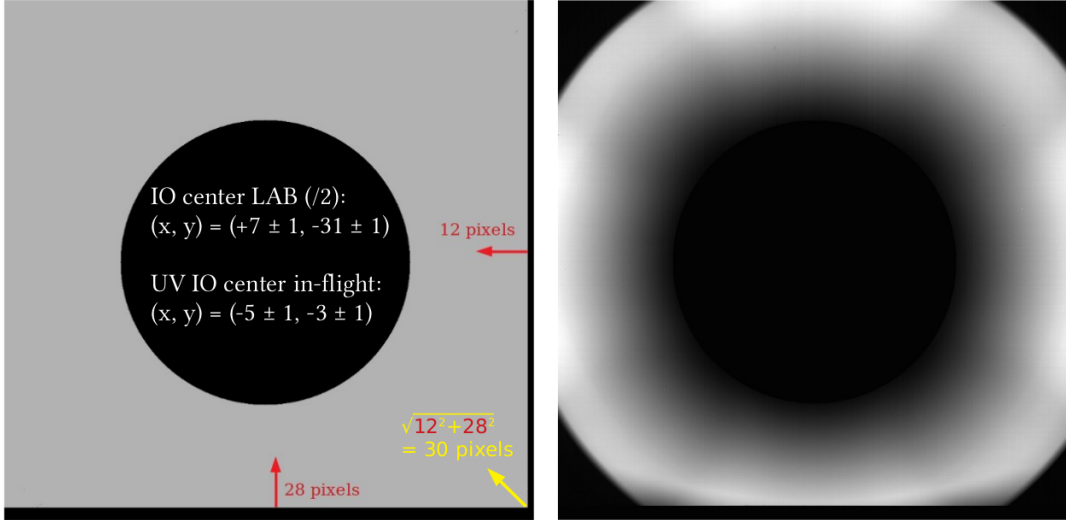
FIGURE 6.13: **Left:** VF for UV channel. It was obtained through the shift of VL vignetting function to recenter the UV and VL IO centres. The black pixels on side of the frame, are due to this shift (SW → NE direction). **Right:** VF for UV channel obtained after the VL vignetting function shift (Liberatore et al., 2021b).

Summarising the results, we have that the IO centre for on-ground VL image (1024×1024) at $(x, y) = (7 \pm 1, -31 \pm 1)$ and the IO centre for in-flight UV image (1024×1024) at $(x, y) = (-5 \pm 1, -3 \pm 1)$ both relative to the centre of the image. Then, shifting the on-ground VL vignetting function of 12 pixels (from +7 to -5) to the left (W → E) and 28 pixels (from -31 to -3) upward (S → N) we obtain the in-flight UV vignetting function.

6.4 Polarimeter in-flight validation

In this section, we are going to deal with the first in-flight validation of the Metis polarimeter carried out during the first data acquisitions.

6.4.1 LCVR retardances evaluation

As explained in Section 3.4, the K-corona results be linearly polarised with a polarisation vector tangent to the solar limb. These properties of the K-corona polarisation vector can be used to perform the in-flight validation of the LCVR retardances. The K-corona polarisation vector crossing the transmission axis of the polarimeter analyzer with an angle (polar angle α, Figure 6.14), results in an intensity modulation in each single i-th image of the set of 4 coronal images, acquired at different voltages of the polarimeter. This modulation is calculated from the recorded signal, m_i, for each sensor element $H(r, \alpha)$ detrended of the total intensity, $I^{(0)}$, and normalized by the $pB^{(0)}$ (Elmore et al., 2000):

$$\frac{2m_i - I^{(0)}}{pB^{(0)}} = -\cos[2(\alpha - \rho_i)] \tag{6.14}$$

where m_i are the in-flight data and the angles ρ_i are equivalent to effective polariser rotations equal to half the LCVR's retardances, $\rho = \delta/2$. The initial evaluations of

$I^{(0)}$ and $pB^{(0)}$ are carried out by using the ground calibrated effective polariser rotation angles, $\rho_i^{(0)} = \delta_i^{(0)}/2$. The in-flight retardance values, δ_i, are retrieved through the following 3-parameters (P0, P1, P2) regression:

$$y_i = P_0 - P_1 \cos\left[2(x - P_2)\right] \tag{6.15}$$

where $y_i = (2m_i - I)/pB$, x is the polar angle α, P_0 is the bias of fitting curve, and P_1 is the modulation amplitude. The P_2 parameter is defined as:

$$P_2 = \rho_i - 45° \tag{6.16}$$

where the shift of $-45°$ is introduced to align the PILS reference frame with the solar coordinate system (aligning the z_{PILS}-axis with the solar East-West direction; Figure 6.14).
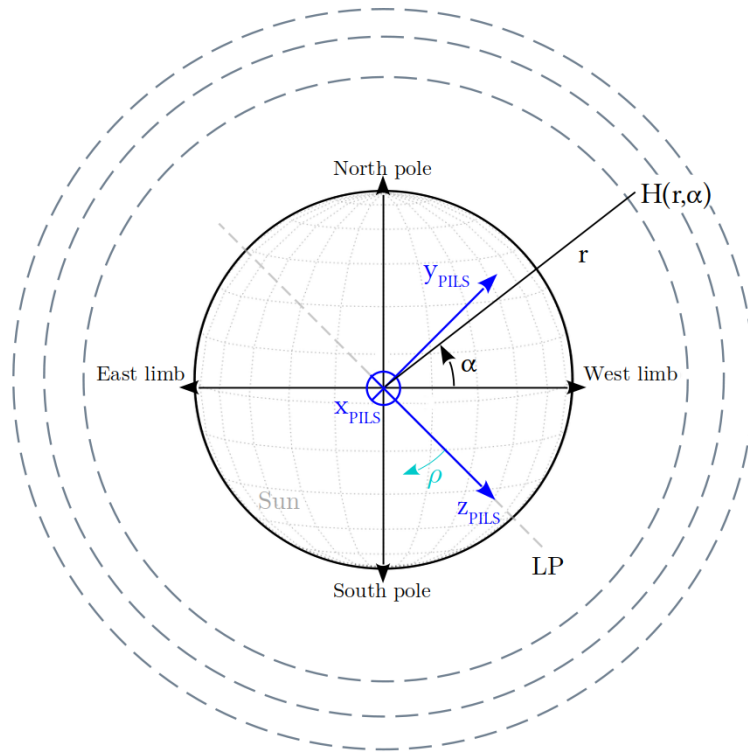
FIGURE 6.14: Positions on the sensors elements, $H(r, \alpha)$, for the LCVR retardances evaluation in Eq. 6.15. We considered different heliocentric distances, r, from 3.14 $R_\odot$ to 3.63 $R_\odot$ and different polar angles, α. The PILS reference frame position (blue) relative to the Sun comes from the *Metis Reference Frames* v37, F. Frassetto et al. (in particular, the z_{PILS} axis results to be at -45° from the West solar limb).

A regression is calculated for each y_i obtained from the respective image of the quadruplet m_i, for a fixed distance from the center of the Sun as obtained by astrometry (Figure 6.15). Since the error is proportional to $\approx 1/pB$, along the coronal streamers regions the error bars are much lower than elsewhere. The reduced χ^2 results are always between 0.3 and 0.6.

The P_2 parameters give the polarisation angles ϑ for different heliocentric heights. We considered 10 heliocentric distances from 3.14 $R_\odot$ to 3.63 $R_\odot$ from the Sun center (SC) in order to avoid noisy regions at the inner and outer edges of the field-of-view.
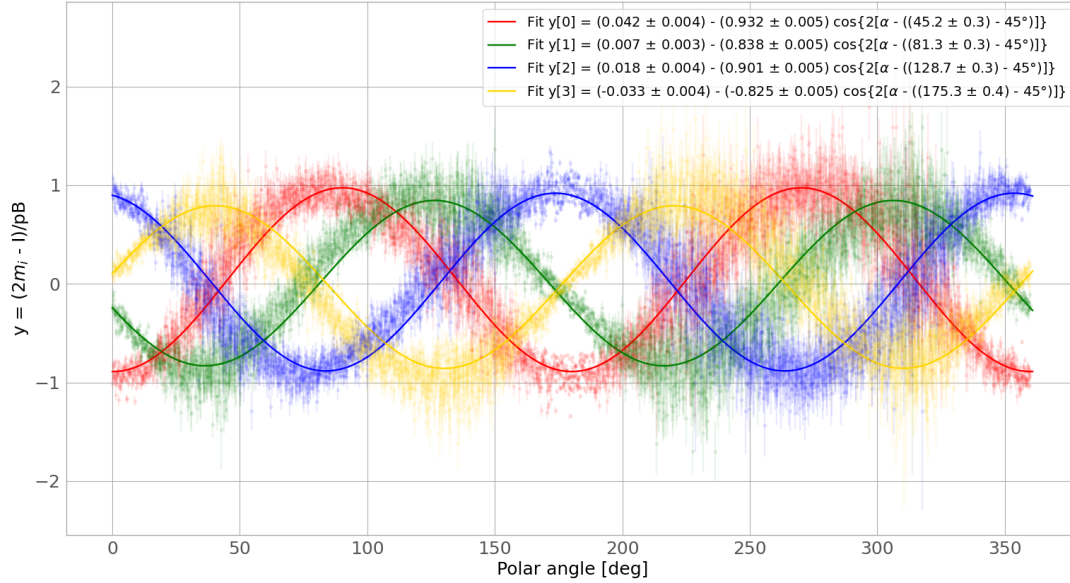
FIGURE 6.15: Intensity modulation in each *i*-th image of the polarisation set of 4 coronal images, expressed in Eq. 6.14, as a function of the polar angle α, shown in Figure 6.14. The LCVR retardances δ_i were derived from the regression in Eq. 6.15. The data come from a quadruplet acquired during the "roll n.0" of the IT-7 campaign (on June 08, 2020 - Figure 6.17) for a fixed heliocentric height.

The data come from a quadruplet ("roll n.0") acquired during the IT-7 campaign (on June 08, 2020 - Figure 6.17). The expected values from ground calibration for the nominal quadruplet polarisation, ρ_i, are: (49.1°, 84.3°, 133.2°, 181.1°) with a pixel-by-pixel, flat-field dispersion $\pm 5°$ each (Q4 in Table 6.5). From the average of the values at different heliocentric heights we obtain the following ρ_i (the very low errors come from the large number of points considered for the regression):

$$\rho_1 = 45.0° \pm 0.1°; \qquad \rho_3 = 128.7° \pm 0.1°;$$
$$\rho_2 = 81.4° \pm 0.1°; \qquad \rho_4 = 175.4° \pm 0.1°. \tag{6.17}$$

Even if these values have a lower error than those obtained during the on ground calibration, it was decided to continue to use the latter ones because they were obtained through a pixel by pixel process (through the use of a demodulation tensor). On the other hand, the in-flight ones were evaluated only for some fixed heliocentric heights and polar angles. However, the great relevance of the obtained results is the consistency between the on-ground and the in-flight results. It may be useful to repeat this process in the future to check the status of the polarimeter over time.

6.4.2 Different voltage configurations

During the first remote sensing checkout window (RSCW1 - June 18th, 2020 - distance to the Sun: 0.52 AU), we acquired polarimetric sequences with different quadruplets of PMP voltages. A quadruplet consists of 4 images at 4 LVCR voltages (i.e., effective "polarisation angles") separated by $\approx 45°$ from each other. The ground calibration yielded the demodulation tensor associated with each of these quadruplets (in addition to the nominal one). The goal of these different acquisitions is to check the polarimeter's response for the other set of 4 voltage configurations. Table 6.5 summarises the calibrated quadruplets, with an effective angle error of $\approx 1°$.

TABLE 6.5: Retardances of the different LCVR quadruplets "Q" (Liberatore et al., 2021b).

Q	**Effective angle, ρ_i [°]** (difference between *input* and *output* polarisation directions)	**Applied voltage** [mV]
1	17.0°, 60.7°, 108.9°, 157.6°	30583, 13216, 8344, 6597
2	24.6°, 72.4°, 121.1°, 169.4°	25362, 11359, 7776, 6313
3	37.3°, 96.4°, 145.5°, 194.6°	19573, 9087, 6924, 5810
4 (nominal)	49.1°, 84.3°, 133.2°, 181.1°	15837, 10048, 7318, 6051

The demodulation tensor associated with each in-flight calibrated quadruplet returns the corresponding $pB^{(1)}$, which are refined values with respect to the initial $pB^{(0)}$ obtained from the ground-calibrated quadruplets (we have 5 pB because we performed two acquisitions with "quadruplet 2"). In the following, these refined values of polarised brightness will be indicated as $pB \equiv pB^{(1)}$, for short. Considering 4 different coronal regions (near the streamers -Region 1, 3- and near coronal holes -Region 2, 4-) and performing an average over the pixels inside these regions (Figure 6.16), we can compare their measured pB with different voltage configurations. The resulting pB should be the same for each configuration. Figure 6.16 shows that the differences between the pB returned by different quadruplets are $\leq 2\%$.
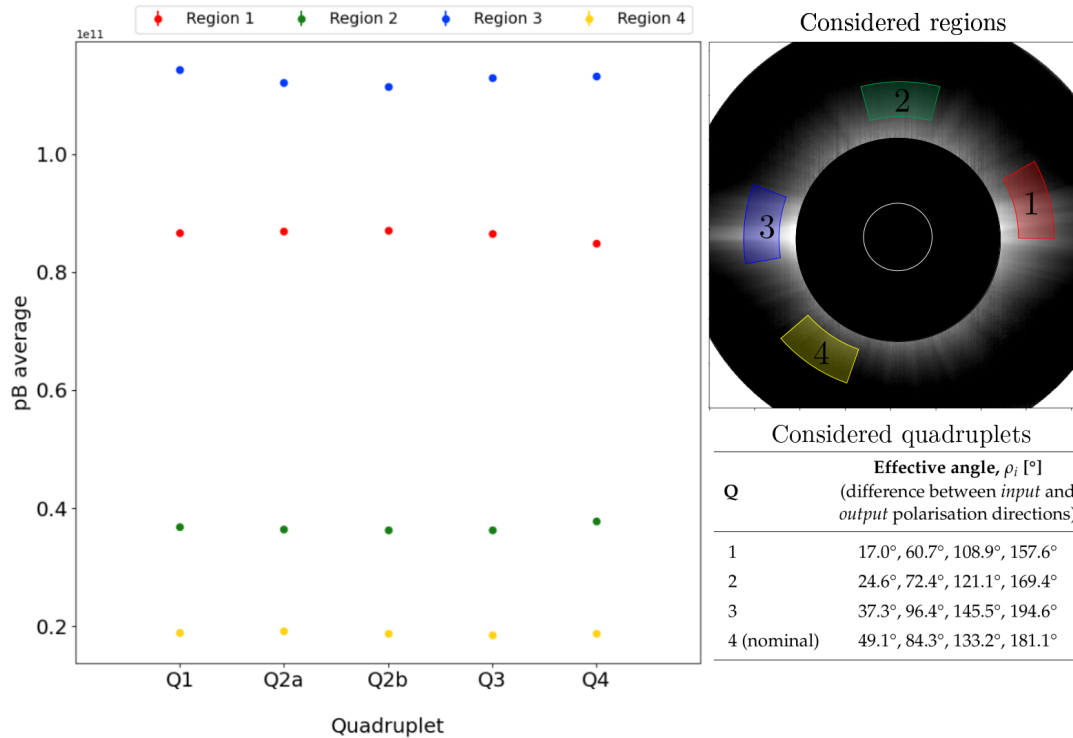
FIGURE 6.16: Comparison between the average of the four pB regions for the different quadruplets Q_i. The differences between the different pB are less than 2%.

6.4.3 Validation during spacecraft roll

We acquired different image sets during a complete roll performed by the spacecraft on June 8th, 2020 (IT-7 campaign; S/C - Sun distance: 0.52 AU). During the roll maneuver, the Metis polarimeter acquired a total of 8 K-corona pB images (one for each roll position - Figure 6.17). The comparison among these images gives indications of the differences in the polarimetric response at different positions across the polarimeter and the detector.
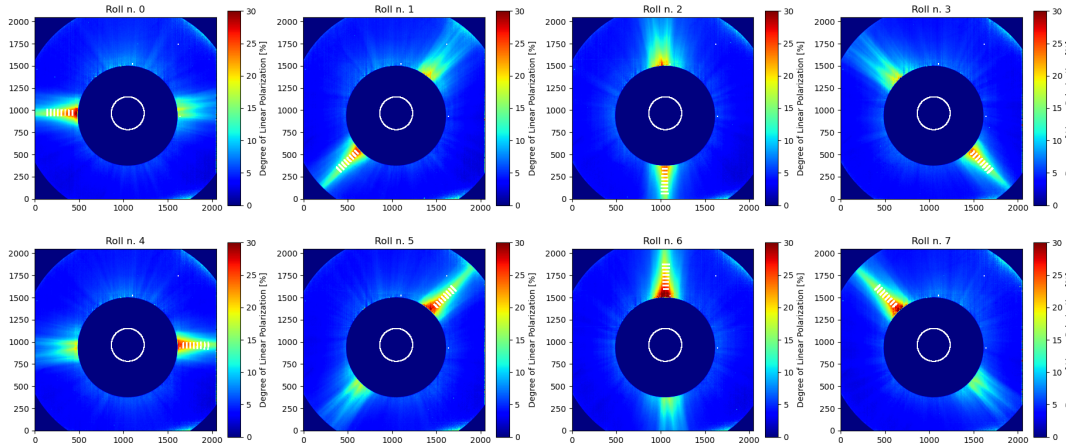
FIGURE 6.17: Degree of linear polarisation (pB/I) of the K-corona for the eight different S/C roll positions and considered region (white rectangles) to evaluate the polarimetric flat field goodness. The white circle inside the internal occulter show the Sun size and position.

The Degree of Linear Polarisation is derived from the ratio between pB and the first Stokes parameter I. Figure 6.17 shows the pB/I images for different spacecraft roll positions. For a few selected coronal regions on the frame (for example along a streamer), at different heliocentric distances (the Sun's center position behind the internal occulter is derived from astrometry measurements), the pB/I is plotted as a function of roll angle.

Check on the LCVR retardances during S/C roll

We made use of the spacecraft rolls to repeat (as an ulterior check) the same type of analysis performed in Subsec. 6.4.1. For a given region in the solar corona, the spacecraft roll acts as a "rotating polariser". Therefore, the recorded intensity of a selected region follows Malus's law (cfr., Figure 6.18). The fitting parameters of this function give an estimation of the LCVR retardances that can be compared with those measured in-flight and during ground calibrations. The estimated retardances values during the roll maneuvers are:

$$\rho_1 = 46° \pm 4°; \qquad \rho_3 = 130° \pm 5°;$$
$$\rho_2 = 82° \pm 4°; \qquad \rho_4 = 176° \pm 5°. \tag{6.18}$$

These values are consistent with both the (previously measured) in-flight and on-ground ones (Table 6.6).
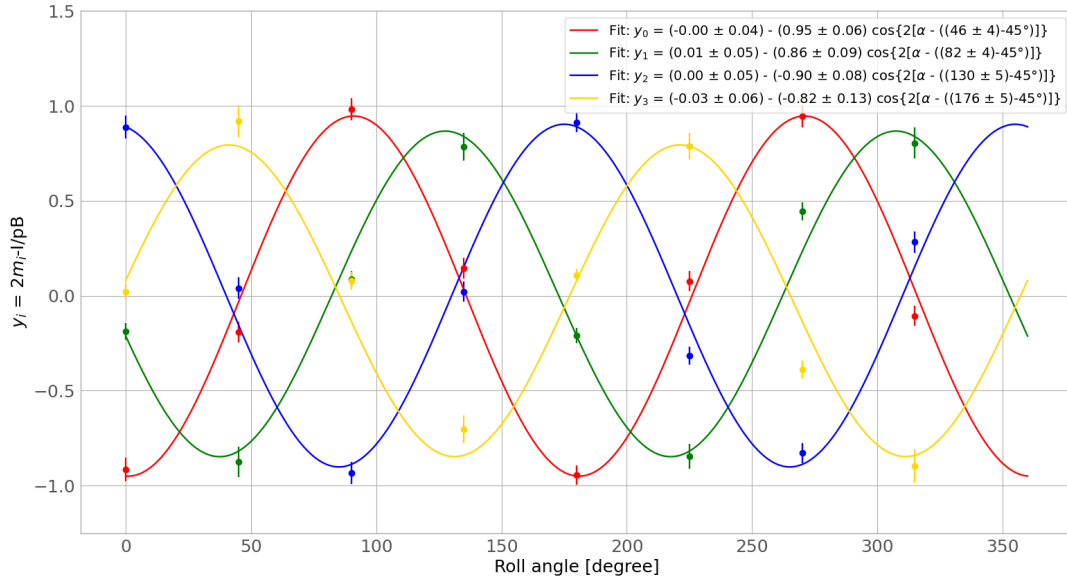
FIGURE 6.18: Malus curves obtained from Eq. 6.15 average values over the pixels in a fixed solar corona region during each roll. The roll angle start from the West solar limb as shown in Figure 6.14.

TABLE 6.6: Comparison between the LCVR polarisation angles from on-ground calibrations and in-flight validation.

On-ground	**In-flight** (Figure 6.15)	**In-flight** (Figure 6.18)
$49° \pm 5°$	$45.0° \pm 0.1°$	$46° \pm 4°$
$84° \pm 5°$	$81.4° \pm 0.1°$	$82° \pm 4°$
$133° \pm 5°$	$128.7° \pm 0.1°$	$130° \pm 5°$
$181° \pm 5°$	$175.4° \pm 0.1°$	$176° \pm 5°$

Polarised flat field verification

We verified in flight the polarised flat field by considering the pB of coronal structures measured as they moved to different locations across the detector, during roll maneuvers of the Solar Orbiter spacecraft as shown in Figure 6.17.

Figure 6.19 shows, as a function of roll angle, the pB/I derived from the demodulation tensor, $X^\dagger$, measured during the on-ground calibrations. The quality of the polarisation flat-fielding obtained by applying the on-ground calibrated demodulation tensor is indicated by the constant pB/I values (i.e., $< 5\%$; except for the heliocentric height 3.39 $R_\odot$, with percentage variation $\approx 12\%$), for different roll angles, at the same heliocentric height. The pB/I decreases for increasing heliocentric distances: from (0.24 ± 0.01) at 3.39 $R_\odot$ to (0.14 ± 0.01) at 4.91 $R_\odot$.

As a comparison, Figure 6.20 shows, as a function of roll angle, the pB/I derived from the theoretical demodulation tensor $X^\dagger$ given by Eq. 6.4. The dispersion of the pB/I mean values using the theoretical $X^\dagger$ is from a factor of two to three higher than those using the demodulation tensor from the on-ground calibration. Table 6.7 summarises the pB/I values for the two cases.
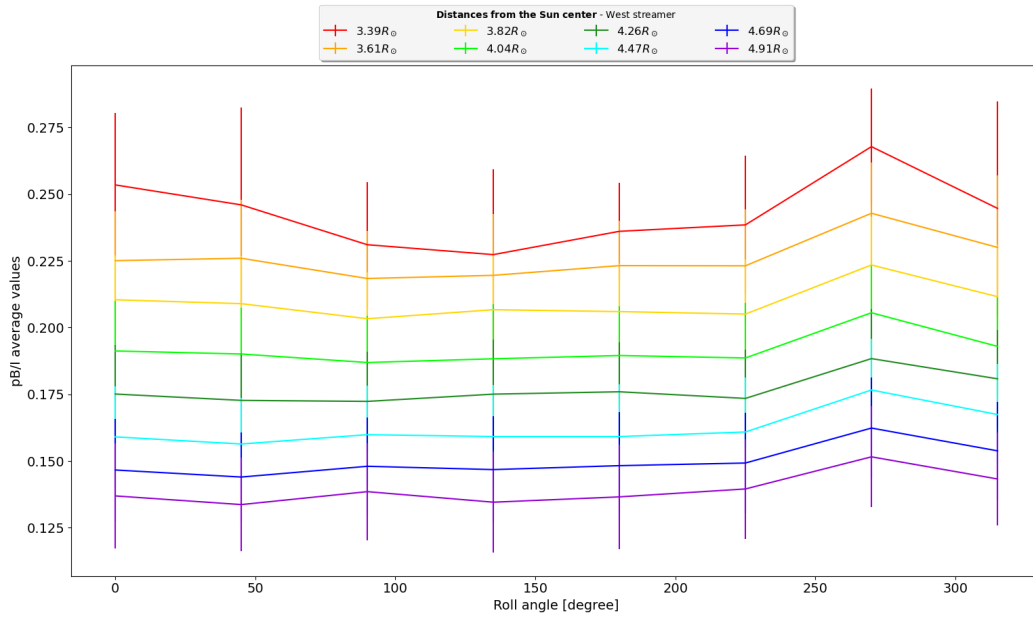
FIGURE 6.19: pB/I average over the pixels inside the selected regions
(for each roll) by using the calibrated demodulation tensor. The bars
represent the intensity dispersion inside the considered area.
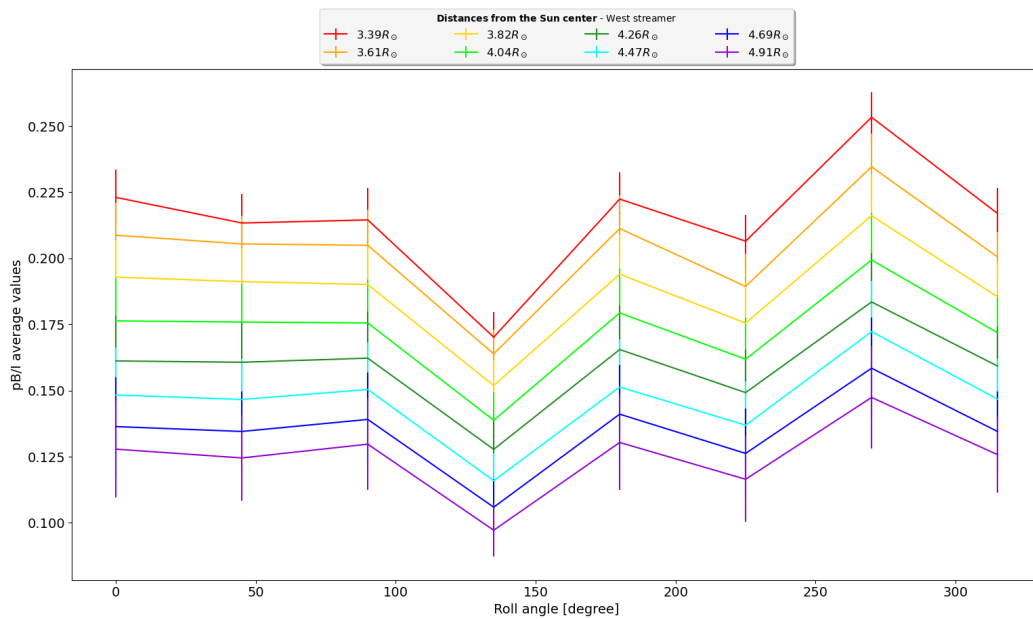
FIGURE 6.20: pB/I average over the pixels inside the selected regions
(for each roll) by using the theoretical demodulation tensor. The bars
represent the dispersion inside the considered area.

Data reduction with the theoretical $X^{\dagger}$ would return the signal state of polarisation, pB/I, with an accuracy of only about 10% (best case). This would be the dominant uncertainty considering that the one due to the dispersion of the pB/I is $\approx 2\%$, in the considered regions. On the other hand, with the experimental $X^{\dagger}$ from ground calibration, the uncertainty in deriving the pB/I values drops to $< 5\%$ (i.e., the experimental $X^{\dagger}$ returns polarisation measurements with an accuracy of $< 5\%$). This is comparable to the $\approx 3\%$ uncertainty of $\approx 1\% - 3\%$ due to the dispersion.

TABLE 6.7: pB/I average values with standard deviation. Dispersion column contains the standard deviation obtained considering the pB/I values in the region at fixed heliocentric distance for each roll.

	On ground $X^\dagger$ - Best		On ground $X^\dagger$ - Worst		Theoretical $X^\dagger$ - Best	
Roll	pB/I	σ	pB/I	σ	pB/I	σ
0	0.175	0.018	0.253	0.027	0.161	0.017
1	0.173	0.018	0.246	0.036	0.160	0.015
2	0.172	0.019	0.231	0.023	0.162	0.017
3	0.175	0.021	0.227	0.031	0.128	0.010
4	0.176	0.019	0.236	0.018	0.166	0.017
5	0.173	0.018	0.239	0.026	0.149	0.016
6	0.188	0.019	0.268	0.022	0.184	0.019
7	0.180	0.018	0.245	0.040	0.159	0.014
Avg.	0.177	0.019	0.243	0.028	0.159	0.016
StD.	0.005	0.001	0.013	0.008	0.016	0.002
StD/Avg	3%	1%	5%	3%	10%	2%

6.5   Polarised Brightness

After the in-flight IO adjustment, it was possible to obtain images not dominated by stray-light and test the new, recentred, vignetting function. A preliminary check of the in-flight validation is performed by comparing the pB as measured by Metis with what obtained by other instruments.

The pB is evaluated as shown in Eq. 2.18:

$$pB = \sqrt{Q^2 + U^2} \qquad (6.19)$$

The Q and U Stokes parameters come from the four images of the nominal quadruplet (which were subtracted for the dark, divided by the flat field, and corrected by the recentred VF). It is possible to compare the pB value along a radial distance as measured by Metis with the pB obtained, the same day, by other instruments. In particular, we compared the Metis, LASCO C2, LASCO-C3, and K-Cor pB of May 15th, 2020, because, at that time, Solar Orbiter was almost aligned with the Sun-Earth axis (Figure 6.21). The Metis pB (Figure 6.22) is consistent with what measured by the other instruments (Figure 6.23).
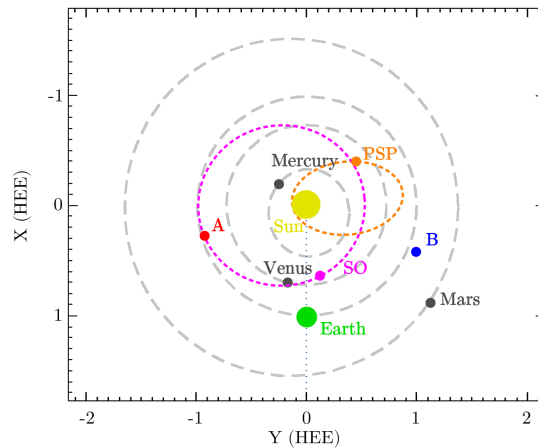
FIGURE 6.21: Position of Solar Orbiter (SO), STEREO-A (A) and Parker Solar Probe (PSP) with respect to Earth on 2020-05-15 (00:00 UT). From STEREO webpage.
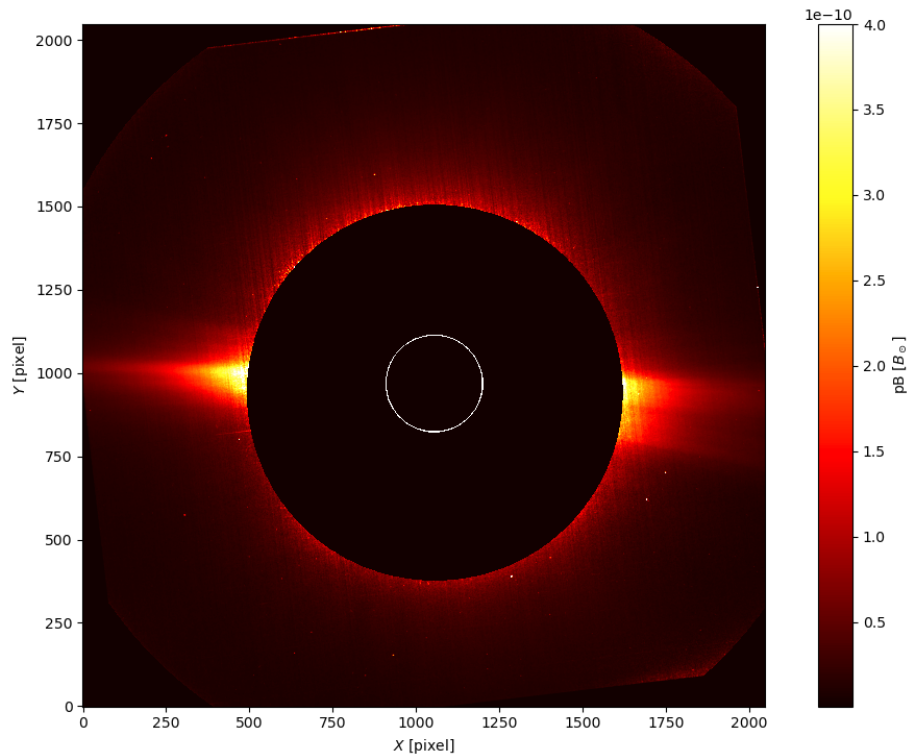
FIGURE 6.22: Image of a Metis polarised brightness in unit of solar brightness (2020-05-15; Sun-S/C distance: 0.64 AU). The white circle show the Sun position and dimension behind the occulter.

(A) East streamer
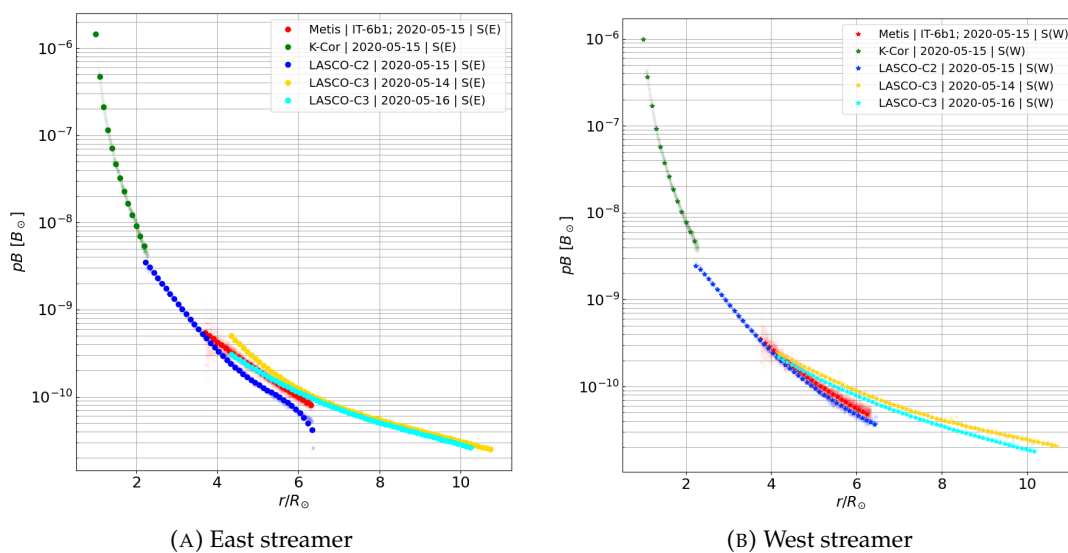
(B) West streamer

FIGURE 6.23: Comparison of pB values along the East and West streamer between Metis, LASCO C2/C3 and K-Cor during an almost Sun-S/C-Earth alignment (2020-05-15; Sun-S/C distance: 0.64 AU). (Liberatore et al., 2021b; Fineschi et al., 2021)

6.6   Electron Density

Thanks to the polarised brightness, it is possible to obtain the electron density (N_e) as described in Section 3.5. Thus, we can interpolate the pB radial profiles with Eq. 3.31:

$$pB\left(\frac{\rho}{R_\odot}\right) = c_0\left(\frac{\rho}{R_\odot}\right)^{-d_0} + c_1\left(\frac{\rho}{R_\odot}\right)^{-d_1} \tag{6.20}$$

It is possible to perform these interpolations on the entire round angle, with a tolerance of one degree. From the fit function we can obtain the c_0, c_1, d_0 and d_1 free parameters. Knowing these parameters it is possible to evaluate the a_i and b_i ones by considering Eq. 3.29 and Eq. 3.24 respectively. It is now possible to perform the N_e calculation through Eq. 3.30:

$$N_e(r) = \frac{\sum_i a_i \left(\frac{r}{R_\odot}\right)^{-b_i}}{[(1-u)A(r) + uB(r)]} \tag{6.21}$$

In particular, we set a limb-darkening coefficient $u = 0.63$ in the considered VL range. Figure 6.24 shows the electron density map as obtained by Metis and a comparison with other instrument as well (obtained with the same procedure, starting from the respective pB [$B_\odot$]). As expected, the electron density is higher in the equatorial regions (with the presence of streamers) than in the solar poles.
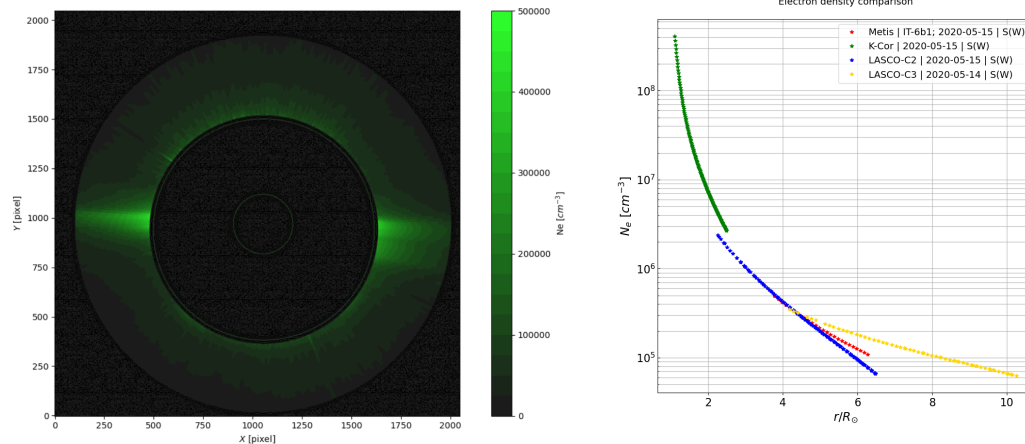
FIGURE 6.24: **(a) Left:** An example of Metis electron density map. **(b) Right:** Comparison of N_e values along the West streamer between Metis, LASCO and K-Cor instruments during an almost Sun-S/C-Earth alignment (data: 2020-05-15; Sun-S/C distance: 0.64 AU).

6.7   HI outflow velocity map

By comparing the Metis VL and UV images (Figure 6.25) we are able to use the Doppler dimming technique (Noci, Kohl, and Withbroe, 1987) to derive the radial outflow velocities of neutral hydrogen atoms in the solar corona (caused by the motion of the coronal plasma along the direction of incidence of the chromospheric photons on the coronal hydrogen atoms).
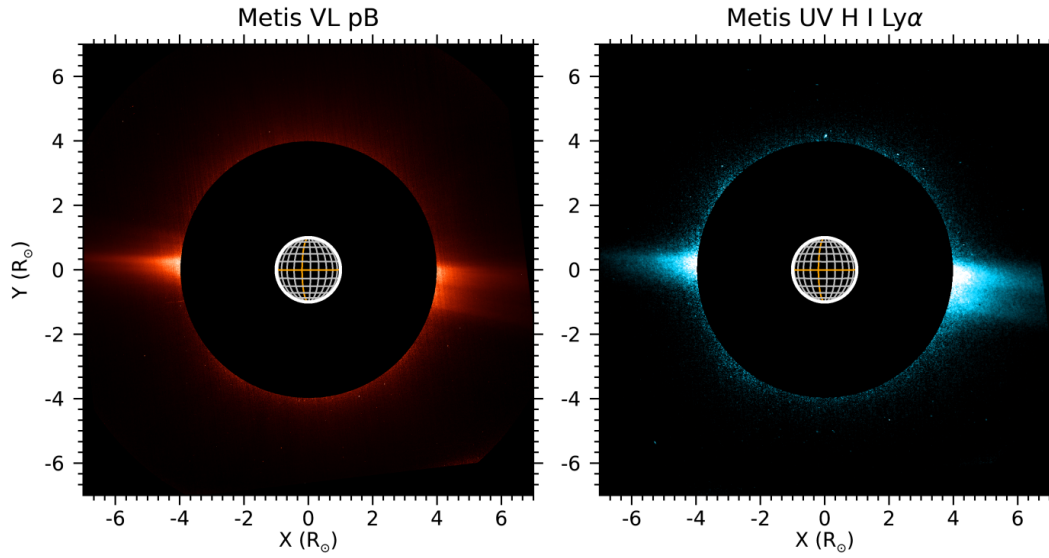
FIGURE 6.25: pB (580-640 nm) and UV (HI Ly-α) images acquired by
Metis on May 15, 2020 at 11:40 UT (Romoli et al., 2021).

In particular, the electron density (derived from the polarised brightness data
as shown in the previous Section) is a necessary ingredient to extrapolate the solar
wind velocity as shown in Romoli et al., 2021. Indeed, this diagnostic technique is
essentially based on the comparison of the HI Ly-α coronal emission, synthesized
based on the simultaneous electron density measurements derived from the polarized brightness data, with the UV emission observed with Metis, as described in
Antonucci et al., 2020. The obtained HI outflow velocity maps (derived by Romoli
et al., 2021) are shown[4] in Figure 6.26.
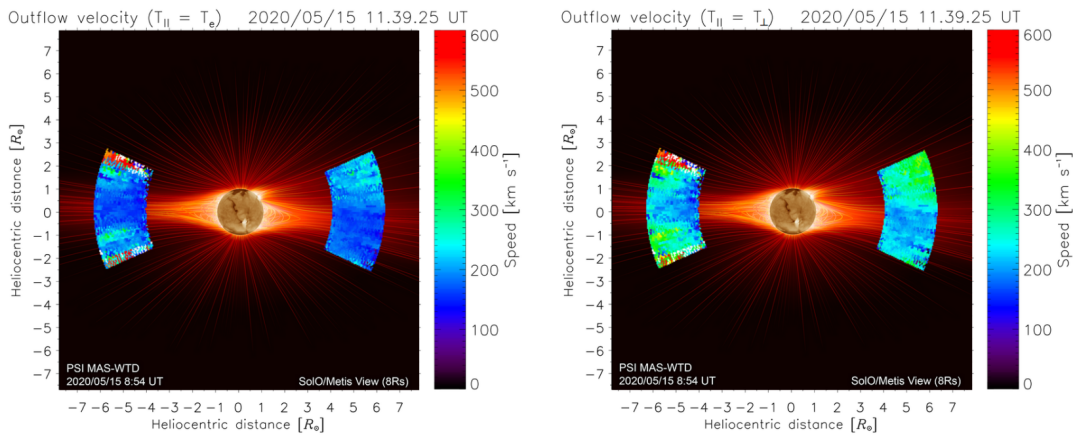
FIGURE 6.26: HI outflow velocity map for both the cases of isotropic
($T_{HI,\parallel} = T_{HI,\perp}$) and anisotropic ($T_{HI,\parallel} = T_e$) distribution of Hydrogen
kinetic temperature T_{HI} (Romoli et al., 2021). Images from the first
Metis observations obtained on May 15, 2020.

---

[4]The field lines in figure come from a magnetohydrodynamic model of the solar corona generated
by Predictive Science Incorporated (PSI).

As expected, the analysis shows the slowest components of the coronal wind have speed values that need further significant acceleration processes beyond 6 R$_\odot$ in order to reach its interplanetary value of $\approx$ 300 km/s measured at L1. Moreover, it is possible to notice an increase in velocity moving from equatorial latitudes to the poles, marking the transition between the slow and fast wind in the corona.

6.8   Eruptive prominences and CMEs

Prominences are large emitting plasma structures in the solar corona that are cooler and denser than the surrounding coronal material. When erupting, they are associated with CMEs. Many of these eruptive/dynamic events were observed during Metis observations. For example, Figure 6.27 shows how it was possible to perform the first coronal mass ejection observation in both visible-light and UV HI Ly$_\alpha$ channels (Andretta et al., 2021).
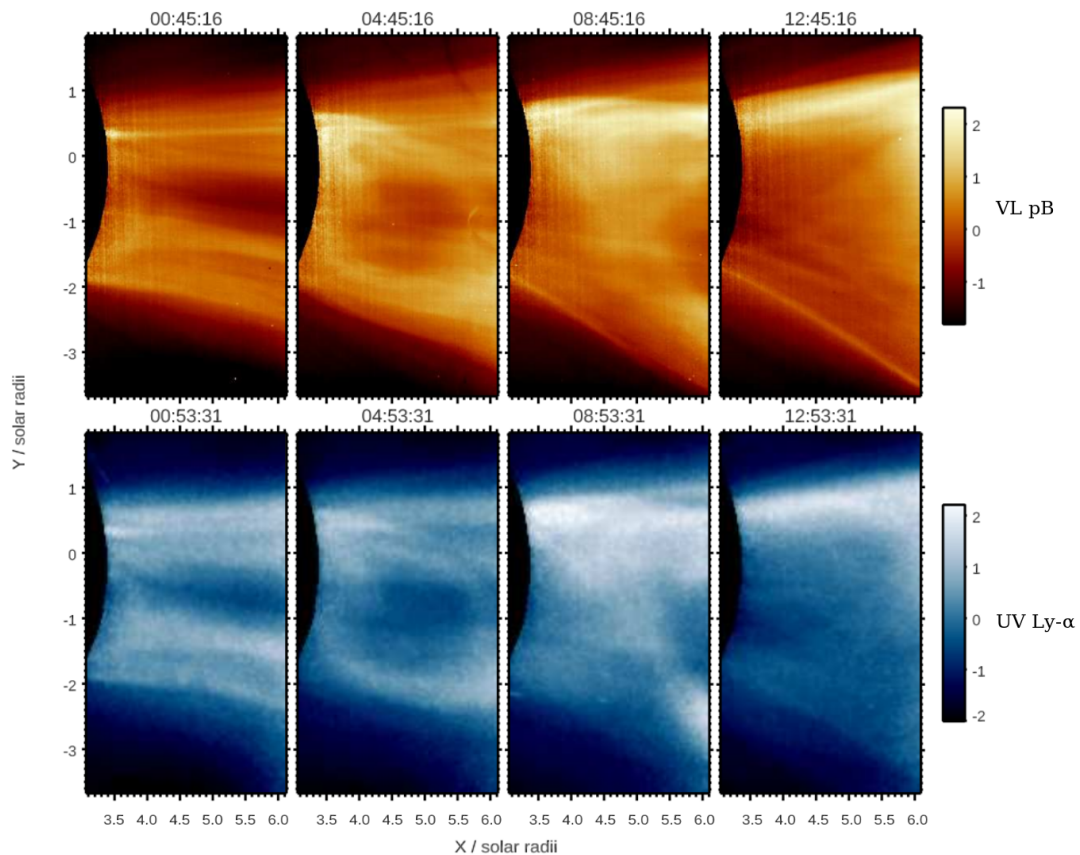
FIGURE 6.27: Development of the CME on January 16–17, 2021 as observed by Metis (Andretta et al., 2021). It this Figure both VL pB and UV Ly-α images are presented. The images are processed via the Normalizing Radial Graded Filter (NRGF) - the output is unit-less as produced by the algorithm (Morgan, Habbal, and Woo, 2006).

Another example is the large eruptive prominence on December 25, 2021 (Figure 6.29). Unfortunately, in that period Solar Orbiter was far away from the Sun and some instruments where not able to perform appropriate event observations.[5] Anyway, it was possible to conduct a multi-perspective space observation of this event (Sasso et al., 2022). Figure 6.28 shows the position of Solar Orbiter and other spacecraft during this event. The eruption was followed continuously[6] to higher heliocentric heights (i.e., same spacecraft, different instrument) and from different perspectives (i.e., different spacecrafts). In particular, different features of the eruption (e.g., prominence -PR- and leading edges -LE-) were tracked during their evolution looking at all the images acquired by different instruments.

FIGURE 6.28: Position of Solar Orbiter (SO), STEREO-A (A) and Parker Solar Probe (PSP) with respect to Earth on 2021-12-25 (00:00 UT). From STEREO webpage.

The height-time (HT) plot of all these features is shown in Figure 6.30. The LE was evaluated by Metis at a fixed polar angle (PA) equal to 75°. A focus on the HT plot on the evolution of the prominence alone is shown in Figure 6.31.
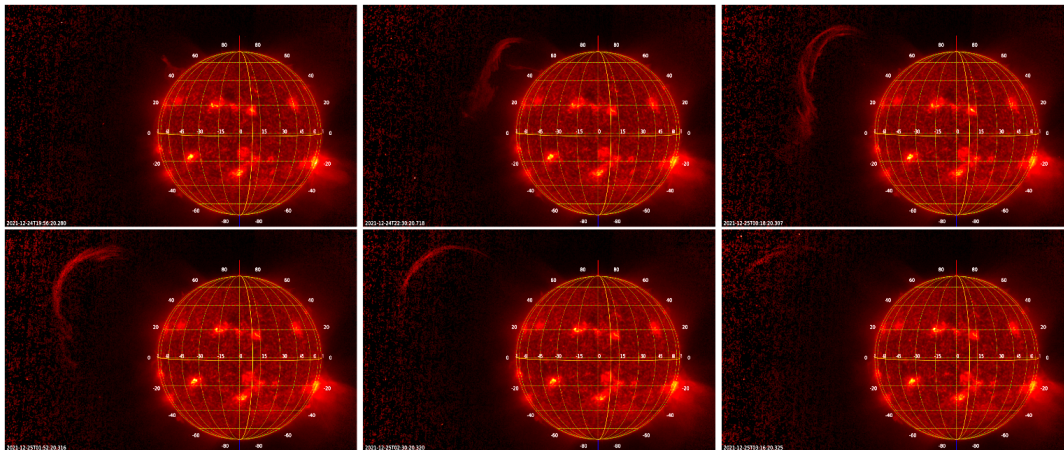
FIGURE 6.29: Large prominence eruption from December 24, 2021 (19:56 UT, upper-left panel) to December 24, 2021 (03:16 UT, lower-right panel) observed by FSI 304. This prominence was initially observed and tracked by FSI from the photosphere to heights of around 2.7 R$_\odot$ thanks to its large FoV ≈ 3.8° (Sasso et al., 2022).

---

[5]For example, being SoloHI designed as a wide FoV heliospheric imager, and considering that the probe position at that time was about 1.01 AU, it received a too low signal to perform an appropriate study of this event.

[6]Indeed, the FSI field of view is nearly contiguous with the Metis one (Rochus et al., 2020; Auchère et al., 2020; Antonucci et al., 2020).
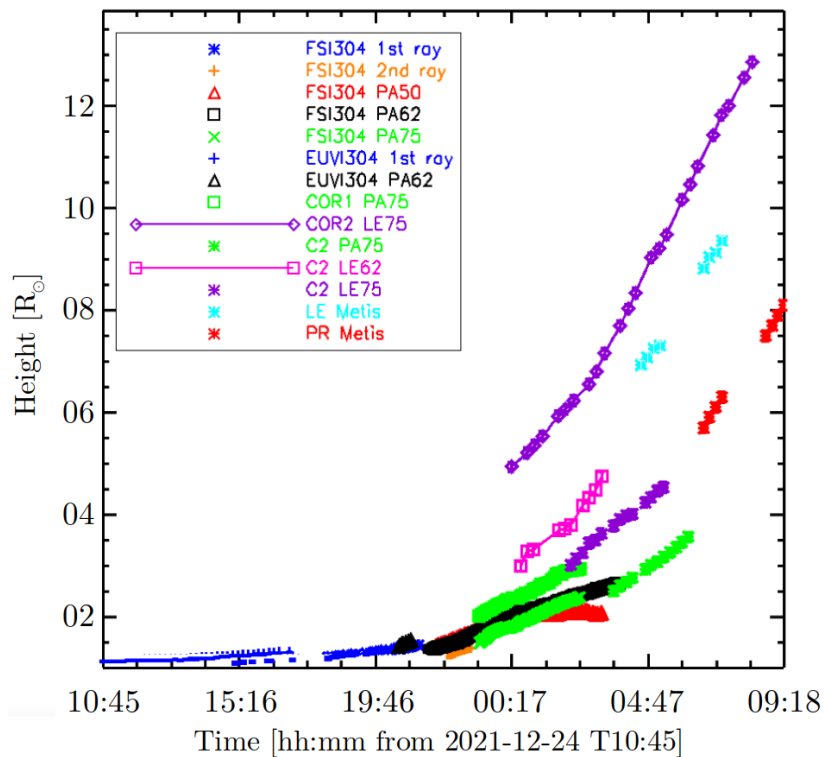
FIGURE 6.30: HT plot of different features of the eruptive event on 2021-12-25. In particular, in cyan and red are the values of the leading edge (LE) and prominence (PR) observed by Metis.
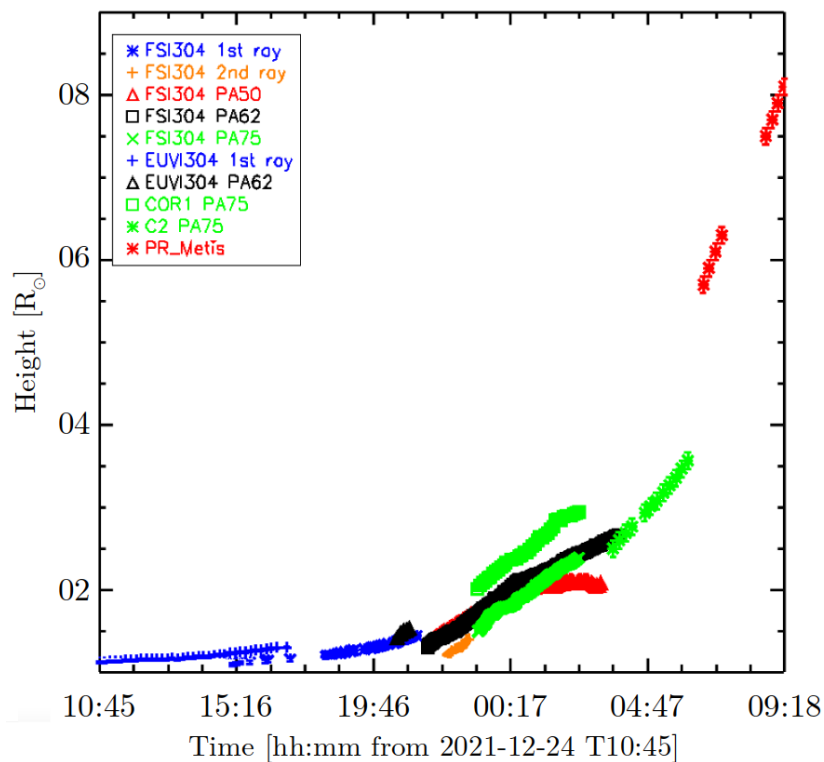

FIGURE 6.31: HT plot of the prominence (PR) observed by different instruments on 2021-12-25.

The evolution of an erupting prominence starts from a quasi-equilibrium state to the eruption. In general, there is an initial slow-rise above the solar limb (the *initiation phase*[7]), a subsequent fast-rise (the impulsive main *acceleration phase*[8]) and finally a *propagation phase* with only slowly varying or constant velocity (Zhang and Dere, 2006; Joshi and Srivastava, 2007; Liu and Su, 2021; Sasso et al., 2022).

As is it possible to see in Figure 6.30 and Figure 6.31, Metis observes the event during the propagation phase (the HT plot show an almost linear variation of heights in time). The Metis leading edge values in the HT plots are extrapolated from Metis images at a fixed polar angle (PA = 75°; the 0° is at the solar north and the angle moves counterclockwise). In particular, we considered base-differences of pB (i.e., to each pB image of the sequence we subtract the first one to highlight the differences between them).To avoid a manual evaluation of the leading edge, we evaluate the maximum of intensity along the radial for all the subsequent images (Figure 6.32) and we add a fixed constant to all the obtained maxima. Then we represent the obtained front for different polar angles to see if it was in aligned with what observed from the sequence of images (Figure 6.33). An analogous process was performed to evaluate the evolution of the prominence (Figure 6.33).
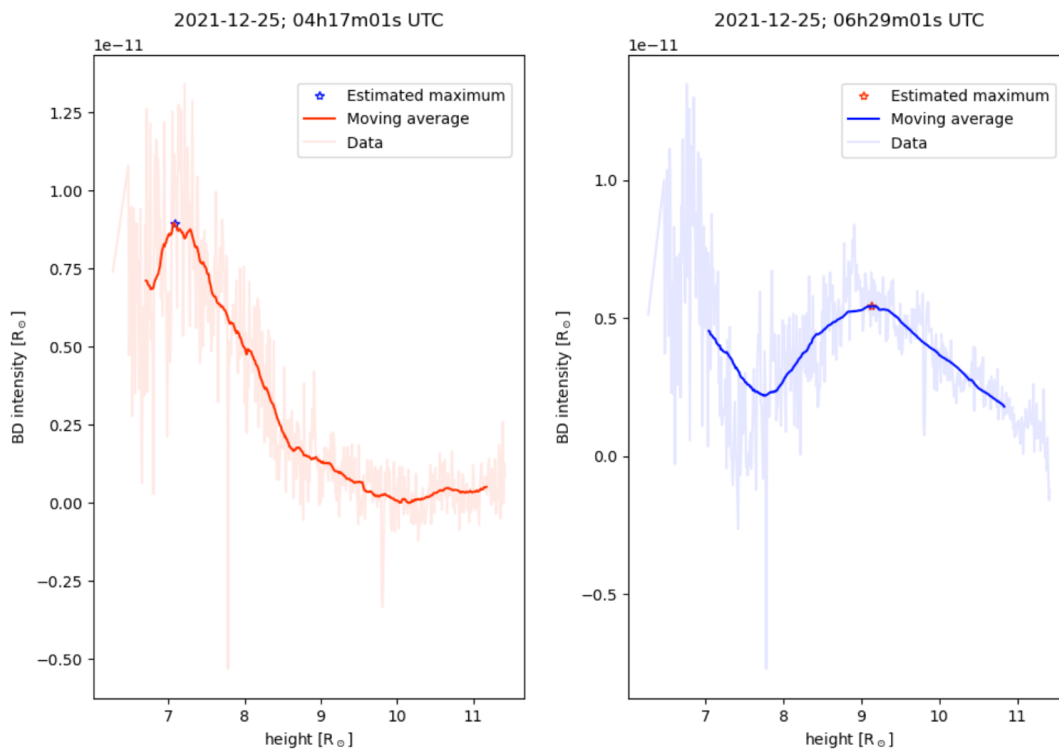
FIGURE 6.32: Examples of evaluation of the base-differences maximum for the leading edge evaluation process. As expected, there is a movement of the maximum in time. The first pick in the right-side image is due to the prominence.

---

[7]The several mechanisms involved in order to start off the initiation phase can be found in (Chen, 2011; Gibson, 2018; Patsourakos et al., 2020).

[8]It is usually assumed that the acceleration is triggered either by magnetic reconnection taking place at the site of the eruption (Zhang et al., 2001) or by an ideal MHD instability (Amari, Luciani, and Aly, 2004; Fan and Gibson, 2007).
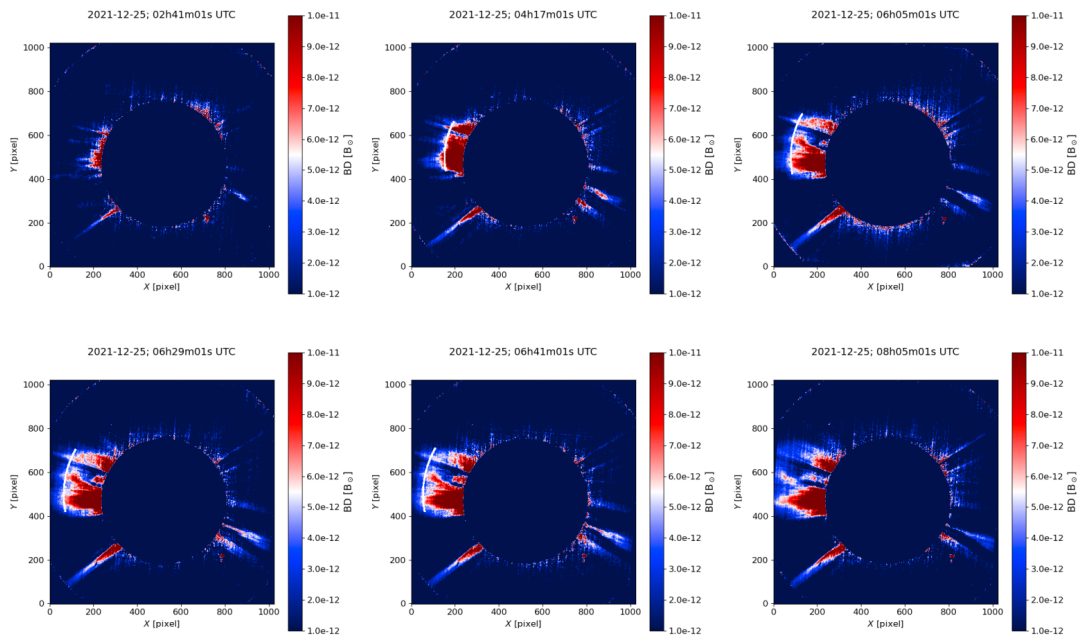
FIGURE 6.33: Selection of some images showing the evolution of the leading edge. We set a diverging color-maps to highlight the differences in the image.
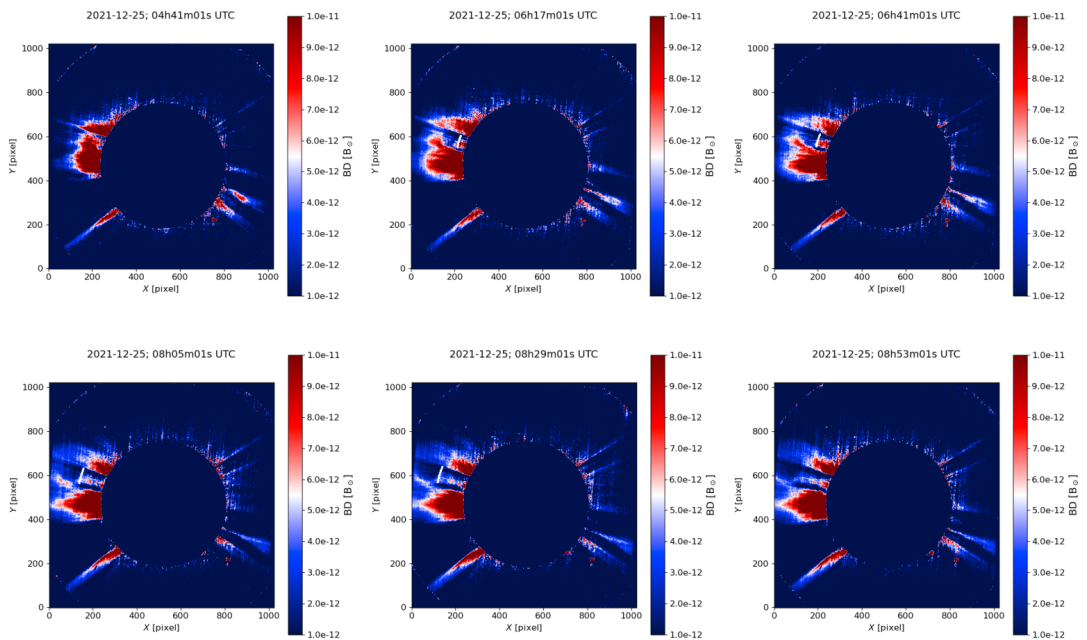

FIGURE 6.34: Selection of some images showing the evolution of the prominence. We set a diverging color-maps to highlight the differences in the image.

6.9 First Solar Orbiter perihelion

As shown in Figure 6.4, in late March 2022 Solar Orbiter has reached the closest point in its current orbit around the Sun. It was the first Solar Orbiter perihelion. The space-craft passes at a distance of about 0.32 A U ($\approx$ 77 million kilometres separated the probe from the Sun). It was possible to acquire several images during this close approach. A preliminary image processing is shown in Figure 6.35. It is possible to notice the high level of details reached by this images. In particular, some special filters (e.g., MGN filter - Figure 6.36) highlight the steady structures while other processes (e.g., difference of sequential images - Figure 6.37) highlight the dynamic ones. Figure 6.38 and Figure 6.39 show a focus on some regions of interest for the dynamic case. The complete view is shown in Figure 6.40. In particular, Figure 6.40 shows the composition of what observed by EUI-FSI and Metis. Figure 6.41 shows the composition with SoloHI as well. Looking at the coronal structures, it is possible to notice the correct alignment of Metis-FSI and Metis-FSI-SoloHI images. Many events were observed during these acquisitions but the data are still under analysis.
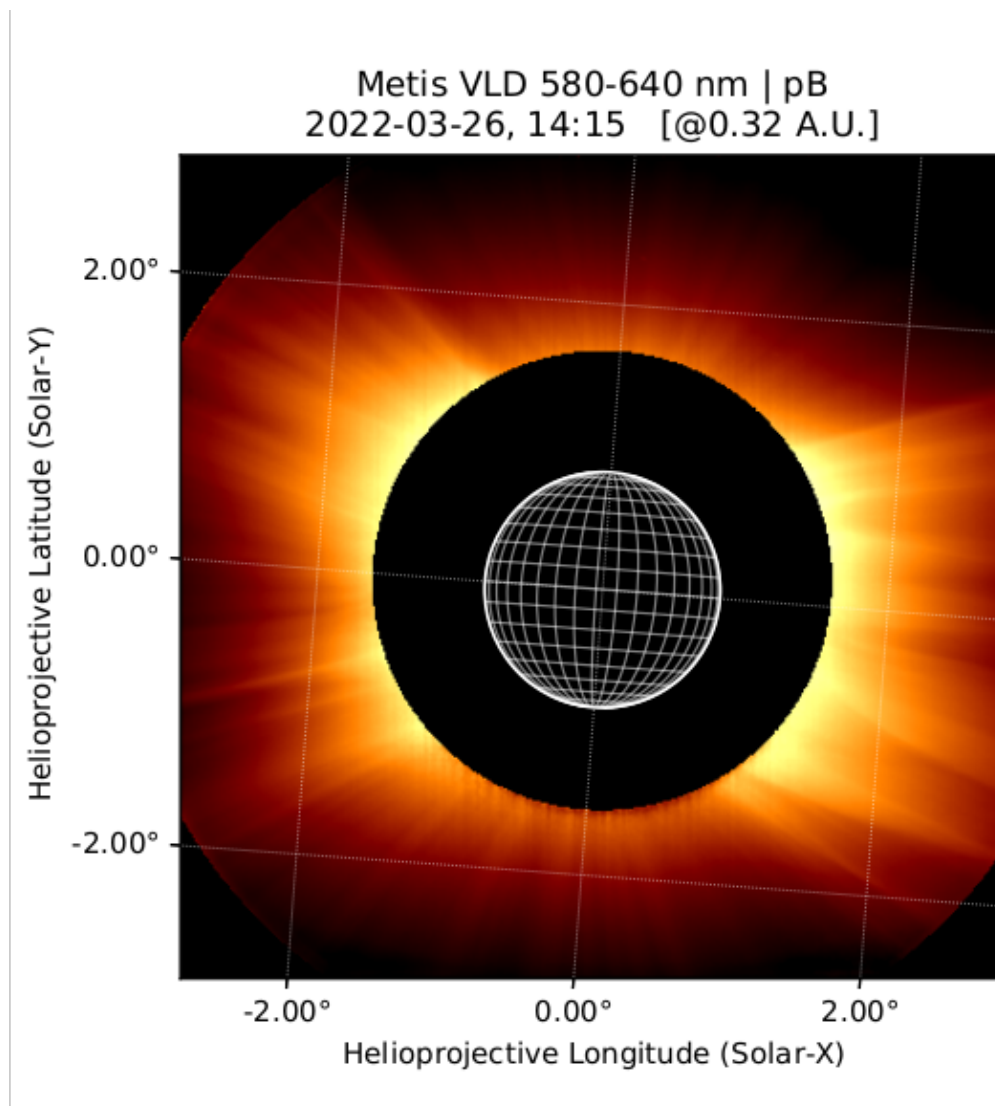
FIGURE 6.35: The solar corona at first perihelion as seen by Metis in visible polarized brightness (logarithmic scale).
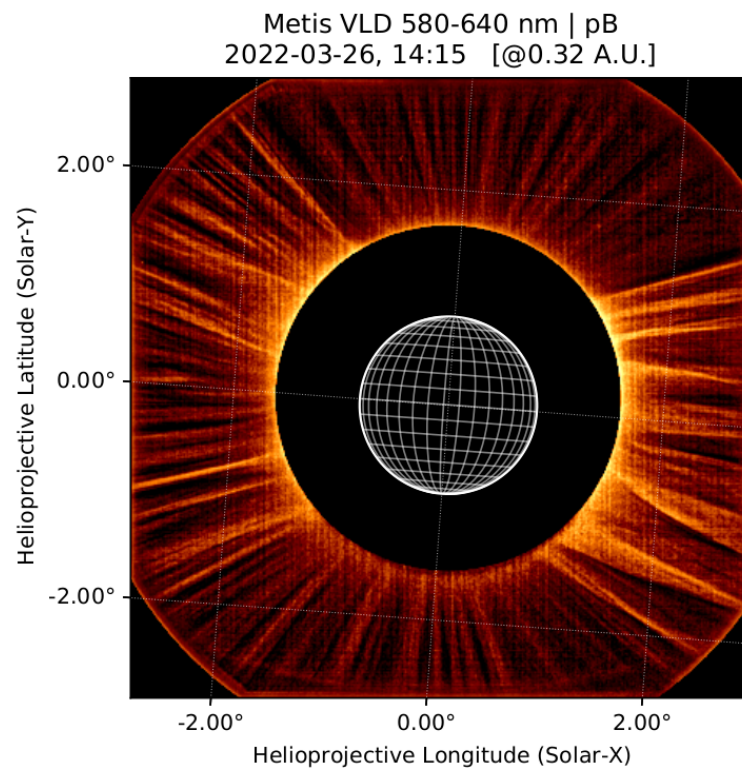
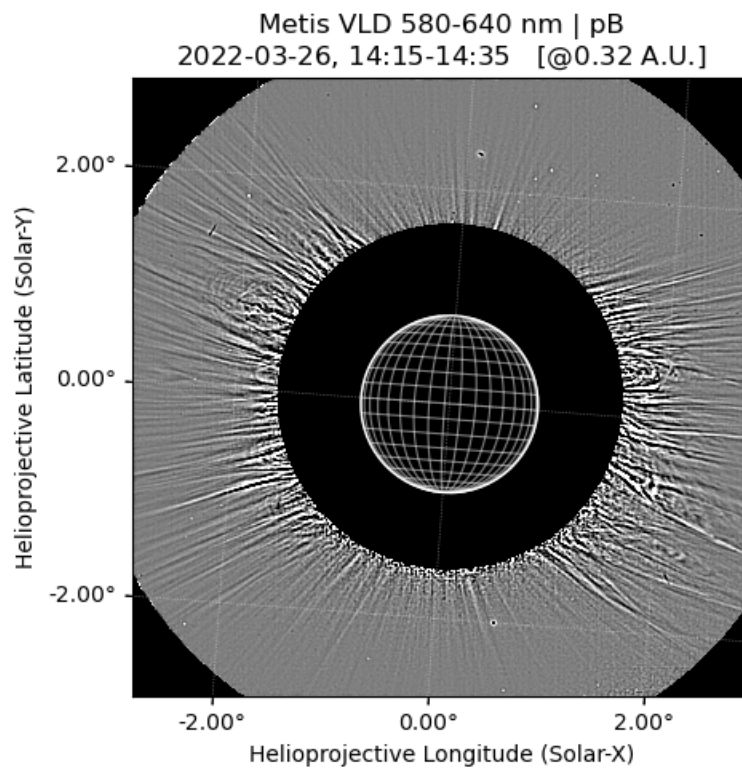FIGURE 6.36: Metis polarized brightness processed through a MGN filter (to enhance fine radial features).

FIGURE 6.37: Difference of two consecutive frames in the observing series taken 20 minutes apart, thus emphasizing moving or evolving features. The output image if then processed through a median filter and finally via a Laplacian filter for the edge-detection.
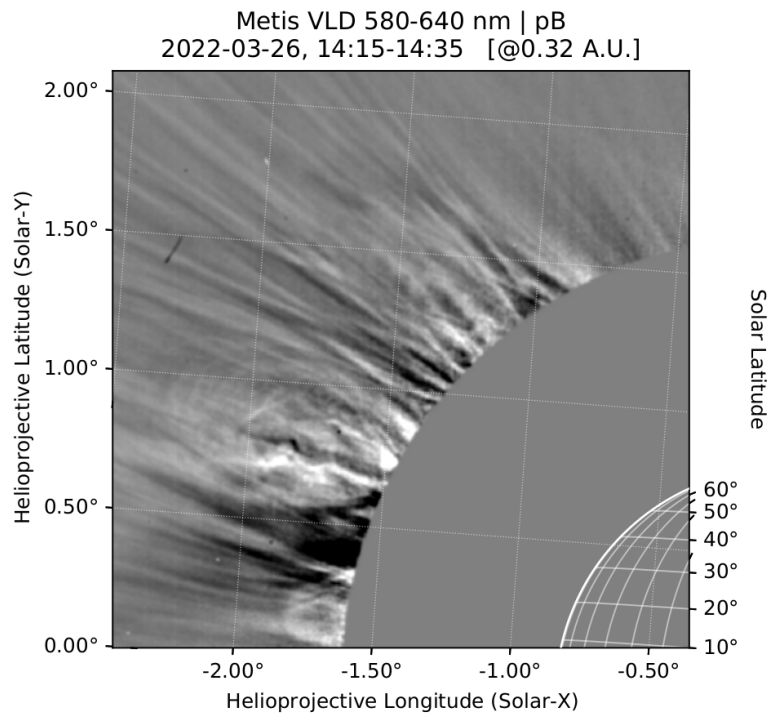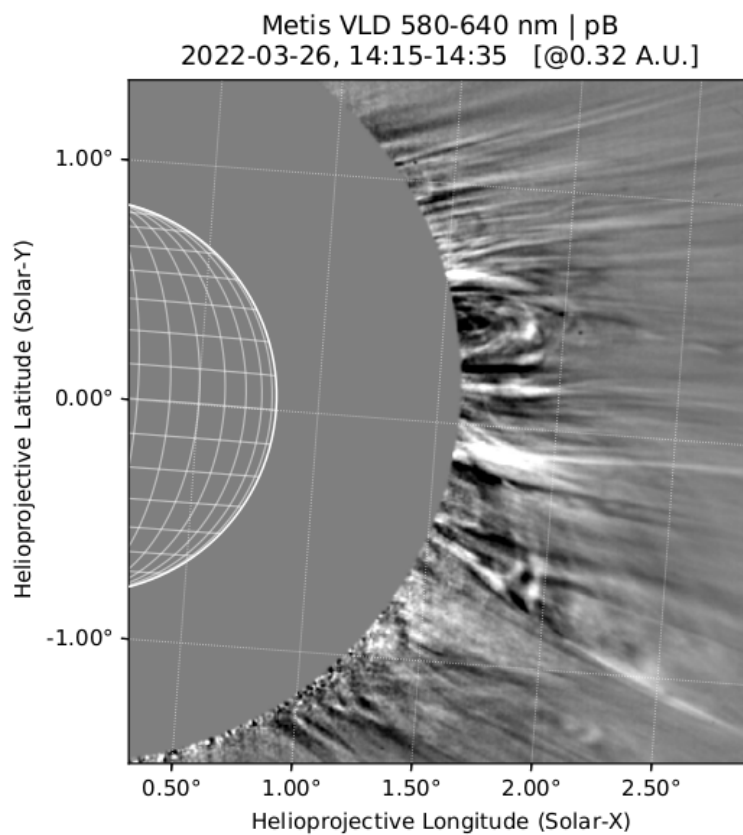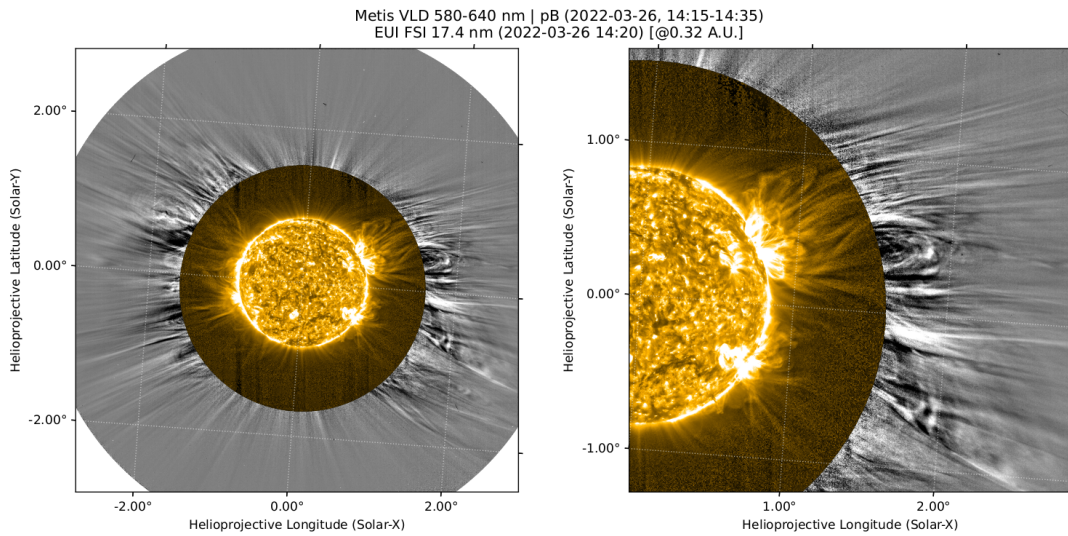
FIGURE 6.38: Detail in the East quadrant of the difference of two consecutive frames in the observing series taken 20 minutes apart, thus emphasizing moving or evolving features.

FIGURE 6.39: Detail in the West quadrant of the difference of two consecutive frames in the observing series taken 20 minutes apart, thus emphasizing moving or evolving features.

FIGURE 6.40: The solar corona at Solar Orbiter perihelion seen by EUI/FSI FeX 17.4 nm (yellow, courtesy of Solar Orbiter/EUI team) and by Metis visible light linearly polarized brightness. The coronal dynamical morphology is shown by the difference of two consecutive frames in the observing series taken 20 minutes apart, thus emphasizing moving or evolving features. The west equatorial quadrant is zoomed in the right panel.
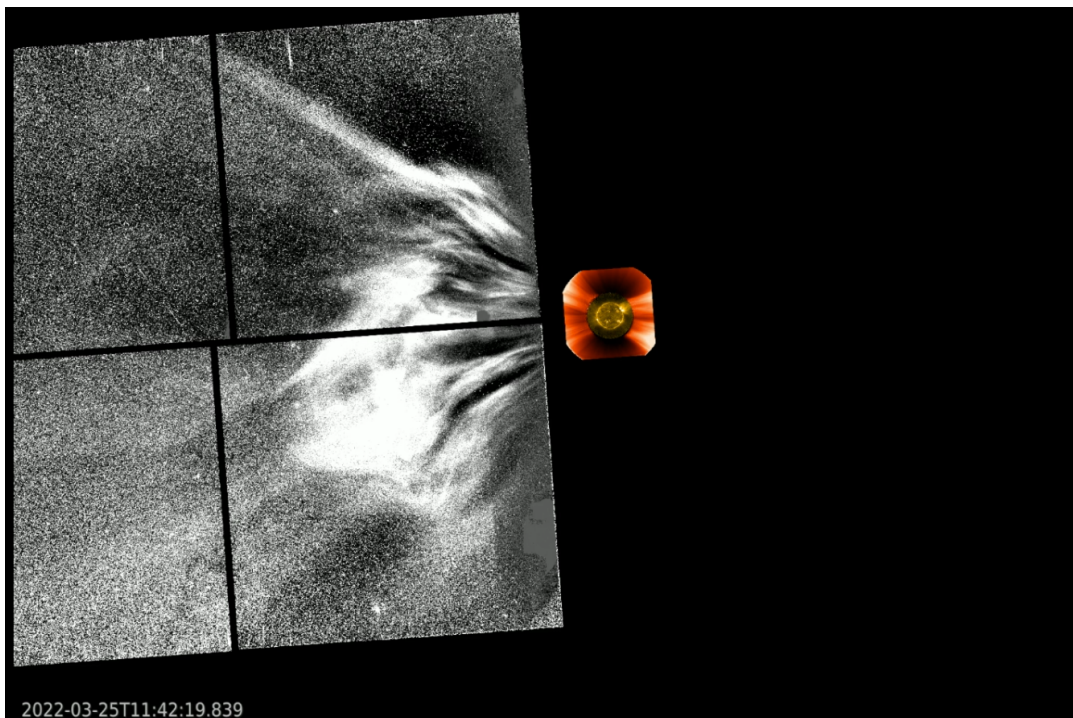

FIGURE 6.41: CME eruption event of March 25th on the east limb is seen by EUI/FSI disk imager in the 17.4 nm FeX line (yellow, courtesy of Solar Orbiter/EUI team), just above the limb, expanding through Metis field of view in VL polarised brightness and finally opening out in the VL running difference images of SoloHI (yellow, courtesy of SoloHI team). The event was captured one day before Solar Orbiter perihelion.

Chapter 7

Conclusion

In this Thesis we presented an experimental study of the solar corona from ground-based and space-based observatories.

We introduced the results obtained during the total solar eclipse on July 2, 2019, in Chile with the EKPol instrument. It is based on electro-optically modulating Liquid Crystal Variable Retarders (LCVRs) for the polarimetric observation of the solar corona. Performing this new observation we verified the on-ground stability of this technology (EKPol was already used for past total solar eclipse observations in 2006 and 2010). The results obtained during this eclipse (from the images composition to the electron density profile evaluation) are consistent with what was observed by other instruments (KCor and LASCO C2) and were compared with past observations. The use of the LCVRs technology has been a great ground-based test for the usage of this technology for space-based environments.

We presented also the first results from the ESCAPE project. We described the internally occulted coronagraph AntarctiCor and the characterisation of its innovative detector (the PolarCam) with arrays of micropolarisers for linear polarization imaging. The AntarctiCor instrument is based on the optical design of the "Association of Spacecraft for Polarimetric and Imaging Investigation of the Corona of the Sun" (ASPIICS) for the ESA formation-flying PROBA-3 mission.

During three different missions (spread over a period of about three years, from November 2018 to January 2022) we evaluated the sky brightness at the Concordia Station (Dome C plateau $\approx$ 3300 m a.s.l., Antarctica) obtaining almost constant values of $\approx 0.7 - 1.0 \times 10^{-6}$ $B_\odot$. We performed measurements of the sky brightness for different declination and different right ascension values as well. All the obtained results quantitatively demonstrate, for the first time, the quality of the Dome C site for coronagraphic observations. We can conclude that the local sky shows the characteristics of a "coronagraphic sky" (i.e., $B_{sky} < 10^{-6}$ $B_\odot$). Indeed, during the last Italian Antarctic Campaign, we were able to observe, for the first time, the solar corona from Antarctica. This holds the promise for Concordia Station to host a permanent coronagraph observatory for continuous studies of the solar corona during the Austral summers. Moreover, due to the extreme environment, the Antarctic plateau gives the possibility to test instrumentation for space-based observations.

Finally, we presented the Metis instrument on-board Solar Orbiter and its first mission results. After a summary of the Metis on-ground calibration, we dealt with its first in-flight polarimeter validation. We evaluated the LCVR retardances considering the geometry of the physical process that polarises the K-Corona obtaining: ($45.0° \pm 0.1°$, $81.4° \pm 0.1°$, $128.7° \pm 0.1°$, $175.4° \pm 0.1°$). We performed, as ulterior

check, the same study considering a fixed region in the solar corona during a complete S/C rotation (equivalent to a polariser rotation) obtaining: ($46° \pm 4°$, $82° \pm 4°$, $130° \pm 5°$, $176° \pm 5°$). These results are consistent with the previous check and with the on-ground calibration.

We evaluated also the polarimetric flat field by considering given coronal regions as it was imaged across different locations of the detector focal plane, during a complete S/C roll. In particular, we considered different heliocentric heights in the pB/I images. As expected, these values have a small percentage variation (i.e., $< 5\%$) at the same heliocentric height during the roll manoeuvre. The percentage variation of the pB/I mean values using the theoretical demodulation tensor is higher (i.e., $\approx 10\%$) than the one obtained using the on-ground calibrations. Quantitatively, by using the calibrated demodulation tensor, the accuracy in the polarisation measurement improves by a factor of ≈ 3.

We acquired also polarimetric sequences with different quadruplets of the LCVR voltages to evaluate the polarimetric response at different voltage configurations. This comparison shows differences within $\leq 2\%$.

Finally, a comparison of Metis polarised brightness with what was obtained by other instruments (LASCO C2, LASCO C3, and K-Cor) validates the new inverse externally occultation scheme and the goodness of the Metis polarimeter calibration. Thanks to the pB, we were able to evaluate also the electron density map necessary for the study of the solar wind velocity.

In a nutshell, the Thesis results are summarised in Table 7.1. It is possible to notice a complementarity between the ground-based and space-based observations.

TABLE 7.1: Conclusion in a nutshell.

EKPol (Total Solar Eclipse)	⋆ On-ground LCVR validation. ⋆ Total Solar Eclipse data analysis ($pB \rightarrow N_e$). ⋆ Comparison with past eclipses (different solar activity).
AntarctiCor (ESCAPE)	⋆ Validation of a new coronagraphic site. ⋆ First coronal observation from Antarctica. ⋆ Micropolariser camera characterisation and usage.
Metis (Solar Orbiter)	⋆ First in-flight LCVR validation (in hard radiation environment). ⋆ First results from Metis ($pB \rightarrow N_e \rightarrow$ solar wind). ⋆ Images from the Solar Orbiter first perihelion (0.32 AU). ⋆ Validation of new inverse external occultation scheme.

Appendix A

Useful constants

Physical constants[1]————————————

Speed of light (vacuum)	c_0	$= 2.997\,924\,58 \times 10^8\,\mathrm{m\,s^{-1}}$ (exact)
Constant of gravitation	G	$= 6.674\,30(15) \times 10^{-11}\,\mathrm{m^3\,kg^{-1}\,s^{-2}}$
Planck constant	h	$= 6.626\,070\,15 \times 10^{-34}\,\mathrm{J\,Hz^{-1}}$ (exact)
Elementary charge	e	$= 1.602\,176\,634 \times 10^{-19}\,\mathrm{C}$ (exact)
Magnetic permeability (vacuum)	μ_0	$= 1.256\,637\,062\,12(19) \times 10^{-6}\,\mathrm{N\,A^{-2}}$
Electric permeability (vacuum)	ϵ_0	$= 8.854\,187\,812\,8(13) \times 10^{-12}\,\mathrm{F\,m^{-2}}$
Bohr radius	a_0	$= 5.291\,772\,109\,03(80) \times 10^{-11}\,\mathrm{m}$
Electron mass	m_e	$= 9.109\,383\,701\,5(28) \times 10^{-31}\,\mathrm{kg}$
Thomson cross section	σ_e	$= 6.652\,458\,732\,1(60) \times 10^{-29}\,\mathrm{m^2}$
Proton mass	m_p	$= 1.672\,621\,923\,69(51) \times 10^{-27}\,\mathrm{kg}$
Neutron mass	m_n	$= 1.674\,927\,498\,04(95) \times 10^{-27}\,\mathrm{kg}$
Hydrogen mass	m_H	$= 1.6733 \times 10^{-27}\,\mathrm{kg}$
Alpha particle mass	m_α	$= 6.644\,657\,230(82) \times 10^{-27}\,\mathrm{kg}$
Boltzmann constant	k	$= 1.380\,649 \times 10^{-23}\,\mathrm{J\,K^{-1}}$ (exact)
Avogadro constant	N_A	$= 6.022\,140\,76 \times 10^{-23}\,\mathrm{mol^{-1}}$ (exact)
Stefan-Boltzmann constant	σ	$= 5.670\,374\,419 \times 10^{-8}\,\mathrm{W\,m^{-2}K^{-4}}$
Molar gas constant	R	$= 8.314\,462\,618\,\mathrm{J\,mol^{-1}\,K^{-1}}$
Fine-structure constant	α	$= 7.297\,352\,568(24) \times 10^{-3}$
Rydberg constant	R_H	$= 1.096\,775\,85 \times 10^7\,\mathrm{m^{-1}}$
Atomic mass unit	amu	$= 1.660\,540\,2(10) \times 10^{-24}\,\mathrm{g}$

TABLE A.1

————————————
[1]A complete detailed list can be found in Tiesinga et al., 2019.

Astronomical constants[2]

Astronomical unit	AU	$= 1.495\,978\,707\,00 \times 10^{11}\,\text{m}$
Parsec	pc	$= 3.086 \times 10^{16}\,\text{m}$
Light year	ly	$= 9.463 \times 10^{15}\,\text{m}$
Solar mass	$M_\odot$	$= 1.99 \times 10^{30}\,\text{kg}$
Solar radius	$R_\odot$	$= 6.957 \times 10^{8}\,\text{m}$
Solar luminosity	$L_\odot$	$= 3.847 \times 10^{26}\,\text{W}$
Solar irradiance	$I_\odot$	$= 1367\,\text{W}\,\text{m}^{-2}$
Solar surface temperature	$T_\odot$	$= 5.780 \times 10^{3}\,\text{K}$
Sun-Earth distance	$d_{\odot\oplus}$	$= 1.495\,978\,707 \times 10^{11}\,\text{m}$
Earth orbit eccentricity	$e_\oplus$	$= 0.0167$
Earth mass	$M_\oplus$	$= 5.9736 \times 10^{24}\,\text{kg}$
Earth radius (equatorial)	$R_\oplus$	$= 6.3781 \times 10^{6}\,\text{m}$
Earth-Moon distance	$d_{\oplus\mathbb{C}}$	$= 3.843\,99 \times 10^{8}\,\text{m}$
Moon mass	$M_\mathbb{C}$	$= 7.342 \times 10^{22}\,\text{kg}$
Moon radius (equatorial)	$R_\mathbb{C}$	$= 1.7381 \times 10^{6}\,\text{m}$

TABLE A.2
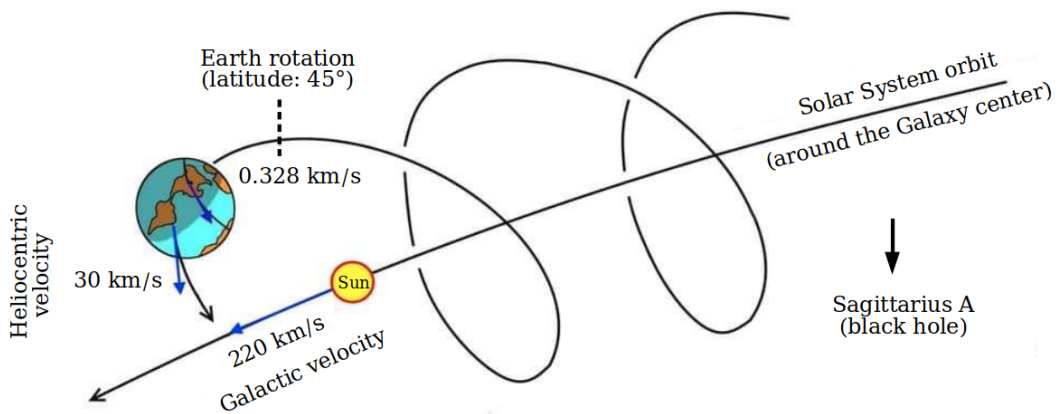
FIGURE A.1: Comparison between Sun-Earth velocities.

---

[2]In Figure A.1 a comparison between the main Sun-Earth velocities.

Mathematical constants[3] **& relations** ⎯⎯⎯⎯⎯

Pi π $= 3.141592653589793238(\dots)$

Euler's number e $= 2.718281828459045235(\dots)$

Imaginary unit i $= \sqrt{-1}$

Golden ration ϕ $= 1.618033988749894848(\dots)$

1 degree $\pi/180 = 0.017$ rad

1 rad $180/\pi = 57.30$ degree

TABLE A.3

─────────────────

[3]A complete detailed list can be found in Weisstein, 2022.

List of Abbreviations

ACCS	**A**ntarcti**C**or **C**ontrol **S**oftware
A.D.	**A**nno **D**omini
ADC	**A**nalog to **D**igital **C**onverter
AG	**A**nalog **G**ain
AIA	**A**tmospheric **I**maging **A**ssembly (SDO)
ALTEC	**A**erospace **L**ogistics **T**echnology **E**ngineering **C**ompany
AntarctiCor	**Antarcti**ca solar**Cor**onagraph (ESCAPE)
AoLP	**A**nlge **o**f **L**inear **P**olarisation
ASI	**A**genzia **S**paziale **I**taliana
a.s.l.	**a**bove **s**ea **l**evel
ASPIICS	**A**ssociation of **S**pacecraft for **P**olarimetric and **I**maging **I**nvestigation of the **C**orona of the **S**un (PROBA-3)
ASTEP	**A**ntarctic **S**earch for **T**ransiting **E**xo**P**lanet
ASTM	**A**merican **S**ociety for **T**esting and **M**aterials
A.Y.	**A**cademic **Y**ear
B.C.	**B**efore **C**hrist
BP	**B**and-**P**ass filter
BSRN	**B**aseline **S**urface **R**adiation **N**etwork
CCD	**C**harge-**C**oupled **D**evice
CD	**C**ollimating **D**oublet
CESAR	**C**ooperation through **E**ducation in **S**cience and **A**stronomy **R**esearch
cgs	**c**entimeter, **g**ram, **s**econd system
CME	**C**oronal **M**ass **E**jection
CIR	**C**orotating **I**nteraction **R**egion
COVID	**CO**rona **VI**rus **D**isease
CS	**C**urrent **S**heet
CSC	**C**oronagraph **S**pace**C**raft
DEC	**DEC**lination
DG	**D**igital **G**ain
DN	**D**igital **N**umber

DoLP	**D**egree **o**f **L**inear **P**olarisation
ENEA	**A**genzia **n**azionale per le nuove tecnologie, l'**e**nergia e lo sviluppo economico sostenibile (old "**E**nte **N**azionale **E**nergia e **A**mbiente")
EKPol	**E**clipse **K**-corona **Pol**arimeter
EPD	**E**nergetic **P**article **D**etector (SolO)
ESA	**E**uropean **S**pace **A**gency
ESCAPE	**E**xtreme **S**olar **C**oronagraphy **A**ntarctic **P**rogram **E**xperiment
ESO	**E**uropean **S**outhern **O**bservatory
ESTEC	**E**uropean **S**pace Research and **TEC**hnology Centre
EUI	**E**xtreme **U**ltraviolet **I**mager (SolO)
FF	**F**lat-**F**ield
FIP	**F**irst **I**onisation **P**otential
FLS	**F**ocus **L**ens **S**ystem
FoV	**F**ield **o**f **V**iew
FS	**F**ield **S**top
FSI	**F**ull **S**un **I**mager
FWHM	**F**ull **W**idth at **H**alf **M**aximum
GAM	**G**ravity **A**ssist **M**anoeuvre
GUI	**G**raphical **U**ser **I**nterface
HAO	**H**aigh-**A**ltitude **O**bservatory
HDR	**H**igh-**D**ynamic **R**ange
HEE	**H**eliocentric **E**arth **E**cliptic
HMI	**H**eliosysmic and **M**agnetic **I**mager (SDO)
HW	**H**alf-**W**ave plate
HWHM	**H**alf **W**idth at **H**alf **M**aximum
ICS	**I**nterplanetary **C**urrent **S**heet
IEO	**I**nverted **E**xternal **O**cculter
INAF	**I**stituto **N**azionale di **A**stro**F**isica
IO	**I**nternal **O**cculter
IPEV	**I**nstitut polaire français **P**aul-**É**mile-**V**ictor
IR	**I**nfra**R**ed light
ISO	**I**nternational **O**rganization for **S**tandardization
ISS	**I**nternational **S**pace **S**tation
ISVL	**I**llumination **S**ystem **V**isible **L**ight
KCor	**K-Cor**onagraph (MLSO)
LASCO	**L**arge **A**ngle and **S**pectrometric **CO**ronagraph (SOHO)

LCVR	**L**iquid **C**rystal **V**ariable **R**etarder
LHC	**L**eft-**H**and **C**ircular Polarisation
LHP	**L**inear **H**orizontal **P**olarisation
LoS	**L**ine **o**f **S**ight
LP	**L**inear **P**olariser
LS	**L**yot **S**top
LTE	**L**ocal **T**hermal **E**quilibrium
LVP	**L**inear **V**ertical **P**olarisation
MAG	**MAG**netometer (SolO)
MGN	**M**ulti-scale **G**aussian **N**ormalization
MHD	**M**agneto**H**ydro**D**ynamics
MLSO	**M**auna **L**oa **S**olar **O**bservatory
MKS	**M**eter, **K**ilogram, **S**econd system
MTF	**M**odulation **T**ransfer **F**unction
NASA	**N**ational **A**eronautics and **S**pace **A**dministration
NOAA	**N**ational **O**ceanic and **A**tmospheric **A**dministration
NRGF	**N**ormalizing **R**adial **G**raded **F**ilter
NRL	**N**aval **R**esearch **L**aboratory
OATo	**O**sservatorio **A**strofisico di **To**rino
OPSys	**O**ptical **P**ayload **Sys**tems facility
OPTEC	**OPT**ical & Optoelectronic Systems and **TEC**hnologies
OSC	**O**cculter **S**pace**C**raft
pB	**P**olarized **b**rightness
PFF	**P**olarimetric **F**lat-**F**ield
PhD	**Ph**ilosophiae **D**octor
PHI	**P**olarimetric **H**elioseismic **I**mager (SolO)
PI	**P**rincipal **I**nvestigator
PILS	**P**olarimeter **I**nstrument **L**evel **S**ystem reference frame
PMP	**P**olarisation **M**odulation **P**ackage
PNRA	**P**rogramma **N**azionale di **R**icerca in **A**ntartide
PROBA-3	**Pro**ject for **O**n-**B**oard **A**utonomy-**3**
PSF	**P**oint **S**pread **F**unction
PSI	**P**redictive **S**cience **I**ncorporated
PSP	**P**arker **S**olar **P**robe
PTC	**P**hoton **T**ransfer **C**urve
QE	**Q**uantum **E**fficiency

QW	**Q**uarter-**W**ave plate
RA	**R**ight **A**scension
RHC	**R**ight-**H**and **C**ircular Polarisation
rms	**r**oot **m**ean **s**quare
ROB	**R**oyal **O**bservatory of **B**elgium
ROI	**R**egion **O**f **I**nterest
RPW	**R**adio and **P**lasma **W**aves (SolO)
SB	**S**ector **B**oundary
SBC	**S**ector **B**oundary **C**rossing
S/C	**S**pace**C**raft
SC	**S**un **C**entre
SDK	**S**oftware **D**evelopment **K**it
SDO	**S**olar **D**ynamics **O**bservatory
SEP	**S**olar **E**nergetic **P**articles
SI	International **S**ystem of Units
SNR	**S**ignal to **N**oise **R**ation
SOHO	**SO**lar and **H**eliospheric **O**bservatory
SolO	**Sol**ar **O**rbiter
SoloHI	**Sol**ar **O**rbiter **H**eliospheric **I**mager (SolO)
SPICE	**S**pectral **I**maging of the **C**oronal **E**nvironment
SPOCC	**S**pace **O**ptics **C**alibration **C**hamber
SPS	**S**hadow **P**osition **S**ensor
SSM	**S**tandard **S**olar **M**odel
STEREO	**S**olar **TE**rrestrial **RE**lations **O**bservatory
STIX	**S**pectrometer/**T**elescope for **I**maging **X**-rays
SWA	**S**olar **W**ind **A**nalyser (SolO)
tB	**T**otal **b**rightness
TRACE	**T**ransition **R**egion **A**nd **C**oronal **E**xplorer
UFF	**U**npolarised **F**lat-**F**ield
UNITO	**UNI**versità degli studi di **TO**rino
URF	**U**nit **R**eference **F**rame
UV	**U**ltra**V**iolet light
UVDA	**U**ltra**V**iolet **D**etector **A**ssembly
VF	**V**ignetting **F**unction
VL	**V**isible **L**ight
VLDA	**V**isible **L**ight **D**etector **A**ssembly

List of Symbols

Symbol	Meaning
⊙	Sun
⊕	Earth
☾	Moon
⋆	Star
☿	Mercury
♀	Venus
♂	Mars
♃	Jupiter
♄	Saturn
♅	Uranus
♆	Neptune
♇	Pluto
$\mathbb{N}$	Set of all Natural number
$\mathbb{Z}$	Set of all Integers number
$\mathbb{R}$	Set of all Real number
$\mathbb{C}$	Set of all Complex number
$\Re$	Real part from complex number
$\Im$	Imaginary part from complex number

List of Figures

List of Tables

Bibliography

4D Technology, Corp. (2021). *An Onto Innovation Subsidiary*. Tucson (AZ). cfr. https://4dtechnology.com/.

Abramowitz, Milton and Irene A. Stegun (1964). *Handbook of Mathematical Functions with Formulas, Graphs, and Mathematical Tables*. ninth Dover printing, tenth GPO printing. New York: Dover. URL: https://digital.library.unt.edu/ark:/67531/metadc40301/m1/2/.

Aime, C. (Oct. 2013). "Theoretical performance of solar coronagraphs using sharp-edged or apodized circular external occulters". In: *Astronomy & Astrophysics* 558, A138, A138. DOI: 10.1051/0004-6361/201322304. URL: https://ui.adsabs.harvard.edu/abs/2013A&A...558A.138A.

Allen, C.W. (2002). "Allen's Astrophysical Quantities". In: DOI: https://doi.org/10.1007/978-1-4612-1186-0. URL: https://rd.springer.com/book/10.1007/978-1-4612-1186-0.

Alvarez-Herrero, A. et al. (2011). "Imaging polarimeters based on liquid crystal variable retarders: an emergent technology for space instrumentation". In: *Polarization Science and Remote Sensing V*. Ed. by Joseph A. Shaw and J. Scott Tyo. Vol. 8160. International Society for Optics and Photonics. SPIE, pp. 312 –329. DOI: 10.1117/12.892732. URL: https://doi.org/10.1117/12.892732.

Amari, T., J. F. Luciani, and J. J. Aly (Nov. 2004). "Coronal Magnetohydrodynamic Evolution Driven by Subphotospheric Conditions". In: *Astrophysical Journal Letters* 615.2, pp. L165–L168. DOI: 10.1086/426317. URL: https://ui.adsabs.harvard.edu/abs/2004ApJ...615L.165A.

Andretta, V. et al. (Dec. 2021). "The first coronal mass ejection observed in both visible-light and UV H I Ly-*α* channels of the Metis coronagraph on board Solar Orbiter". In: *Astronomy & Astrophysics* 656, L14, p. L14. DOI: 10.1051/0004-6361/202142407. URL: https://ui.adsabs.harvard.edu/abs/2021A&A...656L..14A.

Antonucci, Ester et al. (Sept. 2020). "Metis: the Solar Orbiter visible light and ultraviolet coronal imager". In: *Astronomy & Astrophysics* 642, A10. ISSN: 1432-0746. DOI: 10.1051/0004-6361/201935338. URL: http://dx.doi.org/10.1051/0004-6361/201935338.

Aschwanden, Markus (2006). *Physics of the Solar Corona*. Springer-Verlag Berlin Heidelberg New York. ISBN: 3-540-30765-6.

Auchère, F. et al. (Oct. 2020). "Coordination within the remote sensing payload on the Solar Orbiter mission". In: *Astronomy & Astrophysics* 642, A6, A6. DOI: 10.1051/0004-6361/201937032. URL: https://ui.adsabs.harvard.edu/abs/2020A&A...642A...6A.

Baker, D. et al. (2008). *Severe Space Weather Events: Understanding Societal and Economic Impacts: A Workshop Report*. Washington, DC: The National Academies Press. ISBN: 978-0-309-12769-1. DOI: 10.17226/12507. URL: https://www.nap.edu/catalog/12507/severe-space-weather-events-understanding-societal-and-economic-impacts-a.

Baker, D. et al. (2019). *The Scientific Foundation of Space Weather*. Springer Netherlands. ISBN: 978-94-024-1587-2. URL: https://link.springer.com/book/9789402415872.

Balboni, Emanuele (2009). "Corona Solare: Parametri fisici derivati dalle osservazioni svolte durante l'eclissi del 29 marzo 2006". (Italian). MA thesis. University of Turin, Italy: Physics department.

Billings, Donald E. (1966). *A guide to the solar corona*. Academic Press. URL: https://ui.adsabs.harvard.edu/abs/1966gtsc.book.....B.

Bothmer, V. and I. A. Daglis (2007). *Space Weather- Physics and Effects*. Springer, Berlin, Heidelberg. ISBN: 978-3-540-23907-9. DOI: https://doi.org/10.1007/978-3-540-34578-7. URL: https://link.springer.com/book/10.1007/978-3-540-34578-7.

Brueckner, G. E. et al. (Dec. 1995). "The Large Angle Spectroscopic Coronagraph (LASCO)". In: *Solar Physics* 162.1-2, pp. 357–402. DOI: 10.1007/BF00733434.

Capobianco, Gerardo et al. (2019). "OPSys: optical payload systems facility for space instrumentation integration and calibration". In: *International Conference on Space Optics — ICSO 2018*. Ed. by Zoran Sodnik, Nikos Karafolas, and Bruno Cugny. Vol. 11180. International Society for Optics and Photonics. SPIE, pp. 2739 –2748. DOI: 10.1117/12.2536193. URL: https://doi.org/10.1117/12.2536193.

Carroll, Bradley W. and Dale A. Ostlie (2017). *An Introduction to Modern Astrophysics*. 2nd ed. Cambridge University Press. DOI: 10.1017/9781108380980.

Casti, M. et al. (July 2018). "Calibration of the liquid crystal visible-light polarimeter for the Metis/Solar Orbiter coronagraph". In: *Space Telescopes and Instrumentation 2018: Optical, Infrared, and Millimeter Wave*. Ed. by Makenzie Lystrup et al. Vol. 10698. Society of Photo-Optical Instrumentation Engineers (SPIE) Conference Series, 1069831, p. 1069831. DOI: 10.1117/12.2325075. URL: https://ui.adsabs.harvard.edu/abs/2018SPIE10698E..31C.

Casti, M. et al. (July 2019). "Metis/Solar Orbiter polarimetric visible light channel calibration". In: *International Conference on Space Optics — ICSO 2018*. Vol. 11180. Society of Photo-Optical Instrumentation Engineers (SPIE) Conference Series, 111803C, p. 111803C. DOI: 10.1117/12.2536039. URL: https://ui.adsabs.harvard.edu/abs/2019SPIE11180E..3CC.

Chen, P. F. (Apr. 2011). "Coronal Mass Ejections: Models and Their Observational Basis". In: *Living Reviews in Solar Physics* 8.1, 1, p. 1. DOI: 10.12942/lrsp-2011-1. URL: https://ui.adsabs.harvard.edu/abs/2011LRSP....8....1C.

Christensen, L. L. et al. (Sept. 2019). "Science & Outreach at La Silla During the Total Solar Eclipse". In: *The Messenger* 177, pp. 47–53. DOI: 10.18727/0722-6691/5153. URL: https://ui.adsabs.harvard.edu/abs/2019Msngr.177...47C.

Collett, Edward (1992). *Polarized light. Fundamentals and applications*. New York: Marcel Dekker. URL: https://ui.adsabs.harvard.edu/abs/1992plfa.book.....C.

Cranmer, S.R. (Oct. 1997). *On the synthesis of coronal white-light polarization diagnostics*.

Degl'Innocenti, Egidio Landi (Dec. 2007). *Fisica solare*. (Italian). Springer-Verlag Milan. ISBN: 978-88-470-0677-5. DOI: https://doi.org/10.1007/978-88-470-0678-2.

EdmundOptics (2019). *White Diffusing Glass*. www.edmundoptics.com/p/75mm-dia-white-diffusing-glass/3841/.

Elmore, David (2007). *SBM Sky Brightness at Mauna Loa*. Tech. rep. URL: https://opensky.ucar.edu/islandora/object/reports%3A11/datastream/PDF/download/SBM_sky_brightness_at_Mauna_Loa.citation.

Elmore, David F. et al. (Dec. 2000). "Calibration procedure for the polarimetric instrument for Solar Eclipse-98". In: *Instrumentation for UV/EUV Astronomy and Solar Missions*. Ed. by Silvano Fineschi et al. Vol. 4139. Society of Photo-Optical Instrumentation Engineers (SPIE) Conference Series, pp. 370–377. DOI: 10.1117/12.410535. URL: https://ui.adsabs.harvard.edu/abs/2000SPIE.4139..370E.

Evans, John W. (Dec. 1948). "A Photometer for Measurement of Sky Brightness Near the Sun". In: *J. Opt. Soc. Am.* 38.12, pp. 1083–1085. DOI: 10.1364/JOSA.38.001083. URL: http://opg.optica.org/abstract.cfm?URI=josa-38-12-1083.

Fan, Y. and S. E. Gibson (Oct. 2007). "Onset of Coronal Mass Ejections Due to Loss of Confinement of Coronal Flux Ropes". In: *The Astrophysical Journal* 668.2, pp. 1232–1245. DOI: 10.1086/521335. URL: https://ui.adsabs.harvard.edu/abs/2007ApJ...668.1232F.

Faurobert, M., Arnaud, J., and Vernisse, Y. (2012). "Extinction and Sky Brightness at Dome C". In: *EAS Publications Series* 55, pp. 365–367. DOI: 10.1051/eas/1255051. URL: https://doi.org/10.1051/eas/1255051.

Fineschi, S. et al. (Oct. 2011). "OPSys: optical payload systems facility for testing space coronagraphs". In: *Solar Physics and Space Weather Instrumentation IV*. Ed. by Silvano Fineschi and Judy Fennelly. Vol. 8148. Society of Photo-Optical Instrumentation Engineers (SPIE) Conference Series, 81480W, 81480W. DOI: 10.1117/12.897794. URL: https://ui.adsabs.harvard.edu/abs/2011SPIE.8148E..0WF.

Fineschi, S. et al. (Jan. 2019a). "AntarctiCor: Solar Coronagraph in Antarctica for the ESCAPE Project". In: *Nuovo Cimento C Geophysics Space Physics C* 42.1, 26, p. 26. DOI: 10.1393/ncc/i2019-19026-9. URL: https://ui.adsabs.harvard.edu/abs/2019NCimC..42...26F.

Fineschi, S. et al. (May 2020). "Optical design of the multi-wavelength imaging coronagraph Metis for the Solar Orbiter mission". In: *Experimental Astronomy* 49. ISSN: 239–263. DOI: 10.1007/s10686-020-09662-z. URL: https://doi.org/10.1007/s10686-020-09662-z.

Fineschi, S. et al. (June 2021). "First-light Science Observations of the Metis Solar Coronagraph". In: *Society of Photo-Optical Instrumentation Engineers (SPIE) Conference Series*. Vol. 11852. Society of Photo-Optical Instrumentation Engineers (SPIE) Conference Series, 1185211, p. 1185211. DOI: 10.1117/12.2599221. URL: https://ui.adsabs.harvard.edu/abs/2021SPIE11852E..11F.

Fineschi, Silvano et al. (Aug. 2005). "KPol: liquid crystal polarimeter for K-corona observations from the SCORE coronagraph". In: *Solar Physics and Space Weather Instrumentation*. Ed. by Silvano Fineschi and Rodney A. Viereck. Vol. 5901. Society of Photo-Optical Instrumentation Engineers (SPIE) Conference Series, pp. 389–399. DOI: 10.1117/12.626033. URL: https://ui.adsabs.harvard.edu/abs/2005SPIE.5901..389F.

Fineschi, Silvano et al. (2019b). "The Optical Payload System facility". In: *2019 IEEE 5th International Workshop on Metrology for AeroSpace (MetroAeroSpace)*, pp. 309–313. DOI: 10.1109/MetroAeroSpace.2019.8869579.

Fracastoro, M. G. (Jan. 1948). "Uno strumento per la misura della diffusione atmosferica e della radiazione solare". In: *Memorie Società Astronomica Italiana* 19, p. 113. URL: https://ui.adsabs.harvard.edu/abs/1948MmSAI..19..113F.

Fracastoro, Mario G. and G. Righini (Jan. 1949). "Misure della diffusione atmosferica e della radiazione solare eseguite col fotocianometro di Arcetri". In: *Osservazioni e memorie dell'Osservatorio astrofisico di Arcetri* 65, pp. 11–28. URL: https://ui.adsabs.harvard.edu/abs/1949MmArc..65...11F.

Galy, C. et al. (2015). "Design and modelisation of ASPIICS optics". In: *Proc. Spie. Solar Physics and Space Weather Instrumentation VI*. Ed. by Silvano Fineschi and Judy Fennelly. Vol. 9604. International Society for Optics and Photonics. SPIE, pp. 71 –82. DOI: 10.1117/12.2188404. URL: https://doi.org/10.1117/12.2188404.

Galy, C. et al. (July 2019). "Straylight analysis on ASPIICS, PROBA-3 coronagraph". In: *International Conference on Space Optics — ICSO 2018*. Vol. 11180. Society

of Photo-Optical Instrumentation Engineers (SPIE) Conference Series, 111802H, 111802H. DOI: 10.1117/12.2536008. URL: https://ui.adsabs.harvard.edu/abs/2019SPIE11180E..2HG.

García Marirrodriga, C. et al. (Feb. 2021). "Solar Orbiter: Mission and spacecraft design". In: *Astronomy & Astrophysics* 646, A121, A121. DOI: 10.1051/0004-6361/202038519. URL: https://ui.adsabs.harvard.edu/abs/2021A&A...646A.121G.

Gibson, Sarah E. (Oct. 2018). "Solar prominences: theory and models. Fleshing out the magnetic skeleton". In: *Living Reviews in Solar Physics* 15.1, 7, p. 7. DOI: 10.1007/s41116-018-0016-2. URL: https://ui.adsabs.harvard.edu/abs/2018LRSP...15....7G.

Gradshteyn, I.S., I.M. Ryzhik, and A. Jeffrey (1994). *Table of Integrals, Series, and Products*. Academic Press. ISBN: 9780122947551. URL: https://books.google.it/books?id=oDhmngEACAAJ.

Habbal, Shadia Rifai and Ruth Esser (Jan. 1994). "On the Derivation of Empirical Limits on the Helium Abundance in Coronal Holes below 1.5 solar radii". In: *Astrophysical Journal Letters* 421, p. L59. DOI: 10.1086/187187. URL: https://ui.adsabs.harvard.edu/abs/1994ApJ...421L..59H.

Hearnshaw, John B. (Apr. 2014). *The Analysis of Starlight: Two Centuries of Astronomical Spectroscopy*. 2nd ed. Cambridge University Press. ISBN: 9781139382779. DOI: 10.1017/CBO9781139382779.

Held, Gilbert (2009). *Introduction to light emitting diode technology and applications*. Taylor & Francis Group, LLC. ISBN: 978-1-4200-7662-2. URL: https://books.google.it/books?id=bu7_mKpor9kC&pg=PA46&lpg=PA46&dq=steradian+formula&source=bl&ots=sVPdJxv30h&sig=ACfU3U31y5hvueNkb-44bsb-xdrznVUF1A&hl=en&sa=X&ved=2ahUKEwiYxePCuJn3AhUjgP0HHRLiC-AQ6AF6BAgpEAM#v=onepage&q=steradian%20formula&f=false.

Hou, Junfeng, Alfred G. de Wijn, and Steven Tomczyk (Sept. 2013). "Design and measurement of the Stokes polarimeter for the COSMO K-coronagraph". In: *The Astrophysical Journal* 774.1, 85, p. 85. DOI: 10.1088/0004-637X/774/1/85.

Inhester, Bernd (Dec. 2015). "Thomson Scattering in the Solar Corona". In: *arXiv e-prints*, arXiv:1512.00651, arXiv:1512.00651. arXiv: 1512.00651 [astro-ph.SR]. URL: https://ui.adsabs.harvard.edu/abs/2015arXiv151200651I.

Jacobs, A., S. Morgan, and C. Damasio (July 2020). "Thermal Design and Developments for the Solar Orbiter Spacecraft". In: *50th International Conference on Environmental Systems - ICES2020*. URL: https://ttu-ir.tdl.org/handle/2346/86342.

Janesick, James R. (Aug. 2007). *Photon Transfer Curve*. Vol. PM170. SPIE, p. 276. ISBN: 9780819467225. DOI: 10.1117/3.725073.ch5. URL: www.spiedigitallibrary.org/ebooks/PM/Photon-Transfer/5/Photon-Transfer-Curve/10.1117/3.725073.ch5?SSO=1.

Joshi, V. and N. Srivastava (Dec. 2007). "On the study of kinematics of eruptive quiescent p rominences observed in He 304 Å". In: *Bulletin of the Astronomical Society of India* 35, pp. 447–455. URL: https://ui.adsabs.harvard.edu/abs/2007BASI...35..447J.

Kamide, Y. and A. Chian (2007). *Handbook of the Solar-Terrestrial Environment*. Springer-Verlag Berlin Heidelberg. ISBN: 978-3-540-46314-6. DOI: https://doi.org/10.1007/978-3-540-46315-3.

Kirchhoff, G. (Jan. 1860). "Ueber die Fraunhofer'schen Linien". In: *Annalen der Physik* 185.1, pp. 148–150. DOI: 10.1002/andp.18601850115. URL: https://ui.adsabs.harvard.edu/abs/1860AnP...185..148K.

Kohl, J. L. et al. (July 1998). "UVCS/SOHO Empirical Determinations of Anisotropic Velocity Distributions in the Solar Corona". In: *Astrophysical Journal Letters* 501.1, pp. L127–L131. DOI: `10.1086/311434`. URL: `https://ui.adsabs.harvard.edu/abs/1998ApJ...501L.127K`.

Krieger, A. S., A. F. Timothy, and E. C. Roelof (Apr. 1973). "A Coronal Hole and Its Identification as the Source of a High Velocity Solar Wind Stream". In: *Solar Physics* 29.2, pp. 505–525. DOI: `10.1007/BF00150828`. URL: `https://ui.adsabs.harvard.edu/abs/1973SoPh...29..505K`.

Lefebvre, M. et al. (2000). "Propagation of errors for matrix inversion". In: *Nuclear Instruments and Methods in Physics Research Section A: Accelerators, Spectrometers, Detectors and Associated Equipment* 451.2, pp. 520–528. ISSN: 0168-9002. DOI: `https://doi.org/10.1016/S0168-9002(00)00323-5`. URL: `https://www.sciencedirect.com/science/article/pii/S0168900200003235`.

Liberatore, A. et al. (2021a). "PolarCam micropolarizer cameras characterization and usage". In: *International Conference on Space Optics — ICSO 2020*. Ed. by Bruno Cugny, Zoran Sodnik, and Nikos Karafolas. Vol. 11852. International Society for Optics and Photonics. SPIE, pp. 358 –379. DOI: `10.1117/12.2599180`. URL: `https://doi.org/10.1117/12.2599180`.

Liberatore, A. et al. (2021b). "In-flight calibration of Metis coronagraph on board of Solar Orbiter". In: *International Conference on Space Optics — ICSO 2020*. Ed. by Bruno Cugny, Zoran Sodnik, and Nikos Karafolas. Vol. 11852. International Society for Optics and Photonics. SPIE, pp. 1793 –1814. DOI: `10.1117/12.2599646`. URL: `https://doi.org/10.1117/12.2599646`.

Liberatore, A. et al. (Mar. 2022). "Sky Brightness Evaluation at Concordia Station, Dome C, Antarctica, for Ground-Based Observations of the Solar Corona". In: *Solar Physics* 297.29. DOI: `10.1007/s11207-022-01958-x`. URL: `https://link.springer.com/article/10.1007/s11207-022-01958-x`.

Liu, Tie and Yingna Su (July 2021). "Tether-cutting and Overlying Magnetic Reconnections in an MHD Simulation of Prominence-cavity System". In: *The Astrophysical Journal* 915.1, 55, p. 55. DOI: `10.3847/1538-4357/ac013a`. arXiv: `2105.06683 [astro-ph.SR]`. URL: `https://ui.adsabs.harvard.edu/abs/2021ApJ...915...55L`.

Lupi, Angelo (2021). "Basic and other measurements of radiation at Concordia Station (2020-10)". In: In: Lupi, Angelo; Lanconelli, Christian; Vitale, Vito (2021): Basic and other measurements of radiation at Concordia station (2006-01 et seq.). Institute of Atmospheric Sciences and Climate of the Italian National Research Council, Bologna, PANGAEA, https://doi.org/10.1594/PANGAEA.935421. Institute of Atmospheric Sciences and Climate of the Italian National Research Council, Bologna. PANGAEA. DOI: `10.1594/PANGAEA.926643`. URL: `https://doi.org/10.1594/PANGAEA.926643`.

Lyngvi, A. et al. (Oct. 2005). "The Solar Orbiter Thermal Design". In: *56th International Astronautical Congress of the International Astronautical Federation, the International Academy of Astronautics, and the International Institute of Space Law*. DOI: `10.2514/6.IAC-05-C2.6.02`. eprint: `https://arc.aiaa.org/doi/pdf/10.2514/6.IAC-05-C2.6.02`. URL: `https://arc.aiaa.org/doi/abs/10.2514/6.IAC-05-C2.6.02`.

Lyot, Bernard (Jan. 1932). "Étude de la couronne solaire en dehors des éclipses. Avec 16 figures dans le texte." In: *Zeitschrift für Astrophysik* 5, p. 73. URL: `https://ui.adsabs.harvard.edu/abs/1932ZA......5...73L`.

Metis (2020). *Metis programme*. cfr. `http://metis.oato.inaf.it/`.

Meyer, J. P. (Jan. 1985). "Solar-stellar outer atmospheres and energetic particles, and galactic cosmic rays". In: *Astrophysical Journal Supplement* 57, pp. 173–204. DOI: 10.1086/191001. URL: https://ui.adsabs.harvard.edu/abs/1985ApJS...57..173M.

Minnaert, M. (Jan. 1930). "On the continuous spectrum of the corona and its polarisation. With 3 figures. (Received July 30, 1930)". In: *Zeitschrift fur Astrophysik* 1, p. 209. URL: https://ui.adsabs.harvard.edu/abs/1930ZA......1..209M.

MKS-Newport (2019). *Resolution Test Targets*. URL: https://www.newport.com/f/resolution-test-targets?q=resolution\%20target:relevance#features.

Moldwin, Mark (2008). *An Introduction to Space Weather*. Cambridge University Press. DOI: 10.1017/CBO9780511801365.

Morgan, Huw and Miloslav Druckmüller (2014). "Multi-Scale Gaussian Normalization for Solar Image Processing". In: *Solar Physics* 289, pp. 2945 –2955. DOI: 10.1007/s11207-014-0523-9. URL: https://link.springer.com/article/10.1007/s11207-014-0523-9.

Morgan, Huw, Shadia Rifai Habbal, and Richard Woo (July 2006). "The Depiction of Coronal Structure in White-Light Images". In: *Solar Physics* 236.2, pp. 263–272. DOI: 10.1007/s11207-006-0113-6. arXiv: astro-ph/0602174 [astro-ph]. URL: https://ui.adsabs.harvard.edu/abs/2006SoPh..236..263M.

Müller, D. et al. (Sept. 2020). "The Solar Orbiter mission". In: *Astronomy & Astrophysics* 642, A1. ISSN: 1432-0746. DOI: 10.1051/0004-6361/202038467. URL: http://dx.doi.org/10.1051/0004-6361/202038467.

Nelson P. G. Tomczyk S., Burkepile J. T. et al. (Apr. 2010). *Conceptual Design of the COSMO K-Coronagraph*. Tech. rep. High Altitude Observatory, National Center for Atmospheric Research.

Newkirk, Gordon and David Bohlin (Feb. 1963). "Reduction of Scattered Light in the Coronagraph". In: *Appl. Opt.* 2.2, pp. 131–140. DOI: 10.1364/AO.2.000131. URL: http://opg.optica.org/ao/abstract.cfm?URI=ao-2-2-131.

— (Apr. 1964). "Scattered Light in an Externally Occulted Coronagraph". In: *Appl. Opt.* 3.4, 543_1–544. DOI: 10.1364/AO.3.0543_1. URL: http://opg.optica.org/ao/abstract.cfm?URI=ao-3-4-543_1.

Noci, Giancarlo, John L. Kohl, and George L. Withbroe (Apr. 1987). "Solar Wind Diagnostics from Doppler-enhanced Scattering". In: *The Astrophysical Journal* 315, p. 706. DOI: 10.1086/165172. URL: https://ui.adsabs.harvard.edu/abs/1987ApJ...315..706N.

November, Laurence J. and Serge Koutchmy (July 1996). "White-Light Coronal Dark Threads and Density Fine Structure". In: *Astrophysical Journal* 466, p. 512. DOI: 10.1086/177528. URL: https://ui.adsabs.harvard.edu/abs/1996ApJ...466..512N.

Patsourakos, S. et al. (Nov. 2020). "Decoding the Pre-Eruptive Magnetic Field Configurations of Coronal Mass Ejections". In: *Space Science Reviews* 216.8, 131, p. 131. DOI: 10.1007/s11214-020-00757-9. arXiv: 2010.10186 [astro-ph.SR]. URL: https://ui.adsabs.harvard.edu/abs/2020SSRv..216..131P.

Phillips, K. J. H. (1992). *Guide to the Sun*. Cambridge University Press, New York.

PNRA (2021). *Programma nazionale di ricerca in Antartide*. cfr. https://www.pnra.aq/.

Priest, Eric (2014). *Magnetohydrodynamics of the Sun*. Cambridge University Press. DOI: 10.1017/CBO9781139020732.

Raouafi, N. E. (Apr. 2011). "Coronal Polarization". In: *Solar Polarization 6*. Ed. by J. R. Kuhn et al. Vol. 437. Astronomical Society of the Pacific Conference Series, p. 99. arXiv: 1104.0598 [astro-ph.SR]. URL: https://ui.adsabs.harvard.edu/abs/2011ASPC..437...99R.

Renotte, Etienne et al. (2015). "Design status of ASPIICS, an externally occulted coronagraph for PROBA-3". In: *Solar Physics and Space Weather Instrumentation VI*. Ed. by Silvano Fineschi and Judy Fennelly. Vol. 9604. International Society for Optics and Photonics. SPIE, pp. 71 –85. DOI: `10.1117/12.2186962`. URL: `https://doi.org/10.1117/12.2186962`.

Rochus, P. et al. (Oct. 2020). "The Solar Orbiter EUI instrument: The Extreme Ultraviolet Imager". In: *Astronomy & Astrophysics* 642, A8, A8. DOI: `10.1051/0004-6361/201936663`. URL: `https://ui.adsabs.harvard.edu/abs/2020A&A...642A...8R`.

Romoli, M. et al. (Dec. 2021). "First light observations of the solar wind in the outer corona with the Metis coronagraph". In: *Astronomy & Astrophysics* 656, A32, A32. DOI: `10.1051/0004-6361/202140980`. arXiv: `2106.13344 [astro-ph.SR]`. URL: `https://ui.adsabs.harvard.edu/abs/2021A&A...656A..32R`.

Rycroft, M.J. (1993). "Guide to the Sun: Phillips K. J. H., 1992, 386 pp. Cambridge University Press, ISBN 0-521-39483-X". In: *Journal of Atmospheric and Terrestrial Physics* 55.6, p. 937. ISSN: 0021-9169. DOI: `https://doi.org/10.1016/0021-9169(93)90037-Y`. URL: `https://www.sciencedirect.com/science/article/pii/002191699390037Y`.

Ryer, Alexander D. (1998). *Light Measurement Handbook*. International Light Inc. ISBN: 0-9658356-9-3. URL: `http://www.dfisica.ubi.pt/~hgil/fotometria/HandBook/Light-Measurement.1.pdf`.

Sasso, C. et al. (2022). "Multi-Perspective Space Observations of a Large Prominence Eruption". In: *Astronomy & Astrophysics* (in preparation).

Semrock (2019). *Bandpass filter*. URL: `https://www.semrock.com/SearchResults_Semrock.aspx?QueryExpr=FF01-591\%2f6-25+&ResultsPage=1`.

Shurcliff, W. A. (1962). *Polarized light: production and use*. Harvard University Press, pp. 29, 30 and ch.19.

Solanki, S. K. et al. (Oct. 2020). "The Polarimetric and Helioseismic Imager on Solar Orbiter". In: *Astronomy & Astrophysics* 642, A11, A11. DOI: `10.1051/0004-6361/201935325`. arXiv: `1903.11061 [astro-ph.IM]`. URL: `https://ui.adsabs.harvard.edu/abs/2020A&A...642A..11S`.

Soummer, Rémi et al. (Mar. 2011). "Apodized Pupil Lyot Coronagraphs for Arbitrary Apertures. III. Quasi-achromatic Solutions". In: *The Astrophysical Journal* 729.2, 144, p. 144. DOI: `10.1088/0004-637X/729/2/144`. URL: `https://ui.adsabs.harvard.edu/abs/2011ApJ...729..144S`.

Sparks, William B. and David J. Axon (1999). "Panoramic Polarimetry Data Analysis". In: *Publications of the Astronomical Society of the Pacific* 111.764, pp. 1298–1315. ISSN: 00046280, 15383873. URL: `http://www.jstor.org/stable/10.1086/316434`.

Streete J.L. (1989). *Calibration of the HAO Standard Opal Filter Set*. Tech. rep. URL: `https://opensky.ucar.edu/islandora/object/technotes%3A109/datastream/PDF/download/Calibration_of_the_HAO_Standard_Opal_Filter_Set.citation`.

Tiesinga, Eite et al. (May 2019). *NIST - Values of Fundamental Physical Constants*. URL: `https://www.nist.gov/pml/fundamental-physical-constants`.

Tomczyk, S. and D. Elmore (June 2015). *Sky Brightness at Mauna Loa and Haleakala*. Tech. rep. Mauna Loa Solar Observatory.

Tordi, M. et al. (2015). "Illumination system in visible light with variable solar divergence for the solar orbiter METIS coronagraph". In: *Solar Physics and Space Weather Instrumentation VI*. Ed. by Silvano Fineschi and Judy Fennelly. Vol. 9604. International Society for Optics and Photonics. SPIE, pp. 202 –216. DOI: `10.1117/12.2207475`. URL: `https://doi.org/10.1117/12.2207475`.

Tousey, Richard (Apr. 1961). "Solar Spectroscopy in the Far Ultraviolet". In: *J. Opt. Soc. Am.* 51.4, pp. 384–395. DOI: 10.1364/JOSA.51.000384. URL: http://www.osapublishing.org/abstract.cfm?URI=josa-51-4-384.

Van De Hulst, H. C. (Feb. 1950). "The electron density of the solar corona". In: *B.A.N.* 11, p. 135. URL: https://ui.adsabs.harvard.edu/abs/1950BAN....11..135V.

Vorobiev, Dmitry V., Zoran Ninkov, and Neal Brock (Apr. 2018). "Astronomical Polarimetry with the RIT Polarization Imaging Camera". In: *Publications of the Astronomical Society of the Pacific* 130.988, p. 064501. DOI: 10.1088/1538-3873/aab99b. URL: https://doi.org/10.1088/1538-3873/aab99b.

Weisstein, Eric W. (May 2022). *Constant*. cfr. mathworld.wolfram.com.

Wollaston, W. H. (Dec. 1802). "A Method of examining refractive and dispersive Powers, by prismatic Reflection". In: 92. DOI: https://doi.org/10.1098/rstl.1802.0014. URL: https://royalsocietypublishing.org/doi/10.1098/rstl.1802.0014.

Zangrilli, L. et al. (Jan. 2006). "EKPol: Liquid Crystal Polarimeter for Eclipse Observations of the K-Corona". In: *Solar Physics and Solar Eclipses (SPSE 2006)*, pp. 37–45. URL: https://ui.adsabs.harvard.edu/abs/2006spse.conf...37Z.

Zangrilli, Luca, Silvano Fineschi, and Gerardo Capobianco (Aug. 2009). "Calibration of the EKPol K-corona imaging polarimeter". In: *Solar Physics and Space Weather Instrumentation III*. Ed. by Silvano Fineschi and Judy A. Fennelly. Vol. 7438. Society of Photo-Optical Instrumentation Engineers (SPIE) Conference Series, 74380W, 74380W. DOI: 10.1117/12.827247. URL: https://ui.adsabs.harvard.edu/abs/2009SPIE.7438E..0WZ.

Zecchino, Mike (May 2017). *Polarization camera for image enhancement*. 4D Technology Corporation - PolarCam User Manual, https://www.4dtechnology.com/products/polarimeters/polarcam/.

Zender J. and Capobianco G. (May 2019). *2 July 2019 Total Solar Eclipse EKPOL Calibration Plan and Procedure*. Tech. rep.

Zhang, J. and K. P. Dere (Oct. 2006). "A Statistical Study of Main and Residual Accelerations of Coronal Mass Ejections". In: *The Astrophysical Journal* 649.2, pp. 1100–1109. DOI: 10.1086/506903. URL: https://ui.adsabs.harvard.edu/abs/2006ApJ...649.1100Z.

Zhang, Jun et al. (Feb. 2001). "Magnetic Flux Cancellation Associated with the Major Solar Event on 2000 July 14". In: *Astrophysical Journal Letters* 548.1, pp. L99–L102. DOI: 10.1086/318934. URL: https://ui.adsabs.harvard.edu/abs/2001ApJ...548L..99Z.